
**Investigation of Gas Storage/Separation,
Photophysical and Electrochemical Properties
of Metal-Organic Frameworks (MOFs) and
Derived Materials**

**A Thesis Submitted for the Degree of
Doctor of Philosophy**

By

NIVEDITA SIKDAR



Chemistry and Physics of Materials Unit (CPMU)
Jawaharlal Nehru Centre for Advanced Scientific Research
(A Deemed University)
Bangalore – 560064
February, 2017

DEDICATED

TO MY

MOTHER

DECLARATION

I hereby declare that the matter embodied in the thesis entitled “*Investigation of Gas Storage/Separation, Photophysical and Electrochemical Properties of Metal-Organic Frameworks (MOFs) and Derived Materials*” is the result of investigations carried out by me at the Chemistry and Physics of Materials Unit (CPMU), Jawaharlal Nehru Centre for Advanced Scientific Research (JNCASR), Bangalore, India under the supervision of Prof. Tapas Kumar Maji and that it has not been submitted elsewhere for the award of any degree or diploma.

In keeping with the general practice in reporting the scientific observations, due acknowledgements have been made whenever the work described is based on the findings of other investigators. Any omission that might have occurred due to oversight or error in judgement is regretted.

.....
Nivedita Sikdar

Date:

Bangalore 560064

CERTIFICATE

I hereby certify that the work described in this thesis entitled “*Investigation of Gas Storage/Separation, Photophysical and Electrochemical Properties of Metal-Organic Frameworks (MOFs) and Derived Materials*” has been carried out by Ms. Nivedita Sikdar under my supervision at the Chemistry and Physics of Materials Unit (CPMU), Jawaharlal Nehru Centre for Advanced Scientific Research (JNCASR), Bangalore, India and that it has not been submitted elsewhere for the award of any degree or diploma.

.....

Prof. Tapas Kumar Maji
(Associate Professor)
(Research Supervisor)

ACKNOWLEDGEMENTS

I wish to express my sincere gratitude to my research supervisor Prof. Tapas Kumar Maji for his kind support, criticism and valuable suggestions he has given me all through the course of these investigations. I have learnt so much by interacting with him both professionally and personally. I am thankful to him for giving me an opportunity to work under his guidance. I appreciate his constant effort and I am really grateful for his patience and positive attitude toward me during my down time.

I would like to thank Prof. S. Balasubramanian and Prof. C. Narayana, past and present chairmen, respectively, for their support and allowing me to use the facilities of the centre.

I thank Prof. C. N. R Rao, FRS, for allowing me to use various facilities at the centre.

I would like to thank Prof. S. Balasubramanian, Prof. S. Sundaresan, and Prof. T. K. Maji of JNCASR and Prof. T. N. Guru Row of IISc for their beneficial courses that has been extremely helpful to this study.

I would like to sincerely thank Prof. S. Balasubramanian (CPMU), Dr. Satyanarayana Bonakala (CPMU), Prof. Subi J George (NCU), Dr. K. V. Rao (NCU), Prof. U. V. Waghmare (TSU), Ms. M. Bhogra (TSU), Dr. S. Sampath (IISc), Dr. V. Kiran (IISc), Prof. W. Schuhmann (University of Bochum), Dr. B. Konkena (University of Bochum), Dr. J. Masa (University of Bochum), Prof. A. J. Bhattacharya (IISc), Dr. D. Dutta (IISc) for fruitful collaborations.

I sincerely acknowledge the technical staffs namely Mr. Anil, Mr. Vasu, Mr. Mahesh, Mrs. Usha, Mr. Joy, Ms. Selvi, Mr. Jagdish, Mr. Kanan, Mr. Shiva of JNCASR for their help with the various characterization techniques.

I thank JNCASR Library, Complab, Hostel, Health Centre, Academics and Administration staffs for providing and maintaining the various facilities that have helped me immensely.

I thank Ankit, Suman, Abhijit, Somnath, Dheeraj, Amrit, Manjit, Rajkumar, Ramkumar, Devendra, Moumita, Tarak, for their help in experiments and fruitful discussions.

I must thank my **MOLMAT lab** (second family). Their timely help in experiments, suggestions and cooperation have really made things much easier for me. I acknowledge my present lab mates Syamantak, Papri, Sohini, Subhajit, Parul, Dr. Siddhartha De, Dr. Debabrata Samanta, Dr. Sajad A. Bhat and my past lab mates Dr. Prakash Kanoo, Dr. Sudip Mohapatra, Dr. Jayaramulu K, Dr. Ritesh Halder, Dr. Arpan Hazra, Dr. Suresh Mothika, Dr. Anindita Chakaraborty, Ms. Komal and Mr. Deena from the bottom of my heart. I want to thank especially, Dr Ritesh Halder and Dr. Arpan Hazra for teaching various instrumental techniques from scratch. I appreciate my labmates' contribution for creating and maintaining such a vibrant, positive and friendly atmosphere in lab.

I thank all SRFP and POCE students, especially Turjya, Supriya and Souvik for working with me.

I want to thank Supreeti Mam for her wonderful gesture, lots of food, especially Muffins, and Neel, Sonai for their lovely company.

My cordial thanks are to my all friends and well-wishers in JNCASR. Their support and encouragement have been an indispensable in my PhD life.

Particularly, I thank all my Table tennis friends for their wonderful company. I am really grateful to Somnath for his endless patience (and holding his anger and not throwing bat at me!) during teaching me.

I also thank all school, college and university teachers for guiding me to this stage and shaping me into a better person.

Last but not the least, my heartfelt thanks to my parents (Mrs. Minati Sikdar and Mr. Ashim Sikdar), elder sister Nabanita, brother-in-law Abhijit da and nephew Arka for being the pillars of my life. Their advices and encouragements have been the most valuable support during those critical periods of my PhD tenure. I also thank my few beloved ones for their endless support, timely advices and encouragements. I really don't know if there is any perfect word in dictionary to express my acknowledgments to them. I can't imagine a single moment without their love, affection for me. Thanks for accepting me and loving me the way I am. This thesis is a humble offering to the most beautiful person of my life: **MY BELOVED MOTHER**. I have no words to express that how much grateful and proud I am as your child.

PREFACE

The thesis is organized in five chapters and first four chapters report the MOFs in gas-storage/separation and photophysical properties in bulk/nanoscale. Final Fifth chapter describes about MOF-derived nanostructured materials for fuel cell applications.

Chapter 1 gives a brief overview of functional metal-organic frameworks (MOFs) and MOF-derived materials, discusses their importance, properties and potential applications.

Chapter 2 reports selective hydrocarbon (C₂-C₃) storage, CO₂ capture and separation, based on a two-fold interpenetrated dynamic framework $\{[\text{Zn}_2(\text{bdc})_2(\text{bpNDI})] \cdot 4\text{DMF}\}_n$ (H₂bdc = 1,4-benzenedicarboxylic acid, bpNDI = N,N'-bis-(4-pyridyl)-1,4,5,8-naphthalenediimide). Framework showed guest responsive structural change based on the movements of the entangled networks and such dynamics is reflected in stepwise CO₂ and C₂H₂ uptake at 195 K. Framework also showed significant amount of CO₂ and C₂H₂ hydrocarbon uptake at 298 K but completely exclude CH₄ and N₂. Density functional theory (DFT) calculations infer the imide and aromatic π -electrons of the aromatic rings as preferable interaction sites for CO₂ and hydrocarbons. Breakthrough column experiments for binary gas mixtures, CO₂/CH₄, C₂H₆/CH₄ and CO₂/N₂ at 298 K further establishes the separation capability of this framework.

Chapter 3 comprises of two parts: **Part 3A** describes synthesis of a novel redox-active multichromophoric two-fold interpenetrated framework $\{[\text{Cd}(\text{bpdc})(\text{bpNDI})] \cdot 4.5\text{H}_2\text{O} \cdot \text{DMF}\}_n$ (H₂bpdc = 4,4'-biphenyldicarboxylic acid). This framework exhibits a unique photochromic behaviour resulting from inter-net strut-to-strut electron transfer. Furthermore, encapsulation of electron rich guest molecules (e.g. 1,5-/2,6-dinaphthol (1,5/2,6-DAN) and 4,N,N-trimethylaniline (DMPT)) into the electron deficient channels of this framework leads to very stable charge-separated states in ground state.

Part 3B describes synthesis, structural characterizations, and photophysical properties of a non-interpenetrated pillared layer framework

$\{Zn_2(adc)_2(bpNDI)\cdot 4H_2O\cdot 4DMF\}_n$ [$H_2adc = 9,10$ -anthracenedicarboxylic acid]. The donor adc ligands being orthogonally oriented with the acceptor bpNDI linkers in as-synthesized framework, involve in charge transfer (CT) interactions which transforms into complete charge separated state (electron transfer; ET) due to associated structural changes after removal of guest DMF molecules. The PXRD, TGA, 1H NMR data suggest that the residing DMF molecules in the big void space of **1** tends to come out at ambient condition probably due to poor interaction with the framework sites causing accommodation of extra water molecules which facilitates the hydrolyzation of paddle wheel SBUs and changes the overall structure. This structural transformation helps to bring close proximity of donor and acceptor molecules resulting into better π -cloud overlap and complete charge separated state.

Chapter 4 comprises of two parts: **Part 4A** describes synthesis, structural characterizations and gas storage properties of two new two-fold interpenetrated 3D frameworks, $\{[Zn_2(bpdc)_2(azpy)]\cdot 2H_2O\cdot 2DMF\}_n$ (**1**) and $\{[Zn_3(bpdc)_3(azpy)]\cdot 4H_2O\cdot 2DEF\}_n$ (**2**) [$azpy = 4,4'$ -azobipyridine], obtained from a same set of organic linkers by changing the solvent system at different temperatures. Furthermore, **1** has been successfully miniaturized to nanoscale with spherical morphology. The nanoscale MOF shows higher CO_2 uptake properties at 195 and 293 K compared to its bulk counterpart due to lesser diffusion barrier as realized by adsorption kinetics.

Part 4B describes nano/mesoscale synthesis, characterization and growth mechanism of a mixed-linker based 3D MOF, $\{[Zn_2(H_2dht)(dht)_{0.5}(azpy)_{0.5}(H_2O)]\cdot 4H_2O\}_n$ [$H_2dht = 2,5$ -dihydroxyterephthalic acid] fabricated by the coordination modulation method (modulator = n -dodecanoic acid). A tunable morphological transition (hexagonal nanoparticle-nanorod-mesosheet) is observed on alteration in the modulator concentration. The observed morphologies were further investigated by time-dependent experiments which suggest that change in dimensionality 0D-1D-3D is driven by kinetically controlled oriented attachment (OA) growth mechanism. Among all the morphology-controlled NMOFs, hexagonal nanoparticle shows strikingly improved BET surface area (~ 133 fold increment) compared to the analogous bulk (On-Off N_2 porosity) due to decreased diffusion barrier assisted by higher mass transfer kinetics in nanoscale and also supported by theoretical studies.

Chapter 5 comprises of two parts: in **Part 5A**, a dual-MOFs pyrolysis strategy has been employed for the preparation of Fe₃O₄-Co₃O₄@Co embedded N-doped carbon nanotube (N-CNTs) as efficient bi-functional electrocatalysts. Distinct from previous studies, the present synthetic strategy relies on the carbonization of Fe-based mesoscale rods along with Co-based ZIF-67 hexagonal crystals, which results into Fe₃O₄-Co₃O₄@Co/NCNT electrocatalyst. The introduction of ZIF-67 with the co-precursor Fe-MOF guarantees *in situ* homogeneously Fe₃O₄ and core-shell Co₃O₄@Co nanoparticles' distribution in NCNTs, and this has shown satisfactory electrocatalytic activity for both the oxygen reduction reaction (ORR) and oxygen evolution reaction (OER) processes. The figure of merit value of this bi-functional electrocatalyst i.e. total overpotential difference of ORR at -1 mA cm⁻² and OER at 10 mA cm⁻² is 0.91 V, which is much lower than the state-of-art catalysts (e.g. Pt/C, RuO₂, IrO₂ etc.) examined in this chapter.

Part 5B describes synthesis of bi-functional electrocatalysts, Co₃O₄@Co/NCNT and Co-GCN derived from a novel dicyanamide based nitrogen rich framework {[Co(bpe)₂(N(CN)₂)]·(N(CN)₂)·(5H₂O)}_n [Co-MOF-1, bpe = 1,2-bis(4-pyridyl)ethane, N(CN)₂⁻ = dicyanamide]. Pyrolysis of Co-MOF-1 under Ar atmosphere (at 550 °C) yielded Co/CoO nanoparticles embedded N-doped porous carbonaceous matrix (Co-GCN). While pyrolysis under a reductive H₂ atmosphere at higher temperature (at 800 °C) and further mild calcination yielded Co₃O₄@Co core-shell nanoparticles encapsulated in N-doped carbon nanotubes (Co₃O₄@Co/NCNT). However, the Co₃O₄@Co/NCNT nanostructure exhibited superior electrocatalytic activity for both the ORR with a potential of 0.88 V at a current density of -1 mA cm⁻² and the OER with a potential of 1.61 V at 10 mA cm⁻². The difference between the overpotential did not exceed 0.73 V for the Co₃O₄@Co/NCNT catalyst, suggesting that the Co₃O₄@Co/NCNT catalyst is one of the best bi-functional OER and ORR catalysts reported so far.

In summary, in this thesis, we have exploited metal-organic frameworks (MOFs) for various potential applications such as gas storage and separation, photophysical and electrocatalysis in bulk and nanoscale. The idea of blending multifunctional linkers and framework dynamicity together made us to synthesize different mixed-linkers based flexible or interpenetrated frameworks. We have chosen a long linker bpNDI (N,N'-bis-(4-pyridyl)-1,4,5,8-naphthalenediimide) and by tuning the length and size of the carboxylate linkers we could achieve interpenetrated and non-interpenetrated

frameworks. We have first studied the gas storage/separation of one of such interpenetrated frameworks in chapter 2 and have shown that how framework flexibility affects in selective gas uptake and separation behaviour. It is important to mention that, bpNDI is a redox-active molecule and well-known as electron acceptor. Therefore, we continued synthesizing further new bpNDI based MOFs for studying redox-activity in MOFs. Two new bpNDI based frameworks have been synthesized in chapter 3. In chapter 3A, we observed unique inter-net strut/guest-to-strut electron transfer in a same framework for the first time. Using bulkier ligand in chapter 3B, a non-interpenetration framework has been synthesized and we discover reversible guest dependent charge transfer (CT)-electron transfer (ET) process assisted by structural change. Therefore, chapter 2 and 3 detail systematic overview of interpenetrated framework synthesis, controlling interpenetration and their implications in gas storage/separation and photophysical studies such as strut-to-strut and guest-to-strut reversible/irreversible photoinduced electron transfer.

The next aspect of this thesis is downsizing bulk MOF to nanoscale and understanding nano MOFs growth and subsequent mechanistic pathway analysis (chapter 4). For the first time, we have scaled down an interpenetrated framework in nanoscale and studied relative gas adsorption characteristics (chapter 4A). Although, an extensive research has been documented in literature regarding bulk MOF crystallization process but controlling size/morphology of nanoscale MOF is still underexplored. In chapter 4B, we have shown MOF downsizing to multidimensional nano/mesoscale morphologies and for the first time, we have observed a 0D→1D→2D morphological transformation driven by kinetically controlled oriented attachment growth mechanism. We have further shown how size/morphology can control the inherent microporosity of a framework, which has been further implemented in CO₂/N₂ gas separation under ambient condition. Hence, this chapter details deliberate MOF downsizing in nanoscale, analysis of crystal growth mechanism and effect of size/morphology in adsorption properties.

Lastly, in final chapter 5, we have worked on MOF-derived porous carbon materials as electrocatalysts in fuel cell applications. This is a new cutting-edge field started due to high demand of stable and efficient cheap electrode materials. Here, we have synthesized mixed-metal oxides and core-shell nanoparticles embedded carbon nanotube matrix by pyrolyzing MOFs under different conditions. Importantly, these catalysts show better bi-

functional activity compared to state-of-art Pt/C, RuO₂ and IrO₂ catalysts. In summary, this chapter details utilisation of MOFs as self-sacrificial template for electrocatalytic applications.

Table of Contents

Chapter 1	1
<i>Introduction</i>	3
1.1 Introduction of metal-organic frameworks (MOFs): An overview.....	3
1.2 Synthetic methodologies and classifications of MOFs	5
1.3 Applications	8
1.3.1 Gas storage and separation	9
1.3.2 Selective CO ₂ capture and separation	10
1.3.3 H ₂ storage	13
1.3.4 Hydrocarbon storage and separation	14
1.4 Photophysical studies: Photochromism in MOFs and host-guest chemistry	16
1.5 Nanoscale metal-organic frameworks (NMOFs)	19
1.6 Synthetic strategies.....	21
1.7 Applications of nanoscale MOF.....	23
1.8 MOF-derived carbonaceous materials for various applications.....	26
1.8.1 Gas storage of carbonaceous matrix.....	28
1.8.2 In fuel cell applications	28
1.8.2.1 Oxygen reduction reaction (ORR)	29
1.8.2.2 Oxygen evolution reaction (OER).....	33
1.9 Bi-functional electrocatalysts for ORR and OER	37
1.10 Conclusion.....	39
1.11 References.....	40
Chapter 2	49
<i>Dynamic Entangled Porous Framework for Hydrocarbon (C2-C3) Storage, CO₂ Capture and Separation</i>	51
2.1 Introduction	52
2.2 Experimental section	53
2.2.1 Materials.....	53

2.2.2 Synthesis of $\{[\text{Zn}_2(\text{bdc})_2(\text{bpNDI})]\cdot 4\text{DMF}\}_n$ (1)	54
2.2.3 Physical Measurements	54
2.2.4 Adsorption study	54
2.2.5 Calculation of isosteric heat of adsorption	55
2.2.5.1 Virial fitting of pure component isotherms for CO_2 , C_2H_2 and C_2H_6	55
2.2.5.2 Langmuir-Freundlich fitting of pure component isotherms for CH_4	56
2.2.6 Selectivity prediction for binary gas mixtures	57
2.2.7 CO_2/CH_4 , $\text{C}_2\text{H}_6/\text{CH}_4$ and CO_2/N_2 breakthrough column measurements	57
2.2.8 Computational details.....	57
2.3 Results and discussion.....	60
2.3.1 Structural dynamics of the entangled framework 1	60
2.3.2. Permanent porosity and polarity of the pore surface.....	63
2.3.3 CO_2 Capture: Structural dynamics correlated with computational studies	65
2.3.4 Hydrocarbon ($\text{C}_1\text{-C}_3$) adsorption.....	70
2.3.5 Selectivity studies: CO_2 , C_2H_2 , C_2H_4 C_2H_6 vs. CH_4 and CO_2 vs. N_2	77
2.4 Conclusion.....	83
2.5 References	83

Chapter 3

Chapter 3A	89
------------------	----

Redox-Active Metal-Organic Frameworks: Highly Stable Charge-Separated States via Strut/Guest-to-Strut Electron Transfer

3A.1	
Introduction.....	92
3A.2 Experimental section.....	93
3A.2.1 Materials.....	93
3A.2.2 Physical measurements	94
3A.2.3 Electrochemical studies.....	94
3A.2.4 X-ray crystallography	94
3A.2.5 Adsorption studies.....	95

3A.2.6 Synthesis of $\{[\text{Cd}(\text{bpdc})(\text{bpNDI})]\cdot 4.5\text{H}_2\text{O}\cdot \text{DMF}\}_n$ (1).....	95
3A.2.7 Preparation of 1@2,6-DAN, 1@1,5-DAN and 1@DMPT	95
3A.3. Results and discussion	98
3A.3.1 Structural description of 1	99
3A.3.2. TGA, PXRD and permanent porosity	101
3A.3.3 Photophysical properties of 1	102
3A.3.4 Guest encapsulation in the redox active framework 1	108
3A.3.5 Electrochemical studies.....	110
3A.4 Conclusion	111
3A.5 References.....	112
Chapter 3B	115
<i>Redox-Active 3D Charge Transfer MOF: Solvent Responsive Reversible Strut-to-Strut Electron Transfer</i>	117
3B.1 Introduction	118
3B.2 Experimental section	119
3B.2.1 Materials.....	119
3B.2.2 Physical measurements	120
3B.2.3 X-ray crystallography.....	120
3B.2.4 Electrochemical studies.....	121
3B.2.5 Adsorption study	121
3B.2.6 Syntheses of $\{\text{Zn}_2(\text{adc})_2(\text{bpNDI})\}\cdot 4\text{H}_2\text{O}\cdot 4\text{DMF}\}_n$ (1)	121
3B.3 Results and discussion.....	122
3B.3.1 Crystal structure description of $\{\text{Zn}_2(\text{adc})_2(\text{bpNDI})\}\cdot 4\text{H}_2\text{O}\cdot 4\text{DMF}\}_n$ (1)	122
3B.3.2 PXRD, thermal stability and ^1H NMR analyses	124
3B.3.3 FT-IR and Raman spectroscopy	126
3B.3.4 Adsorption studies.....	129
3B.3.5 Photophysical studies	129
3B.3.6 Electrochemical studies.....	131
3B.4 Conclusion.....	132

3B.5 References	133
-----------------------	-----

Chapter 4

Chapter 4A	137
-------------------------	-----

Stoichiometry-Controlled Two Flexible Interpenetrated Frameworks: Higher CO₂ Uptake in a Nanoscale Counterpart Supported by Accelerated Adsorption Kinetics .. 139

4A.1 Introduction	140
4A.2 Experimental section	142
4A.2.1 Materials	142
4A.2.2 Physical measurements	142
4A.2.3 X-ray crystallography	143
4A.2.4 Adsorption study	143
4A.2.5 Analysis of gas adsorption isotherms	144
4A.2.6 Synthesis of {[Zn ₂ (bpdc) ₂ (azpy)]·2H ₂ O·2DMF} _n (1)	145
4A.2.7 Synthesis of {[Zn ₃ (bpdc) ₃ (azpy)]·4H ₂ O·2DEF} _n (2)	145
4A.2.8 Synthetic procedure for nanosphere (MOF1N)	146
4A.3 Results and discussion	146
4A.3.1 Crystal structure description of {Zn ₂ (bpdc) ₂ (azpy)]·2H ₂ O·DMF} _n (1) and {[Zn ₃ (bpdc) ₃ (azpy)]·4H ₂ O·2DEF } _n (2)	146
4A.3.2 TGA and PXRD analyses	153
4A.3.3 Characterizations of nanoscale MOF (MOF1N)	156
4A.3.4 Adsorption studies	158
4A.3.5 Solvent vapour adsorption isotherms	161
4A.4 Conclusion	164
4A.5 References	165

Chapter 4B	169
-------------------------	-----

Oriented Attachment Growth of Anisotropic Meso/Nanoscale MOFs: Tunable Surface Area and CO₂ separation .. 171

4B.1 Introduction	172
4B.2 Experimental section	174
4B.2.1 Materials	174

4B.2.2 Physical measurements	174
4B.2.3 Adsorption studies.....	175
4B.2.4 Preparation of SEM and TEM samples.....	176
4B.2.5 Computational details.....	176
4B.2.6 Synthesis of bulk 1	176
4B.2.7 Synthesis of hex-MOF1, rod-MOF1 and meso-MOF1 using dodecanoic Acid (dda) as a modulator.....	177
4B.3 Results and discussion.....	178
4B.3.1 Modulation of bulk framework to nanoscale	178
4B.3.2 Surface energy calculation	186
4B.3.3 Adsorption studies.....	188
4B.3.4 Theoretical perspective	191
4B.4 Conclusion.....	195
4B.5 References	196

Chapter 5

Chapter 5A	199
<i>Dual-MOFs Derived Bi-functional Electrocatalyst Fe₃O₄-Co₃O₄@Co/NCNT for Oxygen Reduction and Evolution Reactions</i>	201
5A.1 Introduction.....	202
5A.2 Experimental section.....	203
5A.2.1 Materials.....	203
5A.2.2 Synthesis of single crystals of {[Fe(1,4-ndc)(μ -OH)](H ₂ O)} _n (Fe-ndc-1) and mesoscale Fe-ndc (meso-Fe-ndc)	204
5A.2.3 Synthesis of dual-MOFs (Fe-ndc +ZIF-67)	204
5A.2.4 Synthesis of mixed-metallic Fe ₃ O ₄ -Co ₃ O ₄ @Co/NCNT	205
5A.2.5 Physical characterizations	205
5A.2.6 Adsorption measurements.....	205
5A.2.7 X-ray crystallography	206
5A.2.8 Electrochemical measurements.....	206
5A.3 Results and discussion	208
5A.3.1 Structural features of {[Fe(1,4-ndc)(μ -OH)](H ₂ O)} _n (Fe-ndc-1)	208
5A.3.2 Thermal stability and PXRD patterns of Fe-ndc-1	210

5A.3.3 Characterizations of meso-Fe-ndc	211
5A.3.4 Characterizations of dual-MOFs (Fe-ndc + ZIF-67)	211
5A.3.5 Characterizations of dual-MOFs -derived catalyst Fe ₃ O ₄ -Co ₃ O ₄ @Co/NCNT	212
5A.3.6 Electrochemical activity and stability of Fe ₃ O ₄ -Co ₃ O ₄ @Co/NCNT	216
5A.4 Conclusion	221
5A.5 References	221
Chapter 5B	227
<i>Co₃O₄@Co/NCNT Nanostructure Derived from a Dicyanamide Based Metal-Organic Framework as Efficient Bi-functional Electrocatalyst for Oxygen Reduction and Evolution Reactions</i>	229
5B.1 Introduction	230
5B.2 Experimental section	232
5B. 2.1 Materials.....	232
5B. 2.2 Synthesis of {[Co(bpe) ₂ (N(CN) ₂)]·(N(CN) ₂)(5H ₂ O)} _n (Co-MOF-1).....	232
5B.2.3 Syntheses of Co-MOF-1 derived electrocatalysts.....	233
5B.2.3.1 Synthesis of Co-GCN.....	233
5B.2.3.2 Synthesis of Co ₃ O ₄ @Co/NCNT.....	233
5B.2.4 Physical characterizations	233
5B.2.5 Adsorption measurements	234
5B.2.6 Electrochemical measurements	234
5B.3 Results and discussion.....	236
5B.3.1 Characterizations of MOF derived composites.....	236
5B.3.2 Electrocatalytic activity and stability	242
5B.4 Conclusion.....	249
5B.5 References	249
Summary of thesis and future outlook	253

Chapter 1

Introduction

1.1 Introduction of metal-organic frameworks (MOFs): An overview

Metal-organic frameworks (MOFs) or porous coordination polymers (PCPs) are a class of crystalline hybrid materials consisting of infinite array of metal ions/clusters (Figure 1-4) and functionalized organic linkers, connected *via* coordination bonds.¹⁻⁴ These frameworks are modular in nature and follow easy synthetic conditions. It has drawn considerable attention because a large number of structures of different topologies would be possible to synthesize through exploitation of both ligand functionality and nature of metal ions.⁵ The potential advantages of these novel crystalline materials over the contemporary porous materials such as zeolites or porous carbons can be comprehended by their promising applications in gas storage and separation, molecular sensing, catalysis, optics and electronics.⁶⁻¹⁰ Apart from the traditional bulk MOFs, nanoscale MOFs are also of great

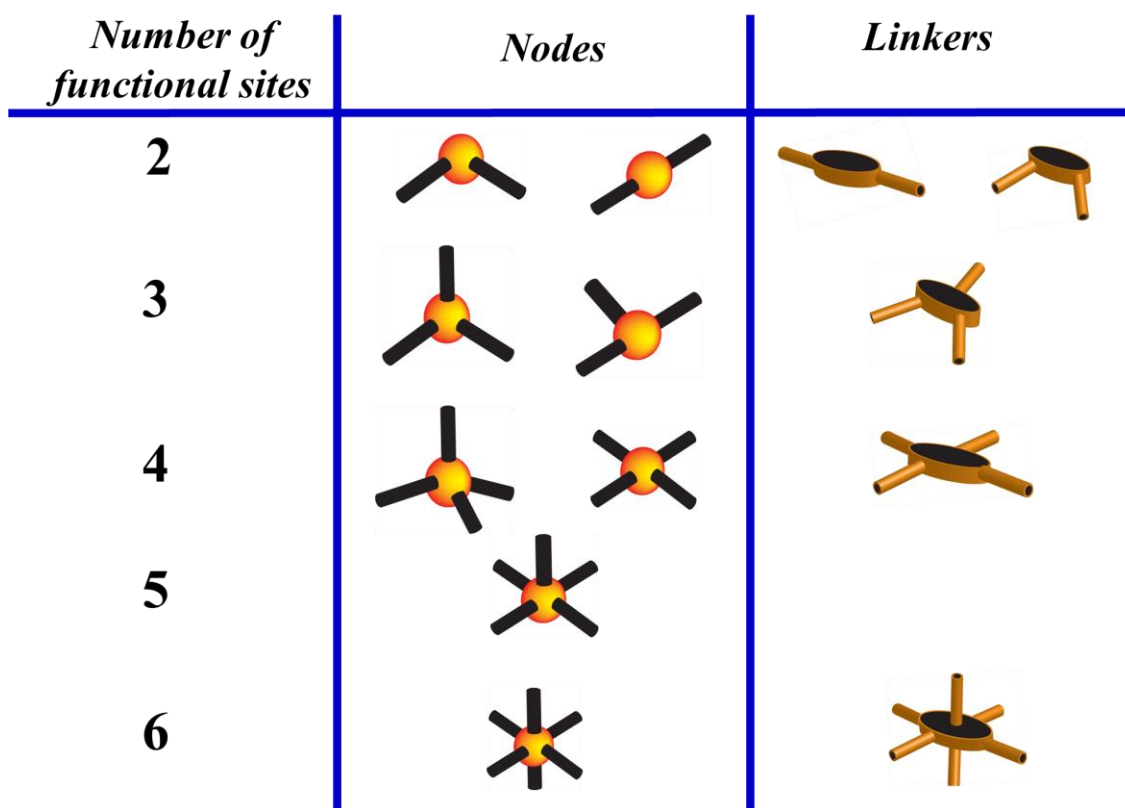


Figure 1: Schematic representation of different types of metal nodes and linkers constituting metal-organic framework.

significance. Downsizing of the MOF particles' size can lead to highly improved adsorption and electronic properties.¹¹ Moreover, nanoscale MOFs are suitable for their utilization in devices for various technologies.^{11c} In this thesis, a significant portion of work has been devoted towards the understanding of nanoscale morphology of MOFs and their structure property relationship. Further, in recent past, MOF derived materials, e.g., metal/metal-oxide doped porous carbon nitride composite materials, have also drawn significant attention owing to their encouraging electrocatalytic applications.¹²⁻¹⁵ In this introductory chapter of the thesis, the possible synthetic methods of MOFs, classifications and possible applications of bulk MOFs, nanoscale MOFs and their advantages over bulk MOFs have been introduced. Subsequently, MOF-derived metal/metal-oxide@carbon materials have been studied for fuel cell applications and finally the future direction of these materials have been discussed.

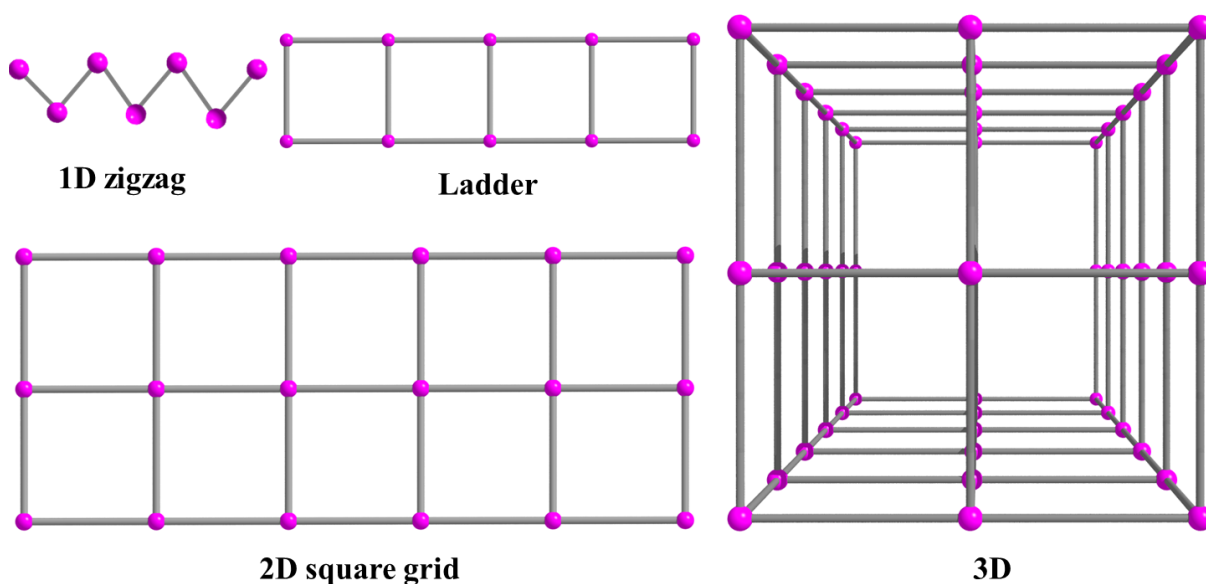


Figure 4: Different dimensionalities of MOFs constructed from nodes and linkers.

1.2 Synthetic methodologies and classifications of MOFs

Synthesis of MOFs can be achieved in ambient or solvo/hydrothermal conditions using metal salts viz. nitrates, sulfates or acetates in combination with functionalized organic linkers, e.g., mono-, di-, tri- and tetracarboxylic acids or N-pyridyl based linkers.¹⁶ Solvent system can be varied from aqueous to organic. Several conditions such as metal/linker stoichiometry, nature of metals, structure/functionality of ligands, temperature, solvent and

pH play pivotal role in determining the final structure of the resulting MOFs. Recently, more advanced techniques such as microwave heating (MW), electrochemical synthesis (EC), ultrasonic methods (US) and mechanochemical synthesis (MC), have been adopted for improvising MOF synthesis (Figure 5).¹⁶

In 1998, Kitagawa *et al.* made a classification of MOFs in three categories, viz. first, second and third generations depending on their structural response upon guest/solvent removal or exchange (Figure 6).¹⁷ The first-generation MOF structures collapse irreversibly after removal of the guest molecules, implying, the absence of permanent porosity in the framework. The second generation has stable and robust structures, which maintain the original porous structures even after the removal/exchange of the guest. Thus, these are useful adsorbents and can be regarded as analogous to zeolites. The third-generation MOFs have flexible or dynamic porous structure, which can reversibly or irreversibly respond to different external stimuli. A wide range of chemistry can be exploited with the third-generation porous solids.

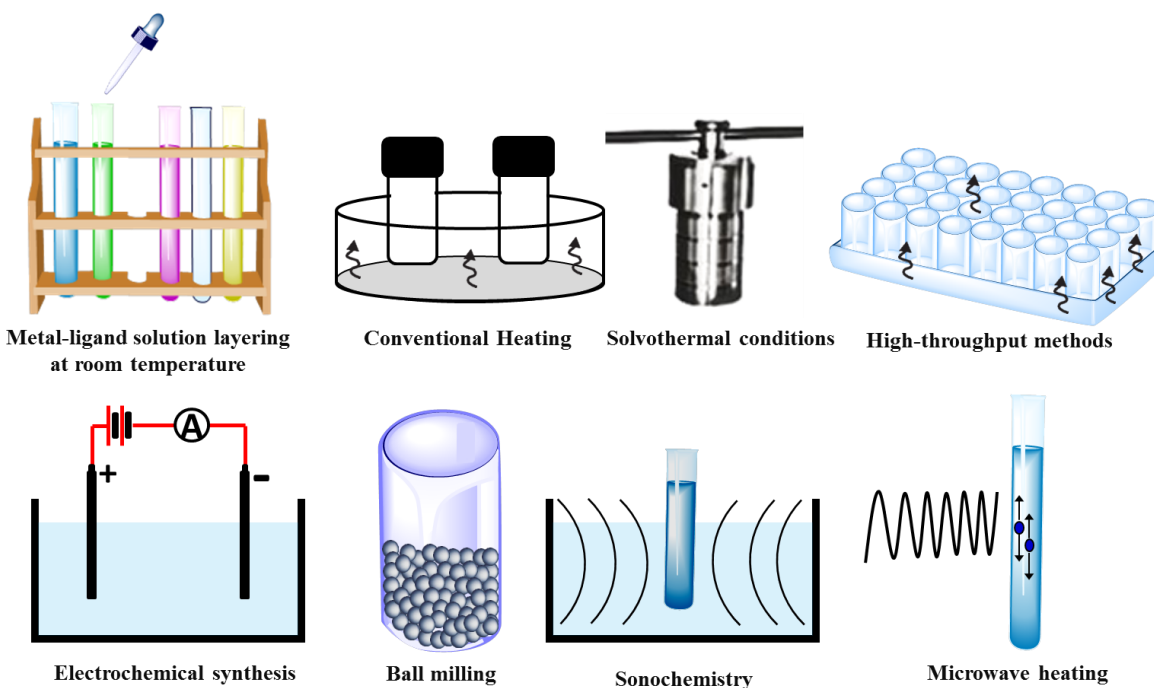


Figure 5: Overview of different syntheses methods in MOF synthesis.

The second and third generation structures, often regarded as rigid and flexible MOFs, respectively, have quite significant differences in their applicability. Rigid structures

having regular and open channel can accommodate a wide range of guest molecules, and hence are promising materials for storage applications. Yaghi *et al.* showed a strategy based on reticulating metal ions and organic carboxylate linkers into rigid 3D extended networks possessing particular $[\text{Zn}_4\text{O}(\text{COO})_6]$ secondary building unit (SBU), to design porous structures in which pore size and functionality could be varied rationally by changing length and functional groups of the linkers (Figure 7).¹⁸ In case of flexible MOFs, structural transformation upon guest removal/exchange is often very drastic. Their structural response towards guest molecules is primarily dependent on several parameters, e.g., (a) chemical nature of the guest molecule, (b) extent of pore deformation and size of the pore window, (c) onset pressure (d) temperature etc.¹⁹⁻²⁰ Guest molecules with significant dipole/quadrupole moment can induce strong interactions with the polar pore surfaces and ultimately diffuse into the channel at definite onset pressure, known as gate opening pressure.¹⁹⁻²⁰ This is very important from the perspective of gas storage, separation and selectivity since only certain molecules will be able to interact whereas other molecules are rejected.

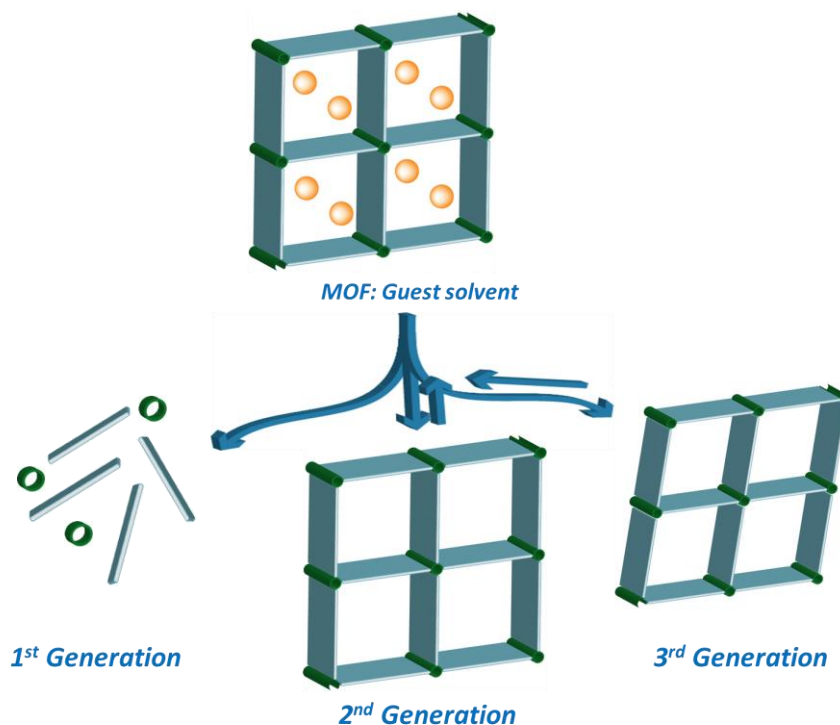


Figure 6: Classification of MOFs into three generations, first, second (rigid) and third (flexible) based on their structural response upon guest removal.

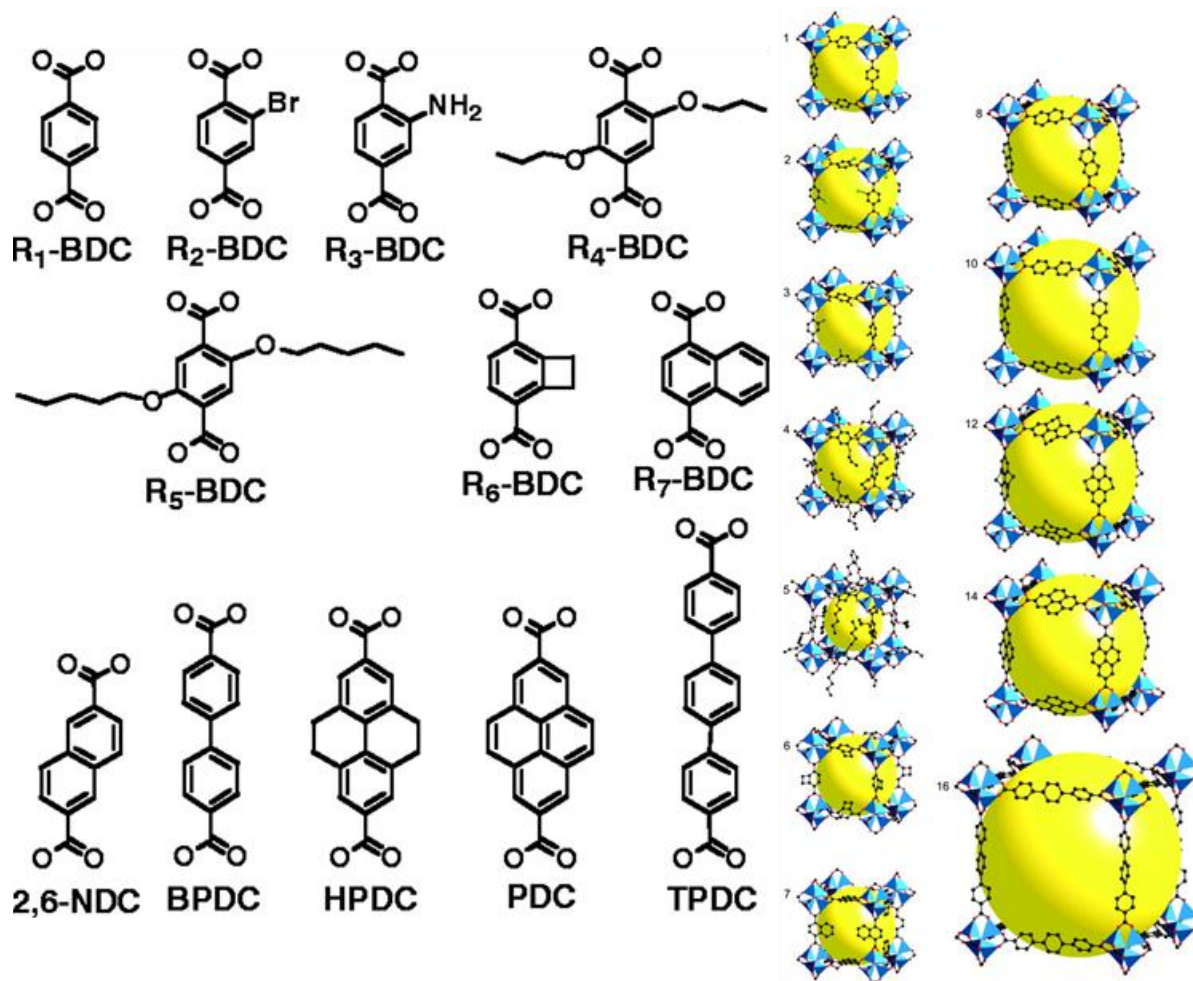


Figure 7: Single crystal X-ray structures of IRMOF-*n* (*n* = 1 to 7, 8, 10, 12, 14, and 16), labelled, respectively. Color scheme is as follows: Zn (blue polyhedra), O (red spheres), C (black spheres), Br (green spheres in 2), amino-groups (blue spheres in 3). The large yellow spheres represent the largest van der Waals spheres that would fit in the cavities without touching the frameworks. From reference 18. Reproduced by permission from *Science*.

1.3 Applications

MOFs are versatile in terms of structural topology and applications. Presence of inorganic metal ions/clusters and organic counterpart make this material potentially attractive for various applications e.g. gas storage and separation, catalysis, magnetism, sensing etc. In this part, mainly gas storage/separation and photophysical properties have been discussed. A schematic appended below briefly summarizes the various possible applications of MOFs (Figure 8).

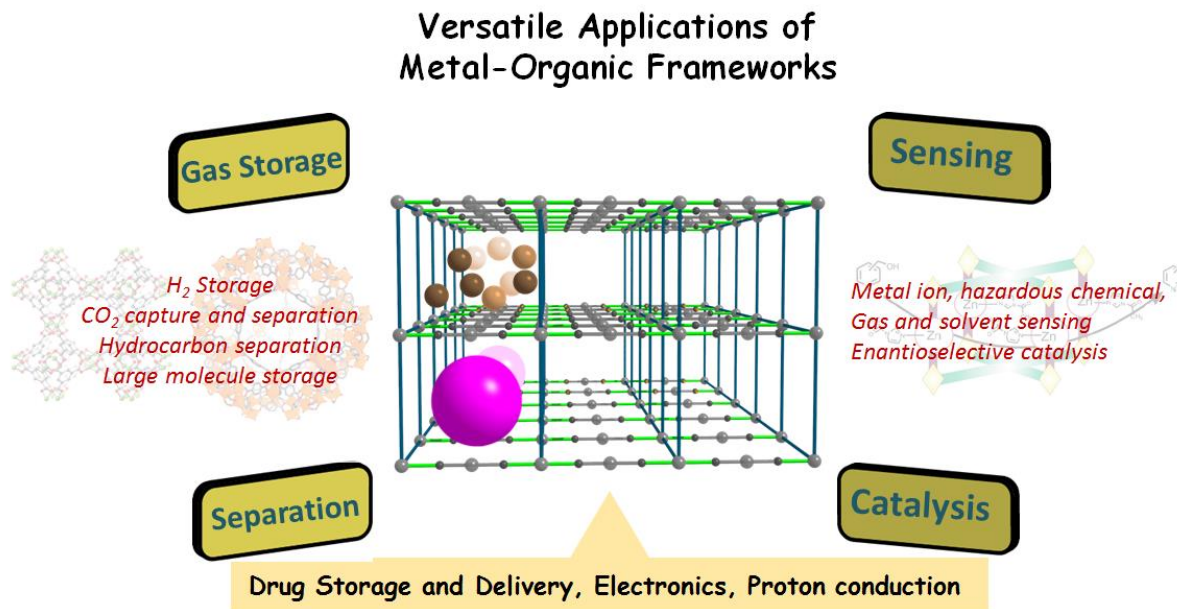


Figure 8: Potential applications of MOFs in different fields.

1.3.1 Gas storage and separation

High capacity of gas storage with selectivity is one of the characteristic features of porous materials. MOFs have already manifested their potential as practically viable gas storage and separation materials. In terms of surface area, these crystalline materials have surpassed their other contemporaries e.g. zeolites or porous carbons. The highest surface areas reported in MOFs till date is $7140 \text{ m}^2 \text{ g}^{-1}$ for NU-110 (NU-Northwestern University) (Figure 9).²¹ Some of the other landmark examples of high surface area MOFs are MOF-177 (surface area, $5640 \text{ m}^2 \text{ g}^{-1}$),²² MIL-101 (surface area, $5900 \text{ m}^2 \text{ g}^{-1}$),²³ UMCM-2 (surface area, $6000 \text{ m}^2 \text{ g}^{-1}$)²⁴ and MOF-210 (surface area, $6240 \text{ m}^2 \text{ g}^{-1}$)²⁵. Featuring such high surface area also promotes these materials as H_2 , CH_4 and other small hydrocarbon storage materials.²⁶⁻²⁷ The other advantage of using such materials is their structural modularity which leads to selective adsorption and separation. Sequestration of CO_2 and selective adsorption/separation of hydrocarbons are thus the primary task for MOFs.²⁸ In this thesis, high capacity of selective adsorption of CO_2 and small (C1-C3) hydrocarbons and separation of different gas mixtures using a breakthrough column experiments have been highlighted. Details of the works are mentioned in the respective sections; however, in this introductory chapter, an insight of the present status and future perspective are provided.

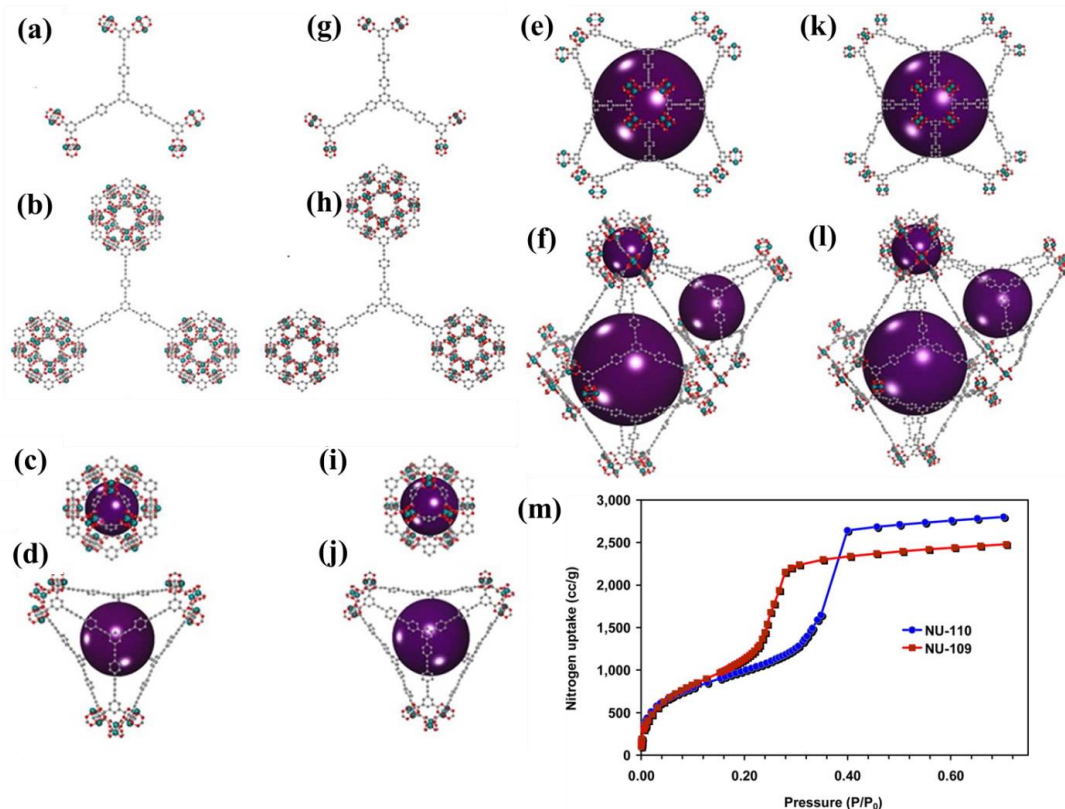


Figure 9: (a–f) Representations of the single-crystal X-ray structure of NU-109 showing: (a) LH₆ connecting six paddlewheel units, (b) cubaooctahedral building blocks, (c–f) different cages, (g–l) representations of the single-crystal X-ray structure of NU-110 showing (g) LH₆ connecting six paddlewheel units, (h) cubaooctahedral building blocks, (i–l) different cages. carbon = grey; oxygen = red; copper = teal. Purple spheres are different cages. From reference 21. Reproduced by permission from *J.Am.Chem.Soc.*

1.3.2 Selective CO₂ capture and separation

Selective capture of CO₂ is an important aspect that can be addressed using MOFs as the capturing porous matrix.²⁸ Importance of CO₂ capture is evident as rising level of this greenhouse gas marks a serious threat to our environment. Particularly post combustion of fossil fuels gives rise to such high level of CO₂ at atmosphere (406.07 ppm in February, 2017). Hence, selective capture of CO₂ at ambient/high temperature and low partial pressure conditions is important. In this regard, a numerous number of MOFs have been reported till date and a detail account of those have been described recently by Long *et al.* and Zhou *et al.*^{28b-c} It is important to mention that, at 1 atm, Mg-MOF-74 shows highest storage capacity of 27.5 wt% at 298 K.^{28b} On the other hand, at 35 bar, the volumetric CO₂ adsorption

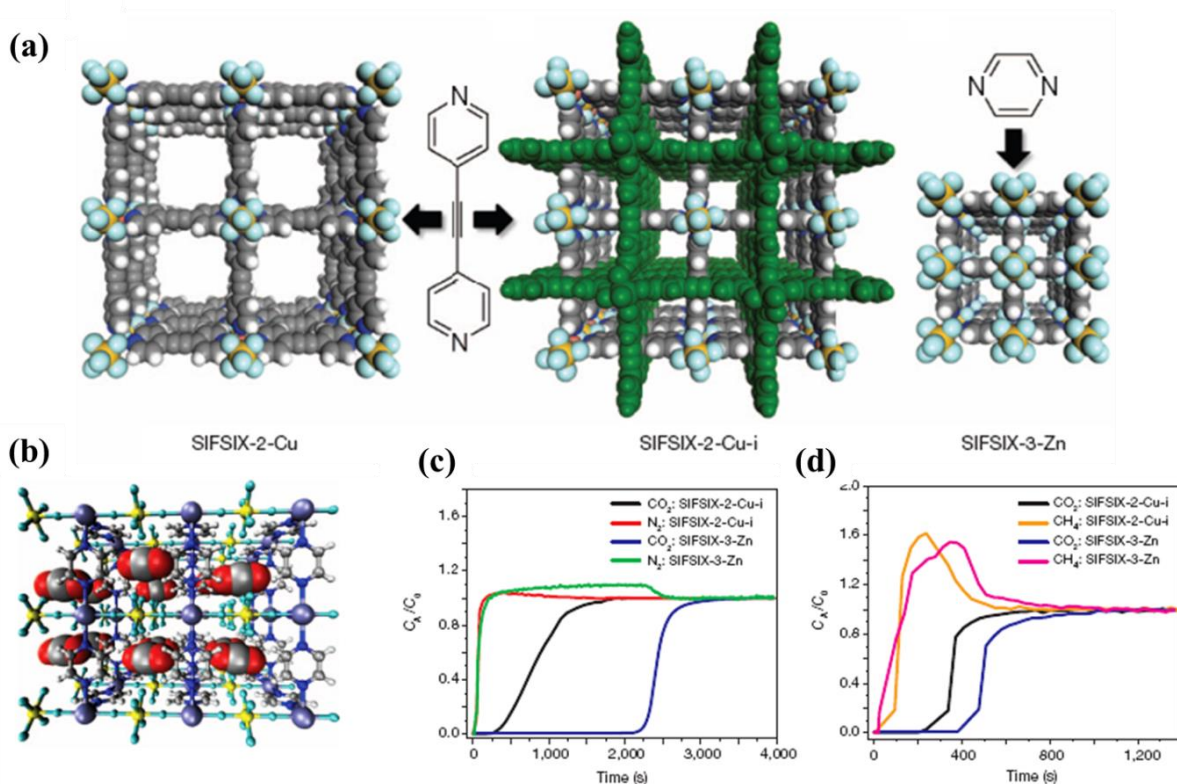


Figure 10: (a) The variable pore size channel structures of SIFSIX-2-Cu, SIFSIX-2-Cu-i and SIFSIX-3-Zn, (b) the modelled structure of a $3 \times 3 \times 3$ box of unit cells of SIFSIX-3-Zn reveals close interactions between the electropositive carbon atoms of CO₂ molecules and fluorine atoms of SIFSIX anions, (c) column breakthrough experiment for a CO₂/N₂:10/90 gas mixture (298 K, 1 bar) and (d) CO₂/CH₄:50/50 gas mixture (298 K, 1 bar). From reference 30. Reproduced by permission from *Nature*.

capacity for MOF-177 (Langmuir surface area of $5640 \text{ m}^2 \text{ g}^{-1}$) reaches a storage density of $320 \text{ cm}^3 \text{ (STP) cm}^{-3}$ ($= 136 \text{ cm}^3 \text{ g}^{-1}$ or 26.7 wt%) which is approximately 9 times higher than the quantity stored at this pressure in a container without the MOF, and is higher than conventional materials, namely, zeolite 13X and MAXSORB.²⁹ With respect to separation of mixture of gases, CO₂/CH₄ separation is an important process for natural gas upgrading and CO₂/N₂ separation is crucial for purifying post-combustion flue gas-mixture.^{28b,30} C₂H₂ and CO₂ exhibit similar size and similar physicochemical properties, making it difficult to separate from each other *via* physisorption process.³⁰ But, the removal of CO₂ impurities from C₂H₂-containing gas mixtures is an important step for purifying C₂H₂, a feedstock chemical used in the production of several commodity chemicals. Here, we have opted to mention few example of MOFs and discussed about the progress in separation of different

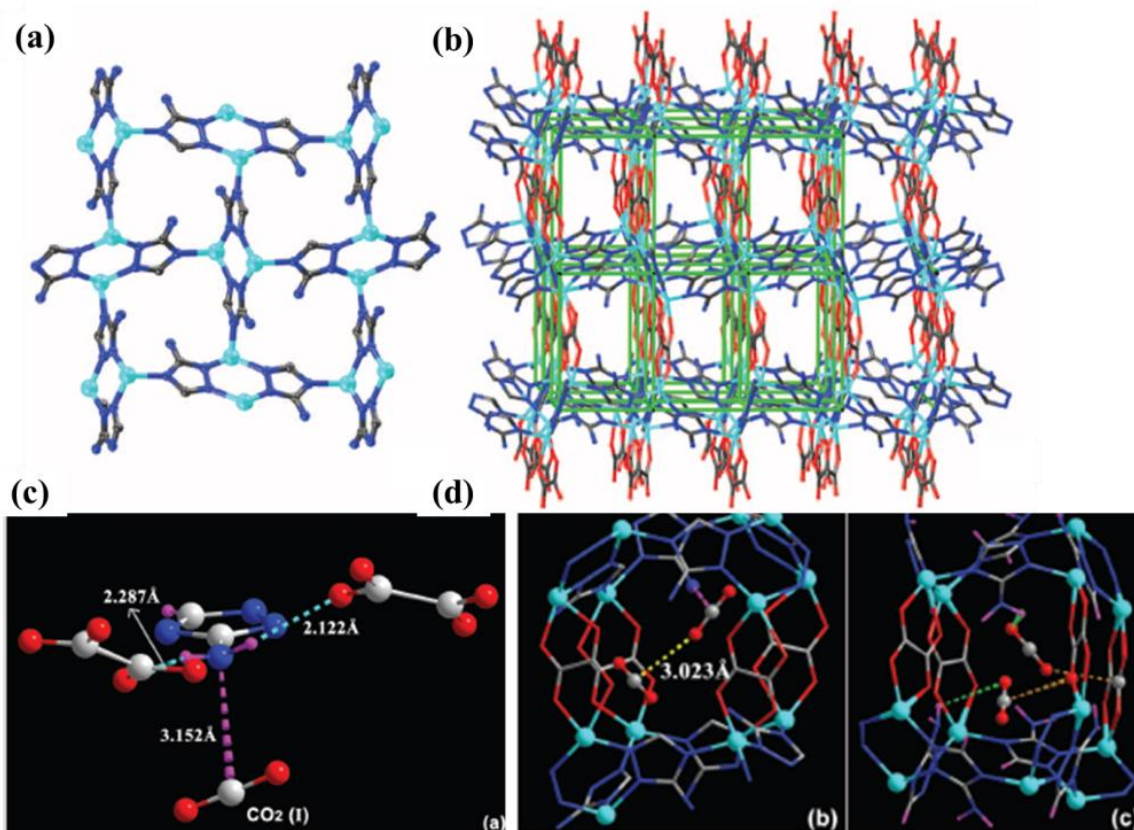


Figure 11: (a) Structure of the Zn-Atz layer in $\text{Zn}_2(\text{Atz})_2(\text{ox})$ (Zn, cyan; C, black; N, blue; H, not shown), (b) three dimensional structure of 1, wherein the Zn-Atz layers are pillared by oxalate moieties (O, red) to form a six-connected cubic network shown as green struts, (c) the role of the amine group of Atz in binding CO_2 -I is depicted, (d) both crystallographically independent CO_2 molecules are shown trapped in a pore, showing the cooperative interaction between CO_2 -I and CO_2 -II molecules. From reference 32. Reproduced by permission from *Science*.

gas-mixtures. A very important class of fluorinated MOFs has been investigated by Zaworotko *et al.* in recent years (Figure 10).³⁰ They have reported syntheses and characterizations of a number of interpenetrated and non-interpenetrated MOFs which showed performances in separation of CO_2 from N_2 and CH_4 at ambient condition. This study also reveals that interpenetrated MOFs with confined spaces are more efficient toward CO_2 capture compared to non-interpenetrated ones. Increasing the density of amine functionalization on the pore surface is also a successful strategy to enhance adsorption capacity and selectivity towards CO_2 .³¹ Jones *et al.* have shown increase in CO_2 capture by loading of tris-(2-amino ethyl) in MIL-101 (Cr).³¹ Direct crystallographic evidence of CO_2

binding with $-NH_2$ group decorated on the pore surface of $\{Zn_2(Atz)_2(ox)\}_n$ (Atz = 3-amino-1,2,4-triazole; ox=oxalate) MOF has been demonstrated by Shimizu *et al.* (Figure 11).³² Along with the functionality, structural flexibility can also be a tool to modulate CO_2 selectivity. In one of the works, Schröder *et al.* showed the presence of pendent carboxylic/pyridine $-N$ groups and their relative flexibility leading to selective stepwise adsorption of CO_2/C_2H_2 .³³ In this thesis, high selectivity and separation performance of CO_2 from N_2 , CH_4 and CH_4 from other C2 hydrocarbons have been achieved based on a combination of structural flexibility and pore functionality in MOFs.

1.3.3 H_2 storage

The possible future energy crisis has to be circumvented by alternative energy resources such as H_2 gas as fuel.²⁶ Primary challenge to its usage is storage and transport. H_2 has an energy density much greater than highly consumed fuel gasoline and it emits no carbon dioxide after burning, which is beneficial for reducing overall greenhouse gas emission. But, H_2 gas is extremely volatile under ambient conditions and has poor volumetric energy density which is much too low for practical applications. For on-board use, H_2 gas should be compressed to very high pressures or stored under cryogenic condition, both of which are energy consuming processes and substantially increase vehicle weight. Hence, the goal is to design low-cost, light-weight materials which can reversibly and rapidly store H_2 near ambient conditions at a density equal to or greater than liquid H_2 . MOFs and certain activated carbons with large surface area and low densities are potential storage materials for this purpose. However, the modular nature of MOFs allows the facile incorporation of new functionalities for enhancing the H_2 storage properties. MOFs showed record high H_2 storage capacities and some of examples are as follows: Hupp *et al.* reported a mesoporous NU-110 which showed hydrogen storage capacity of 9.05 wt% at 77 K and 56 bar, PCN-12, another famous MOF reported by Zhou *et al.* showed 3.05 wt% H_2 uptake at 77 K and 1 atm.^{26, 34} Few other well-known MOFs are HKUST-1 (2.54 wt % at 77 K and 1 atm), PCN-11 (2.59 wt % at 77 K and 1 atm) etc.³⁴

1.3.4 Hydrocarbon storage and separation

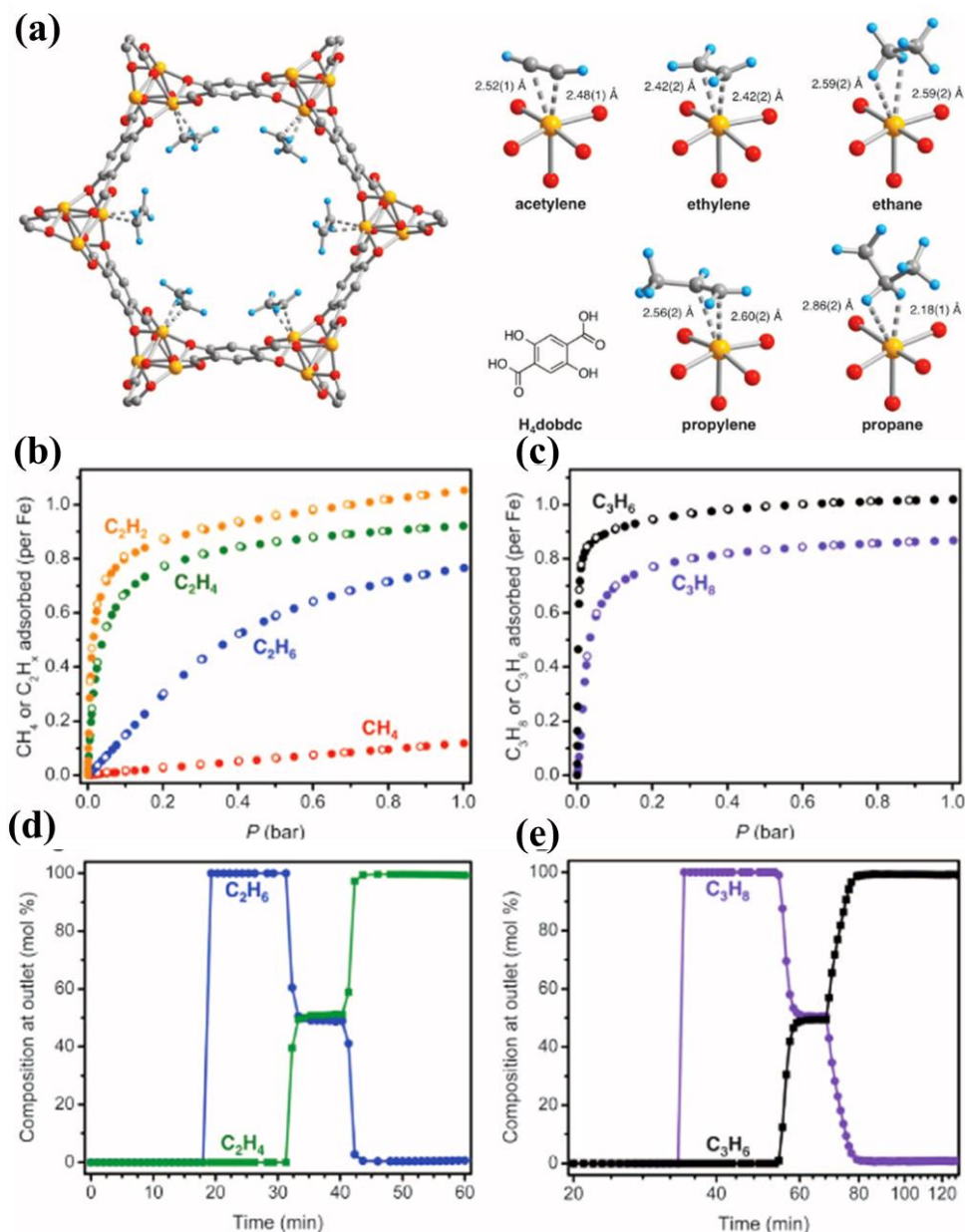


Figure 12: (a) View of the solid-state structure of $\text{Fe}_2(\text{dobdc}) \cdot 2\text{C}_2\text{D}_4$ as determined by analysis of neutron powder diffraction data along [001] direction; orange, red, grey, and blue spheres represent Fe, O, C, and D atoms, $\text{H}_4(\text{dobdc})$ ligand and the first coordination spheres for the iron centers in the solid-state structures obtained upon dosing $\text{Fe}_2(\text{dobdc})$ with acetylene, ethylene, ethane, propylene, and propane. Gas adsorption isotherms for (b) methane, ethane, ethylene and acetylene and (c) propane and propylene in $\text{Fe}_2(\text{dobdc})$ at 318 K. Filled and open circles represent adsorption and desorption data, respectively. Experimental breakthrough curves for the adsorption of equimolar (d) ethane/ethylene and (e) propane/propylene mixtures flowing through a 1.5 mL bed of $\text{Fe}_2(\text{dobdc})$ at 318 K with a total gas flow of 2 mL/minute at atmospheric pressure. From reference 37. Reproduced by permission from *Science*.

Small chain hydrocarbons like CH₄ (methane), C₂H₂ (acetylene), C₂H₄ (ethylene), C₂H₆ (ethane), C₃H₆ (propene) and C₃H₈ (propane) are very important sources of energy and also can be used as chemical feedstock for many industrially important materials.^{35–39} Natural gas mainly consists of CH₄ which has the highest H to C ratio of any fossil fuel, therefore, CO₂ released per unit energy would be minimum. Hence, in order to obtain pure CH₄, separation of other C2-C3 hydrocarbons over CH₄, is an essential task. Natural gas also contains certain percentage of CO₂ which can create pipeline corrosion and thus removal of CO₂ from CH₄ is of utmost importance to obtain high purity of the fuel gas.

The efficient separation of olefins/paraffins is a difficult task to perform in practical field as they have similar physicochemical properties.⁴⁰ Therefore, separation of olefin/paraffin e.g. ethylene/ethane and propylene/propane is generally carried out by cryogenic distillation or at high pressures, which are highly energy expensive procedures. A significant energy penalty is realized upon cooling the gases at low temperature. Among several new energy-efficient technologies such as extractive distillation, absorption, adsorption and membranes based separation, adsorptive separation is one of the most promising methods.⁴⁰ Hence, a variety of solid microporous adsorbents have been studied for separations of these light hydrocarbons. As a strategic method to increase the storage amount and selectivity, high surface area MOFs with suitable functional groups is studied.⁴⁰ Presence of unsaturated metal sites (UMSs) or functional groups such as –NH₂, –OH, –NHCO etc. have been exploited. PCN-14, reported by Zhou *et al.*, showed the highest volumetric CH₄ uptake of 230 cm³ (STP) cm⁻³ at 290 K and 35 bar, which is 28 % higher than the DOE target.⁴¹ In case of acetylene storage, Co₂(dobdc) (dobdc⁴⁻ : 2,5-dioxido-1,4-benzenedicarboxylate) exhibits a volumetric uptake of 230 cm³ (STP) cm⁻³ at 298 K, 1 atm. One more important MOF is FJI-8 ([Cu₄(tddb)·(H₂O)₄·(solvent)_x]_n; H₈tddb = 3,3',5,5'-tetra(3,5-dicarboxyphenyl)-4,4'-dimethoxy-biphenyl) which shows record high gravimetric C₂H₂ uptake of 224 cm³ g⁻¹ and the second-highest volumetric uptake of 196 cm³ (STP) cm⁻³ at 295 K and 1 atm.⁴² In fact, at higher temperature of 308 K, the C₂H₂ storage capacity is ~200 cm³ (STP) g⁻¹.⁴³ Furthermore, FJI-8 exhibits an excellent repeatability with only 3.8% loss of its acetylene storage capacity after five cycles of adsorption–desorption tests. Except these specific examples, only handful of MOFs (such as HKUST-1, MIL-53(cr), MIL-47, Fe₂(dobdc), ZIF-8) were explored as a adsorbents for hydrocarbon storage.⁴³ For example, Fe₂(dobdc)

framework exhibits excellent performance for separation of ethylene/ethane and propylene/propane mixtures at 318 K (Figure 12).³⁷ Breakthrough data obtained for experimental separation is further validated by simulations, which supports experimental high selectivity and separation ability of this MOF for methane/ethane/ethylene/acetylene mixtures. Interestingly, neutron powder diffraction data confirms a side-on coordination of acetylene, ethylene, and propylene at the Fe^{II} centers, but provides weaker interactions of saturated ethane and propane with same metal centers

1.4 Photophysical studies: Photochromism in MOFs and host-guest chemistry

The photochromic materials reversibly change their characteristic colours with different optical readout signals in response to light irradiation. These light stimulated molecular switches are of significant interest by virtue of their various potential applications in optical filters, solar cells, low-cost memory and display devices.⁴⁴ Among several photochromic phenomena, photo/thermal induced electron transfer (ET) is of paramount importance especially in solar energy conversion, molecular photonics and the mimicry of natural photosynthetic systems.^{45a-b} For the fabrication of such materials, the most important parameter is the spatial-organization of organic chromophores (donor or acceptor or both) in an apposite manner in order to construct effective channels for electron transfer.^{45b-e} MOFs are crystalline materials and are well known for exhibiting excellent coordination driven long range ordering of framework chromophoric linkers. Therefore, recently, the perception of photofunctional MOFs as organized matrix of light-harvesters has moved to the forefront.⁴⁶ Coordination driven self-assembly with a luminescent chromophoric or highly electron deficient/ electron rich linker would provide photofunctional porous framework. The two mechanisms which are responsible for driving the energy from one electronically excited molecule to another one are energy transfer and electron transfer.^{45a} For instance, Fu *et al.* reported the photochromic two novel mixed-ligand MOFs, $[\text{Zn}_2(\text{tpt})_2(\text{m-bdc})_2]\cdot\text{H}_2\text{O}$ and $[\text{Zn}_2(\text{tpt})(\text{p-bdc})_2]\cdot\text{H}_2\text{O}$ [bdc = 1,4-benzenedicarboxylate, tpt = 1,4-tris(4-pyridyl)triazine] from a suitable combination of two non-photoactive ligands for the first time.^{47a} It has been observed that the formation of light-induced free-radicals in the MOF material depends on the conformation of the network and nature of the ligands. In another report by Guo *et al.*, a

new 3D $[\text{Cd}_2(\text{ic})(\text{mc})(4,4'\text{-bipy})_3]_n \cdot 4n\text{H}_2\text{O}$ (ic = itaconate, mc = mesaconate) has been introduced (Figure 13a-f), which exhibits reversible photochromic behaviour, from yellow to blue upon UV irradiation.^{47b} This compound is also merited for its unusual five-connected Archimedean type topology and unexpected isomeric ic and mc ligand “capture” as generated *in situ* from *trans*-propene-1,2,3-tricarboxylic acid. Wu *et al.* later reported two photochromic metal-organic cage (MOCs) with adjustable fluorescent intensities, $[\text{Zn}_3(\text{TTHA})(4,4'\text{-bipy})_{1.5}(\text{H}_2\text{O})_2] \cdot 6\text{H}_2\text{O}$ and $[\text{Zn}_3(\text{TTHA})(4,4'\text{-bipy}) \cdot 1.5(\text{H}_2\text{O})_2] \cdot 3\text{H}_2\text{O}$ [H_6TTHA = 1,3,5-triazine-2,4,6-triaminehexaacetic acid], synthesized from a novel triamine-based polycarboxylate ligand containing the $-\text{N}(\text{CH}_2\text{CO}_2\text{H})_2$ group as electron donor and 4,4'-bipy as electron acceptor (Figure 13g-h).^{47c}

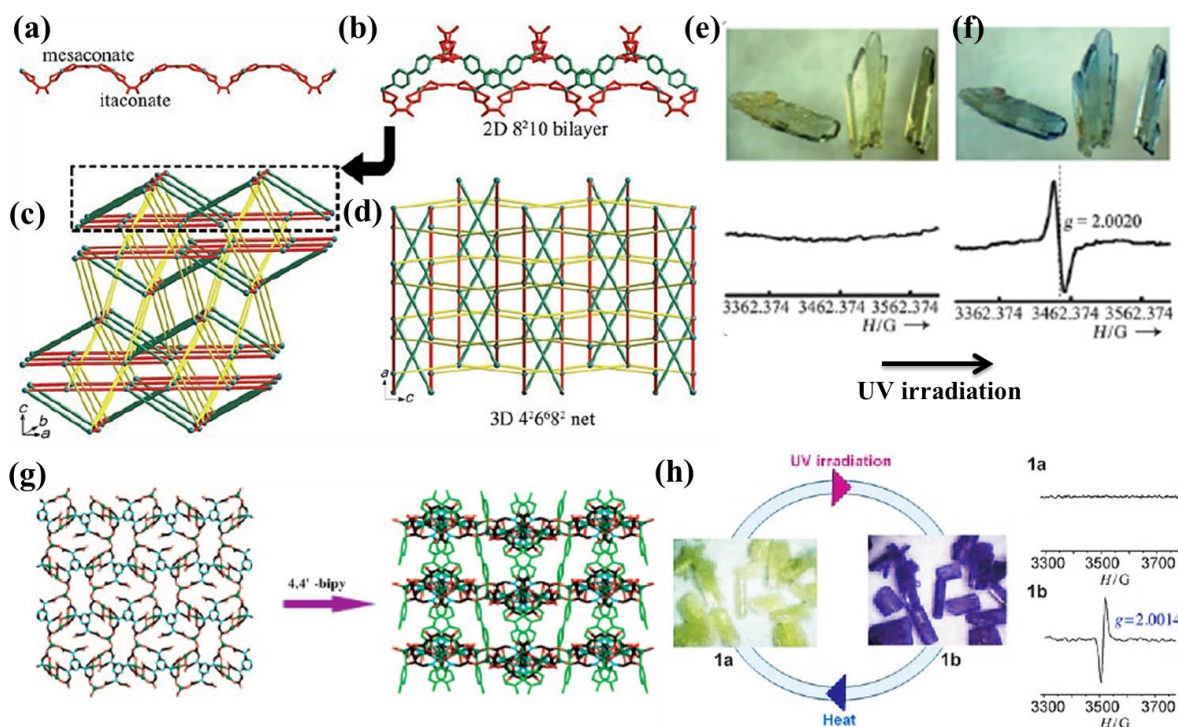


Figure 13: (a) 1D arch-bridge-like chain in $[\text{Cd}_2(\text{ic})(\text{mc})(4,4'\text{-bipy})_3]_n \cdot 4n\text{H}_2\text{O}$, (b) 2D bilayer, (c-d) schematic representations of the 3D $4^2 6^2 8^2$ net. Rods in (c) and (d): green: 4,4'-bipy ligands with N31 atoms; red: carboxylate ligands; yellow: 4,4'-bipy ligands with N41 atoms, (e-f) photochromism and ESR spectral and structural variations before (e) and after (f) irradiation. From reference 47b. Reproduced by permission of *Angew. Chem. Int. Ed.* (g) 2D layer (left) and 3D framework along the c axis (right) in $[\text{Zn}_3(\text{TTHA})(4,4'\text{-bipy})_{1.5}(\text{H}_2\text{O})_2] \cdot 6\text{H}_2\text{O}$, (h) photochromism and ESR spectral differences of corresponding framework before and after irradiation. From reference 47c. Reproduced by permission from *Chem. Eur. J.*

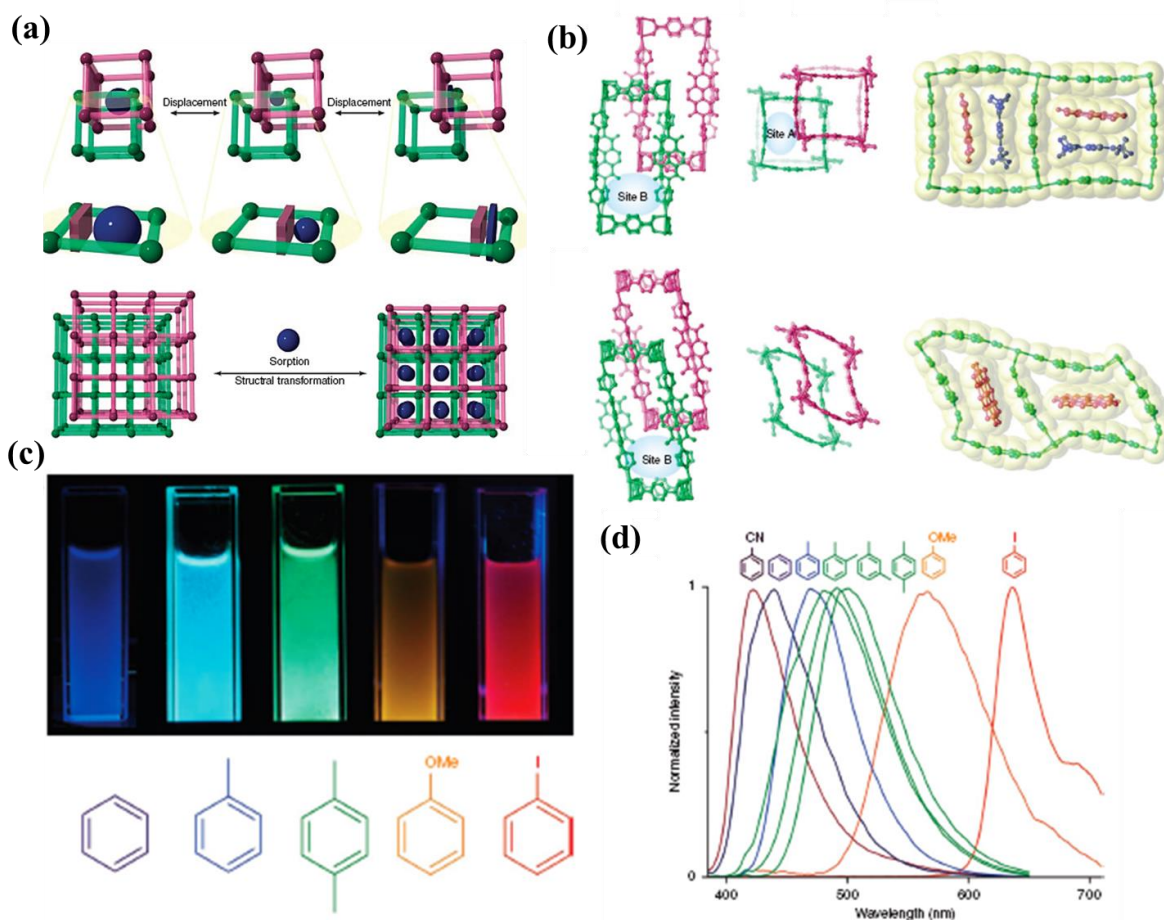


Figure 14: (a) The framework entanglements provide flexibility through spaces when the pore size and shape are altered in response to target guest molecules without changing the total void space. Chemically non-interconnected frameworks show dynamic movement by the dislocation of their mutual positions to effectively trap molecules while maximizing their host–guest interaction, (b) view of $\{[\text{Zn}_2(\text{bdc})_2(\text{dpNDI})] \cdot 4\text{DMF}\}_n$ and corresponding desolvated structure, (c) the resulting luminescence of $\{[\text{Zn}_2(\text{bdc})_2(\text{dpNDI})] \cdot 4\text{DMF}\}_n$ suspended in different aromatic liquids on excitation at 365 nm using a commercial ultraviolet lamp, (d) height-normalized corresponding luminescent spectra after excitation at 370 nm. From reference 49a. Reproduced by permission from *Nat. Commun.*

Porosity of framework would further allow for encapsulation of suitable guests (especially dye molecules) in pores. This would serve not only for energy transfer but also this continuous D-A assembly might lead to the formation of charge-separated species with response to light.⁴⁸ In contrast, to traditional pure organic and inorganic molecular systems, photofunctional MOFs seem to be more promising and beneficial for photovoltaic applications as charge recombination would be inhibited by long D-A distance (mainly

interact through weak interactions such as hydrogen bonding or π -stacking). An excellent piece of work has been carried out by Kitagawa *et al.* based on a redox active MOF, where an entangled porous host framework, $[\text{Zn}_2(\text{bdc})_2(\text{dpNDI})]_n$ (H_2bdc , 1,4-benzenedicarboxylate; dpNDI, *N,N'*-di(4-pyridyl)-1,4,5,8-naphthalenediimide) has been synthesized from redox-active naphthalenediimide linker. Interestingly, the framework exhibits guest responsive structural dynamics due to the movement of two non-interconnected networks (Figure 14).^{49a} An intense turn-on emission is observed on encapsulation of a range of aromatic guest molecules (e.g. benzene, toluene, o,m,p-xylene, aniline etc.), and the resulting luminescence is dependent on the chemical nature of the guest aromatic molecules. In fact, depending upon ionization potential of these molecules, complete charge-separated electron transfer (ET) has been realized. In another report, MOF $[\text{Zn}_3(\text{m-BDC})_4]\text{-MV}$ (MV = methyl viologen) to guest electron transfer has been reported by Dai *et al.*, where, linker m-BDC is acting as a donor and MV as an acceptor.^{49b} The π -stacking arrangements between the D–A components, contribute to the formation of an ultralong-lived charge separated state in the photo/thermo dual stimuli-responsive complex. Recently, a substantial number of related works have been reported⁴⁷ but targeted construction of photochromic porous MOFs from redox- active linkers is yet to be realized. In fact, such frameworks can also confine a variety of donor/acceptor molecules depending upon the design of framework, for channelizing energy/electron transfer processes.

1.5 Nanoscale metal-organic frameworks (NMOFs)

Scaling down to the nanoscale is a very fruitful strategy for the development of new materials (pure inorganic or organic nanomaterials) with novel and often better properties compared to traditional bulk counterparts.⁵⁰⁻⁵¹ It has opened up huge potential for better technological and biomedical applications in future, including drug-delivery, catalysis, diagnostics, solar cells, etc.⁵⁰⁻⁵¹ Till date a reasonable number of materials have been downsized to nanoscale for different purposes such as imaging, therapeutic agents, electronic devices, optics etc. but the majority of them are categorized into either purely inorganic materials (such as quantum dots, Fe_3O_4 , and Au nanoparticles)⁵⁰ or purely organic (such as liposomes, dendrimers, polymers).⁵¹ For last few years, downsizing MOF in nanoregime (NMOF) has shown a great potential due to structural diversity and inherent functionality,

therefore, a whole set of altered properties can be realized distinguishing NMOFs from their bulk counterparts.¹¹ Miniaturization at nanoscale has direct impact on surface area over volume (S/V) ratio, and hence, the diffusion path length, which is one of governing parameters for gas storage and separation.¹¹ Indeed, emerging fields such as porous membranes, thin film etc. are highlighting this fabrication and downsizing MOFs into various shapes and size, which is an essential step toward MOF-based devices.^{11c} Because of its biocompatible nature, NMOFs are also exploited for internalization into cells, and this limits the applications of bulk MOF as delivery vehicles, diagnostics, etc.^{11e} It is easily dispersible in aqueous media or other solvents and can be coated efficiently. Recently, anisotropic NMOFs *i.e.* featuring at least one dimension at the nanoscale are considered to be potential

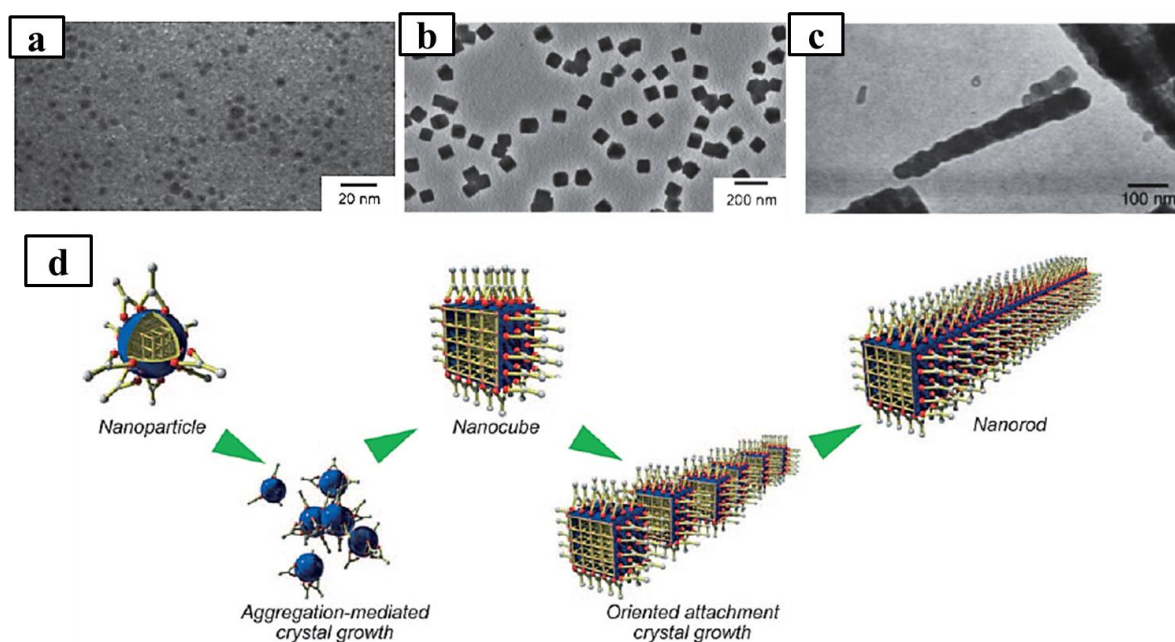


Figure 15: Time-course analysis of the reaction of $[\text{Cu}(\text{ndc})\text{dabco}]_n$ under standard conditions; TEM images of nanocrystals obtained after reaction times of (a) 15 min, (b) 20 min and (c) 1 h, (d) proposed growth mechanism for $[\text{Cu}(\text{ndc})\text{dabco}]_n$ nanorods. The growth process of nanocubes is a consequence of nanoparticle aggregation-mediated crystal growth. The selective coordination modulation on the (100) surfaces of the nanocubes induces the oriented attachment leading the growth of nanorods in the [001] direction. From reference 52b. Reproduced by permission from *Angew. Chem. Int. Ed.*

candidates for customized applications.¹¹ Synthesis of high aspect ratio 1D nanorods, fabrication of 2D NMOFs *i.e.* nano/meso sheets, thin films, membranes are always

challenging and have received considerably less attention. Oh *et al.*, Kitagawa *et al.* and Lin *et al.* have successfully synthesized different types of 1D nanostructures from several MOF systems (especially higher symmetric) and exploited for gas storage, optical and biomedical applications.⁵² But, the crystal growth mechanism of these NMOFs are poorly studied due to insufficient information of nucleation and intermediate phases of nanoparticles during synthesis. Kitagawa *et al.* first gave the breakthrough evidence of classical oriented attachment growth model of 1D nanorod formation of $[\text{Cu}(\text{ndc})\text{dabco}]_n$ (H_2ndc = 1,4-naphthalenedicarboxylic acid, dabco = 1,4-diazabicyclo[2.2.2]octane) MOF, and indicated that the same can also occur in other MOF systems (Figure 15).^{52b} We believe this is a nascent stage where further investigation is necessary for in-depth understanding of specified shape-sized NMOF synthesis, growth mechanism and applications.

1.6 Synthetic strategies

There are several major strategies for synthesizing nanoscale metal–organic materials; (i) confined growth of the supramolecular assembly at nano dimensions by using emulsions or templates, (ii) coordination modulation method, (iii) controlled precipitation of self-assembled metal–organic polymers by the use of poor solvents, (iv) microwave radiation, (v) ultrasounds, and (vi) solvo/hydrothermal method (Figure 16).^{11a}

Nanoemulsion is a suspension of small droplets, usually stabilized by a surfactant (a water-in-oil or reverse microemulsion), with diameters ranging from 50 to 1000 nm. Because of the nanodimensions of these micelle cores, these can be used as “nanoreactors” to confine the self-assembly, nucleation and growth of metal–organic nanostructures. In coordination modulation method, the addition of modulator with the same functionality as of organic linkers impedes the coordination interaction with metal ions and organic linkers and perturbs the rate of growth of crystals which results into nanoscale. In some cases, direct precipitations under the influence of external stimuli, ultrasound sonication, microwave irradiation, even temperature induced miniaturization with or without the presence of additives, are also promising.

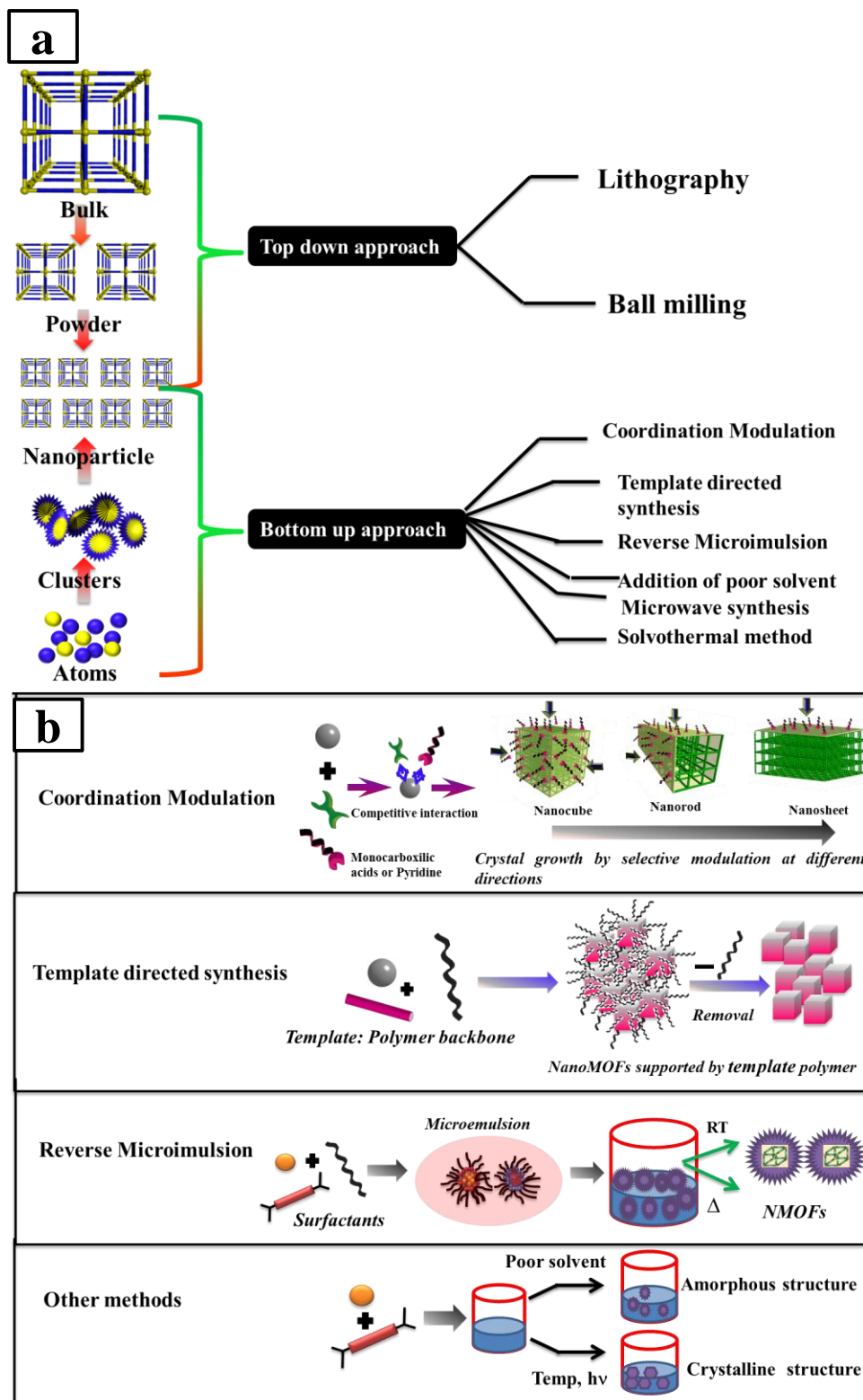


Figure 16: Different synthetic strategies for NMOF preparation.

1.7 Applications of nanoscale MOF

Because of the quite satisfactory properties exhibited by bulk MOFs, their nanoscopic counterparts are expected to exhibit interesting and even improved gas adsorption properties. Kitagawa *et al.* showed that downsizing of bulk to nanorods significantly improves overall surface area as well as CO₂ uptake due to better diffusion of gas molecules in nanoscale.^{52b} Similar behaviour is also reported by Guo *et al.*, fabrication of [Dy(BTC)(H₂O)] (H₃BTC = 1, 3, 5-benzenetricarboxylic acid) to nanoscale using sodium acetate as coordination

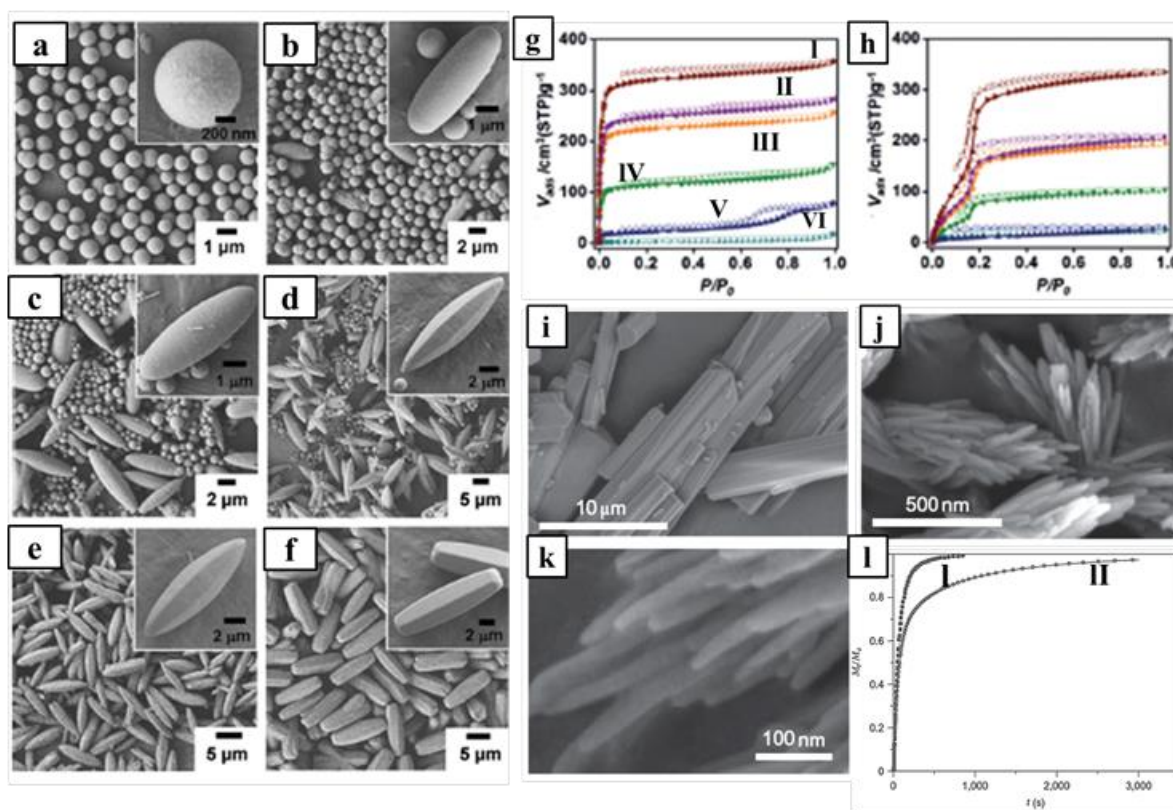


Figure 17: (a–f) SEM images showing the morphological evolution of MOF particles constructed from the solvothermal reactions of $\text{In}(\text{NO}_3)_3$ in the presence of various ratios of H_2IPA and H_2BDC . The ratios of $\text{H}_2\text{IPA}:\text{H}_2\text{BDC}$ (w:w) used during the reactions were (a) 10:5, (b) 7.5:7.5, (c) 6.5:8.5, (d) 5:10, (e) 3.5:11.5, and (f) 2:13, (g) N_2 sorption isotherms measured at 77 K and (h) CO_2 sorption isotherms measured at 195 K of differently shaped MOF particles constructed from the reactions of $\text{In}(\text{NO}_3)_3$ in the presence of various ratios of H_2IPA and H_2BDC . The ratios of $\text{H}_2\text{IPA}:\text{H}_2\text{BDC}$ (w:w) used during the reactions were 10:5 (cyan), 7.5:7.5 (blue), 6.5:8.5 (green), 5:10 (orange), 3.5:11.5 (purple), and 2:13 (brown). Solid symbols are adsorption and open symbols are desorption. From reference 52a. Reproduced by permission of *Angew. Chem. Int. Ed.* (i) FESEM images of bulk synthesized CID-1 (bulk-CID-1), (j–k) nanocrystals of NCID-1a at high magnification, (l) MeOH vapour adsorption kinetics plots of (I) CID-1 (II) NCID-1. From reference 52j. Reproduced by permission from *Nat. Chem.*

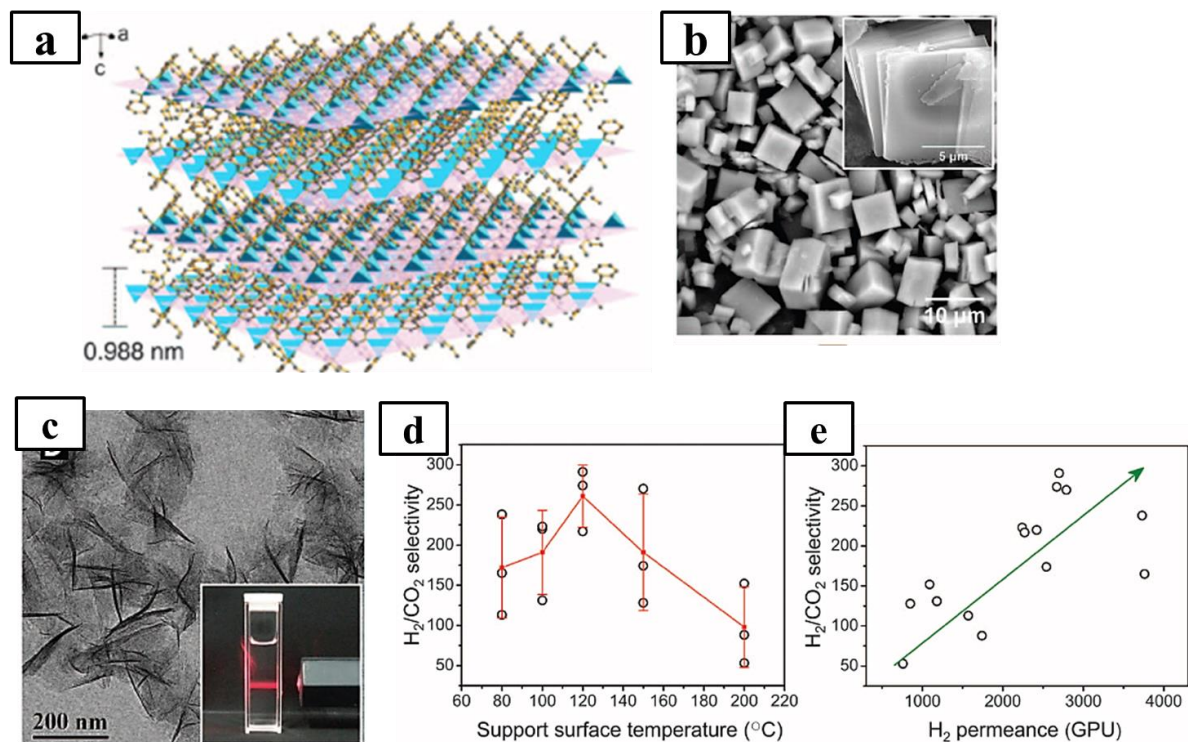


Figure 18: (a) Layered $[\text{Zn}_2(\text{bim})_4]_n$ structure along ab direction (b) scanning electron microscopy (SEM) image of as-synthesized $[\text{Zn}_2(\text{bim})_4]_n$ crystals; the inset image shows the typical flake-like morphology of $[\text{Zn}_2(\text{bim})_4]_n$ crystals (c) TEM image of 2D membranes of $[\text{Zn}_2(\text{bim})_4]_n$; the inset shows the Tyndall effect of a colloidal suspension. (d) Scatterplot of H_2/CO_2 selectivities measured from 15 membranes. The red line with symbols shows the average selectivity and dispersion of selectivity of the membranes prepared at different coating temperatures (e) anomalous relationship between selectivity and permeance measured from 15 membranes. From reference 52k. Reproduced by permission from *Science*.

modulator improves the overall surface area.^{52h} Oh *et al.* successfully synthesized NMOFs based on In^{III} metal ions and H_2BDC (1,4-benzenedicarboxylic acid) ligands, that showed a H_2 and CO_2 uptake of $140 \text{ cm}^3 \text{ g}^{-1}$ (77 K) and $333 \text{ cm}^3 \text{ g}^{-1}$ (195 K), respectively.⁵²ⁱ Later, this group has reported interesting morphological and structural evolutions of In^{III} based NMOFs depending on the contributions of two organic linkers, H_2IPA (isophthalic acid) and H_2BDC during the MOF particle construction (Figure 17a-h).^{52a} Highly crystalline porous hexagonal rods are generated when the BDC linkers contribution is dominant; however, amorphous non-porous spherical particles are formed when the contribution of the IPA linkers is higher. It has been observed that increase in BDC contribution affects the overall morphology and

crystallinity of the NMOFs and hence, higher surface area and CO₂ uptake is realized. Kitagawa *et al.* have synthesized flexible porous coordination polymer nanocrystals of [Zn(ip)(bpy)]_n (ip = isophthalic acid, bpy = 4,4'-bipyridine) from a non-aqueous inverse microemulsion technique combined with ultrasonication. MeOH vapour adsorption measurements showed almost identical overall adsorption capacities of nanoparticles and bulk, but the shapes of the isotherms differ significantly from each other (Figure 17i-l).^{52j} The MeOH vapour adsorption kinetics showed that the NMOF has higher kinetics of mass transfer than the bulk analogue. But till date, adsorption kinetics have not been focused or discussed further in bulk or nanoscale in a comparative fashion, which is important for gas separation. Recently, 2D nanosheets of [Zn₂(bim)₄]_n (bim = benzimidazole) synthesized by Yang *et al.* have shown a good performance as molecular sieving membranes for kinetic gas separation (Figure 18).^{52k}

As mentioned earlier, NMOFs as drug delivery vehicles have attracted a lot of attention in recent times.^{11e} This is achieved by undertaking these different strategies: (i) incorporating drug molecules as one of the building blocks in the MOF scaffolds and (ii) encapsulation of drugs inside the pores.^{11e,53} Lin *et al.* have applied precipitation approach for preparing nanospheres by addition of a poor solvent to the solution containing Tb^{III} metal ions and Pt^{IV} based anticancer drug.^{53a} The same authors also followed a post synthetic approach for covalent grafting of drug molecules in porous NMOFs constructed from Fe^{III} metal ions and 2-aminoterephthalic acid.^{53b} The pendent amino groups on the porous NMOFs covalently attaches with *cis*-platin drug. Horcajada, Gref *et al.* have recently synthesized Fe^{III} based NMOFs from different dicarboxylate ligands (e.g. BDC or BTC) for loading a wide variety of anti-tumoral drugs, e.g. DOX, busulfan, cidofovir and azidothymidine triphosphate.^{11e} Interestingly, in all these cases, successful design as drug delivery systems have been confirmed by controlled and progressive release experiment and their *in vitro* anticancer efficacies. These reports have paved the way for implying NMOFs as novel drug delivery systems.

Indeed, NMOFs are excellent potential candidates as contrast agents because it can be constructed from highly paramagnetic metals ions, such as Gd^{III} and Mn^{II}. For example, Lin *et al.* have first demonstrated that Gd^{III} containing NMOFs as T₁ weighed contrast agent.^{53c}

Gd^{III} containing NMOFs can also act as T₂ weighed contrast agents, which is not possible for small Gd-chelate molecules.^{53c}

1.8 MOF-derived carbonaceous materials for various applications

Among the plethora of porous materials, nanoporous carbonaceous materials have been the most important and have been explored extensively due to their good textural tunability, thermal and chemical stability.⁵⁴ These materials can be prepared by pyrolysis treatment followed by physical/ chemical activation of organic precursors. These porous carbons possess high surface area, but the structures are disordered with broad pore size distribution and thereby, limit their application dealing with molecular discrimination. Hence, hard and soft templating techniques have been developed for featuring ordered porous structures with narrow pore size distributions.⁵⁵⁻⁵⁶ Nanoporous carbons prepared by the second method have diverse structures and morphologies. However, these can be obtained only from a few suitable thermally stable carbon gels and less stable organic templates that can be thermally decomposed before completion of the carbonization process. In contrast, in the former approach, nanoporous carbons with ordered micro-, meso-, and macropores can be obtained depending on the original hard-templates (i.e., zeolites, mesoporous silicas, and colloidal crystals, respectively), although it is slightly complex and unfavourable for large-scale production.

MOFs, having their designable framework structures with large carbon content, different secondary building units of transition-metal clusters, high surface area, and large pore volume have been considered as an alternative precursor to construct nanoporous carbons with or without metal-oxide nanoparticles.⁵⁷ The effect of ligands on the properties of the resulting carbon has been studied.^{58a} It is being demonstrated that highly porous MOF can lead to higher surface area nanoporous carbons compared to non-porous MOF derived carbons which are found to possess a relatively lesser surface area (Figure 19a-b).^{58b} Besides, substitution of heteroatoms, such as boron, nitrogen, and sulphur, into the carbon frameworks can considerably affect the properties of the material. For example, zeolitic imidazolate frameworks (ZIFs) have been explored as a template and precursor to create N-doped nanoporous carbon, due to their highly ordered porous structure and N-containing imidazole-based organic linkers, resulting in an abundant N-doping in the resulting carbon matrix.^{58c-e}

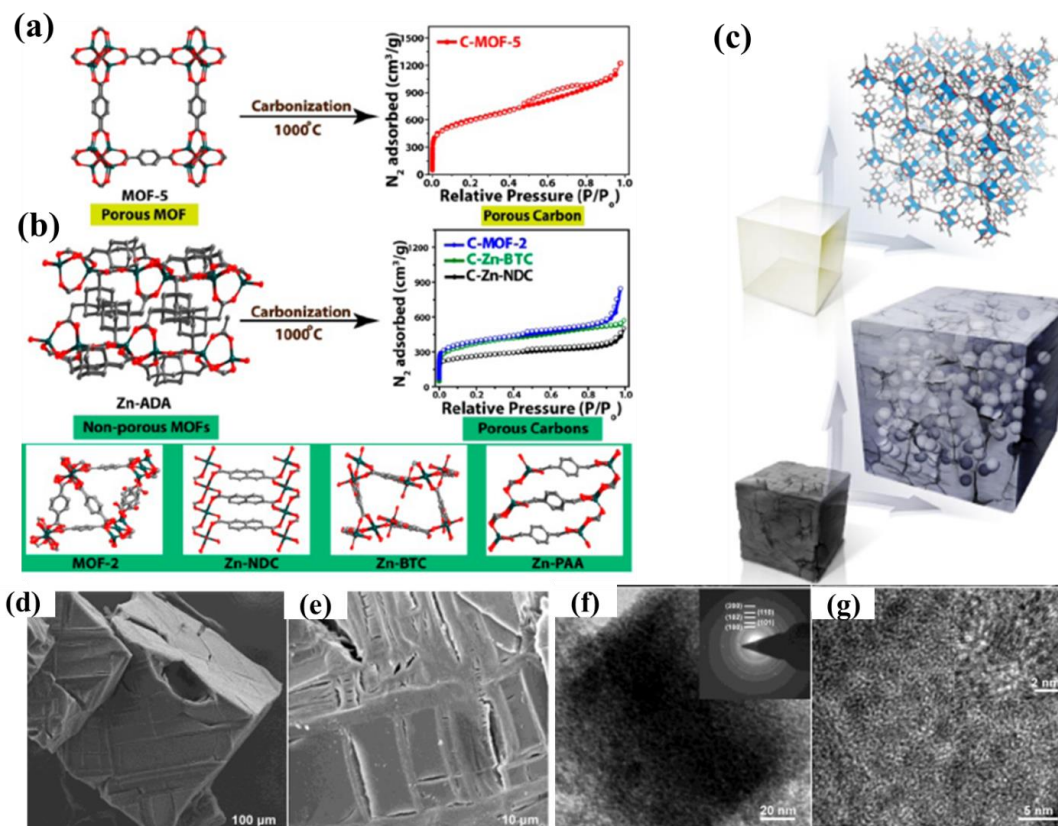


Figure 19: Synthesis of porous carbon on direct carbonization of (a) porous MOF and (b) nonporous MOFs at 1000 °C along with their N₂ adsorption isotherms. From reference 58b. Reproduced by permission from *Cryst. Growth Des.* (c) Schematic diagrams of IRMOF-1 (top) and IRMOF-1 after controlled pyrolysis to produce carbon-coated ZnO QDs without agglomeration (bottom). ZnO QDs@porous carbon (550N) obtained from IRMOF-1: (d- e) SEM images; (f) TEM image (inset: SAED pattern), (g) high resolution TEM image (inset: enlarged view). From reference 59b. Reproduced by permission from *J. Am. Chem. Soc.*

Interestingly, during the high temperature carbonization process, the corresponding metal species can be completely removed by simple tuning of temperature.⁵⁸ In another way the metal/metal-oxide doped carbonaceous matrix can be post treated with simple acid-wash and hence, highly porous nanostructure can be obtained. Such simple porous carbon/N-doped nanoporous carbons have found several applications as base catalysts, CO₂, H₂ adsorbents, and supercapacitor electrodes.⁵⁷

Synthesizing metal/metal-oxide (M/MO)–carbon composites by traditional chemical syntheses leads to poor control over the M/MO particles sizes as the agglomeration severely affect the overall growth of the material. Surface coating of particles is considered as a

promising technique for limiting growth of particle agglomeration while retaining high performance. Since, MOF thermolysis can generate *in situ* carbon coated MO/M particles, this is one of the best ways to prepare uniform sized MO/M-carbon composites.^{59a} For instance, an excellent report recently has shown successful formation of 3D carbon decorated ultra-small (3.5 nm) ZnO quantum dots (QDs) from IRMOFs by controlled pyrolysis (Figure 19c-g).^{59b}

1.8.1 Gas storage of carbonaceous matrix

So far, several MOFs, such as MOF-5, Al-PCP, and ZIF-8, have been explored as promising templates for carbonization to highly nanoporous carbons which show excellent properties in gas adsorption, as electrode materials and in electrochemical applications.^{57a} Xu *et al.* first synthesized porous carbon from MOF-5 but no detailed investigation was presented.^{60a} The first comprehensive study of this approach was investigated by Yamauchi *et al.*, a direct carbonization of Al-PCP at 800 °C, the obtained nanoporous carbon possesses an extremely high surface area of 5000 m² g⁻¹ with a large pore volume of 4.3 cm³ g⁻¹.^{60b} It was also explained that the carbonization temperature is very crucial to achieve such highly nanoporous matrix.^{60b} MOF-derived nanoporous carbons/carbon hybrids have been also proved to be efficient matrix for H₂ storage.^{60a,c-e} At 77 K and 1 atm, the carbonaceous material prepared from direct MOF-5 carbonization, showed the highest 3.25 wt% uptake. Later on, ZIF-8-derived N-doped carbons exhibited H₂ uptake of 6.2 wt% at 77 K and 20 bar.^{60e}

1.8.2 In fuel cell applications

Technologies for renewable energy storage and conversion to replace the fossil fuel have rapidly progressed in recent years. Hence, the storage of energy (e.g. mechanical, thermal, electrochemical, electrical etc.) for running portable electronic devices needs to be improved in design and capacity, and it is indeed a serious concern for the research communities. The arrival of nanotechnology and modern characterization facilities has raised the conquest of the better material syntheses. Electrochemical energy storage is considered as one of the most promising methods of storing energy. A nanostructured electrode for an electrochemical energy storage needs to be systematically improved for gaining the maximum efficiencies.^{57a,d} An active surface area, optimized pore size distribution and

crystallinity are considered to be the most important parameters which affect the performance of nanoporous carbon based electrode materials.⁶¹ A considerable number of materials have been investigated lately in order to determine the best material for this purpose, however, executing an efficient design still remains a big challenge. Among various electrochemical applications, significant part of this thesis contains synthesis and characterization of MOF derived catalysts for oxygen reduction reaction (ORR), oxygen evolution reaction (OER) and associated bi-functional electrocatalytic activity.

1.8.2.1 Oxygen reduction reaction (ORR)

Similar to batteries, fuel cells are also important as they convert chemical energy of fuel and oxidant into electric energy (Figure 20). Besides, they do not require recharging as long as there is a continuous supply of fuel and oxidant, unlike batteries. As compared to thermal engines, fuel cells are highly efficient, without any associated environmental pollution, and with an abundant source of reactants. Therefore, fuel cells are expected to take up major commercial roles in the areas of transportation, stationary and portable power generation, and thus are potential for solving the global problems of energy supply and clean environment. Among all kinds of existing fuel cells, the proton exchange membrane fuel cell (PEMFC) has been actively developed for using in vehicles, portable electronics, and combined heat and power (CHP) systems because of their simplicity, low working temperature, high power density etc. PEMFCs are especially considered to be suitable as the main power sources in automobiles and buses.⁶² Fuel cell vehicles (FCVs) are, in fact, considered as one of the final solutions for automotive business over battery powered electric vehicles (EVs). Indeed, the first mass produced FCV, Toyota Mirai (“future” in Japanese), which has been commercially sold in Japan since 2014, is based on this concept. However, one of the main reasons for the high sale price of the Mirai is the high Pt loading in the fuel cell stacks.⁶²

At the anode of PEMFC, H₂ is oxidized to protons and electrons that are transferred to the cathode through proton exchange membrane and an external circuit, respectively (H₂ → 2H⁺ + 2e⁻). At cathode, O₂ is reduced to water by reaction with protons and electrons (1/2O₂ + 2H⁺ + 2e⁻ → H₂O). Both the anode and cathode consist of highly dispersed Pt-based nanoparticles on carbon black. However, the HOR reaction on Pt is very fast, such

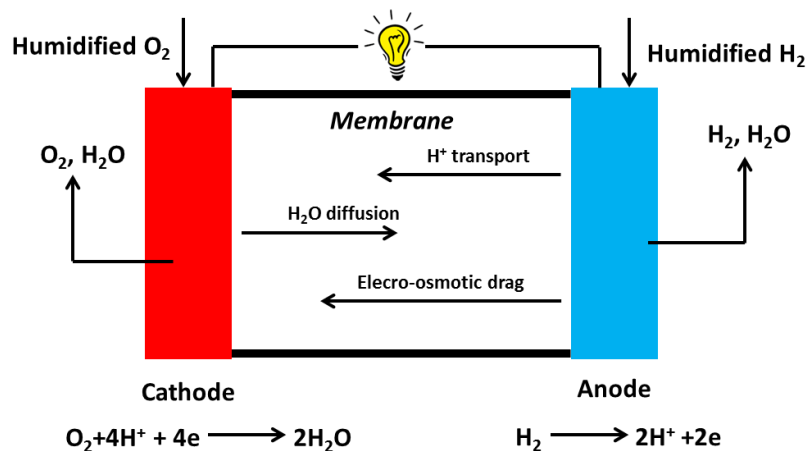


Figure 20: Simplified PEM fuel cell reactions

that, the Pt loading at anode can be reduced to less than 0.05 mg cm^{-2} . But, at the cathode, the sluggish ORR kinetics requires a much higher Pt loading of $\sim 0.4 \text{ mg cm}^{-2}$ to achieve a desirable fuel cell performance. Therefore, reducing Pt loading or even completely replacing it with an abundant and cheap with or without non-precious metal based catalysts is of supreme importance.⁶²

ORR mechanism

The ORR is the primary electrochemical reaction occurring at the cathode of the fuel cells.

The ORR can follow the following two mechanistic paths

(i) The direct 4e^- transfer mechanism:

(a) In alkaline solutions,

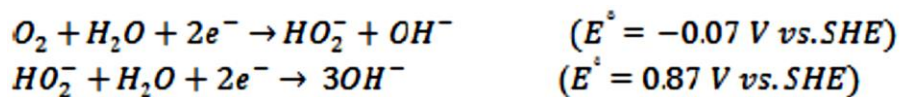


(b) In acidic solutions,

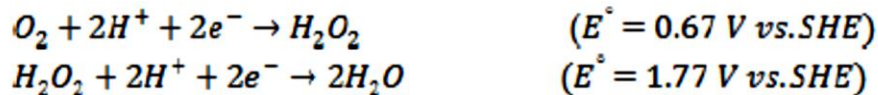


(ii) The 2e^- transfer mechanism or the peroxide path.

(a) In alkaline solutions,



(b) In acid solutions,



The direct $4e^-$ oxygen reduction path is more efficient than $2e^-$ reduction path. The generalized scheme for the ORR represented by Wroblowa *et al.*^{62c} is shown in Figure 21.

where, k_1 = rate constant for $4e^-$ direct reduction to H_2O or OH^-

k_2 = $2e^-$ reduction to H_2O_2 or HO_2^-

k_3 = electrochemical reduction of H_2O_2 to water or OH^-

k_4 = catalytic decomposition of H_2O_2 or HO_2^- yielding reducible product

k_5 = desorption of adsorbed H_2O_2 or HO_2^-

k_6 = adsorption of H_2O_2 or HO_2^-

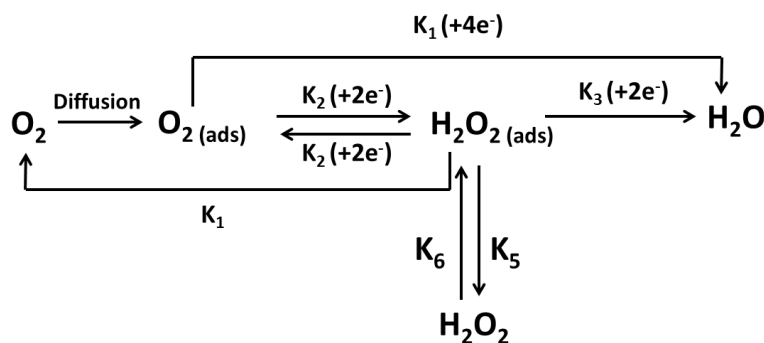


Figure 21: Schematic presentation of ORR pathway

At high potentials k_1/k_2 is constant with $k_1 > k_2$ indicating a direct reduction of oxygen to water. At intermediate potentials, k_1/k_2 ratio decreases indicating an increase in the $2e^-$ reduction of oxygen to peroxide. At lower potentials, k_1/k_2 becomes lower than 1. However, k_3 increases resulting in a further reduction of peroxide to water.

Recent intensive research efforts have led to the development of less expensive and more abundant electrocatalysts for PEMFCs.⁶² These include advanced Pt alloys, core-shell structures, transition metal oxides and chalcogenides, and non-noble metal@porous carbon based composite catalysts.⁶² The first example of using MOFs as template for preparing non-Pt-group-metal (non-PGM) ORR catalysts has been reported by Liu *et al.*^{62d} In this study, Co-based ZIF-67, a subclass of MOF material, has been chosen as precursor to produce

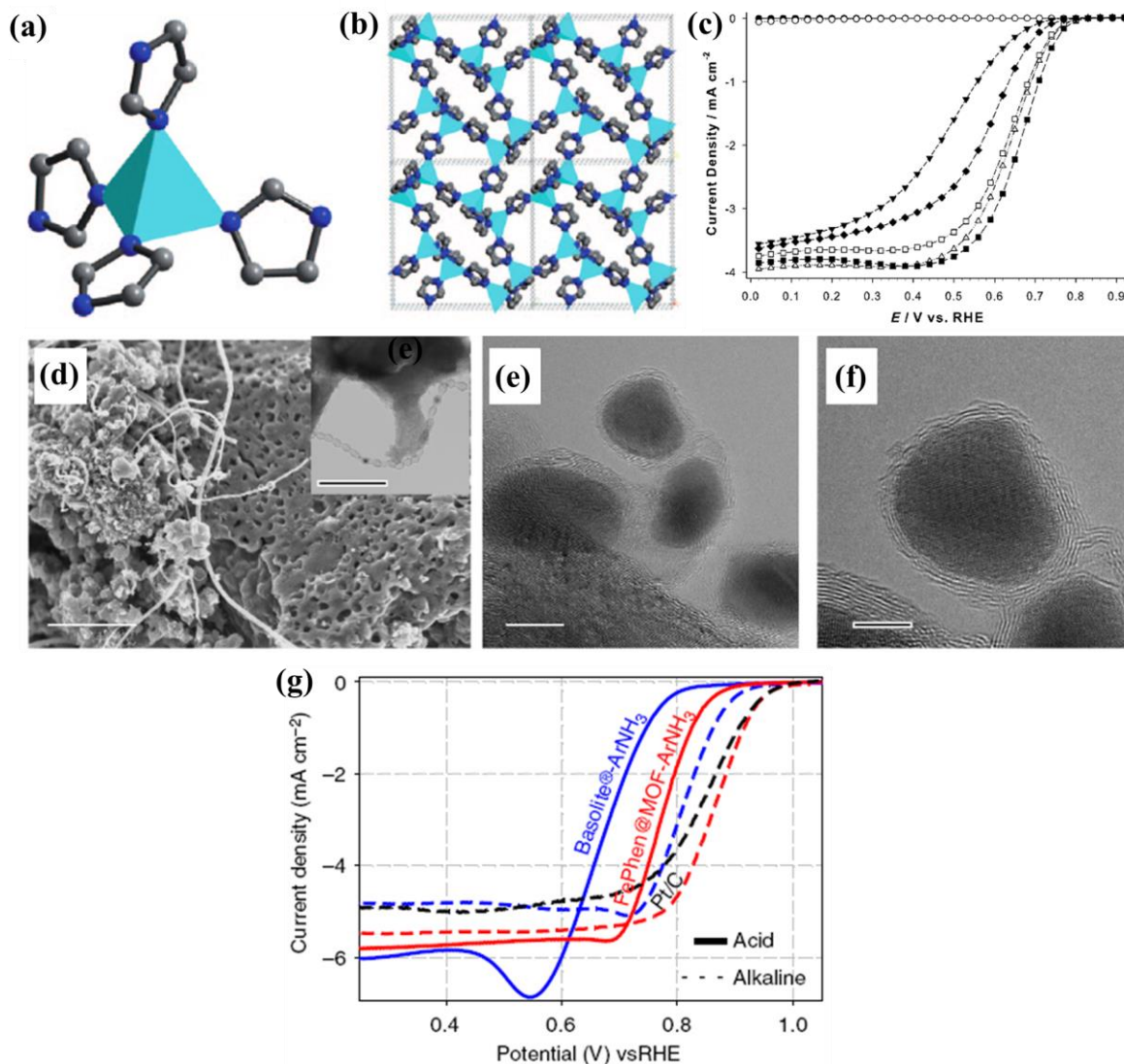


Figure 22: (a) Local Co–N₄ coordination moiety, (b) structure packing of ZIF-67 along the [100] direction (color scheme: turquoise=Co, blue=N, grey= C), (c) faradaic current density as a function of the potential with reference to the reversible hydrogen electrode (RHE) for 1 at different temperatures (● =fresh sample, T=500 (○), 600 (▼), 700 (∼), 750 (■), 800 (□), and 900 °C (◆); rotating speed=1600 rpm, the measurements have been performed 0.1 M HClO₄ solution saturated by oxygen at 25 °C. From reference 62d. Reproduced by permission of *Chem. Eur. J.* (d) SEM image of FePhen@MOF-ArNH₃. Scale bar, 2 mm. Inset TEM image of bamboo-jointed CNT. Scale bar, 100 nm, (e) HRTEM image of iron encapsulated in bamboo joints of CNT in FePhen@MOF-ArNH₃. Scale bar, 10 nm, (f) HRTEM image of Fe/Fe_xC nanoparticle surrounded by graphite layers. Scale bar, 5 nm. From reference 62e. Reproduced by permission from *Nat. Commun.*

highly active Co–N₄ rich electrocatalysts (Figure 22a-c). On pyrolysis under inert atmosphere at 750 °C, ZIF 67 is completely transformed into a highly efficient ORR catalyst with an

onset potential of 0.83 V vs. RHE, and interestingly, this value is comparable to the best cobalt-based non-PGM catalysts. The electron transfer number for this ORR process is calculated to be in the range of 3.2 to 3.5, suggesting a direct four-electron transfer pathway. Recently, Mukerjee *et al.* have synthesized an excellent Fe-based ORR carbonaceous electrocatalysts (FePhen@MOF-ArNH₃) from a Fe-chelated N-complex encapsulated ZIF-8 precursor by heat treatment in Ar followed by NH₃ at 1,050 and 1050 °C, respectively (Figure 22d-g).^{62e} This catalyst shows onset potential of 1.03 and 0.93 V vs. RHE in alkaline and acidic media, respectively. It is believed that the presence of Fe/Fe_xC are imparting synergistic effect on the N-doped carbon layer enabling full 4e⁻ reduction of oxygen to water. These interesting electrocatalytic properties have motivated researchers to develop further MOF-derived active ORR catalysts for better performance.

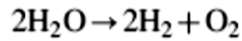
1.8.2.2 Oxygen evolution reaction (OER)

The electrolysis of water to O₂ and H₂ gas is capable of providing a significant amount of renewable energy needed to power a sustainable civilization. The product H₂ gas, an energy dense material, can be burned directly like natural gas or later be used to produce electricity in a fuel cell.^{63a-c} H₂ is also an important feedstock in chemical industry for different purposes such as petroleum refining, Fischer-Tropsch synthesis of hydrocarbons, and the Haber-Bosch process for generation of ammonia.^{63d} Currently, H₂ is mostly produced by steam-reforming of fossil fuels, forming greenhouse gas CO₂ as a byproduct,⁶³ hence, H₂ produced from water electrolysis can be an alternative green pathway. Considering the cathodic part of water electrolysis, i.e., the water reduction to H₂ (hydrogen evolution reaction = HER), Pt/ Pt based catalyst is a nearly ideal catalyst.⁶³ In contrast, for the anodic part, i.e. water oxidation to O₂ (oxygen evolution reactions = OER), the sluggish kinetics of the OER limits the efficiency of this reaction since it is thermodynamically and kinetically unfavourable to remove four electrons to form oxygen–oxygen double bond (O₂). The bottleneck in improving the water electrolysis process is OER, where even the most efficient precious-metal based catalysts suffers a substantial overpotential to reach the desired current densities $\geq 10 \text{ mA cm}^{-2}$.⁶³

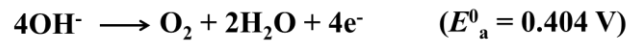
Overall water oxidation reaction

As we have mentioned, the water electrolysis reaction is composed of two half-reactions: HER and OER, respectively, and the reactions are given below. Both the oxidation and reduction steps are pH dependent.

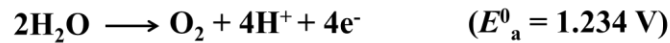
The overall water electrolysis reaction is given below



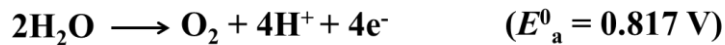
Hence, in alkaline solutions (pH= 14), the corresponding cathode and anode reactions are



where E^0_c and E^0_a are the equilibrium half-cell potentials at standard conditions of 1 atm and 25 °C. In acid solutions (pH = 0),



In neutral conditions (pH = 7), the reactions are



It also explains that water electrolysis is relatively favourable in acid and alkaline conditions than in neutral condition due to the presence of deprotonated water molecules available for OER in alkaline solution or HER in acid solutions. This also explains why water electrolysis in neutral condition is kinetically more difficult.

Thus at standard conditions, the equilibrium or reversible potential of water electrolysis is 1.23 V. Therefore, it takes -475 kJ of energy to produce one mole of O_2 as calculated by thermodynamics i.e. Gibbs free energy equation represented by as follows

$$\Delta G^{\circ} \text{cell} = -nFE^{\circ} \text{cell}$$

However, in reality no process can be so efficient and, systems always suffer from overpotential arising from activation barriers, concentration effects and voltage drops due to resistance. This activation barriers or activation energy is associated with high energy

transition states which need to be crossed during the electrochemical process of OER. The lowering of these barriers allows lower overpotentials, thereby accelerating the rate of OER.

Mechanism

Heterogeneous OER process is sensitive to the surface on which the reaction takes place, and also gets affected by the pH of the medium. The general mechanism in acidic and alkaline solutions is explained below based on Pt and oxide catalysts (Figure 23).⁶⁴ In acidic environment, H₂O molecules bind to the catalyst surface with irreversible removal of one e⁻ and one H⁺ to form a platinum hydroxide.^{64a} In an alkaline solution, a reversible OH⁻ binding coupled to one e⁻ oxidation is considered to be turnover-limiting electrochemical step involving one H⁺ and e⁻ removal forming a surface oxide species.^{64b} Using the Tafel equation, kinetic information can be obtained such as exchange

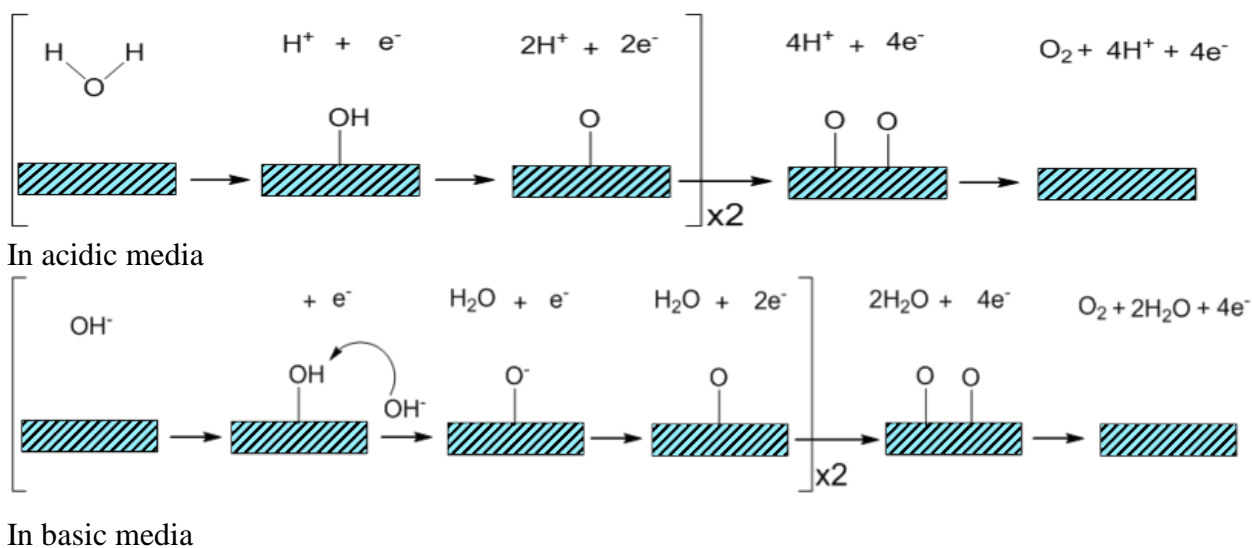


Figure 23: Proposed OER mechanistic pathway on Pt and oxide catalysts.

current density and the Tafel slope.^{64c} Consequently, huge amount of efforts have been dedicated for developing effective catalysts based on different types of chemical compounds and composites. Metal oxides, including RuO₂ and IrO₂-based electrodes, transition metal (Co, Fe, Ni, Mn) oxides or hydroxides layers, spinels, and perovskites have been intensively investigated.^{65a-b} Recently, MOF and MOF-derived materials have also projected themselves as highly promising candidates for water oxidation. For instance, ZIF-67 has been also used

as self-sacrificial template for preparing non-precious-metal electrocatalysts for the HER and OER. Sun *et al.* synthesized a facile ZIF-67 derived porous Co-P/NC nanopolyhedrons consisting of CoP_x nanoparticles by direct carbonization of MOF followed by phosphidation (Figure 24a-e).^{65c} The Co-P/NC electrocatalyst exhibited remarkable performance for both HER and OER process in 1.0 M KOH, with a current density of 10 mA cm^{-2} at low overpotentials of -154 and 319 mV for HER, OER, respectively. Moreover, the Co-P/NC-based alkaline electrolyzer approached 165 mA cm^{-2} at 2.0 V , which was much greater than that of Pt/IrO_2 (89 mA cm^{-2}). In a completely different approach, Qiao *et al.* fabricated

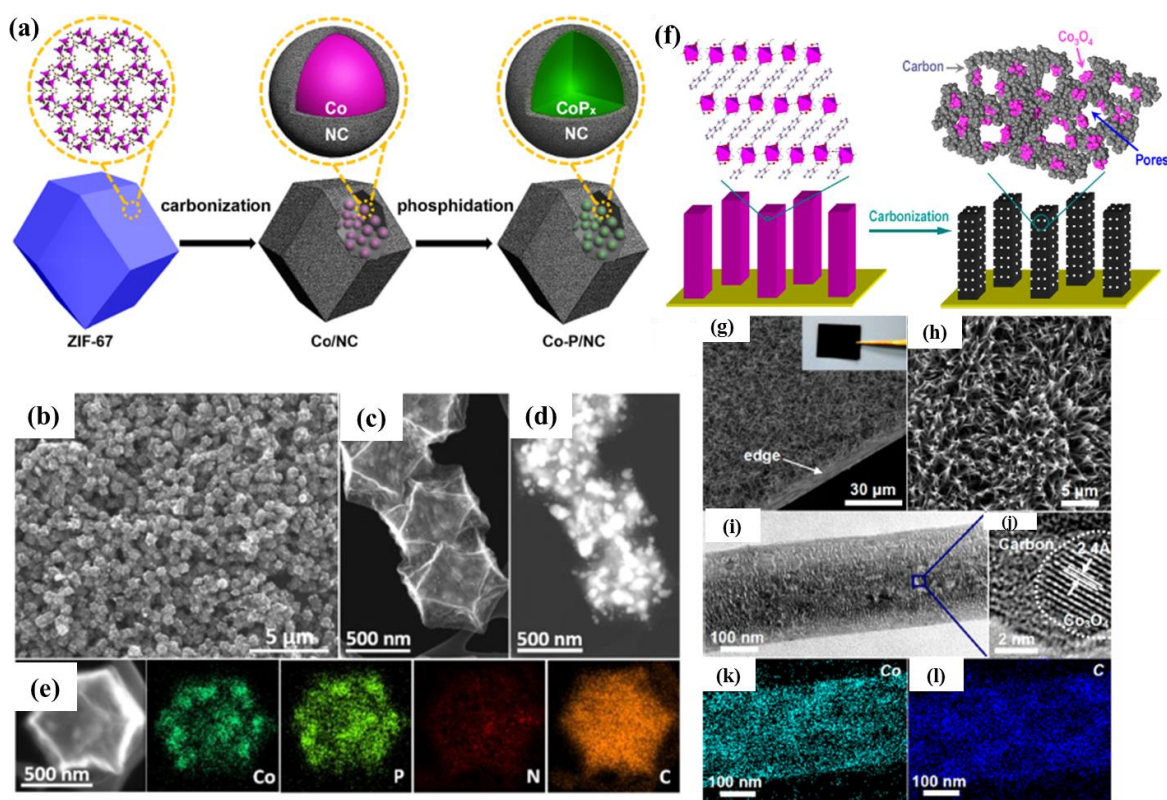


Figure 24: (a) Illustration of the two-step synthesis of Co-P/NC nanopolyhedrons, (b) SEM, (c) highly magnified SEM and (d) the corresponding STEM images of Co-P/NC, (e) STEM and the elemental mapping images of Co-P/NC showing the element distributions of Co, P, N, and C. From reference 65c. Reproduced by permission from *Chem. Mater.* (f) Fabrication of hybrid Co_3O_4 -carbon porous nanowire arrays (g-h) SEM, inset is optical image, (i) TEM image, (j) HRTEM image, and (k-l) EDS elemental mapping images of Co_3O_4 -C-NA. From reference 65d. Reproduced by permission from *J. Am. Chem. Soc.*

advanced electrode of hybrid Co_3O_4 -carbon nanowire arrays directly grown on Cu foil (Figure 24f-1).^{65d} As illustrated, a Co-naphthalenedicarboxylate MOF has been directly grown on Cu foil *via* hydrothermal route at 80 °C. Next, the MOF has been converted into Co_3O_4 -C composite *via* carbonization under N_2 atmosphere, retaining the original nanowire morphology as of the parent MOF. Because of the strong interaction between the Co_3O_4 -C nanowires and the Cu foil (acting as current collector), this could be directly used as the working electrode without using extra substrates or binders. In the OER process, this shows an outstanding electrocatalytic activity with a low onset potential of ~ 1.47 V (*vs.* RHE), which is comparable to the value of ~ 1.45 V for the IrO_2/C noble-metal catalyst. However, the OER current density is much higher than that of IrO_2/C with same loading C content. The high OER performance of this novel electrode has been attributed to the porous nanostructure of the nanowire arrays which led to high active surface area, strong structural stability, and improved mass/charge transport.

1.9 Bi-functional electrocatalysts for ORR and OER

Electrocatalysts for oxygen reduction and oxygen evolution reactions (ORR and OER) are undeniably crucial for various renewable energy technologies; the ORR is the universal cathode reaction in fuel cells and metal–air batteries, while the OER occurs in anode part of electrolysis cells and plays an important role in energy storage such as solar fuel synthesis and water electrolysis.⁵⁷ A unitized regenerative fuel cell (URFC) is a promising energy storage system which mainly works as a fuel cell consuming H_2 and, in a reverse manner, as a water electrolyzer producing H_2 and O_2 . Bi-functional catalysts with high activities for both ORR and OER are desirable in this system to catalyze the process. Till date, Pt and its alloys have always been regarded as the most efficient ORR catalysts.⁶² However, their high cost and poor durability severely hinder their application to broad commercialization. However, Pt has moderate activity for the OER process, which is not satisfactory enough as an ideal bi-functional electrocatalyst in URFC. RuO_2 and IrO_2 are considered to be the state-of-art OER catalysts,⁶³ however, these metals suffer from the scarcity, high cost and, moreover, are not as active for the ORR as Pt. Therefore, it is highly challenging to develop efficient bi-functional electrocatalysts with low cost and superior durability towards both ORR and OER to replace conventional precious state-of-art metals

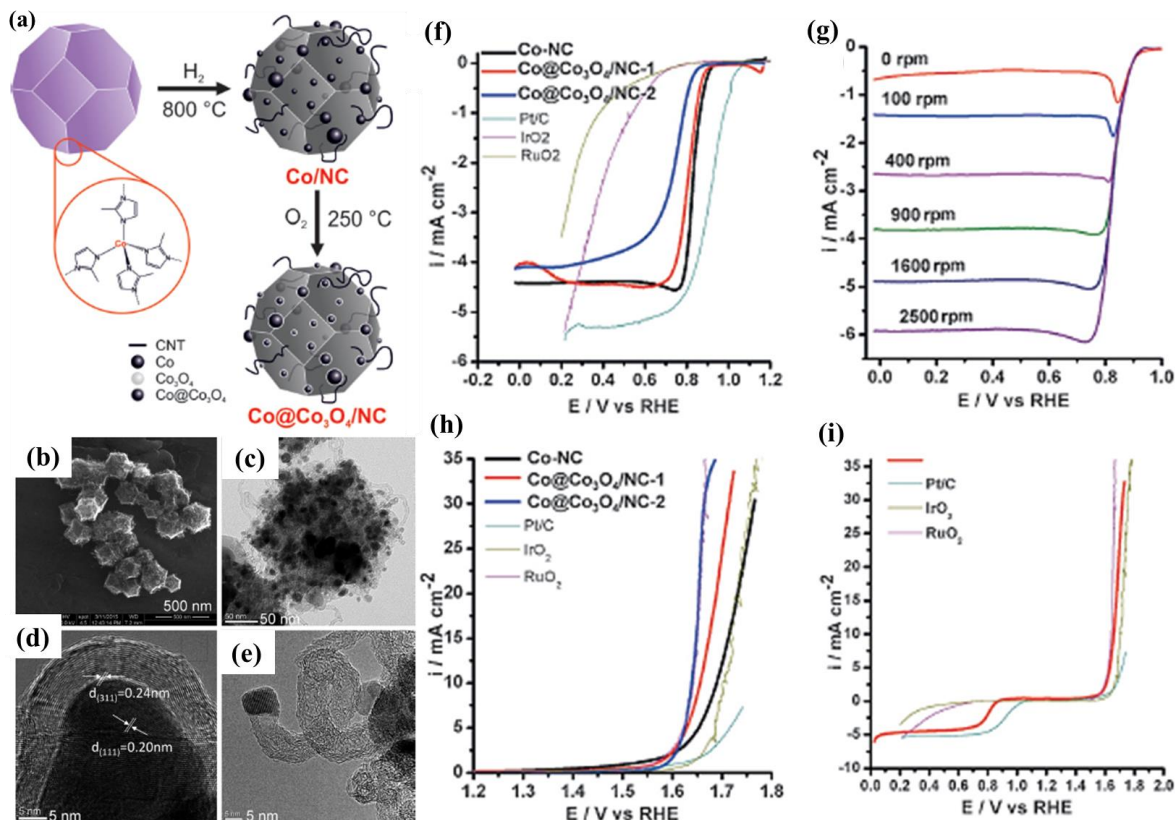


Figure 25: (a) Representation of the formation of core-shell $\text{Co@Co}_3\text{O}_4$ nanoparticles encapsulated in CNT-grafted N-doped carbon polyhedral by use of reductive carbonization of a N-containing MOF (ZIF-67) (b) SEM and (c) TEM images of Co/NC; high resolution TEM images of $\text{Co@Co}_3\text{O}_4/\text{NC-1}$ showing (d) $\text{Co@Co}_3\text{O}_4$ nanoparticles embedded in graphitic layers and (e) wrapped CNT. LSV of different electrocatalysts at 1600 rpm showing RDE electrocatalysis of (f) oxygen reduction (g) LSV of Co/NC at various rotating speeds (h) water oxidation (i) a comparison of ORR and OER bifunctional activities of $\text{Co@Co}_3\text{O}_4/\text{NC-1}$, Pt/C, IrO_2 , RuO_2 . All the voltammograms were recorded in O_2 -saturated 0.1M KOH at a scan rate of 5 mV s^{-1} . From reference 66c. Reproduced by permission from *Angew. Chem. Int. Ed.*

utilized in URFC. In the past few years, various non-precious materials have exhibited excellent catalytic activity for ORR or OER, however, reports on bi-functional activity are limited in literature.⁶⁶⁻⁸⁰ However, most of these reported electrocatalysts suffer from limited catalytic activities due to their small specific surface area and low conductivities. Loading transition metal oxides on conducting carbon support can overcome the limitations and improve the catalytic activity. For example, Muhler *et al.* have successfully synthesized core-shell $\text{Co@Co}_3\text{O}_4$ NPs embedded in N-doped CNT-grafted carbon polyhedra by the pyrolysis of ZIF-67 under H_2 atmosphere followed by controlled oxidative calcination

(Figure 25).^{66c} This catalyst exhibited excellent bi-functional catalytic activity towards both ORR and OER, the OER activity is higher than that of Pt/C and IrO₂, very similar to that of the benchmark OER catalyst RuO₂, and ORR activity is comparable to that of the benchmark ORR catalyst Pt/C. The investigation of MOFs in this area is quite recent and expanding. Hence, it is encouraging and important to study such energy applications of these hybrid carbonaceous composites, which is indeed one of our concerns in this thesis.

1.10 Conclusion

This chapter demonstrates the general overview of MOFs, different synthetic procedures, potential applications of bulk/nano MOFs, especially, gas storage and separation, drug delivery, imaging, photochromism/host-guest chemistry and finally MOF derived materials for gas storage and energy applications. As discussed, applications of MOFs for practical separation of CO₂ and hydrocarbons from a mixture of gases are challenging tasks. Especially, removing CO₂ from flue gas or natural gas is restricted in presence of moisture, and hence, functionalized (such as NH₂, -OH or RNC=O) frameworks would be more helpful for better selectivity and separation than mostly studied unsaturated metal sites (UMSs) containing frameworks. Further, if these features of frameworks blend with structural dynamics or flexibility of MOFs, it might act as better separation materials. In this thesis, we have studied such framework for such applications. Photochromic i.e. light sensitive materials are important for optics and display device applications. But targeted synthesis of such materials is a difficult job to perform as constructing chromophoric donor-acceptor spatial-organizations is tricky and their stability is susceptible to surrounding environment. We envisage that, with the help of suitable metal-oxygen backbone and donor-acceptor pair selection, such properties can be realized in MOF, and here, we have studied this in details.

It is needless to mention that, there is plenty of room for development of MOF based technology in nanoscale. Unfortunately, regardless of their myriad potential applications in several fields, there is insufficient information about crystal growth and mechanism related work, which need to be explored further. In this thesis, detailed in-depth studies have been carried out for understanding such concepts. Recently, a new trend of MOF derived materials has been started for energy applications. With an easy synthetic route, scalable cheap product, room for tunability in various ways, and most importantly, available options for

suitable selection of MOF precursor from a library of frameworks, have made this field very attractive to scientists. In the last part of this thesis, MOF derived materials have been synthesized and experimented for energy applications.

1.11 References

1. M. O’Keeffe, M. A. Peskov, S. J. Ramsden, O. M. Yaghi, *Acc. Chem. Res.* **2008**, *41*, 1782.
2. G. Férey, *Chem. Soc. Rev.* **2009**, *37*, 191.
3. S. Horike, S. Shimomura, S. Kitagawa, *Nat. Chem.* **2010**, *1*, 695.
4. D. J. Tranchemontagne, J. L. Mendoza-Cortes, M. O’Keeffe, O. M. Yaghi, *Chem. Soc. Rev.* **2009**, *38*, 1257.
5. M. Eddaoudi, D. B. Moler, H. Li, B. Chen, T. M. Reineke, M. O’Keeffe, O. M. Yaghi, *Acc. Chem. Res.* **2001**, *34*, 319.
6. U. Mueller, M. Schubert, F. Teich, H. Puetter, K. Schierle-Arndt, J. Pastre, *J. Mater. Chem.* **2006**, *16*, 626.
7. Y. Huang, B. Ding, H. Song, B. Zhao, P. Ren, P. Cheng, H. Wang, D. Liao, S. Yan, *Chem. Commun.* **2006**, 4906.
8. M. Kurmoo, *Chem. Soc. Rev.* **2009**, *38*, 1353.
9. S. Bordiga, C. Lamberti, G. Ricchiardi, L. Regli, F. Bonino, A. Damin, K. Lillerud, M. Bjorgenn, A. Zecchina, *Chem. Commun.* **2004**, 2300.
10. G. J. Halder, C. J. Kepert, B. Moubaraki, K. S. Murray, J. D. Cashion, *Science*, **2002**, *298*, 1762.
11. (a) A. Carne’, C. Carbonell, I. Imaz and D. Maspoch, *Chem. Soc. Rev.* **2011**, *40*, 291
(b) P. Falcaro, R. Ricco, C. M. Doherty, K. Liang, A. J. Hill, M. J. Styles, *Chem. Soc. Rev.* **2014**, *43*, 5513 (c) S. Furukawa, J. Reboul, S. Diring, K. Sumida, S. Kitagawa *Chem. Soc. Rev.* **2014**, *43*, 5700 (d) E. A. Flügel, A. Ranft, F. Haase, B. V. Lotsch, *J. Mater. Chem.* **2012**, *22*, 10119. (e) P. Horcajada, R. Gref, T. Baati, P. K. Allan, u. Maurin, P. Couvreur, G. Férey, R. E. Morris, C. Serre, *Chem. Rev.* **2012**, *112*, 1232.
12. Z. Song, N. Cheng, A. Lushington, X. Sun, *Catalysts* **2016**, *6*, 116
13. W. Chaikittisilp, K. Ariga, Y. Yamauchi, *J. Mater. Chem. A*, **2013**, *1*, 14.

14. R. R. Salunkhe, Y. V. Kaneti, J. Kim, J. H. Kim, Y. Yamauchi, *Acc. Chem. Res.* **2016**, *49*, 2796.
15. M. Shao, Q. Chang, J. P. Dodelet, R. Chenitz, *Chem. Rev.* **2016**, *116*, 3594.
16. N. Stock, S. Biswas, *Chem. Rev.* **2012**, *112*, 933.
17. (a) S. Kitagawa, M. Kondo, *Bull. Chem. Soc. Jpn.* **1998**, *71*, 1739 (b) S. Horike, S. Shimomura, S. Kitagawa, *Nat. Chem.* **2009**, *1*, 695.
18. M. Eddaoudi, J. Kim, N. Rosi, D. Vodak, J. Wachter, M. O’Keeffe, O. M. Yaghi, *Science*, 2002, **295**, 469.
19. R. Haldar, N. Sikdar and T. K. Maji, *Mater. Today*, **2015**, *18*, 97.
20. A. Schneemann, V. Bon, I. Schwedler, I. Senkovska, S. Kaskel, R. A. Fischer, *Chem. Soc. Rev.* **2014**, *43*, 6062.
21. O. K. Farha, I. Eryazici, N. C. Jeong, B. G. Hauser, C. E. Wilmer, A. A. Sarjeant, Q. Snurr, S. T. Nguyen, A. Ö. Yazaydin, J. T. Hupp, *J. Am. Chem. Soc.* **2012**, *134*, 15016.
22. H. K. Chae, D. Y. Siberio-Perez, J. Kim, Y. Go, M. Eddaoudi, A. J. Matzger, M. O’Keeffe, O. M. Yaghi, *Nature* **2004**, *427*, 523.
23. G. Férey, C. Mellot-Draznieks, C. Serre, F. Millange, J. Dutour, S. Surble and I. Margiolaki, *Science*, **2005**, *309*, 2040.
24. K. Koh, A. G. Wong-Foy, A. J. Matzger, *J. Am. Chem. Soc.* **2009**, *131*, 4184.
25. H. Furukawa, N. Ko, Y. B. Go, N. Aratani, S. B. Choi, E. Choi, A. O. Yazaydin, R. Q. Snurr, M. O’Keeffe, J. Kim and O. M. Yaghi, *Science*, **2010**, *329*, 424.
26. M. P. Suh, H. J. Park, T. K. Prasad, D. W. Lim, *Chem. Rev.* **2012**, *112*, 782.
27. Z. R. Herm, E. D. Bloch, J. R. Long, *Chem. Mater.* **2014**, *26*, 323.
28. (a) Z. Zhang, Y. Zhao, Q. Gong, Z. Li, J. Li, *Chem. Commun.* **2013**, *49*, 653 (b) J. R. Li, Y. Ma, M. C. McCarthy, J. Sculleya, J. Yu, H. K. Jeong, P. B. Balbuena, H. C. Zhou, *Coord. Chem. Rev.* **2011**, *255*, 1791 (c) K. Sumida, D. L. Rogow, J. A. Mason, T. M. McDonald, E. D. Bloch, Z. R. Herm, T. H. Bae, J. R. Long, *Chem. Rev.* **2012**, *112*, 724.
29. A. R. Millward, O. M Yaghi, *J. Am. Chem. Soc.* **2005**, *127*, 17998.
30. P. Nugent, Y. Belmabkhout, S. D. Burd, A. J. Cairns, R. Luebke, K. Forrest, T. Pham, S. Ma1, B. Space, L. Wojtas, M. Eddaoudi, M. J. Zaworotko, *Nature*, **2013**, *495*, 80.

31. L. A. Darunte, A. D. Oetomo, K. S. Walton, D. S. Sholl, C. W. Jones, *ACS Sustainable Chem. Eng.* **2016**, *4*, 5761.
32. R. Vaidhyanathan, S. S. Iremonger, G. K. H. Shimizu, P. G. Boyd, S. Alavi, T. K. Woo, *Science*, **2010**, *330*, 650.
33. W. Yang, A. J. Davies, X. Lin, M. Suyetin, R. Matsuda, A. J. Blake, C. Wilson, W. Lewis, J. E. Parker, C. C. Tang, M. W. George, P. Hubberstey, S. Kitagawa, H. Sakamoto, E. Bichoutskaia, N. R. Champness, S. Yang, M. Schröder, *Chem. Sci.* **2012**, *3*, 2993.
34. L. J. Murray, M. Dincă, J. R. Long, *Chem. Soc. Rev.* **2009**, *38*, 1294.
35. Y. He, W. Zhou, G. Qian, B. Chen, *Chem. Soc. Rev.* **2014**, *43*, 5657.
36. C. Y. Lee, Y. S. Bae, C. N. Jeong, O. K. Farha, A. A. Sarjeant, C. L. Stern, P. Nickias, R. Q. Snurr, J. T. Hupp, S. T. Nguyen, *J. Am. Chem. Soc.* **2011**, *133*, 5228.
37. E. D. Bloch, W. L. Queen, R. Krishna, J. M. Zadrozny, C. M. Brown, J. R. Long, *Science* **2012**, *335*, 1606.
38. A. F. P. Ferreira, J. C. Santos, M. G. Plaza, N. Lamia, J. M. Loureiro, A. E. Rodrigues, *Chem. Eng. J.* **2011**, *167*, 1.
39. M. G. Plaza, A. F. Ferreira, J. C. Santos, A. M. Ribeiro, U. Müller, N. Trukhan, J. M. Loureiro, A. E. Rodrigues, *Microporous Mesoporous Mater.* **2012**, *157*, 101.
40. S. J. Geier, J. A. Mason, E. D. Bloch, W. L. Queen, M. R. Hudson, C. M. Brown, J. R. Long, *Chem. Sci.*, **2013**, *4*, 2054.
41. Y. He, W. Zhou, G. Qian, B. Chen, *Chem. Soc. Rev.*, **2014**, *43*, 5657-5678
42. S. Xiang, W. Zhou, Z. Zhang, M. A. Green, Y. Liu, B. Chen, *Angew. Chem.* **2010**, *122*, 4719.
43. J. Pang, F. Jiang, M. Wu, C. Liu, K. Su, W. Lu, D. Yuan, M. Hong, *Nat. Commun.* **2015**, *6*, 7575.
44. (a) A. Pościk, B. Wandelt, *Synth. Met.* **2009**, *159*, 72 (b) K. Kalyanasundaram, M. Grätzel, *Coord. Chem. Rev.* **1998**, *77*, 347 (c) K. Ogawa, Y. Kobuke, *Org. Biomol. Chem.* **2009**, *7*, 2241.
45. (a) M. D. Ward, *Chem. Soc. Rev.* **1997**, *26*, 365 (b) O. S. Wenger, *Chem. Soc. Rev.* **2011**, *40*, 3538 (c) C. Janiak, *J. Chem. Soc. Dalton Trans.* **2000**, 3885 (c) N. Kishi, M. Akita, M. Yoshizawa, *Angew. Chem. Int. Ed.* **2014**, *53*, 3604 (d) A. P. H. J.

- Schenning, E. W. Meijer, *Chem. Commun.* **2005**, 3245 (e) M. Kumar, K. V. Rao, S. J. George, *Phys.Chem.Chem.Phys.* **2014**, *16*, 1300.
46. (a) M. V. Suresh, S. J. George, T. K Maji, *Adv. Funct. Mater.* **2013**, *23*, 5585 (b) R. Haldar, K. V. Rao, S. J. George, T. K. Maji, *Chem. Eur. J.* **2012**, *18*, 5848 (c) C. Y. Lee, O. K. Farha, B. J. Hong, A. A. Sarjeant, S. T. Nguyen, J. T. Hupp, *J. Am. Chem. Soc.* **2011**, *133*, 15858 (d) T. Zhang, W. Lin, *Chem. Soc. Rev.* **2014**, *43*, 5982 (e) K. V. Rao, K. K. R. Datta, M. Eswaramoorthy, S. J. George, *Chem. Eur. J.* **2012**, *18*, 2184 (f) K. V. Rao, A. Jain, S. J. George, *J. Mater. Chem. C* **2014**, *2*, 3055.
47. (a) Z. Fu, Y. Chen, J. Zhang, S. Liao, *J. Mater. Chem.* **2011**, *21*, 7895 (b) M. S. Wang, G. C. Guo, W. Q. Zou, W. W. Zhou, Z. J. Zhang, G. Xu, J. S. Huang, *Angew. Chem. Int. Ed.* **2008**, *47*, 3565 (c) Q. L. Zhu, T. L. Sheng, R. B. Fu, S. M. Hu, L. Chen, C. J. Shen, X. Ma, X. T. Wu, *Chem. Eur. J.* **2011**, *17*, 3358.
48. (a) N. Yanai, K. Kitayama, Y. Hijikata, H. Sato, R. Matsuda, Y. Kubota, M. Takata, M. Mizuno, T. Uemura, S. Kitagawa, *Nat. Mater.* **2011**, *10*, 787 (b) D. Tanaka, S. Horike, M. Ohba, M. Hasegawa, Y. Ozawac, K. Toriumi, S. Kitagawa, *Chem. Commun.* **2007**, 3142 (c) R. Haldar, R. Matsuda, S. Kitagawa, S. J. George, T. K. Maji, *Angew. Chem. Int. Ed.* **2014**, *126*, 11966.
49. (a) Y. Takashima, V. M. Martínez, S. Furukawa, M. Kondo, S. Shimomura, H. Uehara, M. Nakahama, K. Sugimoto, S. Kitagawa, *Nat. Commun.* **2011**, *2*, 168 (b) Y. Zeng, Z. Fu, H. Chen, C. Liu, S. Liaoa, J. Dai, *Chem. Commun.* **2012**, *48*, 8114.
50. (a) S. A. Maier, M. L. Brongersma, P.G. Kik, S. Meltzer, A. A. G. Requicha, H. A. Atwater, *Adv. Mater.* **2001**, *13*, 1501 (b) D. V. Talapin, J. S. Lee, M. V. Kovalenko, E. V. Shevchenko, *Chem. Rev.* **2010**, *110*, 389 (c) E. M. McGarrigle, E. L. Myers, O. Illa, M. A. Shaw, S. L. Riches, V. K. Aggarwal, *Chem. Rev.* **2007**, *107*, 5841 (d) S. Carenco, D. Portehault, C. Boissière, N. Mézailles, C. Sanchez, *Chem. Rev.* **2013**, *113*, 7981 (e) D. Grosso, G. J. A. A. S. Illia, E. L. Crepaldi, B. Charleux, C. Sanchez, *Adv. Func. Mater.* **2003**, *13*, 37 (f) Ganter, L. M. Schoop, B. V. Lotsch, *Adv. Mater.* **2017**, DOI: 10.1002/adma.201604884.
51. (a) M. J. R. Virlan, D. Miricescu, R. Radulescu, C. M. Sabliov, A. Totan, B. Calenic, M. Greabu, *Molecules* **2016**, *21*, 207 (b) H. Yu, D. Y. Kim, K. J. Lee, J. H. Oh, *J Nanosci Nanotechnol.* **2014**, *14*, 1282.

52. (a) H. J. Lee, J. We, J. O. Kim, D. Kim, W. Cha, E. Lee, J. Sohn, M. Oh, *Angew. Chem. Int. Ed.* **2015**, *54*, 10564 (b) T. Tsuruoka, S. Furukawa, Y. Takashima, K. Yoshida, S. Isoda, S. Kitagawa, *Angew. Chem. Int. Ed.* **2009**, *48*, 4739 (c) S. Diring, S. Furukawa, Y. Takashima, T. Tsuruoka, S. Kitagawa, *Chem. Mater.* **2010**, *22*, 4531 (d) A. Umemura, S. Diring, S. Furukawa, H. Uehara, T. Tsuruoka, S. Kitagawa, *J. Am. Chem. Soc.* **2011**, *133*, 15506 (e) W. J. Rieter, K. M. L. Taylor, H. An, W. Lin, W. Lin, *J. Am. Chem. Soc.* **2006**, *128*, 9024 (f) K. M. L. Taylor, A. Jin, W. Lin, *Angew. Chem., Int. Ed.* **2008**, *47*, 7722 (g) W. Lin, W. J. Rieter, K. M. L. Taylor, *Angew. Chem., Int. Ed.* **2009**, *48*, 650 (h) H. Guo, Y. Zhu, S. Wang, S. Su, L. Zhou, H. Zhang, *Chem. Mater.* **2012**, *24*, 444 (i) H. J. Lee, W. Cho, S. Jung, M. Oh, *Adv. Mater.* **2009**, *21*, 674 (j) D. Tanaka, A. Henke, K. Albrecht, M. Moeller, K. Nakagawa, S. Kitagawa, J. Groll, *Nat. Chem.* **2010**, *2*, 410 (k) Y. Peng, Y. Li, Y. Ban, H. Jin, W. Jiao, X. Liu, W. Yang, *Science*, **2014**, *346*, 1356.
53. (a) W. J. Rieter, K. M. Pott, K. M. L. Taylor and W. B. Lin, *J. Am. Chem. Soc.* **2008**, *130*, 11584 (b) K. M. L. T. Pashow, J. D. Rocca, Z. Xie, S. Tran, W. Lin, *J. Am. Chem. Soc.* **2009**, *131*, 14261 (c) J. D. Rocca, D. Liu, W. Lin, *Acc. Chem. Res.* **2011**, *44*, 957.
54. (a) H. Jankowska, A. Swiatkowski, J. Choma, E. Horwood, *Active Carbon*, **1991** (b) B. Fang, M. Kim, S. Q. Fan, J. H. Kim, D. P. Wilkinson, J. Ko, J. S. Yu, *J. Mater. Chem.* **2011**, *21*, 8742 (c) B. Fang, S. Q. Fan, J. H. Kim, M. S. Kim, M. Kim, N. K. Chaudhari, J. Ko, J. S. Yu, *Langmuir*, **2010**, *26*, 11238 (d) J. H. Kim and J. S. Yu, *Phys. Chem. Chem. Phys.* **2010**, *12*, 15301.
55. (a) R. Ryoo, S. H. Joo, S. Jun, *J. Phys. Chem. B* **1999**, *103*, 7743 (b) T. Kyotani, T. Nagai, S. Inoue, A. Tomita, *Chem. Mater.* **1997**, *9*, 609 (c) H. Yang, D. Zhao, *J. Mater. Chem.* **2005**, *15*, 1217.
56. (a) Y. Meng, D. Gu, F. Zhang, Y. Shi, H. Yang, Z. Li, C. Yu, B. Tu, D. Zhao, *Angew. Chem. Int. Ed.* **2005**, *44*, 7053 (b) D. Feng, Y. Lv, Z. Wu, Y. Dou, L. Han, Z. Sun, Y. Xia, G. Zheng, D. Zhao, *J. Am. Chem. Soc.* **2011**, *133*, 15148 (c) Z. Wu, P. A. Webley, D. Zhao, *J. Mater. Chem.* **2012**, *22*, 11379.
57. (a) W. Chaikittisilp, K. Ariga, Y. Yamauchi, *J. Mater. Chem. A*, **2013**, *1*, 14 (b) W. Xia, A. Mahmood, R. Zou, Q. Xu, *Energy Environ. Sci.* **2015**, *8*, 1837 (c) K. Shen, X.

- Chen, J. Chen, Y. Li, *ACS Catal.* **2016**, *6*, 5887 (d) Z. Song, N. Cheng, A. Lushington, X. Sun, *Catalysts* **2016**, *6*, 116.
58. (a) P. Pachfule, B. P. Biswal, R. Banerjee, *Chem. Eur. J.* **2012**, *18*, 11399 (b) H. B. Aiyappa, P. Pachfule, R. Banerjee, S. Kurungot, *Cryst. Growth Des.* **2013**, *13*, 4195 (c) L. Zhang, Z. Su, F. Jiang, L. Yang, J. Qian, Y. Zhou, W. Lia, M. Hong, *Nanoscale*, **2014**, *6*, 6590 (d) W. Xia, J. Zhu, W. Guo, L. An, D. Xia, R. Zou, *J. Mater. Chem. A*, **2014**, *2*, 11606 (e) L. Shang, H. Yu, X. Huang, T. Bian, R. Shi, Y. Zhao, G. I. N. Waterhouse, L. Z. Wu, C. H. Tung, T. Zhang, *Adv. Mater.* **2016**, *28*, 1668.
59. (a) V. P. Santos, T. A. Wezendonk, J. J. Jaen, A. I. Dugulan, M. A. Nasalevich, H. U. Islam, A. Chojecki, S. Sartipi, X. Sun, A. A. Hakeem, A. C. Koeken, M. Ruitenbeek, T. Davidian, G. R. Meima, G. Sankar, F. Kapteijn, M. Makkee, J. Gascon, *Nat. Commun.* **2015**, *6*, 6451 (b) S. J. Yang, S. Nam, T. Kim, J. H. Im, H. Jung, J. H. Kang, S. Wi, B. Park, C. R. Park, *J. Am. Chem. Soc.* **2013**, *135*, 7394.
60. (a) B. Liu, H. Shioyama, T. Akita, Q. Xu, *J. Am. Chem. Soc.* **2008**, *130*, 5390 (b) M. Hu, J. Reboul, S. Furukawa, N. L. Torad, Q. Ji, P. Srinivasu, K. Ariga, S. Kitagawa, Y. Yamauchi, *J. Am. Chem. Soc.* **2012**, *134*, 2864 (c) A. Almasoudi, R. Mokaya, *J. Mater. Chem.* **2012**, *22*, 146 (d) H. L. Jiang, B. Liu, Y. Q. Lan, K. Kuratani, T. Akita, H. Shioyama, F. Zong, Q. Xu, *J. Am. Chem. Soc.* **2011**, *133*, 11854 (e) S. J. Yang, T. Kim, J. H. Im, Y. S. Kim, K. Lee, H. Jung, C. R. Park, *Chem. Mater.* **2012**, *24*, 464.
61. Q. Lu, J. G. Chen, J. Q. Xiao, *Angew. Chem. Int. Ed.* **2013**, *52*, 1882.
62. (a) M. Shao, Q. Chang, J. P. Dodelet, R. Chenitz, *Chem. Rev.* **2016**, *116*, 3594. (b) A. Morozan, B. Jousset, S. Palacin, *Energy Environ. Sci.* **2011**, *4*, 1238 (c) H. S. Wroblowa, Y. C. Pan, G. Razumney, *J. Electroanal. Chem.* **1976**, *69*, 195 (d) S. Ma, G. A. Goenaga, A. V. Call, D. J. Liu, *Chem. Eur. J.* **2011**, *17*, 2063 (e) K. Strickland, E. Miner, Q. Jia, U. Tylus, N. Ramaswamy, W. Liang, M. T. Sougrati, F. Jaouen, S. Mukerjee, *Nat. Commun.* **2015**, *6*, 7343.
63. (a) M. G. Walter, E. L. Warren, J. R. McKone, S. W. Boettcher, Q. Mi, E. a. Santori, N. S. Lewis, *Chem. Rev.* **2010**, *110*, 6446 (b) J. R. Mckone, N. S. Lewis, H. B. Gray, *Chem. Mater.* **2014**, *26*, 407 (c) J. A. Turner, *Science* **2004**, *305*, 972 (d) B. A. Pinaud, J. D. Benck, L. C. Seitz, A. J. Forman, Z. Chen, T. G. Deutsch, B. D. James,

- K. N. Baum, G. N. Baum, S. Ardo, H. Wang, E. Miller, T. F. Jaramillo, *Environ. Sci.* **2013**, *6*, 1983.
64. (a) B. E. Conway, T. C. Liu, *Langmuir* **1990**, *6*, 268 (b) V. I. Birss, A. Damjanovic, P. G. Hudson, *J. Electrochem. Soc.* **1986**, *133*, 1621 (c) K. Zeng, D. Zhang, *Prog. Energy Combust. Sci.* **2010**, *36*, 307.
65. (a) M. S. Burke, L. J. Enman, A. S. Batchellor, S. Zou, S. W. Boettcher, *Chem. Mater.* **2015**, *27*, 7549 (b) Y. Cheng, S. P. Jiang, *Prog. Nat. Sci.* **2015**, *25*, 545 (c) B. You, N. Jiang, M. Sheng, S. Gul, J. Yano, Y. Sun, *Chem. Mater.* **2015**, *27*, 7636 (d) T. Y. Ma, S. Dai, M. Jaroniec, S. Z. Qiao, *J. Am. Chem. Soc.* **2014**, *136*, 13925.
66. (a) K. Parvez, S. Yang, Y. Hernandez, A. Winter, A. Turchanin, X. Feng, K. Mullen, *ACS Nano*, **2012**, *6*, 9541. (b) S. Han, D. Wu, S. Li, F. Zhang, X. Feng, *Adv. Mater.* **2014**, *26*, 849 (c) A. Aijaz, J. Masa, C. Rçsler, W. Xia, P. Weide, A. J. R. Botz, R. A. Fischer, W. Schuhmann, M. Muhler, *Angew. Chem. Int. Ed.* **2016**, *55*, 4087.
67. J. Zhang, Z. Zhao, Z. Xia, L. Dai, *Nat. Nano.* **2015**, *10*, 444.
68. J. Jung, M. Risch, S. Park, M. G. Kim, G. Nam, H. Y. Jeong, Y. S. Horn, J. Cho, *Energy Environ. Sci.* **2016**, *9*, 176.
69. B. Y. Xia, Y. Yan, N. Li, H. B. Wu, X. W. Lou, X. Wang, *Nat. energy*, **2016**, *1*, 15006.
70. S. Gadipelli, T. Zhao, S. A. Shevlin, Z. Guo, *Energy Environ. Sci.* **2016**, *9*, 1661.
71. J. C. Li, P. X. Hou, S. Y. Zhao, C. Liu, D. M. Tang, M. Cheng, F. Zhang, H. M. Cheng, *Energy Environ. Sci.* **2016**, *9*, 3079.
72. P. Chen, T. Zhou, L. Xing, K. Xu, Yun Tong, Hui Xie, L. Zhang, W. Yan, W. Chu, C. Wu, Y. Xie, *Angew. Chem. Int. Ed.* **2017**, *56*, 610.
73. H. Jiang, Y. Yao, Y. Zhu, Y. Liu, Y. Su, X. Yang and C. Li, *ACS Appl. Mater. Interfaces*, **2015**, *7*, 21511.
74. P. Ganesan, M. Prabu, J. Sanetuntikul, S. Shanmugam, *ACS Catal.* **2015**, *5*, 3625.
75. Y. Su, Y. Zhu, H. Jiang, J. Shen, X. Yang, W. Zou, J. Chen, C. Li, *Nanoscale*, **2014**, *6*, 15080.
76. Y. Zang, H. Zhang, X. Zhang, R. Liu, S. Liu, G. Wang, Y. Zhang, H. Zhao, *Nano Res.* **2016**, *9*, 2123.

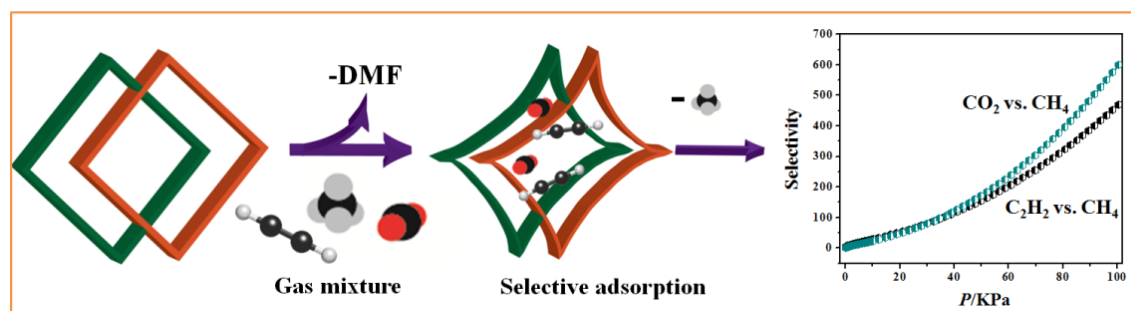
77. J. Wang, H. Wu, D. Gao, S. Miao, G. Wang, X. Bao, *Nano Energy*, **2015**, *13*, 387.
78. S. Dou, L. Tao, J. Huo, S. Wang, L. Dai, *Energy Environ. Sci.* **2016**, *9*, 1320.
79. N. R. Sahraie, J. P. Paraknowitsch, C. Göbel, A. Thomas, P. Strasser, *J. Am. Chem. Soc.* **2014**, *136*, 14486.
80. Z. Wen, S. Ci, Y. Hou, J. Chen, *Angew. Chem. Int. Ed.* **2014**, *53*, 6496.

Chapter 2

*Dynamic Entangled Porous
Framework for Hydrocarbon (C2-
C3) Storage, CO₂ Capture and
Separation*

Chapter 2

Dynamic Entangled Porous Framework for Hydrocarbon (C2-C3) Storage, CO₂ Capture and Separation



Summary: Storage and separation of small (C1-C3) hydrocarbons are of great significance as these are alternative energy resources and also can be used as raw materials for many industrially important materials. Selective capture of greenhouse gas, CO₂ from CH₄ is important to improve the quality of natural gas. Among the available porous materials, MOFs with permanent porosity are the most suitable to serve these purposes. In this chapter, a two-fold entangled dynamic framework $\{[\text{Zn}_2(\text{bdc})_2(\text{bpNDI})] \cdot 4\text{DMF}\}_n$ (H_2bdc = 1,4-benzenedicarboxylic acid, bpNDI = *N,N'*-bis-(4-pyridyl)-1,4,5,8-naphthalenediimide) with pore surface carved with polar functional groups and aromatic π clouds is exploited for selective capture of CO₂, C₂ and C₃ hydrocarbons at ambient condition. The framework shows stepwise CO₂ and C₂H₂ uptake at 195 K but type I profiles are observed at 298 K. The IAST selectivity of CO₂ over CH₄ is the highest (598 at 298 K) among the MOFs without open metal sites reported till date. It also shows high selectivity for C₂H₂, C₂H₄, C₂H₆ and C₃H₈ over CH₄ at 298 K. DFT calculations reveals that aromatic π surface and the polar imide (RNC=O) functional groups are the primary adsorption sites for adsorption. Furthermore, breakthrough column experiments showed CO₂/CH₄, C₂H₆/CH₄, and CO₂/N₂ separation capability at ambient condition.

N. Sikdar, S. Bonakala, R. Haldar, S. Balasubramanian, T. K Maji, *Chem.Eur. J*, 2016, 22, 6059-6070

2.1 Introduction

Light hydrocarbons like CH₄ (methane), C₂H₂ (acetylene), C₂H₄ (ethylene), C₂H₆ (ethane), C₃H₆ (propene) and C₃H₈ (propane) are very important sources of energy and also can be used as feedstock for many industrially important materials.¹⁻⁶ Natural gas consisting mainly of CH₄ has potential as a fuel and has the highest H to C ratio of any fossil fuel, thus CO₂ released per unit energy would be minimum. After CH₄, the other components of natural gas are C₂H₆ (second largest component after methane), C₃H₈, C₄H₁₀ and hence, purification of CH₄ is of prime importance. Steam cracking of ethane is one of the synthetic methods for ethylene production in which separation of ethylene and ethane is required. Similarly, the separation of propylene and propane is also important in industry.³⁻⁶ On the other hand ethylene and propylene are important raw chemicals for large scale production of polymers like polyethylene, polypropylene, etc.² Acetylene is also widely used as feedstock in the synthesis of many chemical products. Therefore, it is essential to have high purity of these hydrocarbons and hence separation of these light hydrocarbons (C₂, C₃ vs. C₁) is a vital industrial process. The present separation processes of hydrocarbons is an energy intensive cryogenic distillation based technology based on the relative vapour pressures and boiling points. Adsorptive based separation of hydrocarbons is a promising one as it takes advantages of other dissimilar properties like kinetic diameters, dipole moments, and polarizability.⁷ Moreover, such separation process can be economically favorable. Further, the presence of non-calorific CO₂ in natural gas also degrades the quality of the fuel and hence removal of CO₂ from CH₄ is also paramount.⁸⁻¹⁵ In addition, the separation of CO₂/N₂ is imperative in the context of energy and environment.¹¹⁻¹⁵

Among solid adsorbents, metal-organic frameworks (MOFs) are the most promising for hydrocarbon storage and as separating material due to its tunable surface area and modular nature.¹⁶⁻¹⁸ The surface area can be as high as 7140 m² g⁻¹ and hence storage quantity can be large.¹⁹ But selectivity or separation ability depends on the pore functionality and size of the channel windows. Hence, achieving high selectivity and high storage capacity together is the primary challenge. Kinetics or thermodynamics based separation using MOFs are feasible for their intriguing characteristics. Thermodynamics based separation using coordinatively unsaturated metal sites (UMSs) and functional sites in MOFs has been studied by Long *et al.* and Chen *et al.*, recently.²⁰⁻²³ The unsaturated hydrocarbons can interact strongly with UMSs and hence separation of C₁ and

unsaturated C2/C3 is viable. Adversely, these MOFs suffer from penalty of high energy release of adsorbate or lack of efficiency in presence of moisture, as water competes with the adsorbates towards binding with the UMSs. Hence, use of functional sites (such as NH_2 , $-\text{OH}$ or $\text{RNC}=\text{O}$) on confined pores would be more helpful.²⁴⁻²⁸ Functional sites are key to thermodynamics while channel window dimensions control the kinetic (diffusion rate) based separation. Further, structural dynamics or flexibility of MOFs renders gated or stepwise adsorption and that can be useful for selective uptake and separation of small hydrocarbons.²⁹ Considering the above mentioned criteria, we envisaged that a flexible framework with moderate surface area with functional adsorption sites can be useful for separation of light weight hydrocarbons and CO_2/CH_4 . We cautiously ignore the UMSs containing MOFs and rather search for MOFs with functionalized pore surface that would induce high potential gradient in the micropores. Here, we have selected a two-fold entangled pillared layer framework, $\{[\text{Zn}_2(\text{bdc})_2(\text{bpNDI})]\cdot 4\text{DMF}\}_n$ (**1**) (H_2bdc = 1,4-benzenedicarboxylic acid, bpNDI = *N,N'*-bis-(4-pyridyl)-1,4,5,8-naphthalenediimide) for this purpose.³⁰ The capability to encapsulate both polar and non-polar solvent molecules as reported earlier indicates that this could be a potential framework for CO_2 capture, storage and separation of small hydrocarbon.³⁰ In this work, we have exploited the framework dynamics and studied CO_2 capture, hydrocarbon storage and selectivity studies of CO_2/N_2 , CO_2/CH_4 , $\text{C}_2\text{H}_2/\text{CH}_4$, $\text{C}_2\text{H}_6/\text{CH}_4$, $\text{C}_2\text{H}_4/\text{CH}_4$. It shows stepwise CO_2 and C_2H_2 uptake profiles at different temperatures due to highly dynamic nature of the framework. CO_2 uptake at 298 K is 12.7 wt% and shows high CO_2/CH_4 selectivity of 598 at 298 K and 1 bar. Propane, ethane, ethylene and acetylene also adsorb selectively against methane at ambient condition (298 K). Density functional theory (DFT) calculations infer the imide and aromatic π electrons of the framework as preferable interaction sites for CO_2 and hydrocarbons. Breakthrough column experiments for binary gas mixtures, CO_2/CH_4 , $\text{C}_2\text{H}_6/\text{CH}_4$ and CO_2/N_2 at 298 K further establishes the separation capability of the framework. Such features propose this entangled framework to be a promising material for selective capture and separation.

2.2 Experimental section

2.2.1 Materials

All the reagents employed were commercially available and used as provided without further purification. $\text{Zn}(\text{NO}_3)_2\cdot 6\text{H}_2\text{O}$ was obtained from Spectrochem. 1,4-benzenedicarboxylic acid (H_2bdc) was obtained from Sigma Aldrich chemicals. *N,N'*-

di(4-pyridyl)-1,4,5,8-naphthalenediimide (bpNDI) was synthesized following the literature procedure.³⁰

2.2.2 Synthesis of $\{[\text{Zn}_2(\text{bdc})_2(\text{bpNDI})]\cdot 4\text{DMF}\}_n$ (**1**)

Compound **1** has been synthesized by adopting a procedure similar as reported in literature. A mixture containing $\text{Zn}(\text{NO}_3)_2\cdot 6\text{H}_2\text{O}$ (0.149 g, 0.50 mmol), H_2bdc (0.083 g, 0.50 mmol) and bpNDI (0.210 g, 0.50 mmol) was suspended in DMF (50 mL) and heated to 95 °C for a period of 3 days. The light yellow crystals of **1** were then collected and washed with DMF for three times. This compound has been characterized through PXRD, TGA, FT-IR and elemental analysis. Yield: 90 %. Elemental analysis for **1** calcd (%) for $\text{Zn}_2\text{C}_{52}\text{O}_{16}\text{H}_{48}\text{N}_8$: C: 53.28; H: 4.09; N: 9.56; Found C: 53.97; H: 3.72; N: 9.91. FT-IR (4000–400 cm^{-1}): 3684 (w), 3065 (w), 2924 (w), 1741 (s), 1704, 1620 (s), 1603 (w), 1575 (s), 1512 (w), 1393 (s), 1337 (s) cm^{-1} .

2.2.3 Physical Measurements

Elemental analysis was carried out using a Thermo Fischer Flash 2000 Elemental Analyzer. Thermogravimetric analysis (TGA) was carried out on METLER TOLEDO TGA850 in nitrogen atmosphere (flow rate = 50 mL min^{-1}) in the temperature range of 30–600 °C (heating rate 3 °C min^{-1}). Powder XRD patterns of compound **1** in different state were recorded by Bruker D8 Discover; 40 kV, 30 mA using Cu-K_α radiation. IR spectra were recorded on a Bruker IFS 66v/S spectrophotometer using KBr pellets in the region 4000–400 cm^{-1} .

2.2.4 Adsorption study

The adsorption isotherms of CO_2 (at 195, 273, 283 and 298 K), N_2 (at 77 K), C_2H_2 (at 195, 273 and 298 K), C_2H_4 (at 195, 273 and 298 K), C_2H_6 (at 195, 285 and 298 K), C_3H_8 (at 195, 273 and 298 K) and CH_4 (at 195, 258, 268 and 298 K) using the desolvated samples of **1** (**1a**) were measured by using QUANTACHROME QUADRASORB-SI analyser and AUTOSORB IQ2 instrument. Compound **1** was activated at 170 °C under 1×10^{-1} Pa vacuum for about 12 h prior to measurement of the isotherms. Helium gas (99.999% purity) at a certain pressure was introduced in the gas chamber and allowed to diffuse into the sample cell by opening the valve. The amount of gas adsorbed was calculated readily from pressure difference ($P_{\text{calc}} - P_e$), where P_{calc} is the calculated pressure with no gas adsorption and P_e is the observed equilibrium pressure. All

operations were computer-controlled and automatic. High pressure CO₂ adsorption measurement at 273 and 298 K were carried out on a fully computer controlled volumetric BELSORP-HP, BEL JAPAN high pressure instrument. CO₂ gas used for the measurement is scientific/research grade with 99.999% purity. For the measurements, approximately 300 mg sample was taken in a stainless-steel sample cell and degassed at 170 °C for a period of 12 h under 1×10⁻¹ Pa vacuum. Dead volume of the sample cell was measured with He gas of 99.999% purity.

The adsorption isotherms of different solvents (MeOH, at 293 K and H₂O at 298 K) for **1a** were measured in the vapour state by using a BELSORP-aqua volumetric adsorption instrument from BEL, Japan. The sample of about ~100–150 mg was prepared by adopting a similar procedure mentioned earlier (*vide supra*) prior to measurement of the isotherms. The solvent molecules used to generate the vapour were degassed fully by repeated evacuation. Dead volume was measured with helium gas. The adsorbate was placed into the sample tube, then the change of the pressure was monitored, and the degree of adsorption was determined by the decrease in pressure at the equilibrium state. All operations were computer controlled and automatic.

2.2.5 Calculation of isosteric heat of adsorption

2.2.5.1 Virial fitting of pure component isotherms for CO₂, C₂H₂ and C₂H₆

Adsorption isotherms of **1a** are fitted to the virial-type expression (eq 1).³¹ An accurate fit was obtained for each case which results a precise prediction over the quantity of gas adsorbed at saturation.

$$\ln P = \ln N + 1/T \sum_{i=0}^m a_i N^i + \sum_{i=0}^n b_i N^i \quad \dots\dots\dots(1)$$

$$Q_{st} = -R \sum_{i=0}^m a_i N^i \quad \dots\dots\dots(2)$$

Here, P is the pressure expressed in torr, N is the amount adsorbed in mmol g⁻¹, T is the temperature in K, a_i and b_i are virial coefficients, and m , n represent the number of coefficients required to adequately describe the isotherms. The values of m and n were gradually increased until the contribution of extra added a and b coefficients were negligible towards the overall final fit. The values of the virial coefficient a_i were taken to calculate the isosteric heat of adsorption using the following expression (eq 2).

2.2.5.2 Langmuir-Freundlich fitting of pure component isotherms for CH₄

The pure component isotherms of CH₄ at 258 and 268 K are fitted into the Langmuir-Freundlich (eq 4).³² An accurate fit was obtained by using this equation which results a precise prediction over the quantity of gas adsorbed at saturation. A variant of the Clausius-Clapeyron equation was used to calculate enthalpy of adsorption (eq 3).

$$\ln \left(\frac{P_1}{P_2} \right) = \Delta H_{\text{ads}} \times \left(\frac{T_2 - T_1}{R \times T_2 T_1} \right) \dots\dots\dots(3)$$

Where, P_n = pressure for isotherm n , T_n = temperature for isotherm n and R is universal gas constant = 8.314 J mol⁻¹ K⁻¹. Pressure as a function of amount of adsorption was determined by using the Langmuir-Freundlich fit for each isotherm (eq 4).

$$\frac{Q_1}{Q_m} = \frac{B \times P^{\frac{1}{t}}}{1 + B \times P^{\frac{1}{t}}} \dots\dots\dots(4)$$

Where, Q = moles adsorbed, Q_m = moles adsorbed at saturation, P = Pressure, B and t = constant

By rearranging this equation we get

$$P = \left(\frac{\frac{Q_1}{Q_m}}{B - B \times \frac{Q_1}{Q_m}} \right)^t \dots\dots\dots(5)$$

Substituting this into Clausius-Clapeyron equation (eq 6) we get

$$\Delta H_{\text{ads}} = \frac{B \times T_2 \times T_1}{T_2 - T_1} \ln \frac{\left(\frac{\frac{Q}{Q_{m1}}}{B_1 - B_1 \times \frac{Q}{Q_{m1}}} \right)^t}{\left(\frac{\frac{Q}{Q_m}}{B_2 - B_2 \times \frac{Q}{Q_m}} \right)^t} \dots\dots\dots(6)$$

Where, the subscript 1 and 2 are representing the data corresponding to 258 and 268 K respectively.

2.2.6 Selectivity prediction for binary gas mixtures

Ideal adsorbed solution theory (IAST) was used to predict binary mixture adsorption from the experimental pure-gas isotherms.³³ Using the pure component isotherm fits, the adsorption selectivities defined by this following equation:

$$S = \frac{\frac{x_1}{y_1}}{\frac{x_2}{y_2}}$$

where x_i and y_i are the mole fractions of component i ($i = 1, 2; A, B$) in the adsorbed and bulk phases, respectively. The IAST calculations were carried out for equimolar binary gas-phase mixtures of CO_2/CH_4 , $\text{C}_2\text{H}_2/\text{CH}_4$, $\text{C}_2\text{H}_6/\text{CH}_4$ and $\text{C}_2\text{H}_4/\text{CH}_4$. To perform the integrations required by IAST, the single-component isotherms should be fitted by a proper model. There is no restriction on the choice of the model to fit the adsorption isotherm, however, data over the pressure range under study should be fitted very precisely. Several isotherm models were tested to fit the experimental pure isotherms for CH_4 , C_2H_4 , C_2H_6 , C_3H_8 , C_2H_6 and CO_2 of **1a** at 298 K. All the data were best fitted into Langmuir-Freundlich isotherm (eq 4). The R^2 values for all of the fitted isotherms and the other parameters are given in the corresponding figure. Hence, the fitted isotherm parameters were applied to perform the necessary integrations in IAST.

2.2.7 CO_2/CH_4 , $\text{C}_2\text{H}_6/\text{CH}_4$ and CO_2/N_2 breakthrough column measurements

Breakthrough experiments were performed using a column (packed with about 200 mg of **1a** powder) with 3 cm long length and 0.3 cm diameter. The sample was first activated at 170 °C for 12 h prior to loading in column. After loading, the sample was again activated with He flow for 30 mins. CO_2/CH_4 (V/V: 50/50 mixture), $\text{C}_2\text{H}_6/\text{CH}_4$ (50/50) and CO_2/N_2 (15/85) streams were passed through the column with He. The flow was continuous and the flow rate was regulated by MFC. The partial pressure of the gas mixture was kept at $p = 5$ kPa. The gas stream at the outlet of the column was analyzed on-line with a GC. The space velocity was kept at 4.71 min^{-1} .

2.2.8 Computational details

All the calculations have been carried out in geometry and cell parameter optimized $\{[\text{Zn}_2(\text{bdc})_2(\text{bpNDI})] \cdot 4\text{DMF}\}_n$ (**1'**) i.e. **1aD** (Table 1). Periodic density functional theory calculations were carried out using the QUICKSTEP module in CP2K software in order

to find the locations of guest molecules in **1aD**.³⁴ All valence electrons were treated on a mixed basis set with an energy cut-off of 280 Ry. The short-range version of the double- ζ single polarization basis set was used. The effect of core electrons and nuclei was considered by using pseudopotentials of Goedecker–Teter–Hutter (GTH).³⁵ The exchange and correlation interaction between electrons was treated with the Perdew–Burke–Ernzerhof (PBE)³⁶ functional. van der Waals interactions between the gas and the framework are imperative, their effects were accounted for by employing empirical corrections developed by Grimme (DFT-D2³⁷ and DFT-D3).³⁸ In addition, we have used the recently developed van der Waals density functional (vdW-DF2), a truly nonlocal exchange and correlation functional, that incorporates van der Waals forces self-consistently and seamlessly into DFT.^{39–41} The vdW-DF2 can correctly capture the interaction and determine the adsorption sites, binding energy, and vibrational frequencies for small molecules and hydrocarbons (e.g. CH₄, C₂H₆, C₄H₁₀) absorbed in different MOFs.^{42–43} Two schemes, DFT-D2 and DFT-D3, were used to calculate the cell volume. Two different exchange correlation functionals were used to calculate binding energies of guest molecules in **1aD** - i) PBE-D3 scheme and ii) the non-local van der Waals density functional kernel, vdW-DF2 functional (LMKLL)⁴⁴ employing a more accurate exchange functional (xGGA) PW86x.⁴⁵ The fast Fourier transform grid was calculated in the LMKLL functionals with a cutoff of 350 Ry. The simulation cell consisted of $2 \times 1 \times 2$ unit cells for **1aD** and $1 \times 1 \times 1$ unit cells for **1**. The optimized cell parameters are shown in Table 2.

Prior to geometry optimization, Born-Oppenheimer Molecular Dynamics (BOMD) simulations were performed to identify the favourable binding regions for CO₂ and C₂H₂ gas molecules in **1aD** at a temperature of 50 K. The coordinates of the framework were constrained during these run. The nuclear equations of motion were integrated using a standard velocity Verlet algorithm with a time step of 0.5 fs. Canonical ensemble (NVT) trajectory was generated for 1.2 ps, with the temperature being maintained using a Nose-Hoover thermostat using a coupling constant of 500 fs.^{46–47} Geometry optimization calculation was performed for the low energy configuration which was identified from this MD trajectory. Optimization proceeded until convergence which was set as the maximum force on any atom to be less than 1×10^{-4} a.u. Binding energies of guest molecules are calculated using following formula

$$\Delta E = E(\text{MOF-guest}) - E(\text{MOF}) - n \times E(\text{guest})$$

Where ΔE , $E(\text{MOF-guest})$, $E(\text{MOF})$, $E(\text{guest})$ and n are the binding energy of a guest molecule, energy of MOF with a guest, energy of MOF without guest, energy of a guest and the number of guest molecules present in the MOF, respectively. Binding energies of guest molecules were corrected for basis set superposition error using the counterpoise method.⁴⁸⁻⁴⁹ All the structures were visualized in VMD,⁵⁰ Mercury^{51a} and GaussView.^{51b}

Table 1. Compound nomenclatures and descriptions used throughout this chapter.

Compounds	Description
1	As-synthesized framework, ($\{[\text{Zn}_2(\text{bdc})_2(\text{bpNDI})] \cdot 4\text{DMF}\}_n$)
1'	After removal of three DMF molecules from 1 , $\{[\text{Zn}_2(\text{bdc})_2(\text{bpNDI})] \cdot \text{DMF}\}_n$
1a	Experimentally fully desolvated 1 , $[\text{Zn}_2(\text{bdc})_2(\text{bpNDI})]_n$
1aD	Geometry and cell parameter optimized structure after removal of one DMF molecule from 1'
1aQ	After loading 27 CO_2 molecules in 1aD
1R	After loading 72 CO_2 molecules in DFT optimized solvent removed 1
1aT	After loading 38 C_2H_2 molecules in 1aD

The DFT calculations are not aimed to capture the experimentally demonstrated flexibility of the framework upon gas uptake, instead to identify specific binding sites of CO_2 and hydrocarbons in the MOF, their natures of interaction, as well as to examine cooperativity in gas adsorption. The calculations have been performed on the desolvated MOF (whose structure is experimentally known) and on the fully gas loaded MOF (whose structure has been assumed in the DFT calculations to be the same as that of the as-synthesized MOF).

Table 2. Optimized cell parameters of **1**, **1'** and gas loaded framework calculated using DFT in different states.

Framework k	Methods	<i>a</i> (Å)	<i>b</i> (Å)	<i>c</i> (Å)	β (°)	Volume (Å ³)	$V_{\text{DFT}} - V_{\text{Exp}}$
							V_{Exp} (%)
1'	Experiment	22.434	17.703	23.052	106.917	8758.91	---
1aD	PBE	22.124	17.843	22.762	105.817	8645.28	-1.3
1aD	PBE-D2	21.464	17.553	22.464	104.317	8199.89	-6.4
1aD	PBE-D3	21.464	17.763	22.462	104.317	8297.99	-5.3
1aQ	PBE-D3	21.464	17.553	22.462	104.317	8200.99	-6.0
1aT	PBE-D3	21.464	17.743	22.462	104.317	8288.65	-5.4
1	Experiment	46.787	15.282	15.436	107.468	10527.8	---
Solvent removed 1	PBE-D3	46.577	15.082	15.456	106.968	10384.8	-1.4
1R	PBE-D3	46.147	15.182	15.326	106.068	10517.8	-2.0

2.3 Results and discussion

2.3.1 Structural dynamics of the entangled framework 1

Compound **1** is a two-fold entangled 3D pillared-layer framework having α -polonium type topology.³⁰ $\{\text{Zn}_2(\text{COO})_4\}$ paddle wheel secondary building units (SBUs) are connected through bdc linkers to form a 2D square grid along *bc* plane (Figure 1a). This 2D network is further pillared by bpNDI along $[10\bar{1}]$ to generate an extended 3D framework (Figure 1b). This is a two-fold entangled framework and this creates two different types of channels (site A and site B) (Figure 2a, 2c) occupied by DMF molecules and removal of those shows ~43% void space to total cell volume (Figure 3, 4a). In framework **1**, the bpNDI and bdc linkers are arranged in a manner that facilitates inter-net $\pi \cdots \pi$ stacking with a distance of 3.35 Å. Such entangled frameworks are often susceptible to structural change/rearrangement upon guest solvent removal as the nets can easily slide over each other or in some cases deform.^{26, 27, 52-58} In this case also, three DMF guests out of four can be easily removed under vacuum rearranging to a new

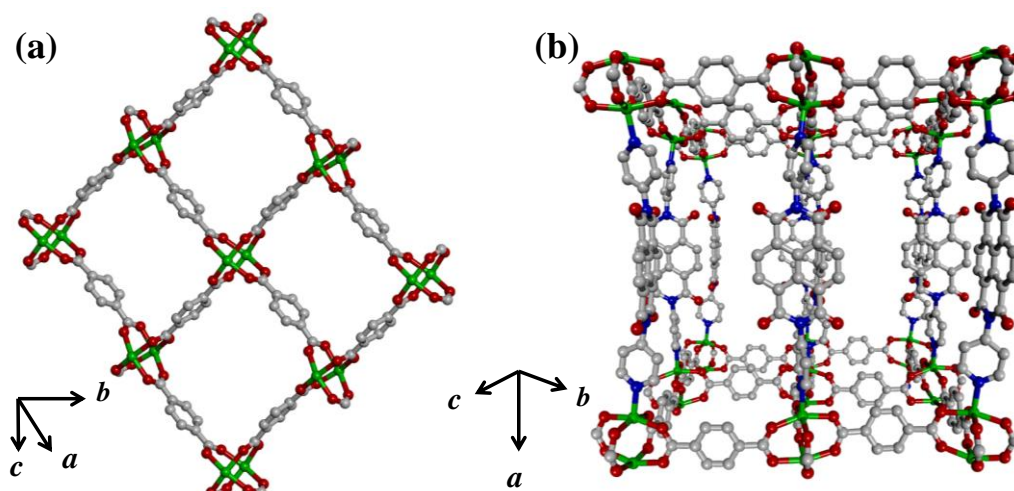


Figure 1: Structural details of compound **1**: (a) 2D layer and (b) 3D α -polonium type pillared layer framework.

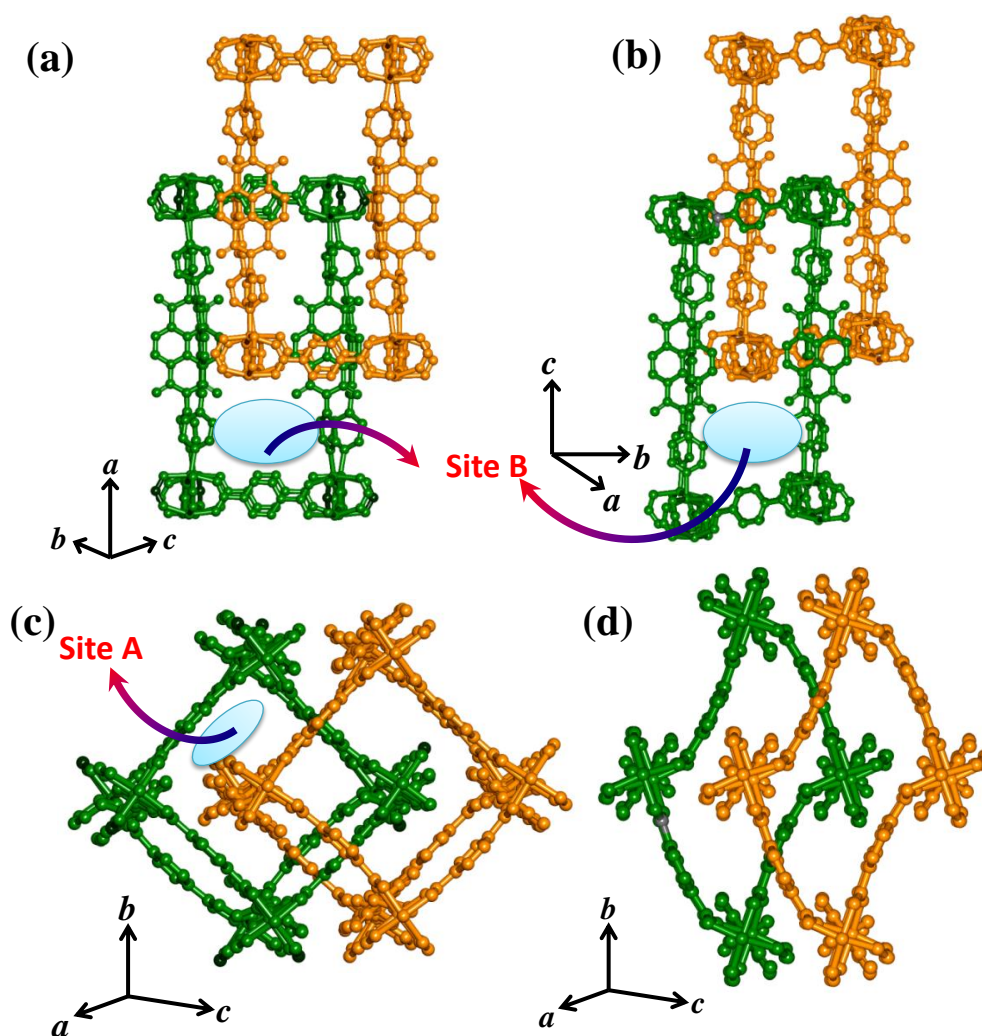


Figure 2: Crystal structure of **1** and **1'**: (a-b) view of two-fold entangled frameworks of **1** and **1'**, respectively, showing the similar adsorption sites (site B), (c) two-fold entangled nets along a -axis in **1** showing site A which is blocked, (d) in **1'** due to the shearing of nets.

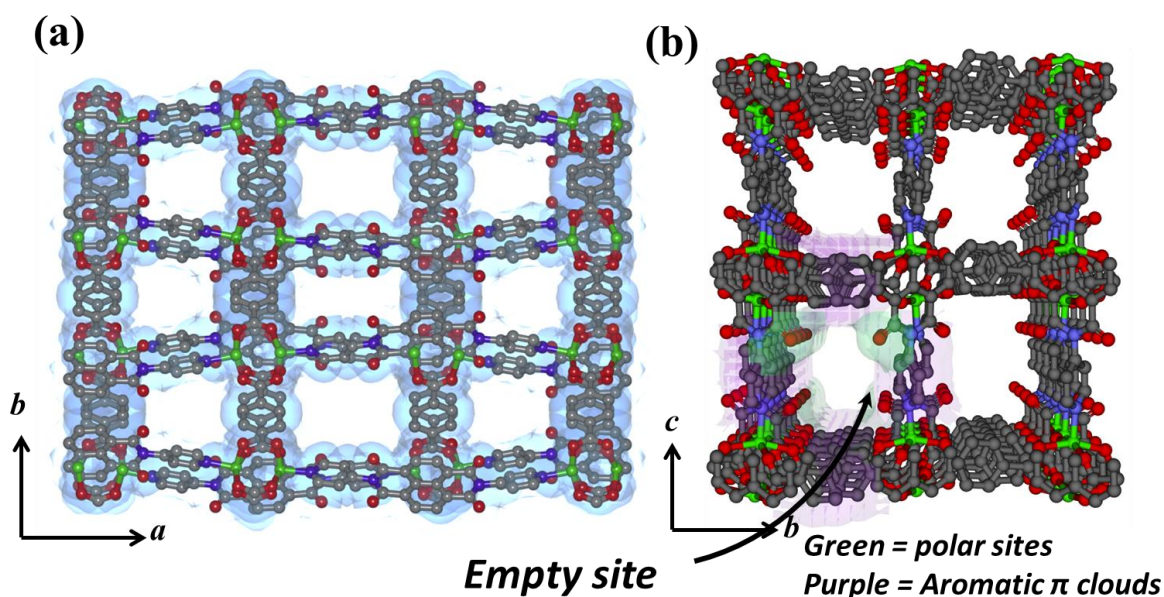


Figure 3: (a) Pore view of **1** along c -direction (van der Waals surface added), (b) pore view of **1'** along a -direction. One of the channels has been highlighted by adding van der Waals surface.

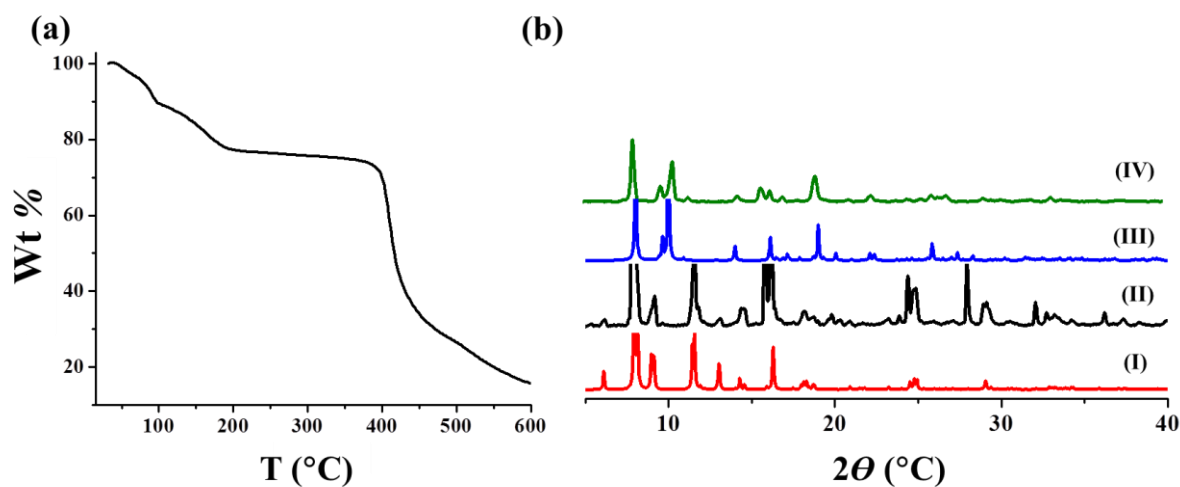


Figure 4: (a) TGA profile of **1** under N_2 atmosphere ($5^\circ C \text{ min}^{-1}$) and (b) PXRD patterns of **1** recorded in different states: (I) simulated of **1**, (II) as-synthesized **1**, (III) simulated of **1'** and (IV) desolvated **1a**.

structural phase, $\{[Zn_2(bdc)_2(bpNDI)] \cdot DMF\}_n$ (**1'**) with $\sim 27\%$ contraction of the cell volume compared to **1** as reported earlier (Figure 2b, 2d, 4b).³⁰ Structure of **1'** shows deformation of square nets and shearing of two such entangled nets leads to blocking of site A whereas site B remains open. It is worth mentioning that the PXRD pattern of complete DMF removed phase $\{[Zn_2(bdc)_2(bpNDI)]\}_n$ (**1a**) matches well with simulated

pattern of **1'**, suggesting the structure of **1'** and **1a** are similar (Figure 4b). This has been also validated further by optimization of geometry and cell parameters of **1'** (**1aD**, Table 1-2).

2.3.2. Permanent porosity and polarity of the pore surface

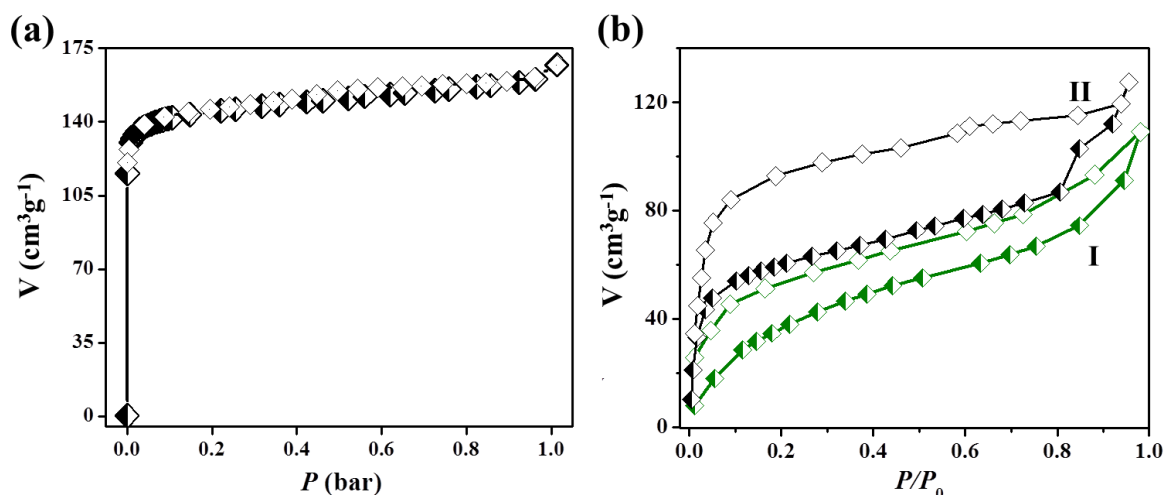


Figure 5: (a) N₂ adsorption isotherm of **1a** at 77 K, (b) H₂O (I) and MeOH (II) vapour adsorption isotherms of **1a** at 298 and 293 K, respectively [P_0 of H₂O = 3.169 kPa and P_0 of MeOH = 12.927 kPa; half symbols represent adsorption and empty symbols represent desorption].

To check the permanent porosity of the desolvated framework **1a**, we have measured N₂ (kinetic diameter = 3.64 Å)⁵⁹ adsorption isotherm at 77 K and it exhibits a type I profile with final uptake amount of 167 cm³ g⁻¹ (Figure 5a) at 1 bar. The Langmuir and BET (Brunauer- Emmett-Teller) surface area are calculated to be 613 and 565 m² g⁻¹, respectively. Such feature clearly indicates the microporous nature of **1a**. To understand the nature of the pore surface, we have carried out solvent vapour (water and methanol) adsorption experiments of **1a** (Figure 5b). The water vapour (kinetic diameter = 2.64 Å)⁵⁹ adsorption isotherm of **1a** shows gradual uptake with total capacity of 109 cm³ g⁻¹ (2.1 molecules per formula unit). This suggests a weak hydrophilic nature of the pore surface. However, methanol vapour (kinetic diameter = 3.62 Å) adsorption isotherm reveals a distinct double-step profile with final uptake amount of 127 cm³ g⁻¹ (2.4 molecules per formula unit). The steep uptake at low pressure regions indicates stronger interaction with the pore surface than water molecules, which is also realized from βE_0 values as obtained Dubinin-Radushkevitch equation (D-R equation).⁶⁰ The βE_0 values, which reveals the

adsorbate-adsorbent interactions, are ~ 4.6 and 8 kJ mol^{-1} for water and MeOH, respectively.

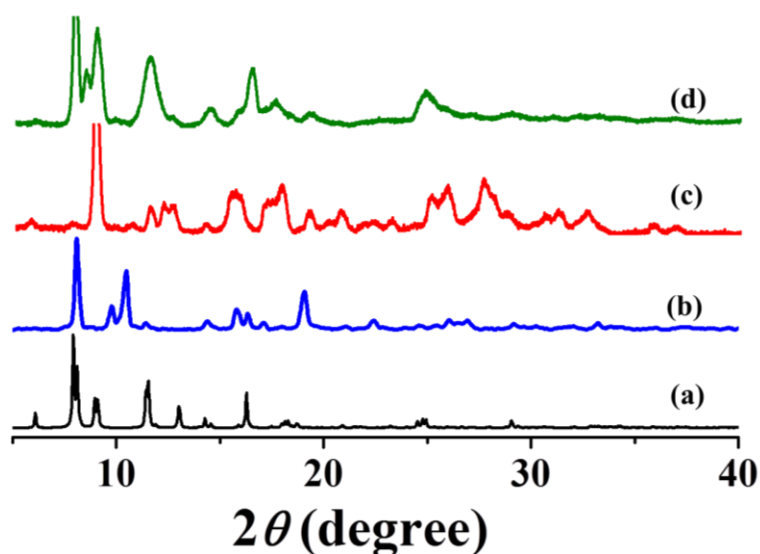


Figure 6: PXRD patterns of (a) simulated **1**, (b) desolvated **1a**, (c) **1a** after MeOH exposure for two days, (d) **1a** after exposing to water for two days.

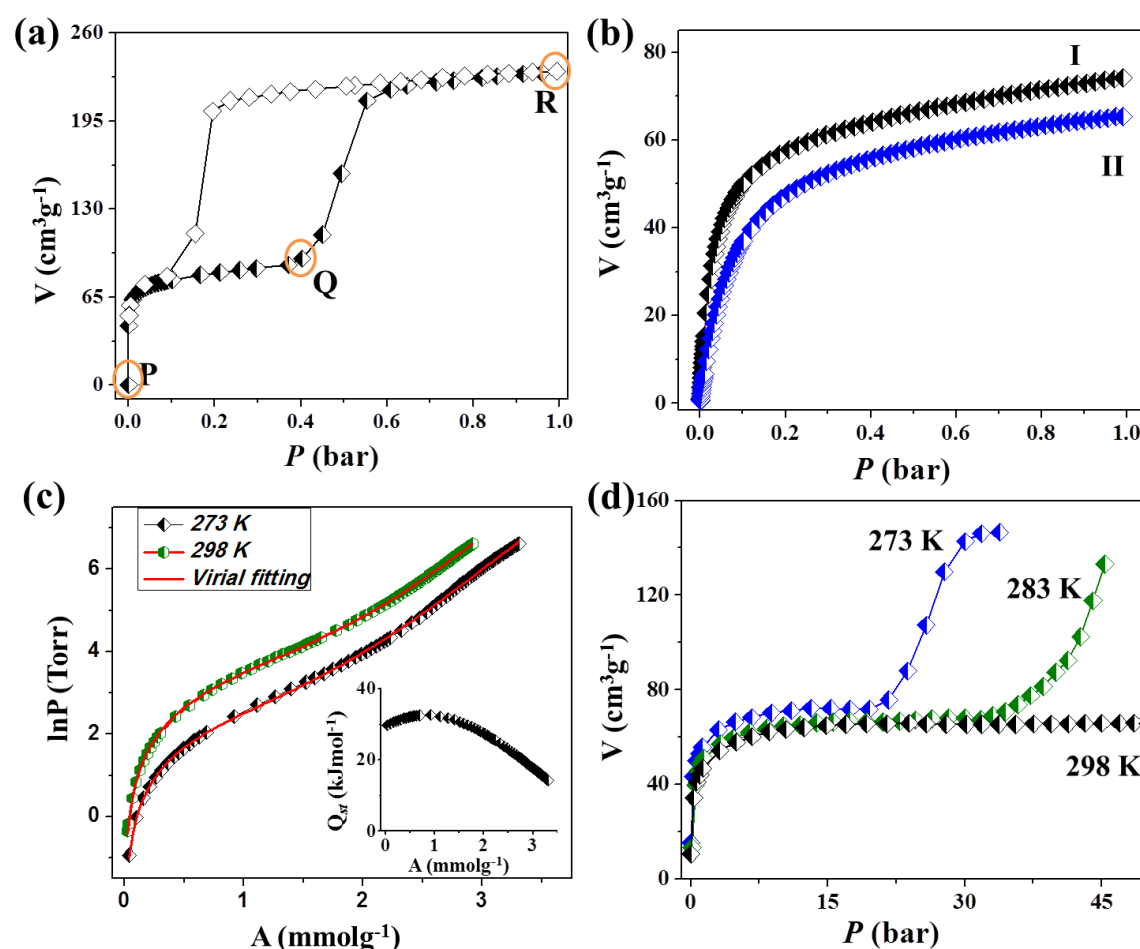
PXRD patterns were recorded after exposing the water and MeOH vapour to desolvated framework **1a** for 48 hours (Figure 6). The PXRD pattern of MeOH exposed sample shows significant change compared to **1a** and is close to PXRD pattern of as-synthesized **1**. On the other hand, water vapour exposed sample reveals different pattern compare to **1a** and **1** and may be some intermediate phase between these two. This result indicates that MeOH molecules can be accommodated in both sites (A and B), which is also supported by the stepwise adsorption. Similar structural transformation is not feasible by water vapour which is also supported by water vapour adsorption.

A careful observation of geometry optimized **1a** (**1aD**) suggests the site B to be decorated by hydrophobic aromatic π -clouds from the bdc molecules and bpNDI molecule from one net. The pendant carbonyl groups of orthogonal bpNDI pillar from another net face towards the channel, introducing a slight polar character to the pore surface. Now, MeOH possesses non-polar $-\text{CH}_3$ part and polar $-\text{OH}$ part which seems to be ideal to fit into the site B, thus justifying initial steep and higher uptake compared to H_2O . On filling of site B, site A opens and accommodates further guest solvent molecules resulting into stepwise uptake. Based on these studies, we envisage that the framework

would be ideal for the CO₂ capture and hydrocarbon storage applications where presence of both aromatic and polar pore surface are essential.

2.3.3 CO₂ Capture: Structural dynamics correlated with computational studies

Although we have observed a type I profile for N₂ adsorption at 77 K, a two-step adsorption profile is observed for CO₂ (kinetic diameter = 3.3 Å) at 195 K for **1a** (Figure 7a). In the first step upto $p = 0.33$ bar, **1a** adsorbs 89 cm³ g⁻¹ of CO₂ (17.5 wt%, 1.7 molecules per formula unit) followed by an abrupt jump in the second step with an uptake amount of 142 cm³ g⁻¹ of CO₂ (27.8 wt%, 2.7 molecules per formula unit) at 1 bar. The total CO₂ storage capacity at 1 bar is 231 cm³ g⁻¹ (45.3 wt% CO₂, 4.5 molecules per



$$R^2 = 0.99982, a_0 = -3526.12334, a_1 = -1008.96768, a_2 = 710.01151, a_3 = -77.49361, a_4 = -12.11449, b_0 = 15.14298, b_1 = 4.10389, b_2 = -3.00817, b_3 = 0.6062$$

Figure 7: CO₂ adsorption studies of **1a** in different conditions: (a) at 195 K (**P** is starting point of adsorption, **Q** and **R** are at the end of first step and second step, respectively), (b) at 273 K (**I**) and 298 K (**II**), (c) pure component isotherms of CO₂ fitted into virial-type expression at 273 K and 298 K for **1a**; inset: the isosteric heat of adsorption plot of CO₂ vs. loading, (d) high pressure isotherms of CO₂; at 273 K (33 bar), 283 K (45 bar) and 298 K (50 bar), (half symbols represent adsorption and empty symbols represent desorption).

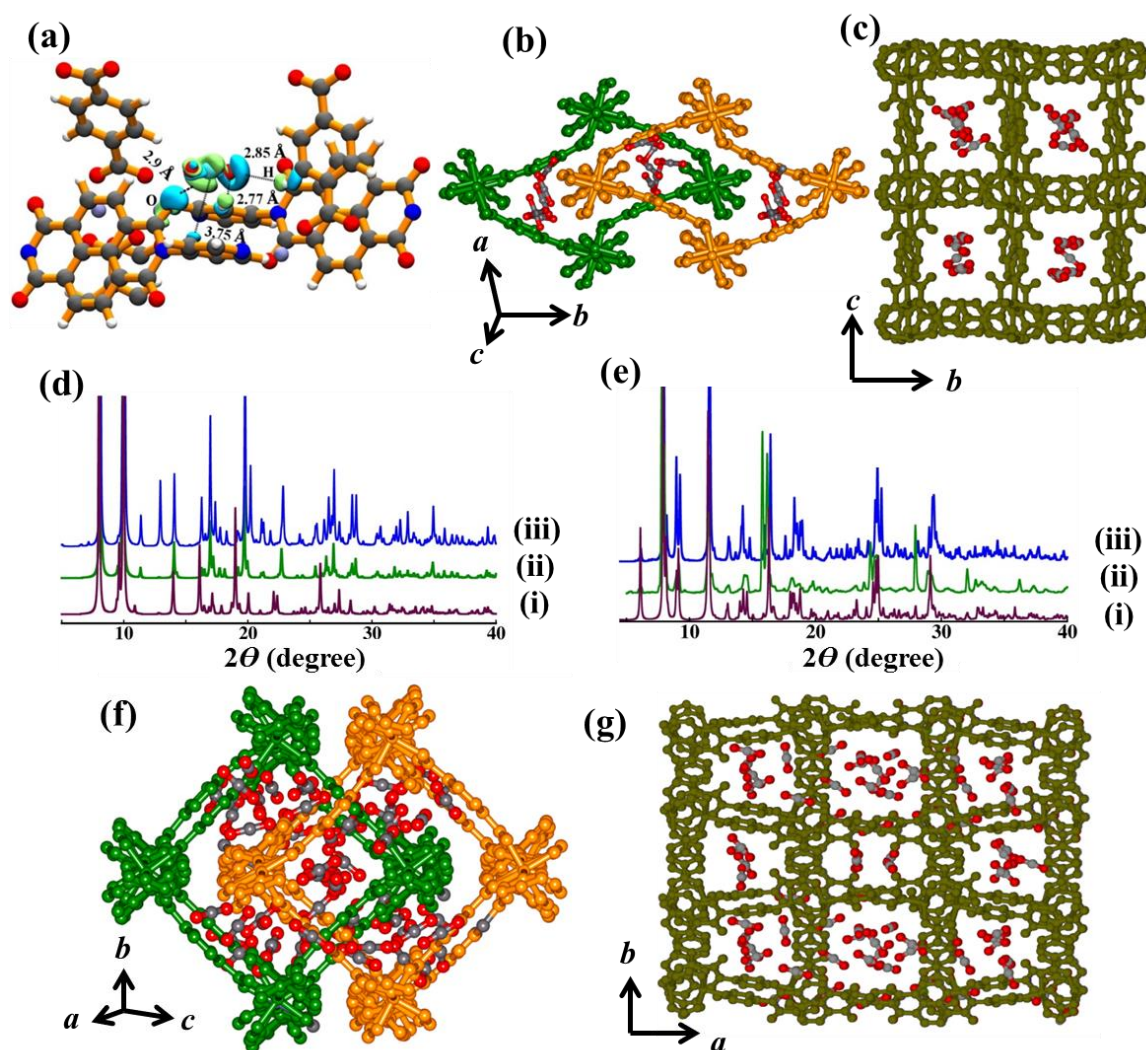


Figure 8: (a) Electron density difference map of CO₂ (1 molecule per unit cell) in **1aD**. CO₂ interacts with pendent O atoms, π cloud as well as with the aromatic C-H groups. The isosurface value is 4.5×10^{-4} a.u. The electron density difference has been calculated for the entire framework. However, only the region around CO₂ is shown for clarity, (b-c) the optimized CO₂ locations in **1aD** along two different axes, (d) comparison of PXR patterns in different states: (i) simulated PXR pattern of **1'** (ii) calculated PXR pattern of DFT optimized **1aD** showing similar diffraction features as **1'** (iii) calculated PXR pattern of **1aQ** showing no structural change even after incorporation of 27 CO₂ molecules in **1aD**, (e) (i) simulated PXR pattern of **1** (ii) experimental PXR of as-synthesized **1** (iii) calculated PXR pattern of **1R**, (f-g) fully CO₂ loaded framework **1** showing the positions of CO₂ molecules along two different axes.

formula unit). The sudden increase of CO₂ uptake at $p = 0.33$ bar indicates structural transformation to further accommodate CO₂ molecules with increasing pressure. The desorption curve does not coincide with the adsorption one till $p = 0.1$ bar thus showing large hysteric sorption profile. This unusual stepwise uptake of **1a** prompted us to measure the CO₂ capture capacity at 273 and 298 K (Figure 7b). The CO₂ adsorption of

1a shows type I profile with uptake capacity of 75 (14.7 wt %, 1.46 CO₂ molecules per formula unit) and 65 cm³ g⁻¹ (12.7 wt %, 1.27 CO₂ molecules per formula unit) at 273 and 298 K, respectively at 1 bar. The room temperature CO₂ uptake capacity observed in the present case is high considering the fact that **1a** does not contain any UMSs and the uptake amount is higher than some of the very well-known MOFs such as ZIF-69 (41 cm³ g⁻¹), ZIF-78 (51 cm³ g⁻¹), ZIF-82 (54 cm³ g⁻¹) and SiF₆-3-Zn (48 cm³ g⁻¹), Cu(bdc-OH) (52 cm³ g⁻¹), UTSA-5, (38.4 cm³ g⁻¹), UTSA-15 (31 cm³ g⁻¹).^{11, 61} A list of MOFs without

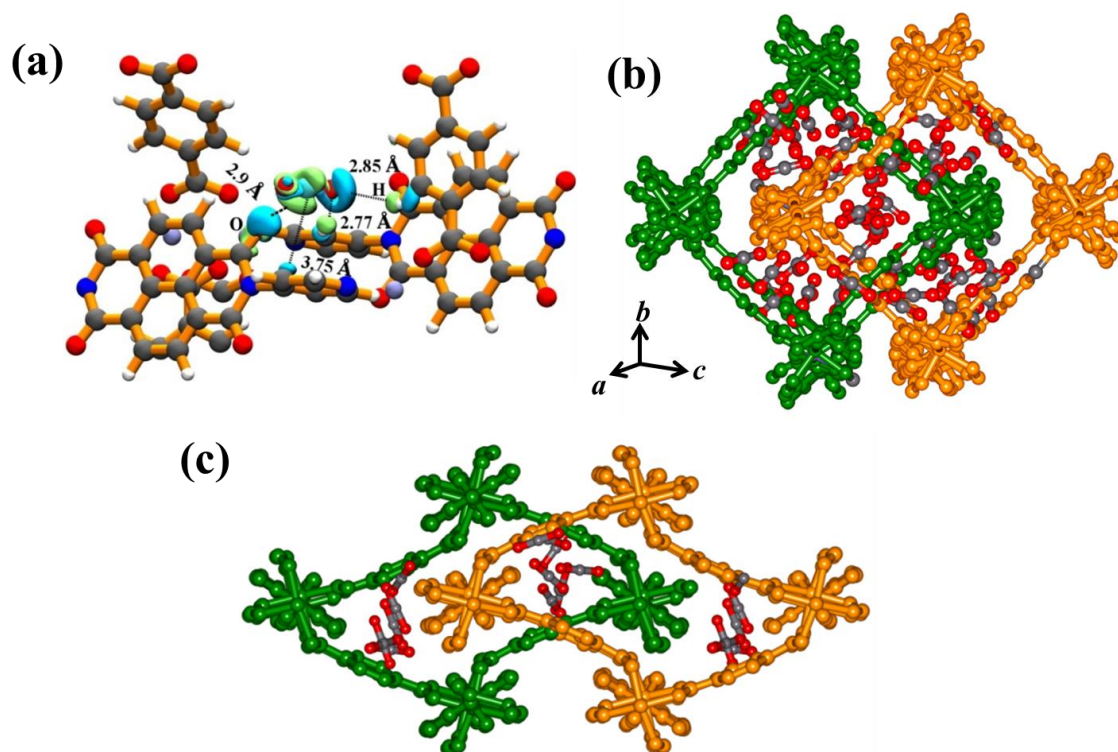


Figure 9: (a) Electron density difference map of CO₂ (1 molecule per unit cell) in **1aD**. CO₂ interacts with pendent O atoms, π cloud as well as with the aromatic C-H groups. Cyan and lime colors indicate increased and decreased electron densities brought about by the adsorption of CO₂ in **1aD**. The isosurface value is 4.5×10^{-4} a.u. The electron density difference has been calculated for the entire framework. However, only the region around CO₂ is shown for clarity. Color scheme: Framework atoms: C-grey, N-blue, H-silver, Zn-ice blue; CO₂ atoms: C-cyan, O-Red, (b-c) the optimized CO₂ locations in **1aD** and in **1**.

UMSs having high CO₂ uptake capacity at 298 K upto 1 bar is listed in Table 4. To extract the coverage-dependent isosteric heat of adsorption, 298 and 273 K data were fitted with a virial-type expression and at zero loading, the isosteric heat of adsorption (Q_{st}) is 29 kJ mol⁻¹ (Figure 7c).⁶²⁻⁶³ With increasing loading, it increases to 32.5 kJ mol⁻¹ (~ 1 mmol g⁻¹ loading) and then again decreases. To check whether there is any pressure induced structural transformation or not, we have carried out CO₂ adsorption experiments

at high pressure at different temperature (Figure 7d). The high pressure CO₂ adsorption measurement at 273 K ($p = 33$ bar) exhibited a two-step isotherm with total uptake capacity of $146 \text{ cm}^3 \text{ g}^{-1}$ (29.0 wt %). Similar double-step uptake profile was also observed at 283 K ($p = 45$ bar) with a total amount of $133 \text{ cm}^3 \text{ g}^{-1}$ (26.1 wt %). Further increase to 298 K ($p = 50$ bar) does not reveal any stepwise adsorption and uptake amount is $65 \text{ cm}^3 \text{ g}^{-1}$ (12.9 wt%). It is worth mentioning that with increasing temperature from 273 to 283 K, the inflection point (i.e. step pressure) increases from 21.6 to 33.3 bar however uptake upto the 1st step at 273 ($71 \text{ cm}^3 \text{ g}^{-1}$) and 283 K ($69 \text{ cm}^3 \text{ g}^{-1}$) are similar, which is equivalent to the total uptake at 298 K $65 \text{ cm}^3 \text{ g}^{-1}$). This suggests that first adsorption sites are occupied based on permanent porosity of the framework whereas the second adsorption site would be available under a particular condition. This can be attributed to the dynamic nature of the framework where temperature and pressure have strong influence on the structural transformation.

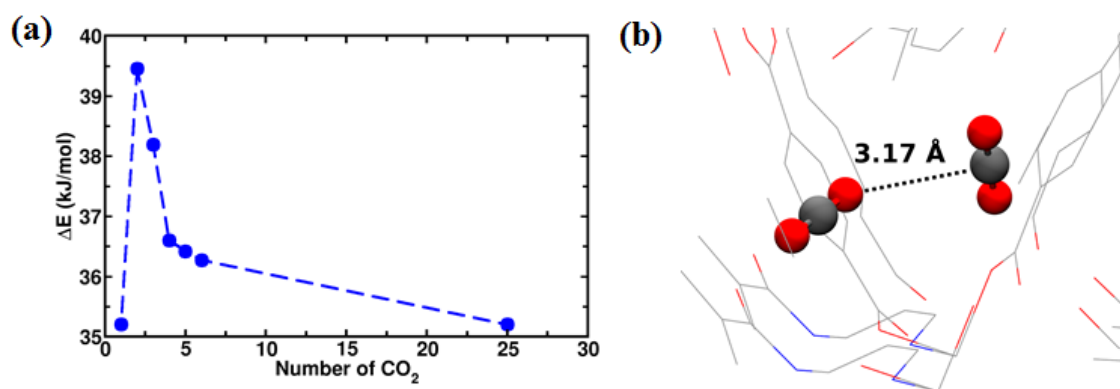


Figure 10: (a) Binding energy with respect to number of CO₂ molecules in **1aD**, (b) orientation of two different CO₂ molecules in the pore of **1aD**. Framework atoms are shown in line representation and CO₂ are in ball and stick representation. Color scheme: C-grey and O-red.

Periodic DFT calculations were carried out to gain an insight into the higher uptake, the adsorption sites and their contribution to CO₂ binding. From point P to Q, we observed a type I profile for CO₂ adsorption at 195 K (Figure 7a). It suggests that the structure of **1aD** does not change with increasing pressure from P to Q. The experimental uptake at Q corresponds to the adsorption of 27 CO₂ molecules in one simulation cell of **1aD**. Thus, simulations carried out with this configuration are hereinafter referred to as **1aQ** (Table 1). Post geometry and cell optimization, the crystal parameters and the calculated PXRD pattern of **1aQ** are found to match closely to the experimental

observations of **1a**, suggesting no structural change between points P and Q (Figure 8d, Table 2).

In this respect, it is important to mention that only site B is accessible in **1'** and **1aD**. Electron density difference maps have been calculated to delineate the types of interactions exhibited by CO₂ with the framework. Three types of interactions are exhibited by the adsorbed CO₂; i) hydrogen bonding (H-bonding) between the aromatic C-H of framework and O of CO₂, ii) Lewis acid-base interaction between O of C=O of framework and C of CO₂, iii) $\pi\cdots\pi$ interactions between the aromatic rings of framework and CO₂ (Figure 8a-c, 9a-c). The binding energies obtained by the PBE-D3 method are 35.68 and 35.19 kJ mol⁻¹ for **1aD** (at P and Q, respectively). These values are close to the experimentally obtained zero coverage isosteric heat of adsorption (Table 3). Such values are reasonable and good for reversible binding of CO₂.^{64a} In addition, the pore in **1aD** is filled with 2 CO₂, 3 CO₂, 4CO₂, 5 CO₂, and 6 CO₂. Binding energy is plotted against number of CO₂ molecules and the same is shown Figure 10a. In this figure, the trend in binding energy is analogous to the experimentally determined isosteric heat of adsorption with respect to amount uptake. It has been observed that the adsorbed two different CO₂ molecules are further stabilized by cooperative interactions, as one O atom of CO₂ contacts the C atom of another CO₂ molecule (O \cdots C = 3.17 Å) in a T-shaped configuration (Figure 10b), similar to the situation in supercritical CO₂.^{64c} These CO₂ \cdots CO₂ interactions are responsible for the enhanced isosteric heat of CO₂ adsorption. In order to model the interactions of gas with the framework at point R of Figure 7a, an assumption of the MOF structure is necessary. The simplest one is to assume that the structure at R is the same as the as synthesized compound. Most flexible MOF systems showing step-wise adsorption behavior reclaim the as-synthesized structure at maximum gas uptake.^{2, 29b-29d} Hence, this assumption is reasonable. Thus, we removed the four DMF molecules from the pores of framework **1** and loaded 72 CO₂ molecules (herein after referred to as **1R**), in one simulation cell. Note that these many CO₂ molecules correspond to the experimentally determined uptake at point R of the adsorption isotherm (Figure 7a). Unlike **1aD**, both site A and site B are accessible in as-synthesized **1**. The minimum energy cell parameters of **1R** are found to be quite close to the as-synthesized experimental cell parameters of **1** (Table 2). The PXRD pattern of the optimized structure of **1R** too compares very well with that of **1** (Figure 8e). The optimized framework with fully loaded CO₂ is shown in Figure 8f-g and 9.

Table 3. Calculated binding energies (ΔE) using DFT and the experimentally determined isosteric heat of adsorption (Q_{st}) of gas molecules in **1aD**. RT value of 2 kJ mol⁻¹ should be added to ΔE to obtain the computed enthalpy of adsorption.

Molecule	Method	ΔE (kJ mol ⁻¹)	Q_{st} (kJ mol ⁻¹)
CO ₂	PBE-D3	35.7	32.5
	vdW-DF2	30.8	
27CO ₂	PBE-D3	35.2	
CH ₄	PBE-D3	27.0	28.0
	vdW-DF2	21.0	
C ₂ H ₂	PBE-D3	41.4	26.0
	vdW-DF2	26.3	
38 C ₂ H ₂	PBE-D3	43.4	
C ₂ H ₄	PBE-D3	39.7	--
	vdW-DF2	35.0	
C ₂ H ₆	PBE-D3(3-body term)	35.3	26.0
	vdW-DF2	29.0	
C ₃ H ₈	vdW-DF2	39.0	--

2.3.4 Hydrocarbon (C1-C3) adsorption

The structural dynamics observed in case of CO₂ adsorption is very unique and driven by adsorbate-adsorbent interactions. Hence, we thought of studying small chain hydrocarbon storage in **1a**. At 195 K, **1a** shows 70 cm³ g⁻¹ (5.0 wt % and 1.36 molecules per formula unit) of CH₄ (kinetic diameter = 3.64 Å) uptake (at 1 bar) whereas at 298 K, the uptake is negligible (8 cm³ g⁻¹ at 1 bar) (Figure 11a). The adsorption profile is completely different from that of CO₂ probably because dipole or quadrupole moments of CH₄ have weak interaction with the framework of **1a**. The isosteric heat of adsorption (Q_{st}) was calculated based on adsorption isotherms at 258 and 268 K (Figure 11b-c). The zero coverage Q_{st} value is ~ 28 kJ mol⁻¹ as calculated from Clausius-Clapeyron equation (Figure 11d). However, with loading, the Q_{st} value drastically drops to 21 kJ mol⁻¹. Binding energy calculation using the PBE-D3 method shows heat of adsorption value of 27.0 kJ mol⁻¹, which is close to the experimental value. The electron density difference map also reveals weak interaction between CH₄ and framework (Table 3, Figure 11d inset). In contrast to CH₄, C₂H₂ has a rod-shaped linear geometry with kinetic diameter of 3.3 Å similar to CO₂ (kinetic diameter 3.3 Å). Its acidic hydrogens are present at both

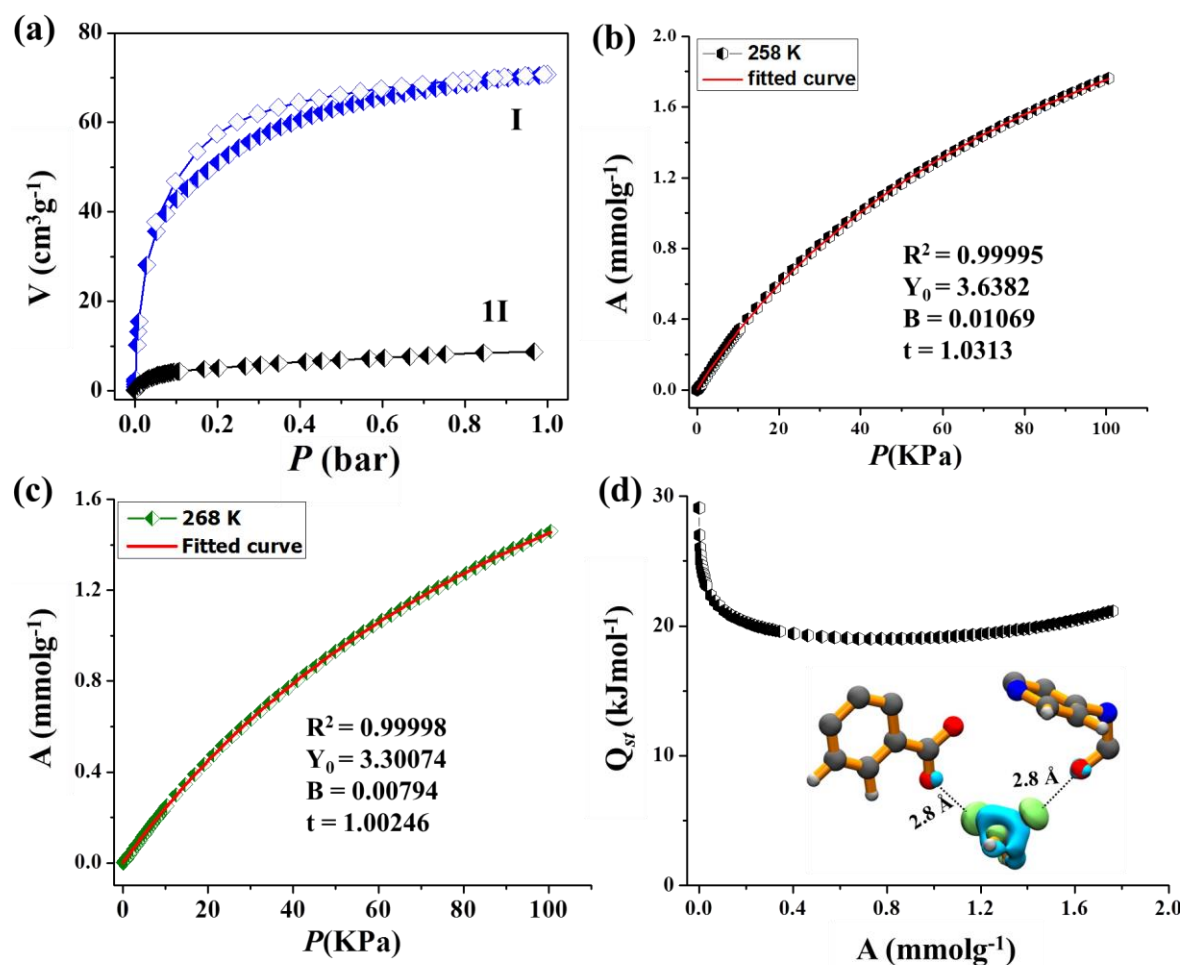
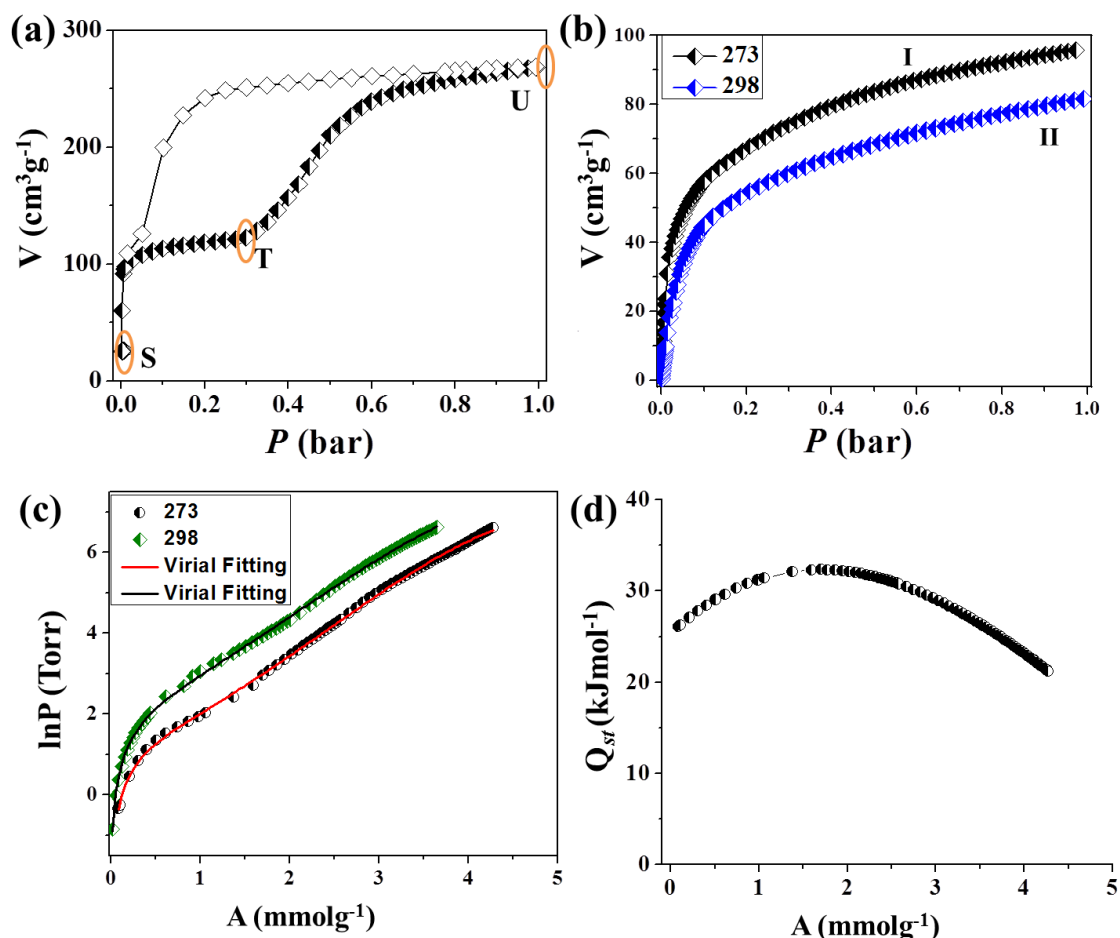


Figure 11: (a) CH₄ adsorption profiles of **1a** at 195 (I) and 298 K (II), (b) pure component isotherm of CH₄ at 258 K, fitted into Langmuir-Freundlich equation, (c) pure component isotherm of CH₄ at 268 K, fitted into Langmuir-Freundlich equation, (d) the isosteric heat of adsorption plot of CH₄ vs. loading; inset shows electron density difference map for CH₄ in **1aD**. Cyan and lime colors indicate the increased and decreased electron densities brought about by the adsorption of gas molecules in desolvated **1aD**, respectively. The isosurface value is 4.5×10^{-4} a.u.

ends ($pK_a = 25$), we thus expected **1a** to be a good adsorbent for C₂H₂ too. Similar to CO₂, C₂H₂ also shows two-step adsorption isotherm followed by a distinct large hysteresis at 195 K (Figure 12a). In the first step upto $p \sim 0.3$ bar, the uptake amount is $123 \text{ cm}^3 \text{ g}^{-1}$ (14.3 wt % and 2.4 molecules per formula unit) followed by an abrupt jump of $145 \text{ cm}^3 \text{ g}^{-1}$ (16.8 wt % and 4.3 molecules per formula unit) in the second step at 1 bar. The total C₂H₂ storage capacity is $268 \text{ cm}^3 \text{ g}^{-1}$ corresponding to 31.1 wt % and 5.2 molecules per formula unit at 1 bar. But the desorption path does not trace the adsorption path at all and shows a large hysteresis indicating barrier for release of C₂H₂ from the



$$R^2 = 0.99952, a_0 = -3053.24727, a_1 = -1050.66772, a_2 = 365.24265, a_3 = -21.46573$$

$$a_4 = -0.08414, b_0 = 13.33712, b_1 = 3.11123, b_2 = -0.66261$$

Figure 12: (a) C₂H₂ adsorption profile at 195 K (S is starting point of adsorption, T and U are at the end of first and second step, respectively), (b) C₂H₂ adsorption profiles at 273 and 298 K (half symbols represent adsorption and empty symbols represent desorption), (c) pure component isotherms of C₂H₂ fitted into virial-type expression at 273 and 298 K, (d) the isosteric heat of adsorption plot of C₂H₂ vs. loading.

pore surface. We have also studied C₂H₂ storage capacity at 273 and 298 K and the total uptake amounts are 95 cm³ g⁻¹ (11 wt % and 1.8 molecules per formula unit) and 81 cm³ g⁻¹ (9.4 wt % and 1.58 molecules per formula unit), respectively at 1 bar (Figure 12b). The room temperature C₂H₂ uptake capacity is promising and it is higher than several reported well known MOFs (without UMSs) such as MIL-53 (72 cm³ g⁻¹), UTSA-35a (65 cm³ g⁻¹), Cu(etz) (70 cm³ g⁻¹), M¹MOF-20 (21 cm³ g⁻¹), UTSA-15 (34 cm³ g⁻¹), ZJU-31 (71.1 cm³ g⁻¹), UTSA-4 (59.8 cm³ g⁻¹), (H₃O)₄[Ni₆(μ₃-O)₂(μ₂-OSC₂H₆)₂(SO₄)₂(TATB)_{8/3}].4C₂H₆O·13H₂O (64.1 cm³ g⁻¹).⁴³ The two isotherms at 273 and 298 K are fitted to a virial-type expression and the zero-coverage Q_{st} value is 26 kJ mol⁻¹ (Figure 12c-d).

C_2H_2 loading versus binding energy profile is very similar to that of CO_2 . Thus, to understand the adsorption phenomenon of C_2H_2 in **1aD**, periodic DFT calculations were

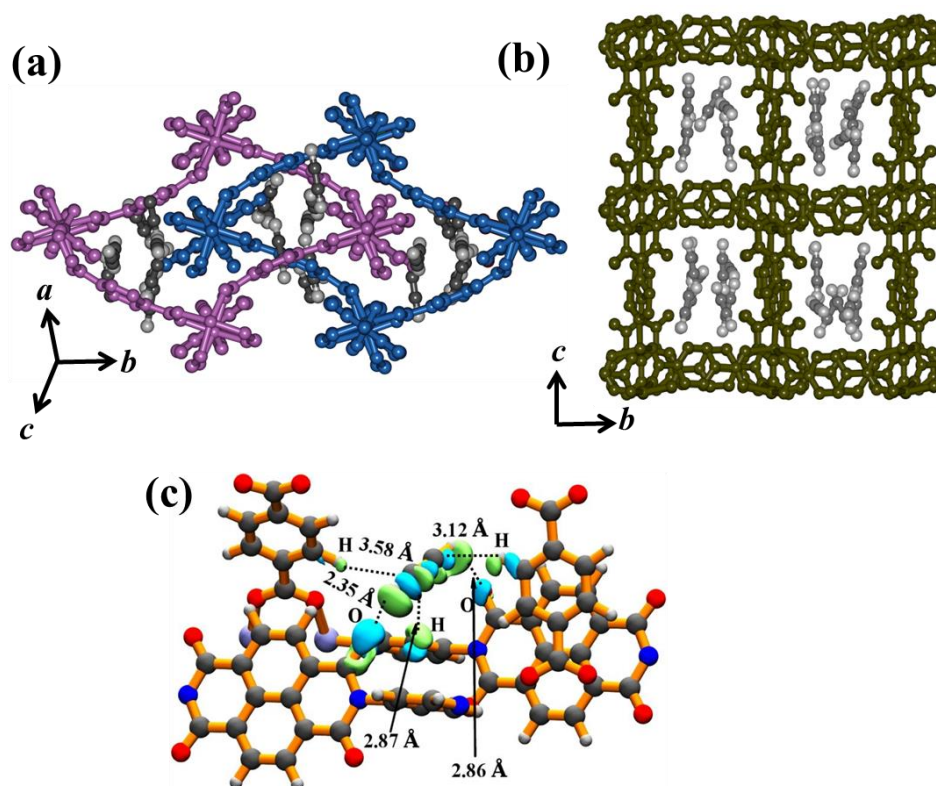


Figure 13. (a-b) Optimized C_2H_2 locations in **1aD** shown along two different axes, (c) electron density difference map of C_2H_2 in desolvated **1aD**. Cyan and lime colors indicate increased and decreased electron densities brought about by the adsorption of C_2H_2 in **1aD**. The isosurface value is 4.5×10^{-4} a.u. Color scheme: Framework atoms: C-grey, N-blue, H-silver, Zn-ice blue; C_2H_2 : C-grey, H-silver.

carried out in a similar fashion as in case of CO_2 to locate the interaction sites. $HC \equiv CH$ is involved in $C-H \cdots O$ H-bonding between the $RNC=O$ group of bpNDI with the acidic hydrogens of C_2H_2 . Such interactions can be realized from the electron density difference maps (Figure 13). The PBE-D3 method overestimated the binding energy of C_2H_2 as can be seen in Table 3. Thus, we resorted to non-local density functional, PW86x-based vdW-DF2 calculations which yield binding energy of C_2H_2 in good agreement with the experimentally determined isosteric heat of adsorption (26.3 kJ mol^{-1} , Table 3). Following the experimental observations, 38 C_2H_2 molecules are loaded in the desolvated framework of **1aD** (hereafter referred to as **1aT**, corresponding to point T in isotherm shown in Figure 12a). The optimized cell parameters and calculated PXRD pattern of **1aT** closely resembles to those of **1aD** (Figure 14).

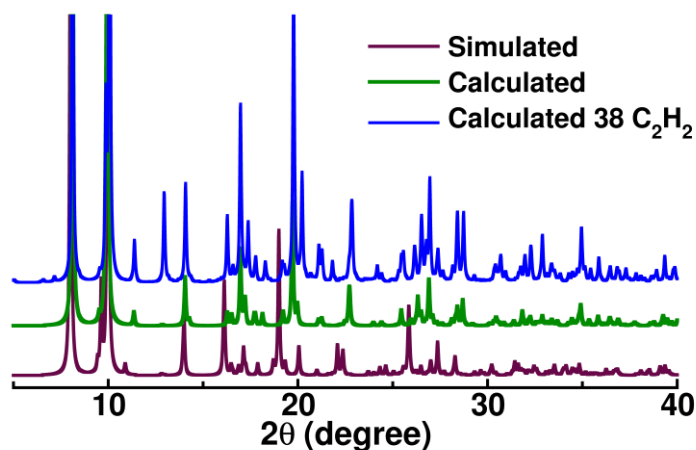


Figure 14: PXRD patterns: maroon: **1'** simulated, green: DFT calculated (**1aD**) and blue: 38 C_2H_2 loaded structure (**1aT**).

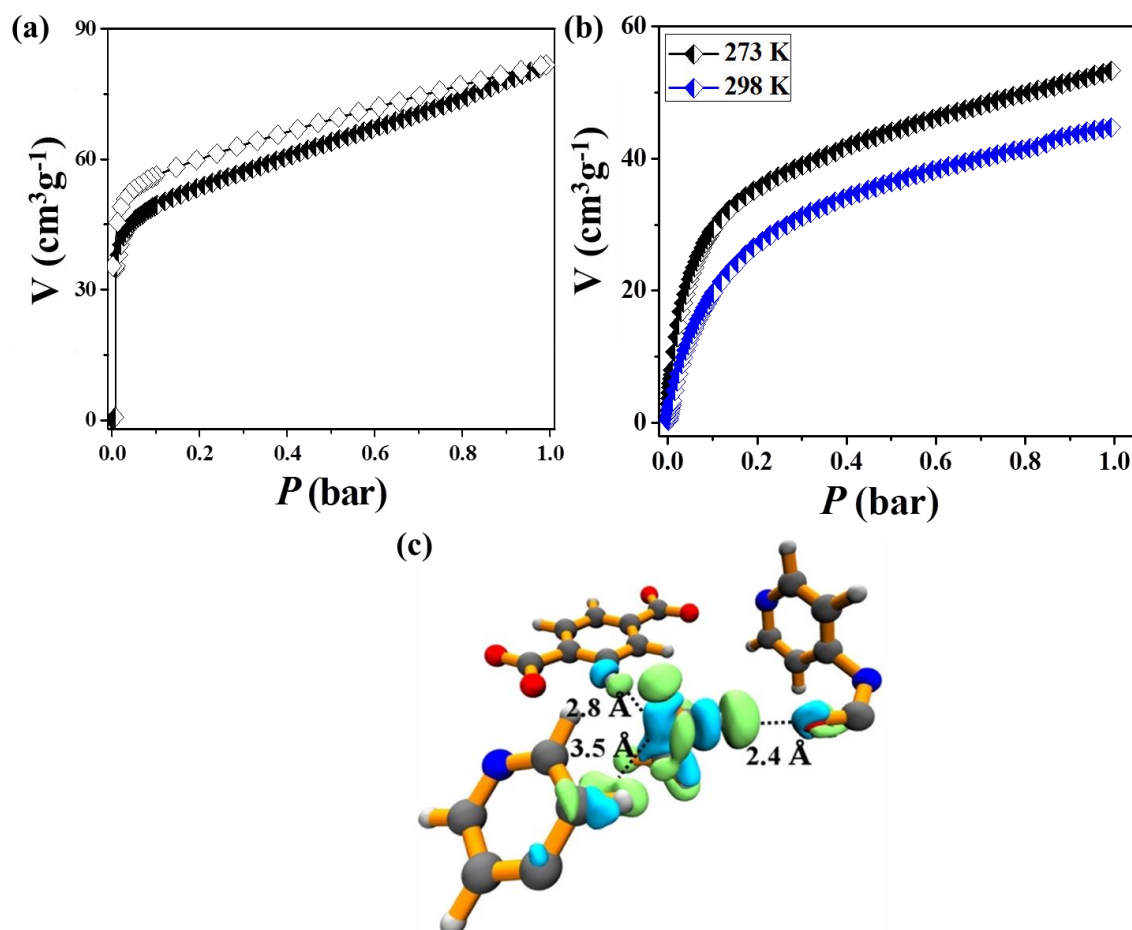
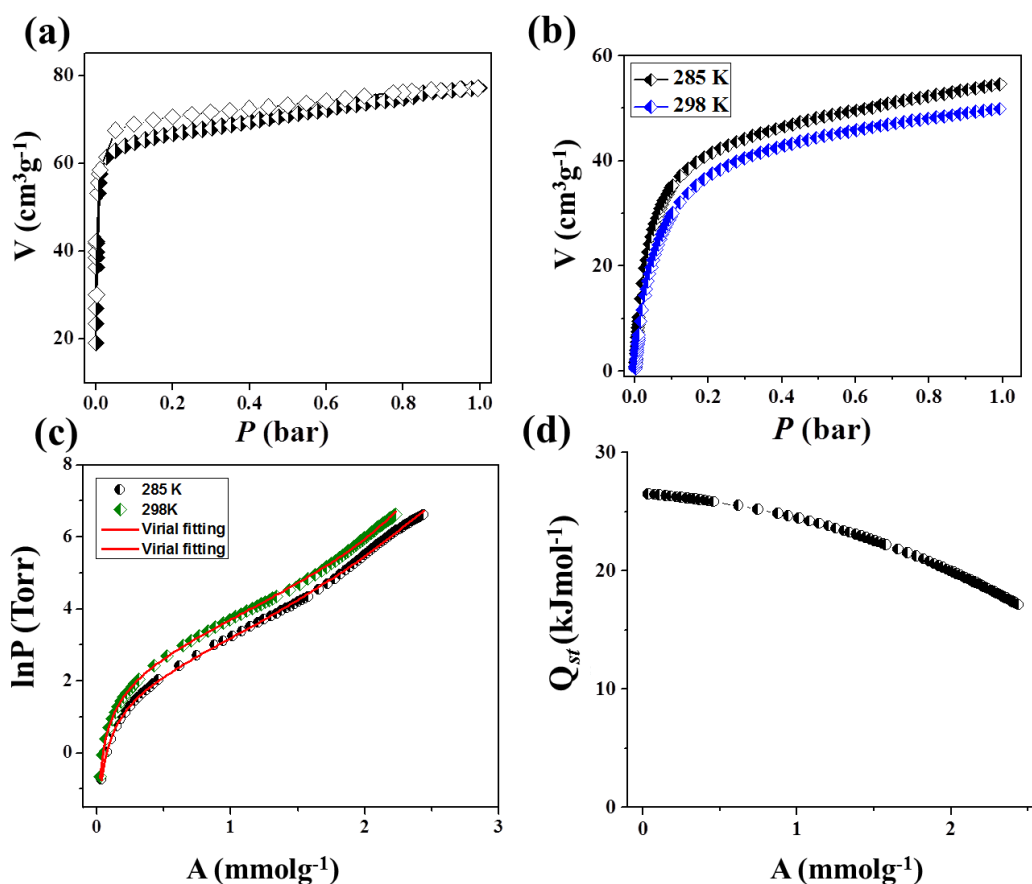


Figure 15: C_2H_4 adsorption profiles at (a) 195 K and (b) 273 (black) and 298 K (blue), (half symbols represent adsorption and empty symbols represent desorption), (c) electron density difference map of C_2H_4 in **1aD**. Cyan and lime colours indicate the increased and decreased electron densities brought about by the adsorption of gas molecules in desolvated **1aD**, respectively. The isosurface value is 4.5×10^{-4} a.u.

Further, we have also carried out the adsorption experiments of C₂H₄ (kinetic diameter = 4.16 Å), C₂H₆ (kinetic diameter = 4.44 Å) and C₃H₈ (kinetic diameter = 4.4 - 5.11 Å) at 195 K and at ambient conditions. Unlike C₂H₂ and CO₂, C₂H₄ showed a completely different adsorption profile at 195 K. The C₂H₄ uptake profile is type I and the total storage capacity is 81 cm³ g⁻¹ (7.4 wt % and 1 molecule per formula unit) at 1 bar (Figure 15a). The profiles at 273 and 298 K are type I too and the final adsorbed amounts are 53 (6.6 wt%, 1.0 molecule per formula unit) and 44 cm³ g⁻¹ (5.5 wt%, 0.86 molecule per formula unit), respectively (Figure 15b). But the isotherm at 273 K could not be fitted to any known model and thus we could not derive the isosteric heat of adsorption experimentally. Instead, we have used the vdW-DF2 method which has been shown to satisfactorily estimate the binding energy of C₂H₄. The binding energy value is found to be 35 kJ mol⁻¹ (Table 3). The electron density difference map shows two types of favourable interactions: a) aromatic C-H interacts with the π electrons of C₂H₄; b) H of C₂H₄ is hydrogen bonded to the O of RNC=O from bpNDI linker (Figure 15c). In addition, H-bonding and π···π interaction distances reveal that C₂H₄ molecules interact strongly with **1aD** compared to CH₄.

Similar to C₂H₄, the other saturated C2 hydrocarbon, C₂H₆ also shows type I profile at 195 K and finally adsorbs 77 cm³ g⁻¹ (10.3 wt % and 1.5 molecule per formula unit) (Figure 16a) at 1 bar. Adsorption measurements at 285 and 298 K show type I nature with total uptake of 54 (7.4 wt % and 1 molecule per formula unit) and 49 cm³ g⁻¹ (6.5 wt % and 0.95 molecule per formula unit), respectively (Figure 16b). The steepness of the curves at very low pressures can be attributed to the high polarizability of ethane molecules which enhances the interactions with the pore surface of the framework.^{64b} The data obtained from 285 and 298 K are fitted into virial-type expression and the zero coverage isosteric heat of adsorption is found to be 26 kJ mol⁻¹ (Figure 16c-d). The vdW-DF2 calculations were carried out for C₂H₆ and we obtained a binding energy of 29 kJ mol⁻¹ (Table 3). The electron density difference map shows interactions between the H of C₂H₆ and O of RNC=O from bpNDI linker (Figure 16e). The number of interaction sites with C₂H₆ and C₂H₄ is more compared to CH₄ as clearly observed from the electron density difference map Figure 12, 17 and 20. Further we have measured larger C3 alkane, propane C₃H₈ (kinetic diameter: 4.4-5.11 Å) adsorption in **1a** at different condition. The low-pressure C₃H₈ adsorption isotherm shows type I nature at 195 K and saturates to 39 cm³ g⁻¹ (7.6 wt % and 0.76 molecule per formula unit) at 0.1



$$R^2 = 0.99961, a_0 = 3188.87439, a_1 = 15.13482, a_2 = 121.72462, a_3 = 8.60124, b_0 = 13.83394, b_1 = -0.31513$$

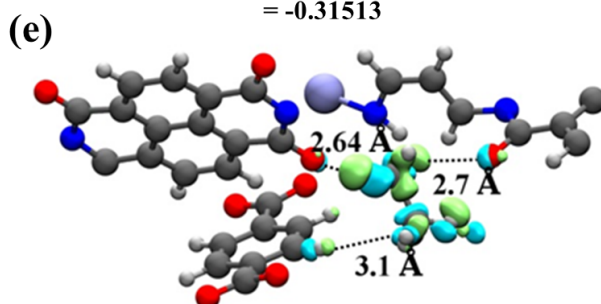


Figure 16: C_2H_6 adsorption profiles at (a) 195 K and (b) 285 (black) and 298 K (blue), (half symbols represent adsorption and empty symbols represent desorption), (c) pure component isotherms of C_2H_6 fitted into virial-type expression at 285 and 298 K, (d) the isosteric heat of adsorption plot of C_2H_6 vs. loading, (e) electron density difference map of C_2H_6 in **1aD**. Cyan and lime colors indicate the increased and decreased electron densities brought about by the adsorption of gas molecules in desolvated **1aD**, respectively. The isosurface value is 4.5×10^{-4} a.u.

bar (Figure 17a). Measurements at 273 and 298 K also reveal type I uptake profiles and storage capacities are 47 (9.2 wt % and 0.91 molecule per formula unit) and $43 \text{ cm}^3 \text{ g}^{-1}$ (8.4 wt % and 0.84 molecule per formula unit), respectively (Figure 17b). However, we could not fit the 273 and 298 K data for C_3H_8 to any of the models to calculate the isosteric heat of adsorption value. A remarkable steep uptake at very low pressure (in 195,

273 and 298 K) can be attributed to the high polarizability of C_3H_8 and also comparable size to the pore of **1a** ($4.8 \times 5.5 \text{ \AA}^2$), which provide strong confinement effect on the pore surface. This has been also realized from the binding energy value of 39 kJ mol^{-1} of C_3H_8 as calculated using vdW-DF2 (Table 3) which is higher compared to other saturated or unsaturated hydrocarbons. The electron density difference map shows stronger interactions between H of C_3H_8 and O of $RNC=O$ from bpNDI linker (Figure 17c) compared to other hydrocarbons such as C_2H_4 , C_2H_6 and CH_4 .

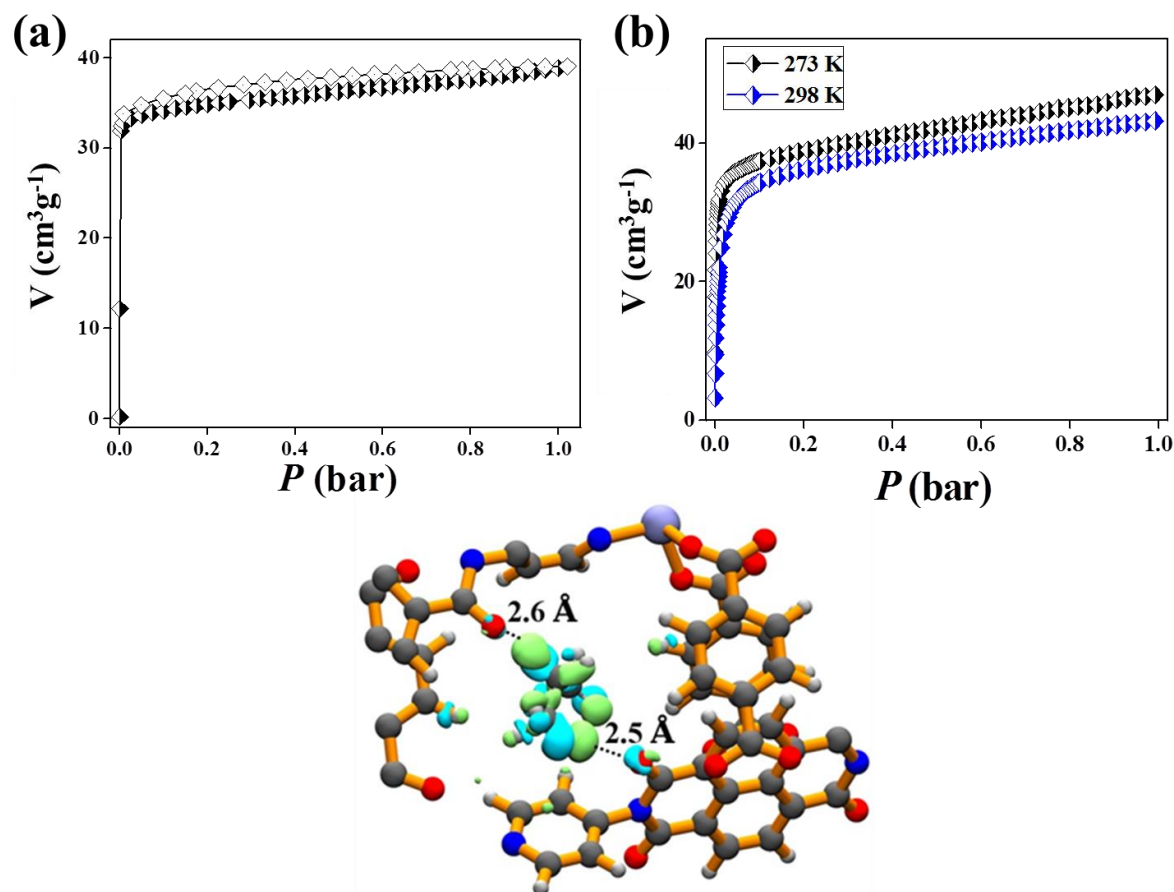


Figure 17: C_3H_8 adsorption profiles at (a) 195 K and (b) 273 (black) and 298 K (blue), (half symbols represent adsorption and empty symbols represent desorption), (c) electron density difference map of C_3H_8 in **1aD**. Cyan and lime colors indicate the increased and decreased electron densities brought about by the adsorption of gas molecules in desolvated **1aD**, respectively. The isosurface value is 4.5×10^{-4} a.u.

2.3.5 Selectivity studies: CO_2 , C_2H_2 , C_2H_4 C_2H_6 vs. CH_4 and CO_2 vs. N_2

We have already mentioned previously the importance of purification of CH_4 (C1) from CO_2 and other C2/C3 hydrocarbons. Hence, high uptake (Figure 18a) and reasonable good binding energy prompted us to calculate the selectivity for CO_2 , C_2H_2 ,

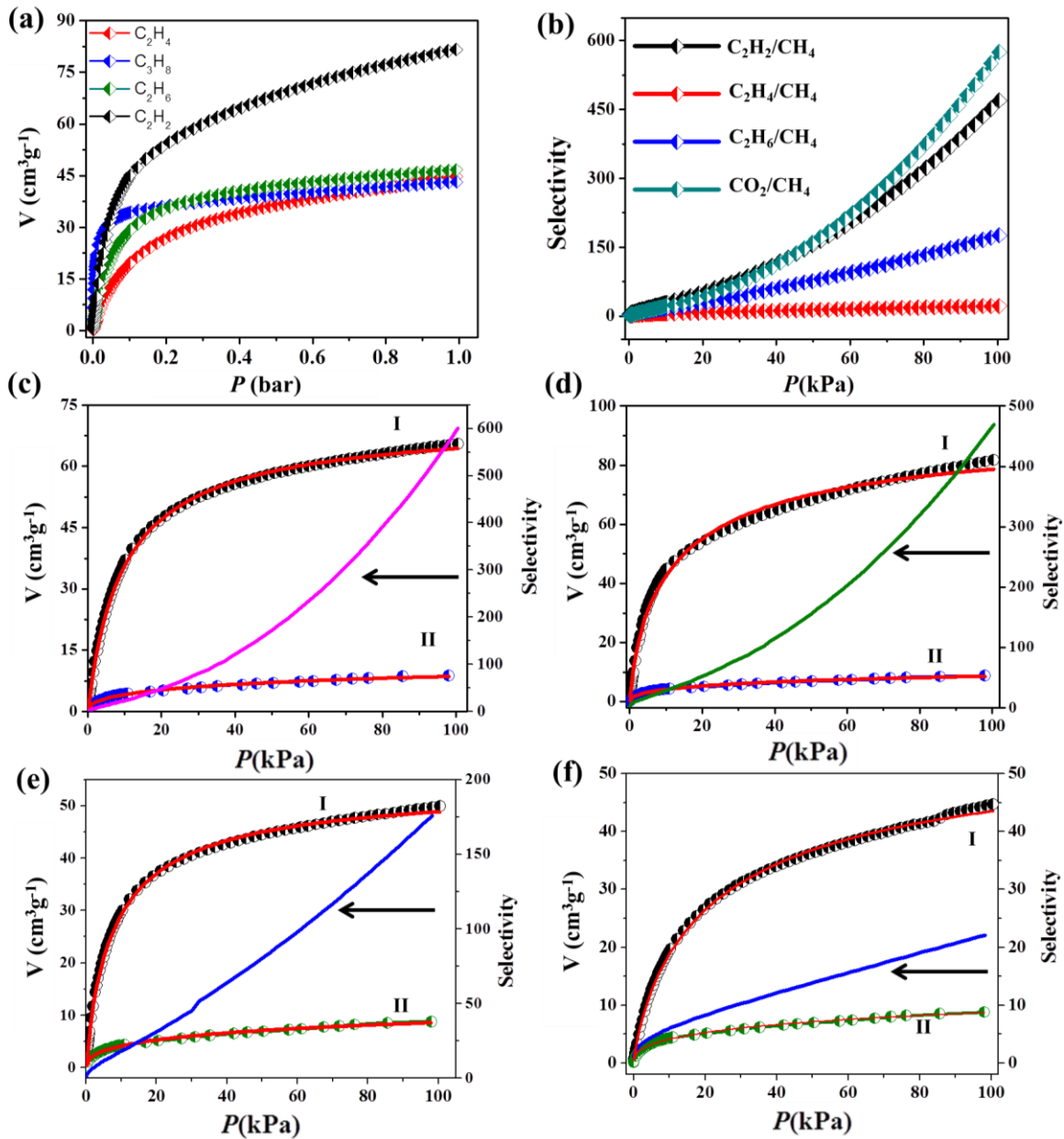


Figure 18: (a) Pure component isotherms of C_2H_2 (black), C_3H_8 (blue), C_2H_6 (green) and C_2H_4 (red) of **1a** at 298 K and 1 bar, (b) selectivity plots of CO_2 , C_2H_2 , C_2H_6 vs. CH_4 at 298 K obtained from IAST calculations, (c) Langmuir-Freundlich fitting for CO_2 (I) vs. CH_4 (II) and corresponding selectivity plot, (d) Langmuir-Freundlich fitting for C_2H_2 (I) vs. CH_4 (II) and corresponding selectivity plot, (e) Langmuir-Freundlich fitting for C_2H_6 (I) vs. CH_4 (II) and corresponding selectivity plot, (f) Langmuir-Freundlich fitting for C_2H_4 (I) vs. CH_4 (II) and corresponding selectivity plot [half symbols represent adsorption].

C_2H_4 , C_2H_6 vs. CH_4 (considering 1:1 mixture) using the ideal adsorbed solution theory (IAST)⁶⁶⁻⁶⁸ by fitting the pure component experimental isotherms at 298 K into Langmuir-Freundlich equation. As mentioned earlier, we could not fit the C_3H_8 isotherm data at 298 K to any of the model equations and hence, the C_3H_8/CH_4 selectivity

calculation was not possible. The selectivity values of CO₂, C₂H₂, C₂H₆ and C₂H₄ over CH₄ at zero coverage are 3.8, 3.8, 3.3 and 3.1, respectively. The calculated selectivity values increase with pressure and the final values at 1 bar are 598, 469, 175 and 22 for CO₂, C₂H₂, C₂H₆ and C₂H₄ over CH₄, respectively (Figure 18). This can be rationalized based on different adsorption sites in the framework **1a** which are gradually occupied with increasing pressure as obtained from theoretical calculation. To the best of our knowledge, the value of CO₂/CH₄ selectivity at high loading is the highest value reported so far in MOFs without UMSs (Figure 18a-c). Well-known MOFs such as MOF-508b, SIFSIX-2-Cu-I, MIL-101, ZIF-78/79/81/82, UTSA-16 also show much lesser CO₂/CH₄ selectivity compared to that of **1a** (Table 4).^{11, 61} The C₂H₂ vs. CH₄ selectivity (Figure 18d) is also higher than a number of well-known functional frameworks such as UTSA-36a (16.1), [Ni₄(OH)₂(ina)₂(dpda)₂(H₂O)₃].(H₂O)₉(C₂H₆O)₃ (32.8), [Cu(BDC-OH) (9.3), UTSA-5 (28.4), (H₃O)₄[Ni₆(μ₃-O)₂(μ₂-OSC₂H₆)₂(SO₄)₂(TATB)_{8/3}].4C₂H₆O·13H₂O (16.3), ZJU-31 (18.8), M'MOF-20 (34.9), UTSA-15 (55.6), ZJU-61(74.4).^{61, 65} It is worth mentioning that C₂H₆ and C₂H₄ have comparable uptake amounts along with similar Q_{st} values but the selectivity of C₂H₆ is quite higher than C₂H₄ (Figure 18a, e-f). Here, confinement of bigger molecule, C₂H₆ into the pore overweighs the functional role of C₂H₄ which is also evident from the steep uptake at low pressure adsorption curves at 298 K. The IAST selectivities for C₂H₆, C₂H₄ vs. CH₄ are calculated to be higher in MOF **1a** compared to the other reported MOFs without UMSs in the literature and such comparison are listed in Table 5. The IAST selectivities are calculated to be higher than UTSA-36a (C₂H₆ vs. CH₄ = 14.7 and C₂H₄ vs. CH₄ = 24.7), [Ni₄(OH)₂(ina)₂(dpda)₂(H₂O)₃].(H₂O)₉(C₂H₆O)₃ (C₂H₆ vs. CH₄ = 27.0 and C₂H₄ vs. CH₄ = 17.3), FIR-7, porphyrinic MOFs such as PAF-40 (C₂H₆ vs. CH₄ = 15.2 and C₂H₄ vs. CH₄ = 10.5), PAF-40-Fe (C₂H₆ vs. CH₄ = 16.2 and C₂H₄ vs. CH₄ = 16.1) and PAF-40-Mn (C₂H₆ vs. CH₄ = 30.8 and C₂H₄ vs. CH₄ = 24.9), (H₃O)₄[Ni₆(μ₃-O)₂(μ₂-OSC₂H₆)₂(SO₄)₂(TATB)_{8/3}].4C₂H₆O·13H₂O (C₂H₆ vs. CH₄ = 10.4 and C₂H₄ vs. CH₄ = 18.7), ZJU-61 (C₂H₆ vs. CH₄ = 49.5 and C₂H₄ vs. CH₄ = 11.0) (Table 5).^{61, 65}

To evaluate experimental separation ability of any solid adsorbents, the kinetic study under flowing conditions for a mixed gas is of prime importance. Encouraged by the CO₂/CH₄ selectivity value, we investigated the separations of CO₂/CH₄ (50:50) binary mixtures in terms of breakthrough column experiments to confirm the separation performance of **1a** (Figure 19a) at 298 K. Notably CH₄ breakthrough occurred within few

seconds indicating poor interaction with the framework. After 372 seconds (6.2 min) of retention time CO_2 reaches breakpoint and goes back to the gas mixture. This experiment clearly suggests that **1a** is selective towards CO_2 rather than CH_4 and it is also verified from DFT calculations. We have also performed breakthrough experiment of hydrocarbon mixture, C_2H_6 and CH_4 (50:50) at 298 K (Figure 19b). Similar to CO_2/CH_4 , here also CH_4 emerges immediately but C_2H_6 retained for longer time of 627 seconds (10.5 min). This is evident from DFT calculations that the numbers of interacting sites are more for CO_2 and C_2H_6 compared to CH_4 and hence higher selectivity.

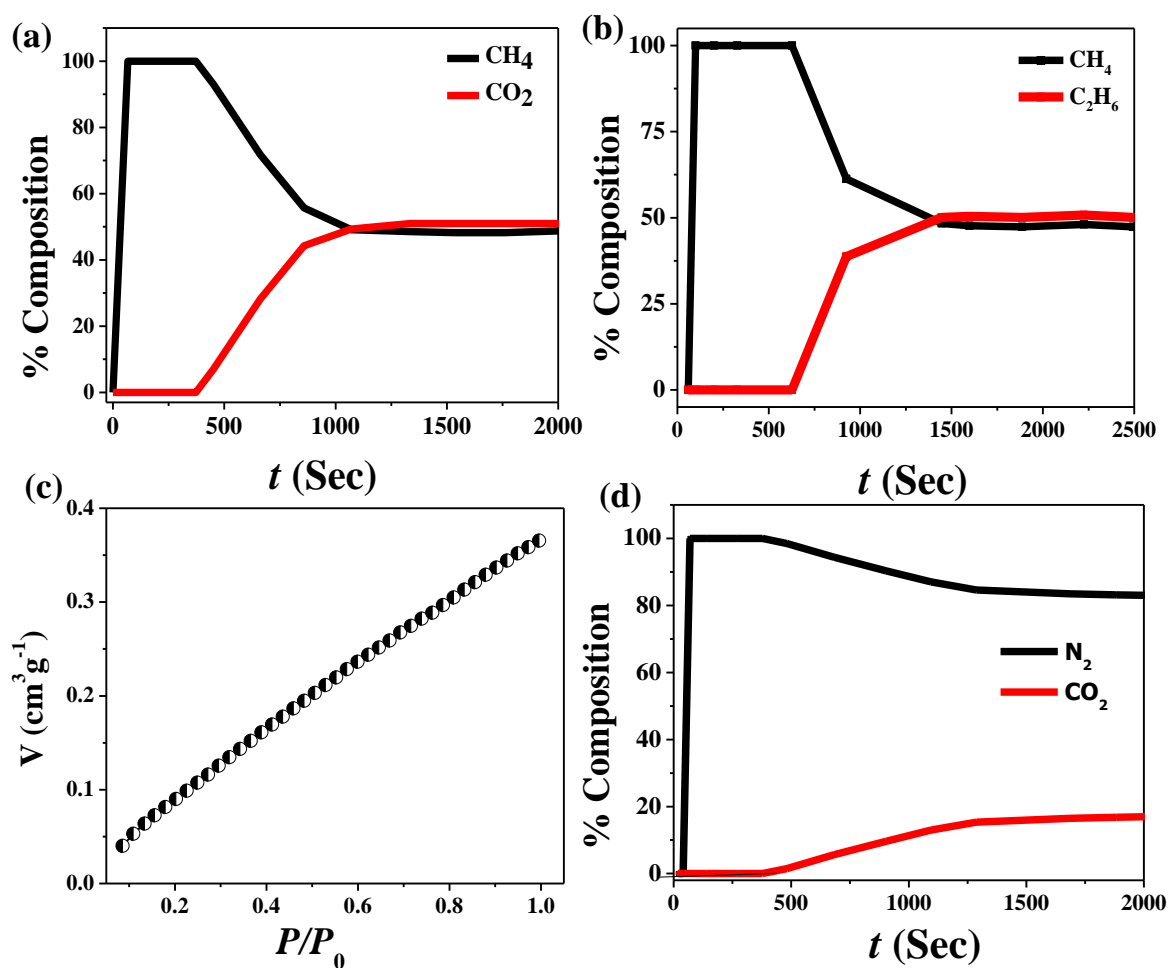


Figure 19: Breakthrough curves for binary mixture of (a) CH_4/CO_2 (50:50), (b) $\text{CH}_4/\text{C}_2\text{H}_6$ (50:50); $p = 5$ kPa, (c) N_2 adsorption isotherm of **1a** at 298 K, (d) breakthrough curves for binary mixture of N_2/CO_2 (85:15) at 298 K. $p = 5$ kPa.

For CO_2/N_2 selectivity at 298 K, we have measured N_2 adsorption isotherm at 298 K and the total uptake is $\sim 0.4 \text{ cm}^3 \text{ g}^{-1}$ (Figure 19c). But it was not possible to fit the data satisfactorily to any of the models and hence, we could not calculate the selectivity for

CO₂ vs. N₂ at 298 K based on IAST. But we performed CO₂/N₂ (15:85) breakthrough column experiment at 298 K (Figure 19d) to understand the separation ability of **1a**. Similar to earlier results, the CO₂ breakthrough occurs after 378 seconds (6.3 min) indicating high selectivity of CO₂ over N₂ in **1a**.

Table 4. Comparative uptake of CO₂ vs. CH₄ (1:1 gas mixture) and selectivity in different MOFs without UMSs at 298 K.

Frameworks	Uptake of CO ₂ vs. CH ₄ (cm ³ g ⁻¹)	Temperature (K)	Pressure (bar)	Selectivity	Ref.
SiF ₆ -3-Zn	57 vs. 17	298	1	231 ^a	11
[ZIF-69]	41 vs. 12	298	1	5.6 ^b	61
[ZIF-78]	51 vs. 14.5	298	1	10.5 ^b	61
[ZIF-82]	54 vs. 11.5	298	1	9.8 ^b	61
Cu(bdc-OH)	52 vs. 13	296	1	6.7 ^b	61
SiF ₆ -2-Cu-i	41 vs. 10	298	1	140 ^a	11
SiF ₆ -2-Cu	121 vs. 8.6	298	1	33 ^a	11
UTSA-5	38.4 vs. 5.2	296	1	10.2 ^c	61
UTSA-15	31 vs. 2.5	296	1	24.2 ^c	40
13X	111 vs. 6	298	1	103 ^a	11
[{Zn ₂ (bdc) ₂ (bpNDI)}·4DMF]	65 vs. 8	298	1	598	Present work

a = IAST selectivity. b = from slopes of adsorption isotherms at low pressure, c = Henry's Law

Table 5. Comparative selectivity values of C₂H₂, C₂H₆, C₂H₄ vs. CH₄ [1:1 gas mixture] in different MOFs without UMSs.

Frameworks	Selectivity				
	C ₂ H ₂ vs. CH ₄	C ₂ H ₆ vs. CH ₄	C ₂ H ₄ vs. CH ₄	Condition	Ref.
[{Zn ₂ (bdc) ₂ (bpNDI)} ₂ ·4D MF]	469 ^a	175 ^a	22 ^a	At 298 K and 1 bar	Present work
UTSA-36a	16.1 ^b	14.7 ^b	24.7 ^b	At 296 K and 1 bar	65a
[Ni ₄ (OH) ₂ (ina) ₂ (dpda) ₂ (H ₂ O) ₃].(H ₂ O) ₉ (C ₂ H ₆ O) ₃	32.8 ^a	27.0 ^a	17.3 ^a	At 297 K and 1 bar	65b
[Cu(BDC-OH)]	9.3 ^b	-	-	At 296 K and 1 bar	65c
UTSA-5	28.4 ^b			At 296 K and 1 bar	61b
FIR-7	-	14.6 ^a	8.6 ^a	At 298 K and 1bar	65d
PAF-40	-	15.2 ^a	10.5 ^a	At 298 K and 1.1 bar	65e
PAF-40-Fe	-	16.2 ^a	16.1a	At 298 K and 1.1 bar	65e
PAF-40-Mn	-	30.8 ^a	24.9 ^a	At 298 K and 1.1 bar	65e
(H ₃ O) ₄ [Ni ₆ (μ ₃ -O) ₂ (μ ₂ - OSC ₂ H ₆) ₂ (SO ₄) ₂ (TATB) 8/3]·4C ₂ H ₆ O·13H ₂ O	16.3 ^a	10.4 ^a	18.7 ^a	At 298 K and 1 bar	65f
ZJU-31	18.8 ^b	63.9 ^b	29.5 ^b	At 298 K and 1 bar	65g
M'MOF-20	34.9 ^b	-	-	At 295 K and 1 bar	65h
UTSA-15	55.6 ^b	-	-	At 295 K and 1 bar	61c
ZJU-61	74.4 ^b	49.5 ^b	11.0 ^b	At 298 K and 1 bar	65i
a = IAST selectivity. b = Henry's Law					

2.4 Conclusion

In summary, in this chapter, an entangled porous coordination polymer $\{[\text{Zn}_2(\text{bdc})_2(\text{bpNDI})]\cdot 4\text{DMF}\}_n$ has been explored for CO_2 capture and storage and separation of C2-C3 hydrocarbons. The framework is highly flexible in nature as realized from stepwise uptake of CO_2 and C_2H_2 which can be attributed to the sliding of the entangled nets to occupy the adsorption sites at low temperature or high pressure. The heat of adsorption and different binding sites for different adsorbates were unearthed by the DFT based calculations. The framework showed good CO_2 uptake and hydrocarbon storage capacity at ambient conditions with moderate isosteric heats of adsorption. Such flexible MOF material without UMSs is paramount as a low energy adsorbent. The present finding also showed the highest CO_2/CH_4 selectivity value in MOFs (without UMSs) at ambient condition as realized from single component adsorption isotherms through IAST calculation. The C2 hydrocarbons vs. CH_4 selectivity values were also calculated based on single component isotherms at ambient conditions and the moderate values are comparable to the reported MOFs and may find potential application as separation materials. Separation ability of binary mixtures of CO_2/CH_4 (50:50), CO_2/N_2 (15:85) and $\text{C}_2\text{H}_6/\text{CH}_4$ (50:50) were tested by breakthrough experiments and the material showed good selectivity of CO_2 , C_2H_6 compared to CH_4 or N_2 at 298 K. It is worth mentioning that till date very few MOFs without UMSs have been studied for hydrocarbon storage and separation and porous entangled frameworks for such applications are underexplored. Therefore these results will provide a new strategy for designing novel entangle and flexible porous framework with inherent functional sites for CO_2 capture and as hydrocarbon storage materials.

2.5 References

1. Y. He, W. Zhou, G. Qian, B. Chen, *Chem. Soc. Rev.* **2014**, 43, 5657.
2. Z. R. Herm, E. D. Bloch, J. R. Long, *Chem. Mater.* **2014**, 26, 323.
3. C. Y. Lee, Y. S. Bae, C. N. Jeong, O. K. Farha, A. A. Sarjeant, C. L. Stern, P. Nickias, R. Q. Snurr, J. T. Hupp, S. T. Nguyen, *J. Am. Chem. Soc.* **2011**, 133, 5228.
4. E. D. Bloch, W. L. Queen, R. Krishna, J. M. Zadrozny, C. M. Brown, J. R. Long, *Science* **2012**, 335, 1606.

5. A. F. P. Ferreira, J. C. Santos, M. G. Plaza, N. Lamia, J. M. Loureiro, A. E. Rodrigues, *Chem. Eng. J.* **2011**, *167*, 1.
6. M. G. Plaza, A. F. Ferreira, J. C. Santos, A. M. Ribeiro, U. Müller, N. Trukhan, J. M. Loureiro, A. E. Rodrigues, *Microporous Mesoporous Mater.* **2012**, *157*, 101.
7. J. A. Mason, M. Veenstra, J. R. Long, *Chem. Sci.* **2014**, *5*, 32.
8. S. Xiong, Y. Gong, H. Wang, Q. Liu, M. Gu, X. Wang, B. Chen, *Chem. Commun.* **2014**, *50*, 12101.
9. X. Duan, R. Song, J. Yu, H. Wang, Y. Cui, Y. Yang, B. Chen, G. Qian, *RSC Adv.* **2014**, *4*, 36419 (b) R. Babarao, C. J. Coghlan, D. Rankine, W. M. Bloch, G. K. Gransbury, H. Sato, S. Kitagawa, C. J. Sumby, M. R. Hill, C. J. Doonan, *Chem. Commun.* **2014**, *50*, 3238.
10. J. Duan, M. Higuchi, S. Horike, M. L. Foo, K. P. Rao, Y. Inubushi, T. Fukushima, S. Kitagawa, *Adv. Funct. Mater.* **2013**, *23*, 3481.
11. P. Nugent, Y. Belmabkhout, S. D. Burd, A. J. Cairns, R. Luebke, K. Forrest, T. Pham, S. Ma, B. Space, L. Wojtas, M. Eddaoudi, M. J. Zaworotko, *Nature* **2013**, *495*, 80.
12. (a) Y. S. Bae, O. K. Farha, J. T. Hupp, R. Q. Snurr, *J. Mater. Chem.*, **2009**, *19*, 2131. (b) C. H. Lau, K. Konstas, A. W. Thornton, A. C. Y. Liu, S. Mudie, D. F. Kennedy, S. C. Howard, A. J. Hill, M. R. Hill, *Angew. Chem. Int. Ed.* **2015**, *54*, 2669.
13. H. A. Patel, S. H. Je, J. Park, D. P. Chen, Y. Jung, C. T. Yavuz, A. Coskun, *Nat. Commun.* **2013**, *4*, 1357.
14. S. Xiang, Y. He, Z. Zhnag, H. Wu, W. Zhou, R. Krishna, B. Chen, *Nat. Commun.* **2012**, 3954.
15. B. Liu, B. Smit, *J. Phys. Chem. C.* **2010**, *114*, 8515.
16. (a) S. Kitagawa, R. Kitaura, S. I. Noro, *Angew. Chem. Int. Ed.* **2004**, *43*, 2334 (b) S. Kitagawa, K. Uemura, *Chem. Soc. Rev.* **2005**, *34*, 109.
17. (a) H. Furukawa, N. Ko, Y. B. Go, N. Aratani, S. B. Choi, E. Choi, A. O. Yazaydin, R. Q. Snurr, M. O'Keeffe, J. Kim, O. M. Yaghi, *Science* **2010**, *329*, 424 (b) Z. Chang, D. S. Zhang, Q. Chen, X. H. Bu, *Phys. Chem. Chem. Phys.* **2013**, *15*, 5430 (c) J. Liu, P. K. Thallapally, B. P. McGrail, D. R. Brown, J. Liu, *Chem. Soc. Rev.* **2012**, *41*, 2308 (d) R. M. Kishan, J. Tian, P. K. Thallapally, C. A. Fernandez, S. J. Dalgarno, J. E. Warren, B. P. McGrail, J. L. Atwood, *Chem. Commun.* **2010**, *46*, 538.

18. K. Koh, A. G. Wong-Foy, A. J. Matzger, *J. Am. Chem. Soc.* **2009**, *131*, 4184.
19. O. K. Farha, I. Eryazici, N. C. Jeong, B. G. Hauser, C. E. Wilmer, A. A. Sarjeant, R. Q. Snurr, S. T. Nguyen, A. Ö. Yazaydın, J. T. Hupp, *J. Am. Chem. Soc.* **2012**, *134*, 15016.
20. D. Wu, T. M. McDonald, Z. Quan, S. V. Ushakov, P. Zhang, J. R. Long, A. J. Navrotsky, *J. Mater. Chem. A* **2015**, *3*, 4248.
21. W. L. Queen, M. R. Hudson, E. D. Bloch, J. A. Mason, M. I. Gonzalez, J. S. Lee, D. Gygi, J. D. Howe, K. Lee, T. A. Darwish, M. James, V. K. Peterson, S. J. Teat, B. Smit, J. B. Neaton, J. R. Long, C. M. Brown, *Chem. Sci.* **2014**, *5*, 4569.
22. N. Planas, A. L. Dzubak, R. Poloni, L. C. Lin, A. McManus, T. M. McDonald, J. B. Neaton, J. R. Long, B. Smit, L. Gagliardi, *J. Am. Chem. Soc.* **2013**, *135*, 7402.
23. (a) Y. He, R. Krishna, B. Chen, *Energy Environ. Sci.* **2012**, *5*, 9107 (b) T. M. McDonald, J. A. Mason, X. Kong, E. D. Bloch, D. Gygi, A. Dani, V. Crocella, F. Giordanino, S. O. Odoh, W. S. Drisdell, B. Vlasisavljevich, A. L. Dzubak, R. Poloni, S. K. Schnell, N. Planas, K. Lee, T. Pascal, L. F. Wan, D. Prendergast, J. B. Neaton, B. Smit, J. B. Kortright, L. Gagliardi, S. Bordiga, J. A. Reimer, J. R. Long, *Nature* **2015**, *519*, 303 (c) E. D. Bloch, M. R. Hudson, J. A. Mason, S. Chavan, V. Crocella, J. D. Howe, K. Lee, A. L. Dzubak, W. L. Queen, J. M. Zadrozny, S. J. Geier, L. C. Lin, L. Gagliardi, B. Smit, J. B. Neaton, S. Bordiga, C. M. Brown, J. R. Long, *J. Am. Chem. Soc.* **2014**, *136*, 10752 (d) B. Vlasisavljevich, S. O. Odoh, S. K. Schnell, A. L. Dzubak, K. Lee, N. Planas, J. B. Neaton, L. Gagliardi, B. Smit, *Chem. Sci.* **2015**, *6*, 5177 (e) P. Verma, X. Xu, D. G. Truhlar, *J. Phys. Chem. C* **2013**, *117*, 12648.
24. (a) A. Hazra, S. Bonakala, S. K. Reddy, S. Balasubramanian, T. K. Maji, *Inorg. Chem.* **2013**, *52*, 11385 (b) J. Duan, M. Higuchi, M. L. Foo, S. Horike, K. P. Rao, S. Kitagawa, *Inorg. Chem.* **2013**, *52*, 8244.
25. P. Kanoo, S. K. Reddy, G. Kumari, R. Haldar, C. Narayana, S. Balasubramanian, T. K. Maji, *Chem. Commun.* **2012**, *48*, 8487.
26. T. K. Maji, R. Matsuda, S. Kitagawa, *Nat. Mater.* **2007**, *6*, 142.
27. R. Haldar, S. K. Reddy, V. M. Suresh, S. Mohapatra, S. Balasubramanian, T. K. Maji, *Chem. Eur. J.* **2014**, *20*, 4347.
28. S. Hasegawa, S. Horike, R. Matsuda, S. Furukawa, K. Mochizuki, Y. Kinoshita, S. Kitagawa, *J. Am. Chem. Soc.* **2007**, *129*, 2607.

29. (a) S. Horike, K. Kishida, Y. Watanabe, Y. Inubushi, D. Umeyama, M. Sugimoto, T. Fukushima, M. Inukai, S. Kitagawa, *J. Am. Chem. Soc.* **2012**, *134*, 9852 (b) N. Nijem, H. Wu, P. Canepa, A. Marti, K. J. Balkus, Jr., T. Thonhauser, J. Li, Y. J. Chabal, *J. Am. Chem. Soc.* **2012**, *134*, 15201 (c) H. R. Fu, J. Zhang, *Cryst. Growth Des.* **2015**, *15*, 1210 (d) S. Couck, T. R. C. V. Assche, Y. Y. Liu, G. V. Baron, P. V. D. Voort, J. F. M. Denayer, *Langmuir* **2015**, *31*, 5063.
30. (a) Y. Takashima, V. M. Martínez, S. Furukawa, M. Kondo, S. Shimomura, H. Uehara, M. Nakahama, K. Sugimoto, S. Kitagawa, *Nat. Commun.* **2011**, *2*, 168 (b) V. M. Martínez, S. Furukawa, Y. Takashima, I. L. Arbeloa, S. Kitagawa, *J. Phys. Chem. C* **2012**, *116*, 26084 (c) V. M. Martínez, R. S. Llano, S. Furukawa, Y. Takashima, I. L. Arbeloa, S. Kitagawa, *ChemPhysChem*. **2014**, *15*, 2517.
31. (a) M. Dincă, A. Dailly, Y. Liu, C. M. Brown, D. A. Neumann, J. R. Long, *J. Am. Chem. Soc.* **2006**, *128*, 16876 (b) J. L. C. Rowsell, O. M. Yaghi, *J. Am. Chem. Soc.* **2006**, *128*, 1304 (c) L. Czepirski, J. Jagiello, *Chem. Eng. Sci.* **1989**, *44*, 797.
32. R. T. Yang, *Gas Separation by Adsorption Processes*; Butterworth: Boston, **1997**.
33. (a) A. L. Myers, J. M. Prausnitz, *AIChE J.* **1965**, *11*, 121. (b) Y. S. Bae, K. L. Mulfort, H. Frost, P. Ryan, S. Punnathanam, L. J. Broadbelt, J. T. Hupp, R. Q. Snurr, *Langmuir*, **2008**, *24*, 8592 (c) J. Peng, H. Y. Ban, X. T. Zhang, L. J. Song, Z. L. Sun, *Chem. Phys. Lett.* **2005**, *401*, 94 (d) B. S. Zheng, J. F. Bai, J. G. Duan, L. Wojtas, M. J. Zaworotko, *J. Am. Chem. Soc.* **2011**, *133*, 748 (e) Y. L. Huang, Y. N. Gong, L. Jiang, T. B. Lu, *Chem. Commun.* **2013**, *49*, 1753 (f) J. Qian, F. Jiang, D. Yuan, M. Wu, S. Zhang, L. Zhang, M. Hong, *Chem. Commun.* **2012**, *48*, 9696.
34. J. VandeVondele, M. Krack, F. Mohamed, M. Parrinello, T. Chassaing, J. Hutter, *Comput. Phys. Commun.* **2005**, *167*, 103.
35. M. Elstner, D. Porezag, G. Jungnickel, J. Elsner, M. Haugk, T. Frauenheim, S. Suhai, G. Seifert, *Phys. Rev. B* **1998**, *58*, 7260.
36. J. P. Perdew, K. Burke, M. Ernzerhof, *Phys. Rev. Lett.* **1996**, *77*, 3865.
37. S. Grimme, *J. Comput. Chem.* **2006**, *27*, 1787.
38. S. Grimme, J. Antony, S. Ehrlich, H. Krieg, *J. Chem. Phys.* **2010**, *132*, 154104.
39. M. Dion, H. Rydberg, E. Schröder, D. C. Langreth, B. I. Lundqvist, *Phys. Rev. Lett.* **2004**, *92*, 246401.
40. T. Thonhauser, V. R. Cooper, S. Li, A. Puzder, P. Hyldgaard, D. C. Langreth, *Phys. Rev. B* **2007**, *76*, 125112.

41. D. C. Langreth, B. I. Lundqvist, S. D. Chakarova-Käck, V. R. Cooper, M. Dion, P. Hyldgaard, A. Kelkkanen, J. Kleis, K. Lingzhu, L. Shen, P. G. Moses, E. Murray, A. Puzder, H. Rydberg, E. Schröder, T. Thonhauser, *J. Phys. Condens. Matter* **2009**, *21*, 084203.
42. N. Nijem, P. Thissen, Y. Yao, R. C. Longo, K. Roodenko, H. Wu, Y. Zhao, K. Cho, J. Li, D. C. Langreth, Y. J. Chabal, *J. Am. Chem. Soc.* **2011**, *133*, 12849.
43. L. Kong, Y. J. Chabal, D. C. Langreth, *Phys. Rev. B* **2011**, *83*, 121402.
44. K. Lee, É. D. Murray, L. Kong, B. I. Lundqvist, D. C. Langreth, *Phys. Rev. B* **2010**, *82*, 081101.
45. É. D. Murray, K. Lee, D. C. Langreth, *J. Chem. Theory Comput.* **2009**, *5*, 2754.
46. S. Nosé, *J. Chem. Phys.* **1984**, *81*, 511.
47. S. Nosé, *Mol. Phys.* **1984**, *52*, 255.
48. H. B. Jansen, P. Ros, *Chem. Phys. Lett.* **1969**, *3*, 140.
49. B. Liu, A. D. McLean, *J. Chem. Phys.* **1973**, *59*, 4557.
50. W. Humphrey, A. Dalke, K. Schulten, *J. Mol. Graphics* **1996**, *14*, 33.
51. (a) C. F. Macrae, P. R. Edgington, P. McCabe, E. Pidcock, G. P. Shields, R. Taylor, M. Towler, J. van de Streek, *J. Appl. Crystallogr.* **2006**, *39*, 453 (b) S. Couck, T. R. C. V. Assche, Y. Y. Liu, G. V. Baron, P. V. D. Voort, J. F. M. Denayer, *Langmuir*, **2015**, *31*, 5063.
52. R. Haldar, N. Sikdar, T. K. Maji, *Mater. Today*. **2015**, *18*, 97.
53. R. Haldar, T. K. Maji, *CrystEngComm*. **2012**, *14*, 684.
54. S. Yang, L. Liu, J. Sun, K. M. Thomas, A. J. Davies, M. W. George, A. J. Blake, A. H. Hill, A. N. Fitch, C. C. Tang, M. Schröder, *J. Am. Chem. Soc.* **2013**, *135*, 4954.
55. B. Chen, S. Ma, F. Zapata, E. B. Lobkovsky, J. Yang, *Inorg. Chem.* **2006**, *45*, 5718.
56. P. K. Thallapally, J. Tian, M. R. Kishan, C. A. Fernandez, S. J. Dalgarno, P. B. McGrail, J. E. Warren, J. L. Atwood, *J. Am. Chem. Soc.* **2008**, *130*, 16842.
57. V. Bon, I. Senkovska, D. Wallacher, D. M. Többens, I. Zizak, R. Feyerherm, U. Mueller, S. Kaskel, *Inorg. Chem.* **2014**, *53*, 1513.
58. H. J. Park, M. P. Suh, *Chem. Commun.* **2010**, *46*, 610.
59. T. Borjigrin, F. Sun, J. Zhang, K. Cai, H. Ren, G. Zhu, *Chem. Commun.* **2012**, *48*, 7613.
60. R. Haldar, T. K. Maji, *J. Chem. Sci.* 2011, **123**, 883.

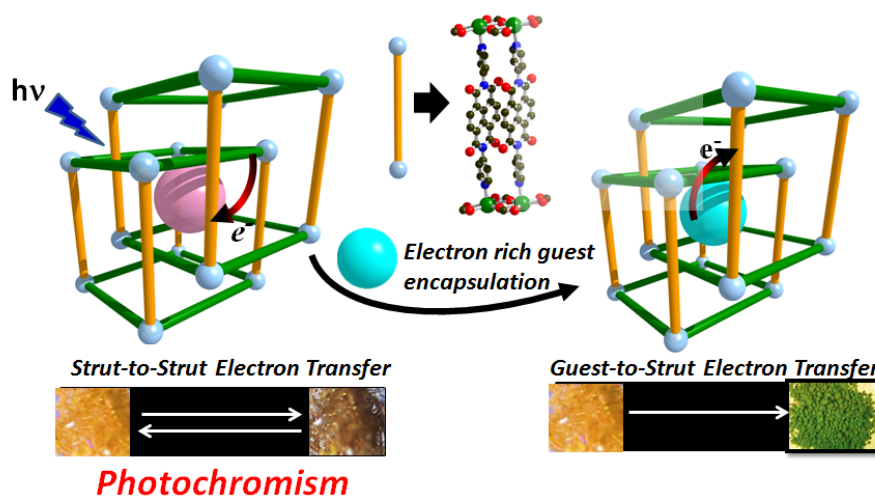
61. (a) J. R. Li, Y. Ma, M. C. McCarthy, J. Sculley, J. Yu, H. K. Jeong, P. B. Balbuena, H. C. Zhou, *Coord. Chem. Rev.* **2011**, 255, 1791 (b) G. Chen, Z. Zhang, S. Xiang, B. Chen, *CrystEngComm.* **2013**, 15, 5232 (c) Z. Chen, S. Xiang, H. D. Arman, J. U. Mondal, P. Li, D. Zhao, B. Chen, *Inorg. Chem.* **2011**, 50, 3442.
62. O. Talu, *Adv. Colloid Interface Sci.* **1998**, 227, 76.
63. J. Purewal, Hydrogen adsorption by alkali metal graphite intercalation compounds. Ph.D. Dissertation, California Institute of Technology, Pasadena, CA, **2010**.
64. (a) J. Duan, M. Higuchi, R. Krishna, T. Kiyonaga, Y. Tsutsumi, Y. Sato, Y. Kubota, M. Takata, S. Kitagawa, *Chem. Sci.* **2014**, 5, 660 (b) S. J. Geier, J. A. Mason, E. D. Bloch, W. L. Queen, M. R. Hudson, C. M. Brown, J. R. Long, *Chem. Sci.* **2013**, 4, 2054 (c) M. Saharay and S. Balasubramanian, *J. Chem. Phys.* **2004**, 120, 9694.
65. (a) Y. He, Z. Zhang, S. Xiang, F. R. Fronczek, R. Krishna, B. Chen. *Chem. Eur. J.* **2012**, 18, 613 (b) J. Li, Y. Guo, H. R. Fu, J. Zhang, R. B. Huang, L. S. Zheng, J. Tao, *Chem. Commun.* **2014**, 50, 9161 (c) Z. Chen, S. Xiang, H. D. Arman, P. Li, S. Tidrow, D. Zhao, B. Chen, *Eur. J. Inorg. Chem.* **2010**, 3745 (d) Y. P. He, Y. X. Tan, J. Zhang, *Chem. Commun.* **2013**, 49, 11323 (e) S. Meng, H. Ma, L. Jiang, H. Ren, G. Zhu, *J. Mater. Chem. A*, **2014**, 2, 14536 (f) J. Li, H. R. Fu, J. Zhang, L. S. Zheng, J. Tao, *Inorg. Chem.* **2015**, 54, 3093 (g) J. Cai, J. Yu, H. Wang, X. Duan, Q. Zhang, C. Wu, Y. Cui, Y. Yang, Z. Wang, B. Chen, B. Qian, *Cryst. Growth Des.* **2015**, 15, 4071 (h) Z. Zhang, S. Xiang, K. Hong, M. C. Das, H. D. Arman, M. Garcia, J. U. Mondal, K. M. Thomas, B. Chen, *Inorg. Chem.* **2012**, 51, 4947 (i) X. Duan, Q. Zhang, J. Cai, Y. Cui, C. Wu, Y. Yang, G. Qian, *Microporous Mesoporous Mater.* **2014**, 190, 32.
66. A. L. Myers, J. M. Prausnitz, *AIChE J.* **1965**, 11, 121.
67. J. Peng, H. Ban, X. Zhang, L. Song, Z. Sun, *Chem. Phys. Lett.* **2005**, 401, 94.
68. Y. S. Bae, K. L. Mulfort, H. Frost, P. Ryan, S. Punnathanam, L. J. Broadbelt, J. T. Hupp, R. Q. Snurr, *Langmuir.* **2008**, 24, 8592.

Chapter 3A

*Redox-Active Metal-Organic
Frameworks: Highly Stable Charge-
Separated States via Strut/Guest-to-
Strut Electron Transfer*

Chapter 3A

Redox-Active Metal-Organic Frameworks: Highly Stable Charge-Separated States via Strut/Guest-to-Strut Electron Transfer



Summary: Molecular organization of donor and acceptor chromophores in self-assembled materials is of paramount interest in the field of photovoltaics or mimicry of natural light harvesting systems. Contemplating this in this chapter, a redox-active porous interpenetrated MOF, $\{[\text{Cd}(\text{bpdc})(\text{bpNDI})]\cdot 4.5\text{H}_2\text{O}\cdot \text{DMF}\}_n$ (**1**) (bpNDI = *N,N'*-di(4-pyridyl)-1,4,5,8-naphthalenediimide; H_2bpdc = 4,4'-biphenyldicarboxylic acid) has been constructed from a mixed chromophoric system. The μ -oxo-bridged SBU, $\{\text{Cd}_2(\mu\text{-OCO})_2\}$ guides the parallel alignment of bpNDI acceptor linkers which are tethered with bpdc linkers of another entangled net in the framework resulting in a photochromic behaviour through inter-net e^- transfer. Encapsulation of electron donating aromatic molecules in the electron deficient channels of **1**, leads to a perfect donor-acceptor co-facial organization resulting in long-lived charge-separated states of bpNDI. Furthermore, **1** and guest encapsulated species are characterised through electrochemical studies for understanding of redox properties.

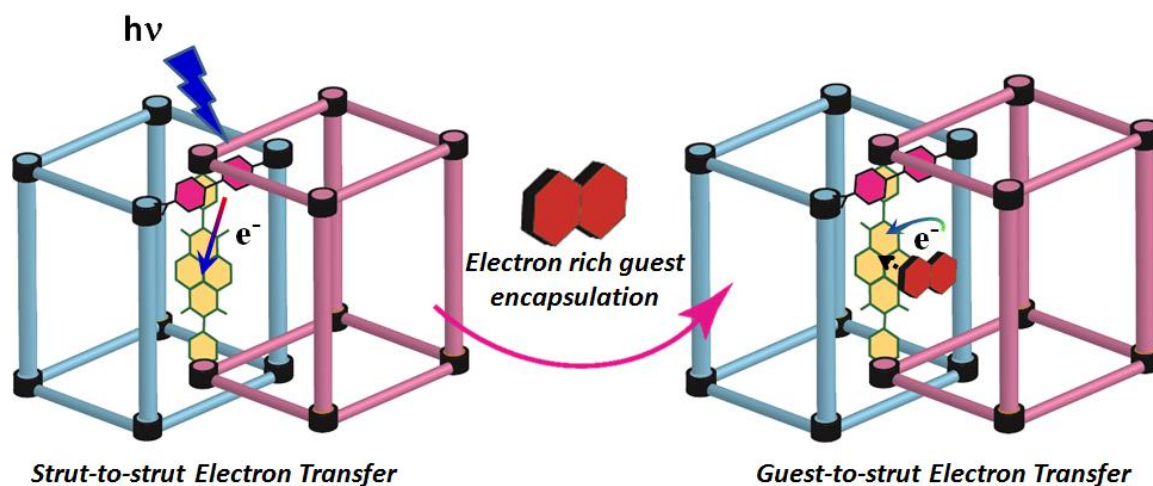
N. Sikdar, K. Jayaramulu, V. Kiran, K. V. Rao, S. Sampath, S. J. George, T. K Maji, *Chem. Eur. J.*, 2015, 21, 11701-11706.

3A.1 Introduction

The spatial organizations of organic chromophores in self-assembled scaffolds has immense importance for understanding and controlling the processes in artificial light harvesting systems and in various optoelectronic devices.¹ However the development of such impeccable supramolecular organizations that can harvest visible light and guide excitation energy or electron transfer in a controlled manner impose a real challenge. But recently, the perception of photofunctional metal-organic framework (MOF) with chromophoric linkers as organized matrix of light harvestors has moved to the fore.² It is regardless to mention that the concept of crystal engineering and reticular chemistry based on predesigned organic linkers and secondary building units (SBU) allow the desired spatial organization of organic chromophores in MOFs, hence the intermolecular distances and angles between the organic linkers can be controlled.³ MOFs have already drawn substantial attention for its several potential applications such as gas storage, separation, catalysis and drug delivery based on permanent porosity.⁴ However, the well-defined nanopores provide an additional design for incorporating chromophoric guest molecules to modulate the photophysical processes.⁵ This design has been extensively used for light harvesting in MOFs with tunable luminescent properties.^{2a,2e,5c} On the other hand, redox-active multichromophoric frameworks exhibiting electron transfer between the linkers or with the guest molecules have been underexplored. Such a design, would give extended donor-acceptor arrays with specific organization which would exhibit interesting charge-transport, ferroelectric properties or may act as a shape-selective sensors.⁶ Although co-facial donor-acceptor assemblies are well studied, which often leads to partial charge-transfer complexes, achieving complete electron transfer require a better control on the spatial organization of the molecular components.^{1c} In this respect, we envisaged that, the mixed chromophoric MOFs can be a useful strategy for grafting suitable donor (D) and acceptor (A) in a long range order. Entanglement of frameworks would be one of the strategies for bringing close contacts of D and A chromophoric linkers to realize photoinduced charge- or electron transfer.

For this purpose, the aromatic redox-active naphthalenediimides (NDIs) are interesting. NDIs are planar, chemically robust and easily reducible molecules that have been utilized as an efficient electron accepting chromophores (n-type) in different applications such as in photosynthesis, solar energy conversion, electrochromic devices, molecular electronics, and as photochromic material.⁷ We have chosen pyridine

substituted NDI derivative bpNDI (*N,N'*-di(4-pyridyl)-1,4,5,8-naphthalenediimide) as the pillar⁸ and H₂bpdc (4,4'-biphenyldicarboxylic acid) as linker for the construction of a novel redox-active framework {[Cd(bpdc)(bpNDI)]·4.5H₂O·DMF}_n (**1**), which is a two-fold interpenetrated 3D multichromophoric porous framework. This chapter describes that this framework exhibits a unique photochromic behaviour resulting from the long-lived charge-separated chromophores, as a result of inter-net strut-to-strut electron transfer (Scheme 1). Furthermore, encapsulation of electron rich guest molecules (e.g. 1,5-/2,6-dinaphthol (1,5-/2,6-DAN) and 4,*N,N*-trimethylaniline (DMPT)) into the electron deficient channels of this framework leads to very stable charge-separated states in ground state. Although, NDI and dinaphthols is a well-known charge-transfer pair,^{7f, 7g} this is the first report of the incorporation of them into a MOF which resulted in the formation of a highly stable bpNDI radical anion by the complete electron transfer process.



Scheme 1. Schematic showing ground state strut-to-strut/guest-to-strut electron transfer in a multichromophoric redox-active interpenetrated 3D framework.

3A.2 Experimental section

3A.2.1 Materials

All the reagents employed were commercially available and used as provided without further purification. Cd(NO₃)₂·4H₂O was obtained from Spectrochem. 4,4'-biphenyldicarboxylic acid, 1,5-dinaphthol, 2,6-dinaphthol and 4,*N,N*-trimethylaniline were obtained from Sigma Aldrich Co. *N,N'*-di(4-pyridyl)-1,4,5,8-naphthalenediimide was synthesised following the literature procedure.⁹

3A.2.2 Physical measurements

Elemental analyses were carried out using a Thermo Fischer Flash 2000 Elemental Analyzer. FT-IR spectra were recorded on a Bruker IFS 66v/S spectrophotometer using KBr pellets in the region 4000-400 cm^{-1} . Thermogravimetric analysis (TGA) was carried out on METTLER TOLEDO TGA850 in nitrogen atmosphere (flow rate = 50 mL min^{-1}) in the temperature range of 30–700 $^{\circ}\text{C}$ (heating rate 3 $^{\circ}\text{C min}^{-1}$). Powder XRD pattern of the compounds were recorded by using Cu-K α radiation (Bruker D8 Discover; 40 kV, 30 mA). Electronic absorption spectra were recorded on a Perkin Elmer Lambda 900 UV-VIS-NIR Spectrometer and emission spectra were recorded on Perkin Elmer Ls 55 Luminescence Spectrometer. ^1H NMR spectra were obtained with a Bruker AVANCE 400 (400 MHz) Fourier transform ^1H NMR spectrometer with chemical shifts reported in parts per million (ppm). For EPR spectra measurements, Bruker EMX spectrometer has been used in the X-band operating at 9.43 GHz.

3A.2.3 Electrochemical studies

All the electrochemical measurements were performed with a CHI 660A electrochemical analyzer (CH instruments, TX, USA). Electrochemical measurements were carried out in conventional three electrode system where in, the compound coated glassy carbon electrode acts as a working electrode, large Pt foil and Ag wire act as auxiliary and reference electrodes, respectively. A known amount (7 mg) of bpNDI/1/1@2,6-DAN was dispersed in 1 mL of ethanol and 20 μL of Nafion solution for 30 min. A 20 μL aliquot of the above dispersion was drop casted onto pre-cleaned glassy carbon electrode and dried under ambient conditions for fabrication of working electrode. Electrochemical measurements were performed in distilled acetonitrile under deaerated conditions. 0.1 M TBAP ($[(n\text{-Bu})_4\text{N}]\text{PF}_6$) acts as a supporting electrolyte.

3A.2.4 X-ray crystallography

X-ray single crystal structural data of **1** was collected on a Bruker Smart-CCD diffractometer equipped with a normal focus, 2.4 kW sealed tube X-ray source with graphite monochromated Mo-K α radiation ($\lambda = 0.71073 \text{ \AA}$) operating at 50 kV and 30 mA. The program SAINT¹⁰ was used for integration of diffraction profiles and absorption correction was made with SADABS¹¹ program. The crystal structure was solved by SIR 92¹² and refined by full matrix least square method using SHELXL-97.¹³ All the

hydrogen atoms were fixed by HFIX and placed in ideal positions. All the non-hydrogen atoms were refined anisotropically. Crystal data and structure refinement parameters of **1** are given in Table 1. Selected bond lengths and angles of **1** are given in Table 2-3. All calculations were carried out using SHELXL 97, PLATON,¹⁴ SHELXS 97¹⁵ and WinGX system, Ver 1.70.01.¹⁶

3A.2.5 Adsorption studies

The adsorption isotherms of N₂ at 77 K and CO₂ at 195, 298 K, using the dehydrated sample of **1** (**1'**), **1@1,5/2,6-DAN** and **1@DMPT** were measured by using QUANTACHROME QUADRASORB-SI analyzer. The compound **1** has been activated at 160 °C for 24 hour, whereas **1@1,5/2,6-DAN** and **1@DMPT** are heated at 140 °C respectively for 8 hour under 1×10⁻¹ Pa vacuum prior to measurement of the isotherms. All the gases used for adsorption measurement are of scientific/research grade with 99.999% purity. Dead volume was measured with helium gas. The adsorbates were placed into the sample tubes, and then the change of the pressure was monitored and the degree of adsorption was determined by the decrease in pressure at the equilibrium state. All operations were computer-controlled and automatic.

3A.2.6 Synthesis of {[Cd(bpdC)(bpNDI)]·4.5H₂O·DMF}_n (**1**)

A mixture containing Cd(NO₃)₂·4H₂O (0.1 mmol, 0.030 g), bpdC_H₂ (0.1 mmol, 0.012 g) and bpNDI (0.05 mmol, 0.021 g) was suspended in DMF (10 mL) in a 30 mL glass vial and heated at 80 °C for a period of 3 days. The light yellow needle shaped crystals of **1** were collected after washing with DMF for several times. Yield: 88%. Anal. Calc. for C₈₂O₂₇Cd₂H₇₂N₁₀: C: 53.59; H: 3.81; N: 7.62; found C: 53.53; H: 3.76; N: 7.60. FT-IR (4000–400 cm⁻¹): 3358 (w), 3066 (w), 2925 (w), 1715 (s), 1675 (s), 1602 (w), 1577 (s), 1507 (w), 1395 (s), 1339 (s) cm⁻¹.

3A.2.7 Preparation of **1@2,6-DAN**, **1@1,5-DAN** and **1@DMPT**

Around 140 mg (0.16 mmol) of activated sample of **1** (i.e. **1'**) was stirred with methanolic solution (8 mL) of 2,6-dinaphthol (2,6-DAN; 98 % inclusion), 1,5-dinaphthol (1,5-DAN, 90 % inclusion) (0.32 mmol) and 4,*N,N*-trimethylaniline (DMPT) (0.32 mmol for 100 % inclusion) for 3 days for encapsulation into the channels of **1'**. The resulting different guest encapsulated compounds are collected, washed with MeOH for 3-4 times to remove the 2,6-DAN, 1,5-DAN and DMPT molecules adsorbed on the surface of **1'**, then dried in

open atmosphere and used for several experiments. The guest encapsulated compounds have been characterized through TGA (Figure 1), PXRD (Figure 2) ^1H NMR (Figure 3-5) and elemental analyses which suggest 0.9, 0.98 and 1 molecules of 1,5-DAN, 2,6-DAN and DMPT have been encapsulated per formula unit of **1**'.

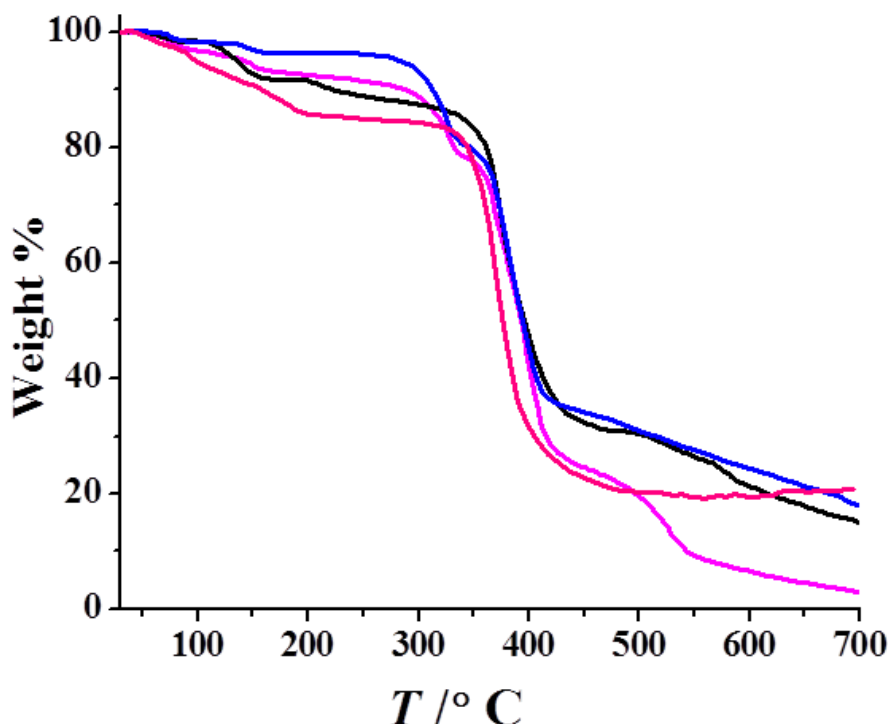


Figure 1: TGA profiles for compound **1** and guest encapsulated compounds: black: **1** (expt., 11.15 % calcd., 11.09 %), red: **1@DMPT** (100%, expt., 15.1% calcd., 15.4%), purple: **1@1,5-DAN** (90%, expt., 14.3% calcd., 14.4 %), blue: **1@2,6-DAN** (98%, expt., 15.6% calcd., 15.68 %) (at heating rate of $3\text{ }^\circ\text{C min}^{-1}$ in the temperature range of $30 - 700\text{ }^\circ\text{C}$ under continuous N_2 flow).

Anal. Calcd. for **1@DMPT** ($\text{C}_{38}\text{O}_8\text{CdH}_{20}\text{N}_4$, 1DMPT, $2\text{H}_2\text{O}$): C: 64.84; H: 3.97; N: 7.76; found C: 64.82; H: 4.89; N: 7.70; FT-IR ($4000-400\text{ cm}^{-1}$): 3387 (w), 3065 (w), 2899 (w), 1715 (s), 1671 (s), 1604 (w), 1576 (s), 1418 (w), 1395 (s), 1340 (s); for **1@1,5-DAN** ($\text{C}_{38}\text{O}_8\text{CdH}_{20}\text{N}_4$, 0.91,5-DAN, $1.5\text{H}_2\text{O}$): C: 64.25; H: 3.14; N: 6.14; found C: 64.21; H: 3.10; N: 7.81; FT-IR ($4000-400\text{ cm}^{-1}$): 3408 (w), 3058 (w), 2823 (w), 1714 (s), 1672 (s), 1609 (w), 1579 (s), 1507 (s), 1487 (s), 1345 (s) and for **1@2,6-DAN** ($\text{C}_{38}\text{O}_8\text{CdH}_{20}\text{N}_4$, 0.982,6-DAN): C: 64.31; H: 3.64; N: 6.14; found C: 64.30; H: 3.62; N: 6.10; FT-IR ($4000-400\text{ cm}^{-1}$): 3401 (w), 3062 (w), 2918 (w), 1715 (s), 1680 (s), 1606 (w), 1573 (s), 1501 (w), 1390(s), 1329 (s).

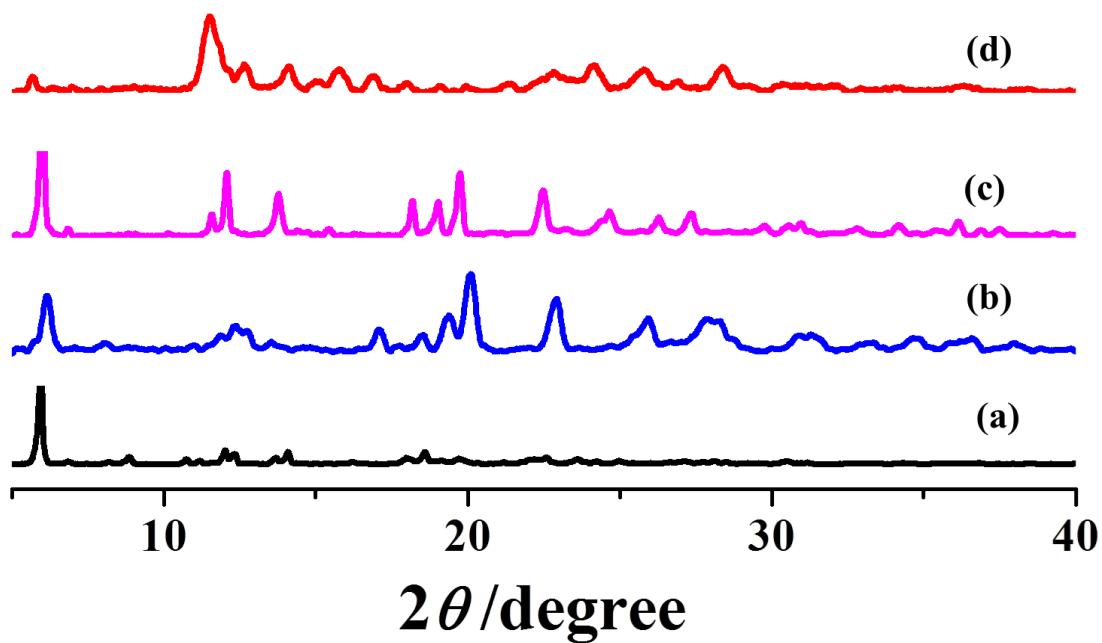


Figure 2: Comparison of PXRD patterns between **1** and guest loaded composites (a) **1**, (b) **1@2,6-DAN**, (c) **1@1,5-DAN** and (d) **1@DMPT**.

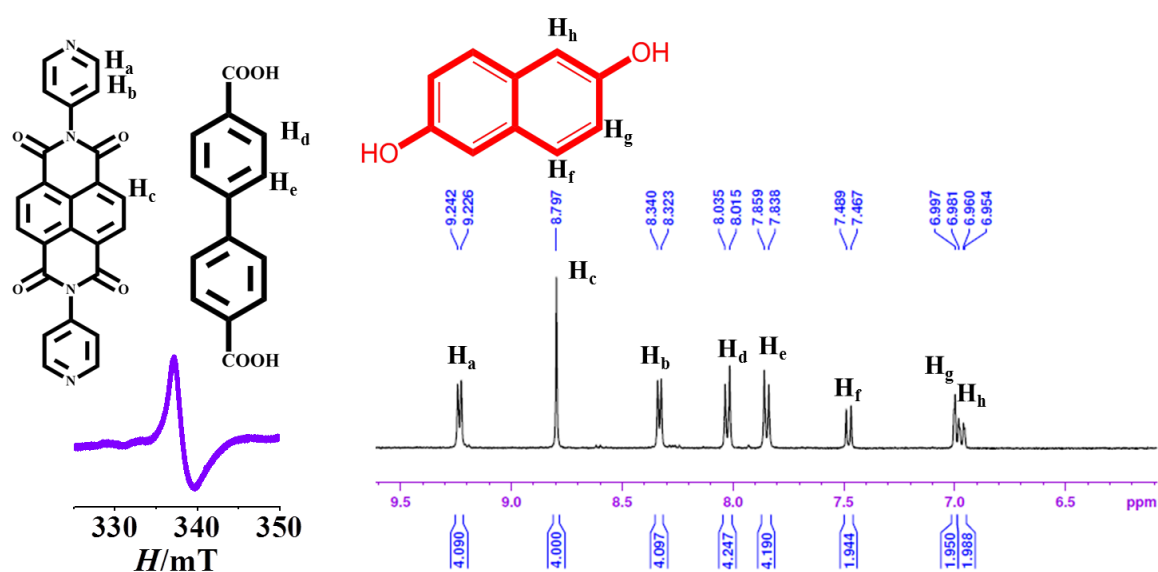


Figure 3: ^1H NMR spectra of **1@2,6-DAN** in $\text{DMSO-}d_6$ after digestion with DCl showing 98 % inclusion.

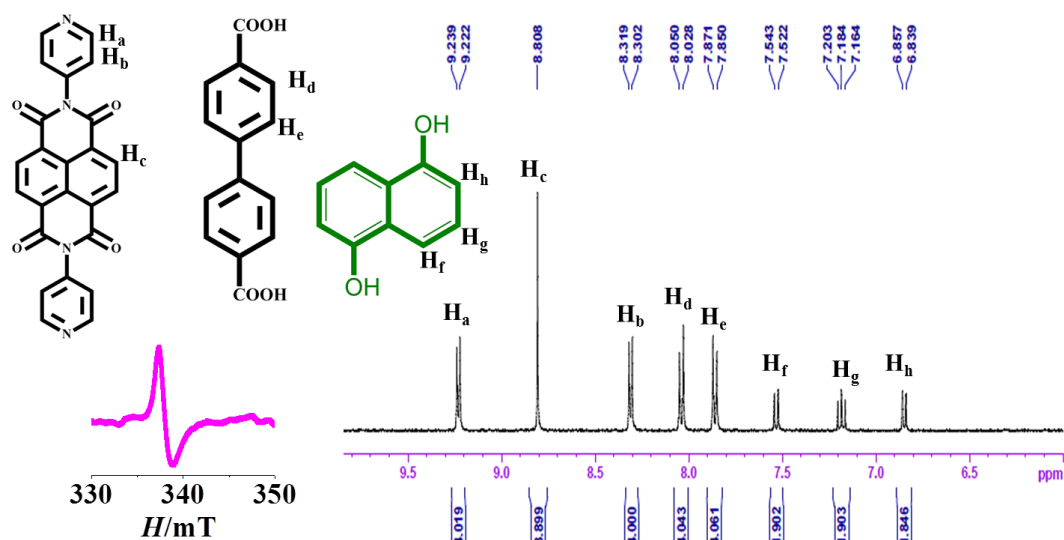


Figure 4: ^1H NMR spectra of $1@1,5\text{-DAN}$ in DMSO-d_6 after digestion with DCl showing 90 % inclusion.

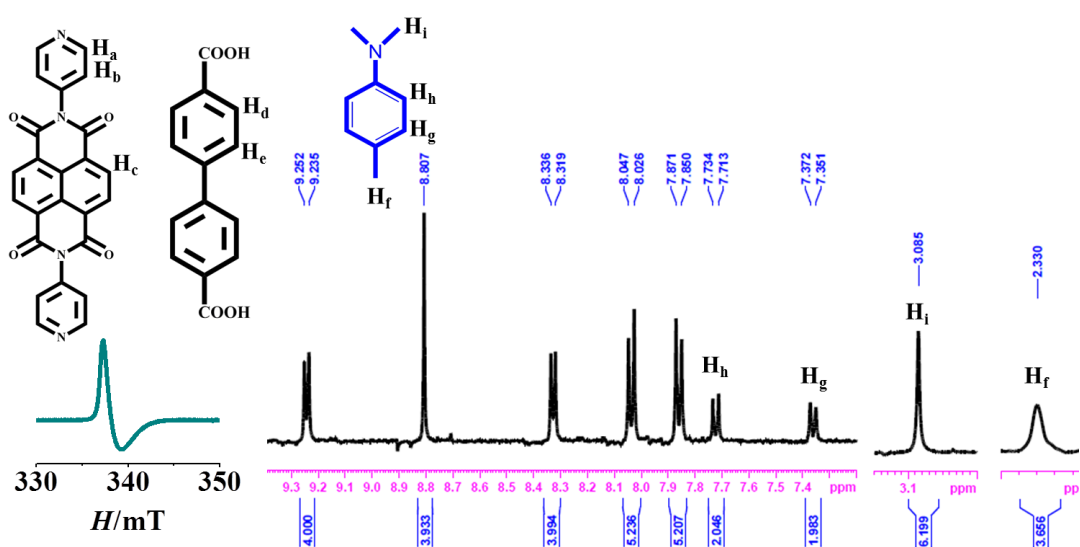


Figure 5: ^1H NMR spectra of $1@DMPT$ in DMSO-d_6 after digestion with DCl showing 100% inclusion.

3A.3. Results and discussion

The compound **1** was synthesized using a solvothermal condition and single crystal X-ray diffraction analysis suggests that **1** crystallizes in monoclinic $P2_1/n$ space group. The Cd^{II} metal center is heptacoordinated and two of such metal centers form a $\{\text{Cd}_2(\mu_2\text{-OCO})_2\}_n$ SBU. These SBUs are connected by bpdC linkers to form an extended 2D rhombic network along $(10\bar{1})$ plane (Figure 6a). This 2D layer is further bipillared by bpNDI linkers to form a (2,8)-c connected 3D framework structure (Figure 6b). It is worth

mentioning that μ_2 -oxo bridged dinuclear SBU ensures stacking of two bpNDI in a face-to-face fashion ($cg \cdots cg$ distance is $\sim 3.844 \text{ \AA}$) resulting in a bipillared-layer framework. The NDI cores of the pillar bpNDI linkers maintain the perfect parallel arrangement with respect to each other (the dihedral angle between the NDI cores is 0°). However, the pyridine ring of bpNDI is not in a same plane with NDI core and the corresponding tilting angle between them is 58.32° . Moreover, the presence of long linkers results in large void space in the 3D net and hence induces two-fold interpenetration in the framework (Figure 6c). Upon interpenetration, this framework shows a 1D rectangular channel with dimension of $6.4 \times 7.1 \text{ \AA}^2$ along the $[10\bar{1}]$ direction, (Figure 6d) and is filled with guest water and DMF molecules.

3A.3.1 Structural description of 1

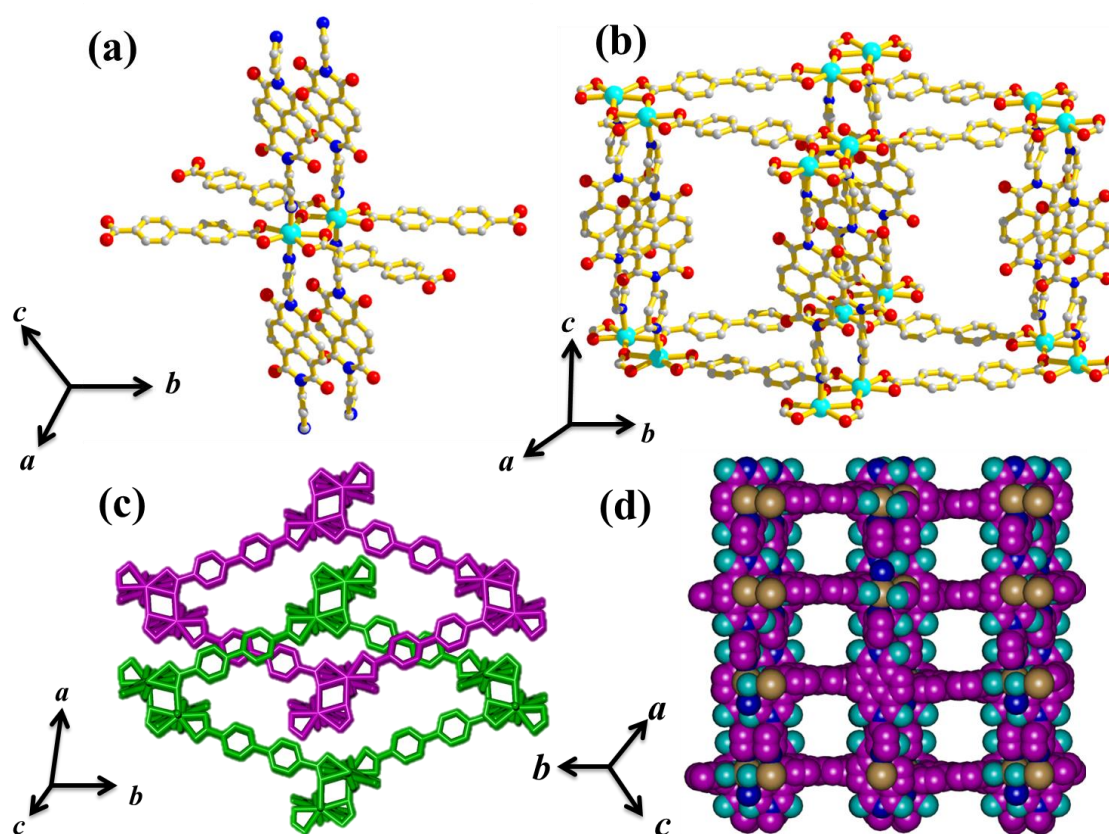


Figure 6: Crystal structure of **1**: (a) coordination environment of Cd^{II} with $\{\text{Cd}_2(\mu_2\text{-OCO})_2\}_n$ SBU, (b) 3D bipillared-layer framework, (c) two-fold interpenetration along crystallographic c -axis, (d) pore view along crystallographic $[10\bar{1}]$ direction.

Table 1. Crystal data and structure refinement parameters of **1**.

Parameters	1
Empirical formula	C ₈₂ O ₂₇ Cd ₂ H ₇₂ N ₁₀
Formula weight	1836.15
Crystal system	Monoclinic
Space group	<i>P</i> 2 ₁ / <i>n</i>
<i>a</i> , Å	11.7797(6)
<i>b</i> , Å	29.1825(9)
<i>c</i> , Å	14.2285(6)
<i>α</i> , deg	90
<i>β</i> , deg	100.679(4)
<i>γ</i> , deg	90
<i>V</i> , Å ³	4806.5(4)
<i>Z</i>	2
<i>T</i> , K	293
<i>μ</i> , mm ⁻¹	0.516
<i>D</i> _{calcd.} , g/cm ³	1.269
<i>F</i> (000)	1836
Reflections [<i>I</i> > 2σ(<i>I</i>)]	5383
Total reflections	50585
Unique reflections	9453
λ(Mo-Kα)	0.71073
<i>R</i> _{int}	0.102
GOF on <i>F</i> ²	1
<i>R</i> ₁ [<i>I</i> > 2σ(<i>I</i>)] ^a	0.0667
<i>R</i> _w [all data] ^b	0.2156

$$^a R = \sum ||F_o| - |F_c|| / \sum |F_o|. \quad ^b R_w = [\sum \{w(F_o^2 - F_c^2)^2\} / \sum \{w(F_o^2)^2\}]^{1/2}.$$

Table 2. Selected bond lengths (Å) for **1**.

N1-Cd1	2.344(5)	N4-Cd1	2.336(5)	O1-Cd1	2.469(5)	O2-Cd1	2.319(4)
O3-Cd1	2.379(5)	O3-Cd1	2.555(4)	O4-Cd1	2.342(4)	Cd1-N4	2.336(5)
Cd1-O4	2.342(4)	Cd1-O3	2.379(5)	Cd1-O3	2.555(4)		

Table 3. Selected bond angles (°) for **1**.

O2-Cd1-N4	87.28(18)	O2-Cd1-O4	142.66(18)	N4 Cd1- O4	94.74(18)
O2-Cd- N1	90.48(18)	N4-Cd1-N1	174.5(2)	O4-Cd1-N1	90.07(18)
O2-Cd1-O3	92.20(17)	N4-Cd1-O3	88.07(18)	O4-Cd1-O3	125.11(15)
N1-Cd1-O3	87.03(18)	O2-Cd1-O1	54.36(17)	N4-Cd1-O1	87.11(19)

O4-Cd1-O1	88.45(17)	N1-Cd1-O1	95.64(19)	O3-Cd1-O1	146.39(15)
O2-Cd1-O3	164.46(18)	N4-Cd1-O3	90.01(16)	O4-Cd1-O3	52.82(15)
N1-Cd1-O3	90.83(16)	O3-Cd1-O3	72.41(16)	O1-Cd1-O3	140.78(16)

3A.3.2. TGA, PXRD and permanent porosity

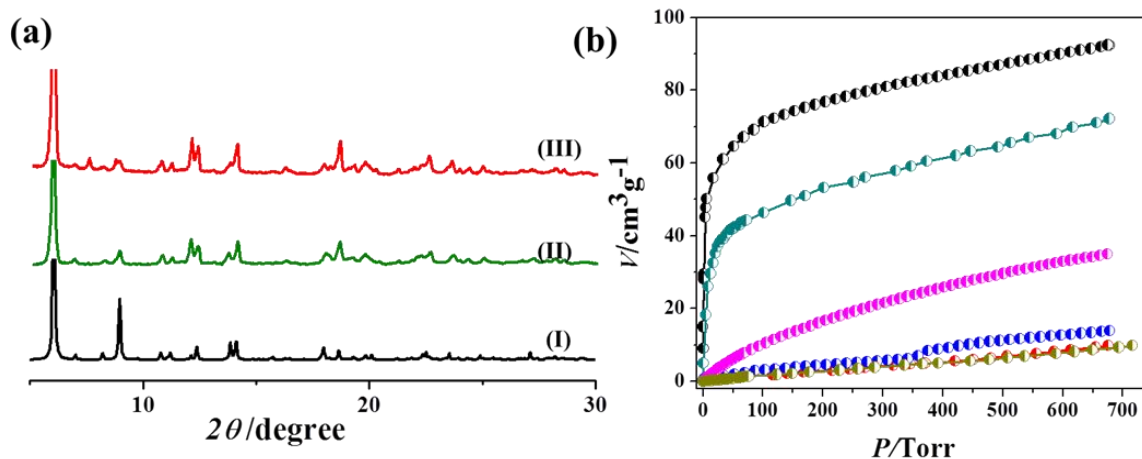


Figure 7: (a) PXRD patterns of **1** in different state: (I) simulated, (II) as-synthesized **1**, (III) desolvated **1** (**1'**), (b) Olive green: N₂ adsorption isotherm of **1'** at 77 K; CO₂ adsorption isotherms at 195 K: black: **1'**, cyan: **1@DMPT**, blue: **1@1,5-DAN** and red : **1@2,6-DAN**. Magenta: CO₂ adsorption isotherm of **1'** at 298 K.

Thermogravimetric analysis (TGA) shows that the guest molecules are removed in a stepwise manner in the temperature range of 55-240 °C (Figure 1) and the desolvated structure of **1**, i.e. **1'** remains stable till 345 °C. The PXRD pattern of **1'** (Figure 7a) shows no distinct change compared to that of **1** suggesting robust nature of the framework. As realized from the single crystal structure, **1** contains high void space but it does not show any N₂ uptake at 77 K (Figure 7b). This might be due to the low thermal energy of the adsorbate relative to the high diffusion barrier as the framework contain 1D channel structure.¹⁷ But CO₂ adsorption measurements at 195 K showed a typical type I profile (Figure 7b), unveiling the microporous nature of the framework. The saturated CO₂ uptake is 92 cm³ g⁻¹ (18 wt%, 3.2 CO₂ molecules per formula unit) which corresponds to Langmuir surface area of 286 m² g⁻¹. **1'** is also able to capture CO₂ at 298 K in a considerable amount of 34 cm³ g⁻¹ (6.8 wt%, 1.1 CO₂ per formula unit) (Figure 7b). The uptake of CO₂ in **1'** can be accounted for the quadrupolar nature of the CO₂ molecules

(quadrupole moment of CO_2 : $4.3 \times 10^{26} \text{ esu}^{-1} \text{ cm}^{-2}$) which interact with the pendent carbonyl oxygens of bpNDI pillars which are aligned along the pore surface.

3A.3.3 Photophysical properties of 1

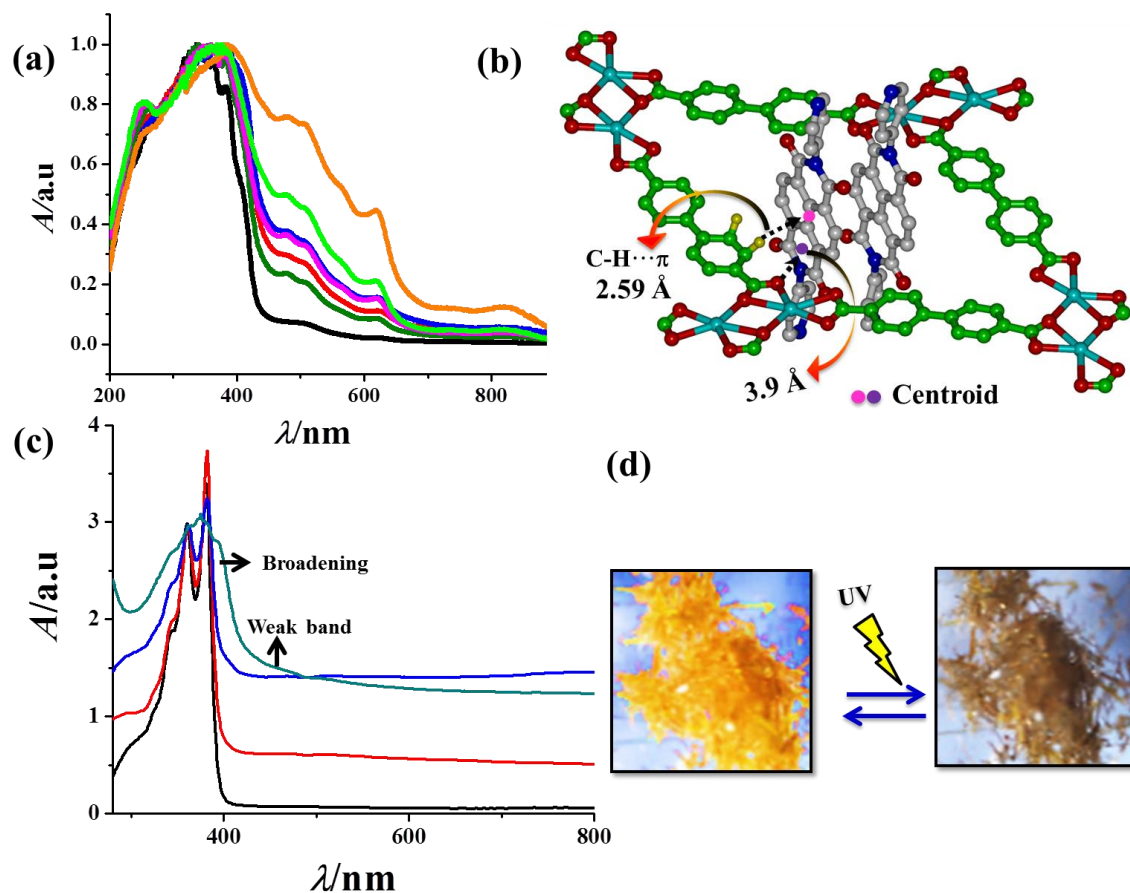


Figure 8: (a) UV-Vis time dependent absorbance spectra of **1** on UV irradiation, (b) possible supramolecular interactions between two different struts realized by interpenetration (cyan = Cd^{II} , red = oxygen, green: C atoms of bpdc, grey: C atoms of bpNDI, blue N and yellow: hydrogen), (c) UV-Visible spectra of bpNDI (10^{-3} M) in DMF and after addition of different amount of water. Black: bpNDI (10^{-3} M) in DMF; red: on addition of 0.5 mL water; blue: on addition of 1 mL water; light green: on addition of 2 mL water, (d) photographs of **1** before and after UV radiation (365 nm).

The compound **1** shows broad absorption in the range of 200-400 nm, characteristic of typical π - π^* and n - π^* transitions (Figure 8a). The presence of a very weak band in the visible region (400-600 nm) corresponds to π -stacked bpNDI chromophores, as evident in the crystal structure as well (Figure 8b). The origin of this band is further confirmed by the solution state self-assembly studies of bpNDI chromophores in DMF/water solvent mixtures. Higher percentage of water induced

aggregation of these chromophores which resulted in similar feature in absorption bands (Figure 8c). We have further studied the photophysical responses of this framework upon exposure to UV light irradiation where two chromophores of different electronic nature are parts of integrated framework. Interestingly, crystals of **1** on shining UV light (365 nm, even for 20-30 seconds), showed an immediate drastic colour change (Figure 8d) from golden yellow to dark brown while retaining its crystal structure intact as supported by PXRD pattern (Figure 9). The colour of these crystals was reverted by keeping in air for 7 to 8 hours (Figure 10a). UV-Vis spectra of irradiated crystals of **1** showed the appearance of new bands with maxima at 478, 617, 737 and 617 nm, intensity of which incessantly enhances on longer exposure of UV light (Figure 10a). The possible origin of these peaks is the formation of radical anions of bpNDI linker molecules (*vide infra*). The formation of radical anion is further confirmed by the chemical reduction of the bpNDI linker with *t*-butylammonium fluoride and comparing the corresponding UV-Vis spectra (Figure 10b).^{18a} Appearance of strong EPR signal with a *g* value of 2.001 for the irradiated crystals of **1** corroborates the formation of radical anion of bpNDI where the radical is on C atom (Figure 11).^{7e} On the other hand, free bpNDI ligands also showed a similar photochromic behaviour (radical anion formation) upon UV irradiation

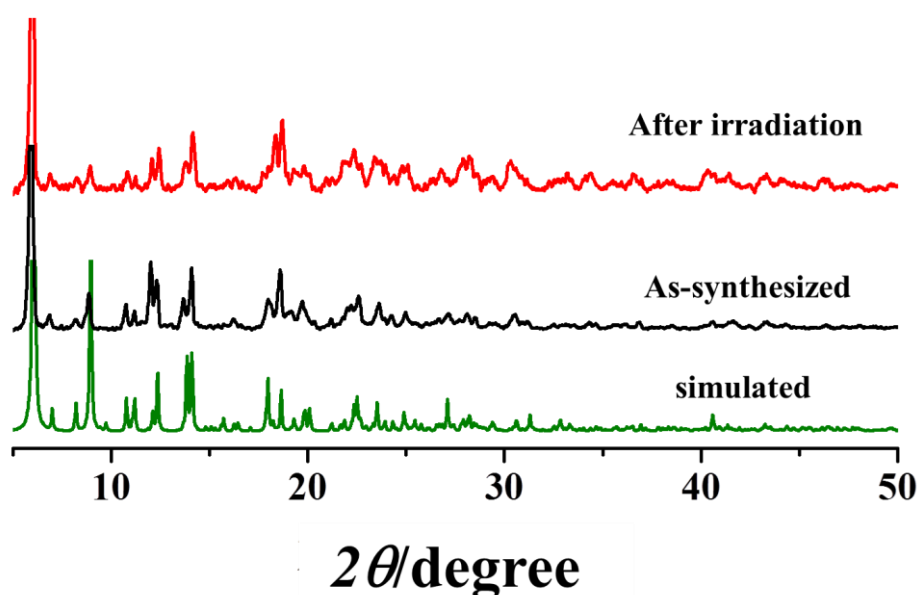


Figure 9: PXRD patterns of **1** in different states.

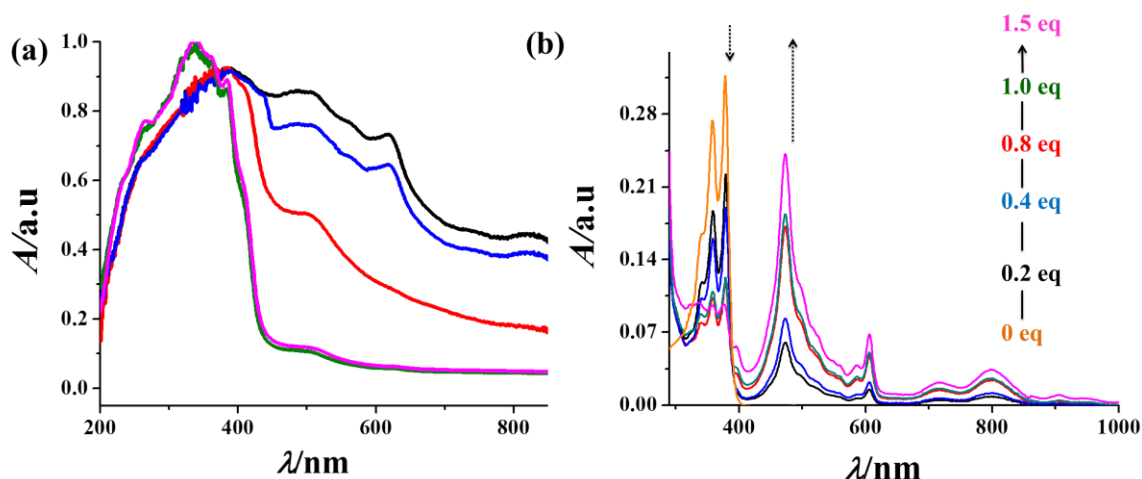


Figure 10: (a) Solid state UV-Visible spectra of **1** recorded in different time interval before and after UV irradiation. Green: before irradiation; black: after 15 min of irradiation; blue: after keeping the irradiated sample for two hours in ambient condition; red: keeping for four hours in ambient condition and purple: keeping for seven hours in ambient condition, (b) UV-Visible titration of bpNDI (10^{-4} M in DMF) with F^- (*t*-butylammonium fluoride) showing transition from bpNDI neutral form to bpNDI radical anion (considering 10^{-4} M concentration as 1 equivalent, F^- is added gradually).

due to the intramolecular photoinduced electron transfer from the pyridine N to the NDI aromatic core (Figure 12).^{7e} The PET mechanism operating in the free bpNDI linkers is reiterated from the fact that the diprotonated bpNDIH₂²⁺ showed no colour change upon irradiation. We envisage a similar diprotonated coordination environment for the bpNDI linker in the framework **1** after binding with Cd^{II}, and hence it is clear that the PET mechanism in the framework is quite different from that of the free linker molecule. Hence, we believe that the PET mechanism operating in the framework should be an intermolecular phenomenon, possibly between different strut molecules. Hence, control experiments were performed in order to understand the possible origins of the PET pathways. Interestingly, a 1:1 mixture of the biphenyldicarboxylate (bpdcNa₂) with bpNDIH₂²⁺ showed similar photochromic behaviour upon UV irradiation (Figure 13-15). These linkers mimic the coordination environment of the framework and the formation of the radical ion is again confirmed by the UV-Vis spectroscopy and EPR measurements (Figure 15-16). It is very important to note that UV irradiation of bpNDIH₂²⁺ and bpdcH₂ (1:1) mixture do not show any photochromic behaviour. These results clearly indicate that the photochromic behaviour in such systems is indeed due to an inter-strut photoinduced electron transfer process and in the present case, it is from the bpdc to the bpNDI acceptor linkers. This has been only possible because of the perfect orientation of the struts in the

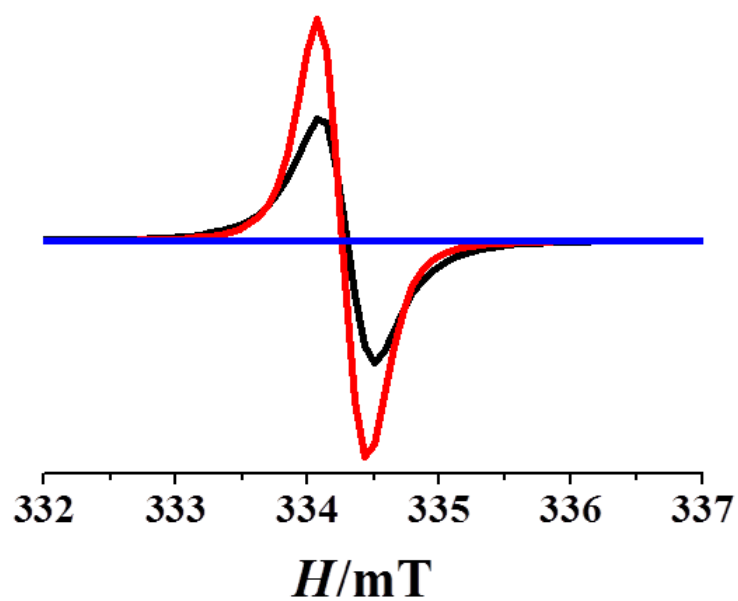


Figure 11: EPR spectra of **1**: blue: **1** without irradiation, black: 3 min, red: 7 min of irradiation.

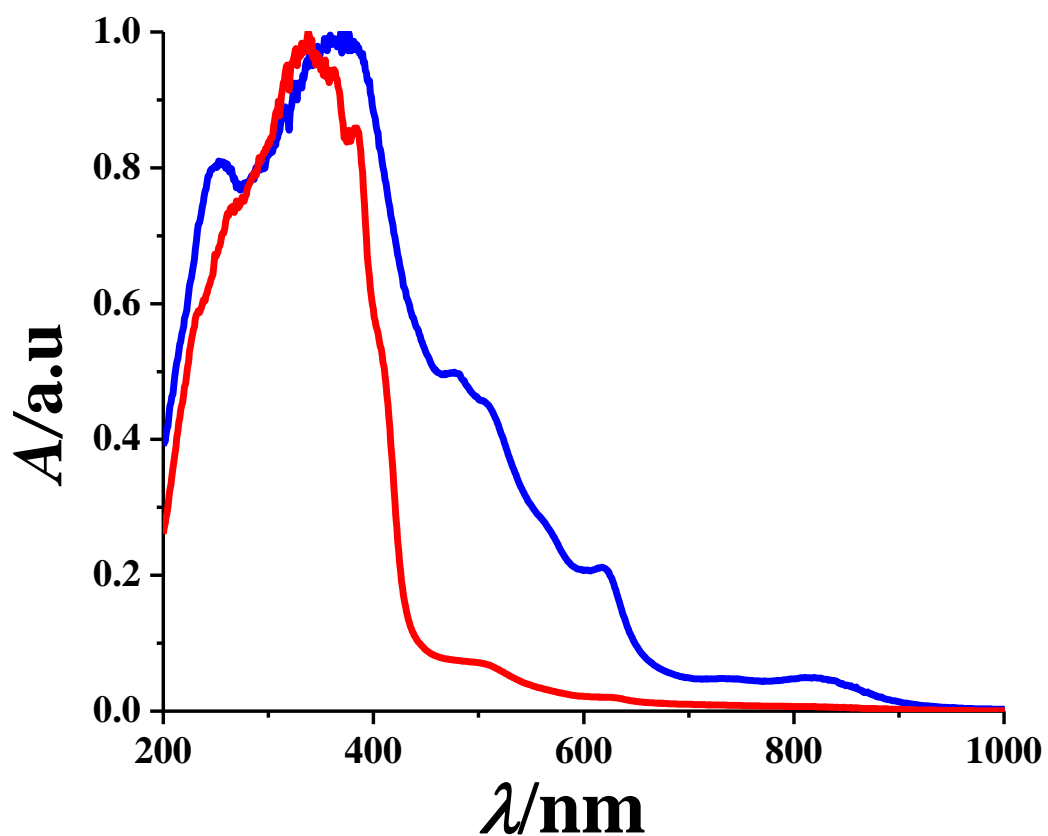


Figure 12: UV-Visible spectra of free bpNDI recorded in solid state before and after UV irradiation: red: bpNDI before irradiation and blue: bpNDI after 15 min irradiation.

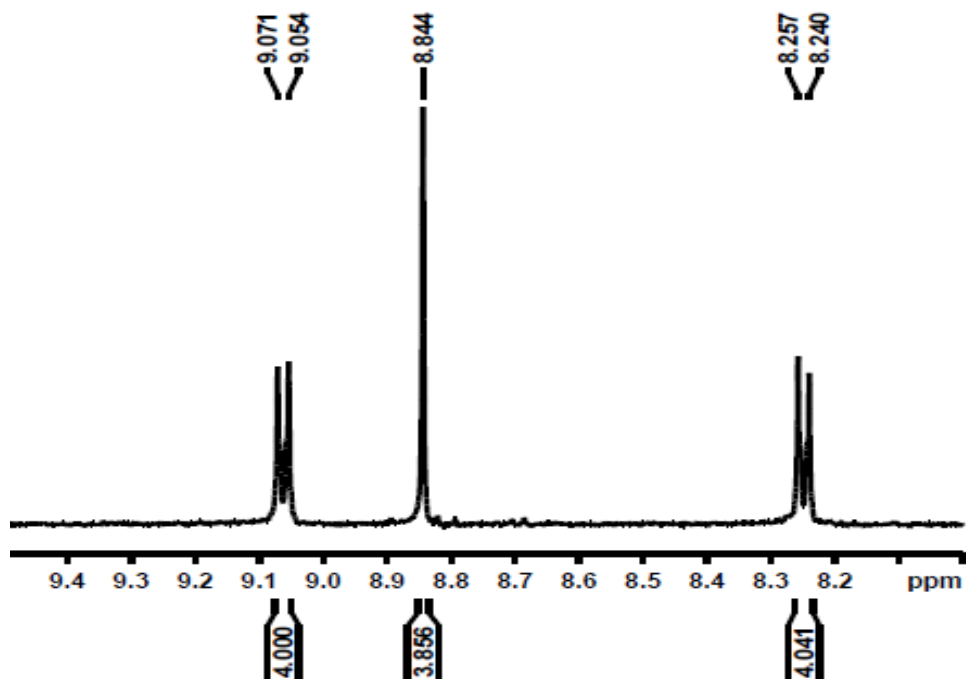


Figure 13: ^1H NMR spectra of bpNDIH_2^{2+} in D_2O .

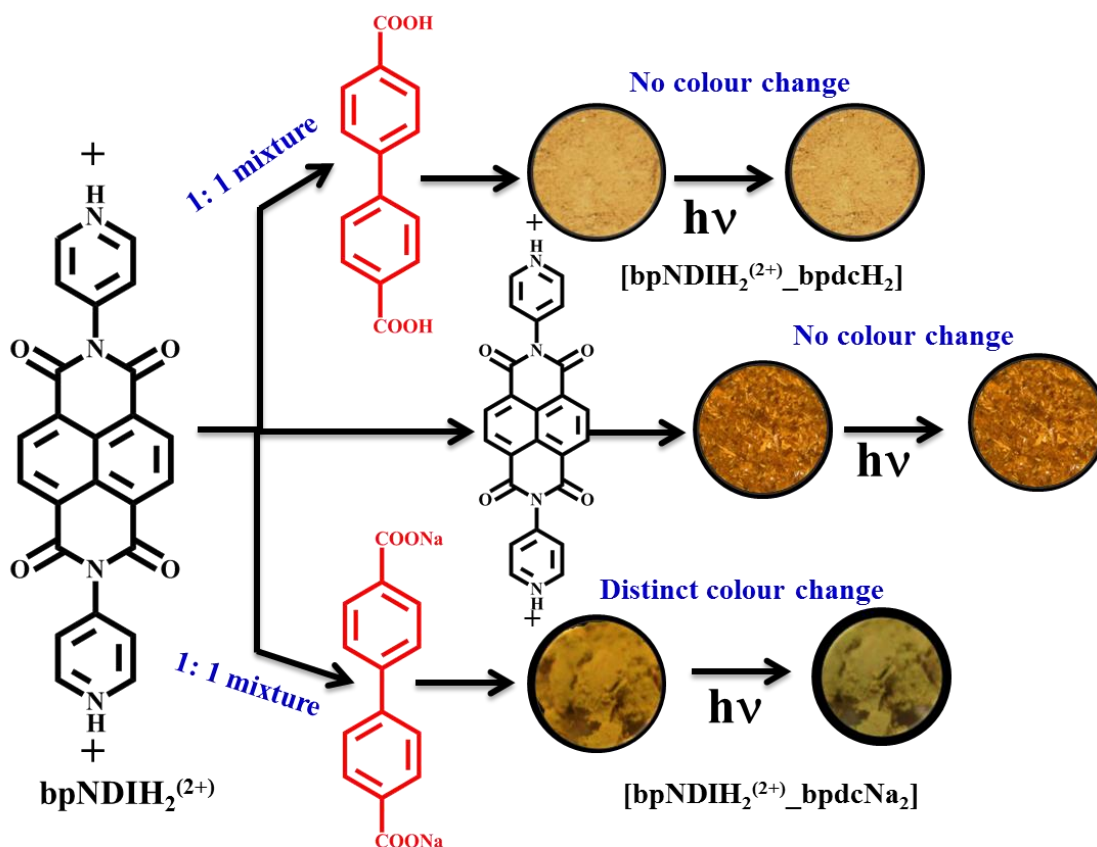


Figure 14: Control experiments: photographs of physical mixtures of different chromophores taken in solid state before and after UV irradiation (on 15 min of UV irradiation, 1:1 mixture of bpNDIH_2^{2+} _ bpdcH_2 or bpNDIH_2^{2+} _ bpNDIH_2^{2+} do not show any colour change whereas 1:1 mixture of bpNDIH_2^{2+} _ bpdcNa_2 shows colour change).

framework, credited to the $\{\text{Cd}_2(\mu_2\text{-OCO})_2\}_n$ SBU and the framework interpenetration which causes close contacts of the struts (Figure 8b, 17). The donor component in this PET process can be either the carboxylate oxygen of the bpdc or the bpdc chromophoric linker itself, which are located at distances of 3.9 and 2.59 Å, respectively from the electron deficient bpNDI linker (Figure 8b).^{18b} Although similar photochromic behaviour in NDI based MOFs has been ascribed to a so called “ π - π^* electron transfer”^{8d,8e}, we show here that the reduction of bpNDI acceptors to radical anion would indeed require a PET mechanism wherein the presence of an electron donor group/molecule is mandatory.

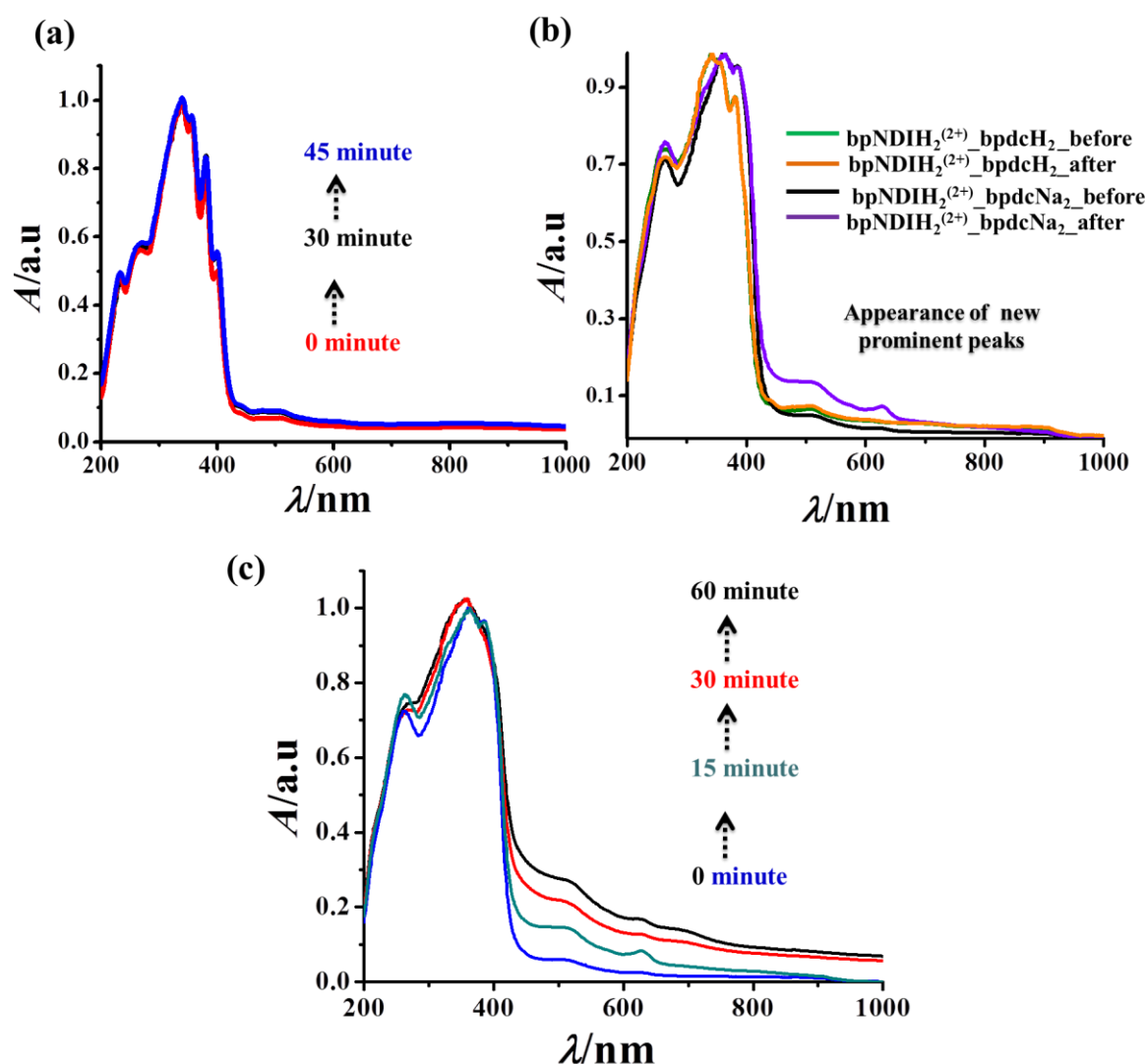


Figure 15: Control experiments: (a) time dependent solid state UV-Vis spectra of bpNDIH_2^{2+} (from 0 min to 45 min of irradiation), (b) solid state UV-Vis spectra of bpNDIH_2^{2+} _ bpdcH_2 and bpNDIH_2^{2+} _ bpdcNa_2 before/after UV irradiation, (c) time dependent solid state UV-Vis spectra of bpNDIH_2^{2+} _ bpdcNa_2 (from 0 min to 60 min of irradiation).

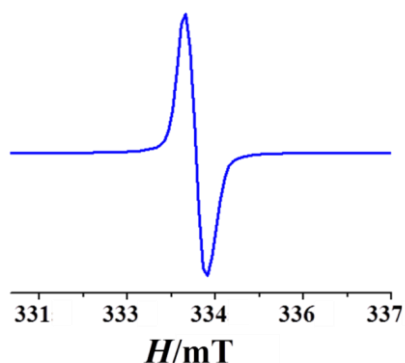


Figure 16: EPR spectra of bpNDIH₂²⁺ _ bpdCN a₂ after 15 min of UV irradiation.

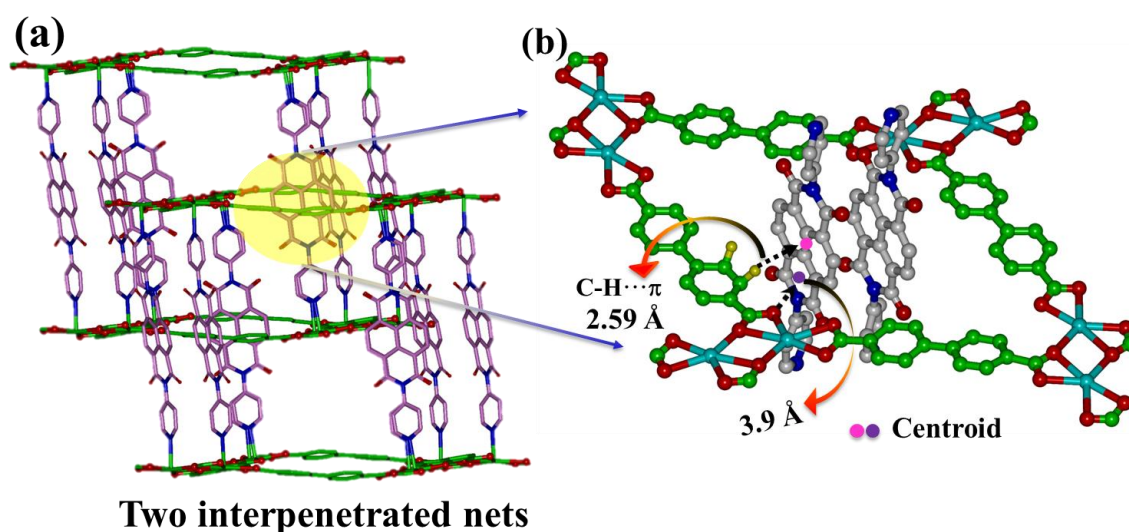


Figure 17: (a) Two interpenetrated nets of the 3D framework **1**, (b) closer view of the two nets showing non-covalent interactions between the linkers of two different nets suggesting the probable pathways for PET process.

3A.3.4 Guest encapsulation in the redox active framework **1**

Host-guest chemistry in luminescent, porous MOFs are of great interest as various bimolecular photophysical properties such as exciplex emission, charge-transfer or energy transfer processes can be modulated in a unique manner in the constrained spaces available inside the frameworks.^{2,5} We further envisaged guest induced modulation of the charge-transfer properties of this MOF with electron deficient channels. Here three different electron rich guest molecules such as 4,*N,N*-trimethylaniline (DMPT) and 1,5-/2,6-dinaphthol (1,5-/2,6-DAN) have been encapsulated successfully into **1'** (**1**@DMPT, **1**@1,5-DAN and **1**@2,6-DAN) and striking colour changes are immediately observed, from golden yellow to dark brown, green and dark green, respectively suggesting ground

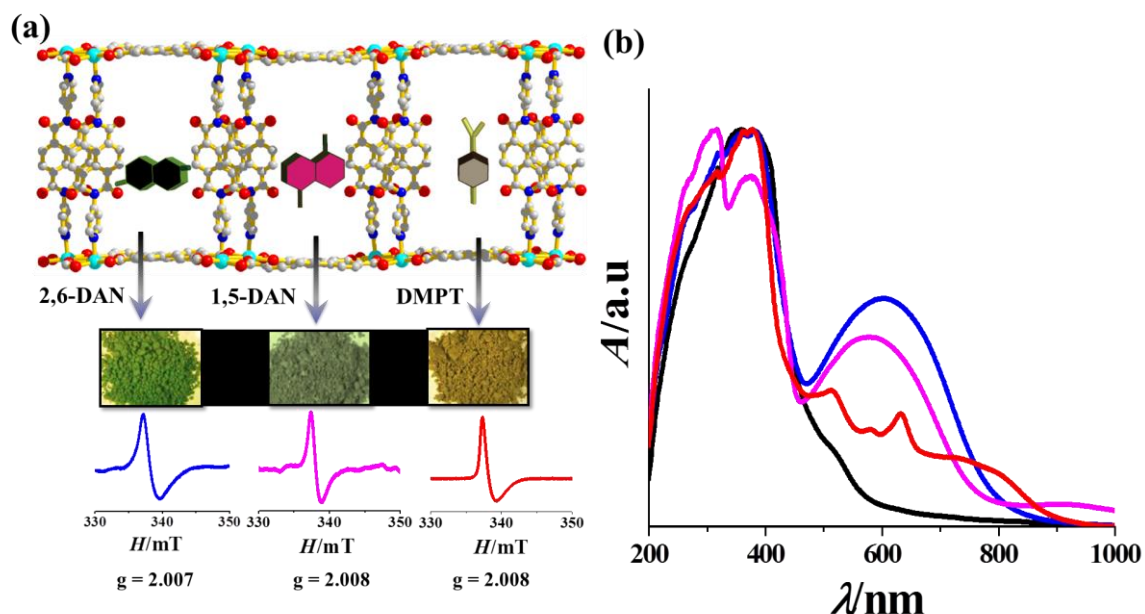


Figure 18: (a) Encapsulation of electron rich aromatic guest molecules (1,5-, 2,6-DAN and DMPT) in **1'** with corresponding colour change and EPR spectra [cyan = Cd^{II} , red = oxygen, grey: C atoms, blue N], (b) solid state UV-Vis spectra of **1** (black), **1@2,6-DAN** (blue), **1@1,5-DAN** (magenta) and **1@DMPT** (red).

state interactions between the host and guest chromophores (Figure 18). The guest loading is confirmed through ^1H NMR (Figure 3-5), TGA (Figure 1), PXRD (Figure 2) and elemental analyses. ^1H NMR spectra of the composites were recorded on digestion with DCl in DMSO-d_6 and confirmed the percentages of guest loading per formula unit are 100%, 90%, 98% for **1@DMPT**, **1@1,5-DAN** and **1@2,6-DAN**, respectively. Change in powder diffraction pattern of **1** on encapsulation also reiterates the successful loading of guest molecules. Furthermore, CO_2 adsorption isotherms (Figure 7b) for guest encapsulated composites **1@2,6-DAN**, **1@1,5-DAN** and **1@DMPT** were measured at 195 K. Expectedly both **1@2,6-DAN** and **1@1,5-DAN**, do not show any uptake of CO_2 up to 1 atm, unequivocally proving that the 2,6/1,5-DAN are occupied in the regular channel of **1**. But **1@DMPT** exhibits type I profile with total CO_2 uptake amount is $72 \text{ cm}^3 \text{ g}^{-1}$ (2.49 CO_2 molecules per formula unit) which is smaller compared to the framework **1'**. Probably DMPT being smaller in size leaves sufficient void space for further CO_2 inclusion. The dark colours of the three composites are indicative of ground state charge-transfer interactions and this is distinctly reflected in the appearance of broad bands in entire visible region of UV-Vis spectra (Figure 18b). Specifically for **1@DMPT**, bands are well resolved and the newly appeared bands at 513, 630, 728 and 792 nm can

be attributed to the radical anion of bpNDI suggesting a guest-to-host electron transfer process. Furthermore, EPR measurements were carried out and strong EPR signals were obtained for each case clearly confirming the fact of guest-to-host electron transfer (Figure 18). Hence, it can be stated that the occlusion of suitable guest molecules in the functionalized channels gives rise to extended co-facial arrangement between guest and the pillar of the host, hence reflecting the importance of confinement effect in a porous framework. It is worth mentioning that even after three to four months, the colour of the guest encapsulated compounds do not change and the EPR signals remain same suggesting long-lived charge-separated states of bpNDI and guest molecules.

3A.3.5 Electrochemical studies

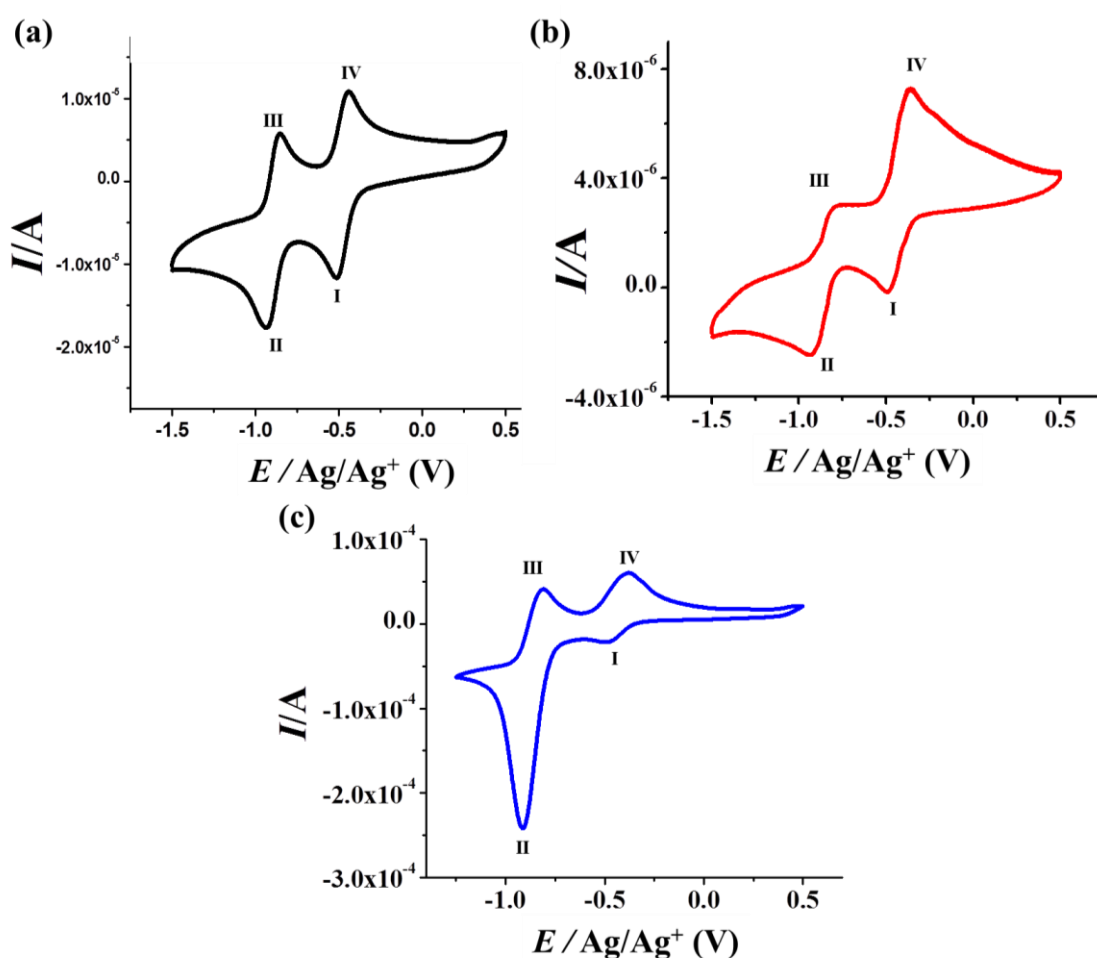


Figure 19: (a) Cyclic voltammogram of bpNDI, (b) CV of **1** and (c) **1@2,6-DAN** in 0.1 M TBAP in acetonitrile at a scan rate of 50 mV sec⁻¹.

Since the bpNDI linker is redox-active, electrochemical studies of the frameworks **1** and **1@2,6-DAN** were performed to test their chemical change after guest inclusion on

electrodes on passing electrical energy.^{7a,1119} The cyclic voltammogram of pristine bpNDI exhibits the existence of two sets of fully reversible redox peaks that correspond to $[\text{bpNDI}]^{0/\cdot-}$ at $E_{1/2} = -0.52$ V and $[\text{bpNDI}]^{\cdot-}/^{2-}$ at $E_{1/2} = -0.94$ V (Figure 19a). The redox peaks obtained in case of pure bpNDI retain even after formation of MOF ($[\text{bpNDI}]^{0/\cdot-}$ at $E_{1/2} = -0.49$ V and $[\text{bpNDI}]^{\cdot-}/^{2-}$ at $E_{1/2} = -0.94$ V), confirming that **1** is a redox-active porous framework (Figure 19b). But the feature is quasi-reversible in nature unlike pristine bpNDI,¹⁹ this might be due to the integrated bpNDI whose electronic environment is not same as free ligand. However drastic changes in the voltammogram of guest encapsulated **1@2,6-DAN** were observed when compared with pristine bpNDI and **1** (Figure 19c). The very small current density of peak I ($[\text{bpNDI}]^{0/\cdot-}$ at $E_{1/2} = -0.49$ V) compared to peak II ($[\text{bpNDI}]^{\cdot-}/^{2-}$ at $E_{1/2} = -0.91$ V) suggests that bpNDI is in a mono radical anion state formed by the electron transfer from 2,6-DAN. The small current density of peak I suggests that minute amount of bpNDIs are present in the system which are not involved in electron transfer process. This results further suggest the role of included guest (2,6-DAN) in the electron transfer process in guest loaded framework. The high peak current for peak II can be attributed to the combination of both electrochemical reduction and chemically generated mono anion radicals ($[\text{bpNDI}]^{0/\cdot-}$ and un-reduced bpNDI linker. In the next step, the potential scan is inverted and the presence of two anodic peaks correspond to oxidation of bpNDI^{2-} to $\text{bpNDI}^{\cdot-}$ followed by further oxidation of $\text{bpNDI}^{\cdot-}$ to bpNDI.

3A.4 Conclusion

In summary, this chapter describes synthesis and characterization of a multichromophoric 3D interpenetrated redox-active porous framework with a unique photoinduced inter-net strut-to-strut electron transfer characteristics. Furthermore, electron deficient and dynamic coordination spaces enabled facile encapsulation of different electron rich aromatic molecules that resulted into strut-to-strut long-lived charge-separated state in the ground state. The unique ability of such multichromophoric system to encapsulate various guest molecules with electron transfer response holds a great promise for designing novel functional redox-active materials. Therefore, such host materials can alter the physical and chemical properties in presence of guest molecules in their cavities, thereby, giving room of finding new phenomenon with potential applications in sensing, charge-transport and photocatalysis.

3A.5 References

1. (a) N. Kishi, M. Akita, M. Yoshizawa, *Angew. Chem. Int. Ed.* **2014**, *53*, 3604 (b) A. P. H. J. Schenning, E. W. Meijer, *Chem. Commun.* **2005**, 3245 (c) M. Kumar, K. V. Rao, S. J. George, *Phys.Chem.Chem.Phys.* **2014**, *16*, 1300.
2. (a) M. V. Suresh, S. J. George, T. K Maji, *Adv. Funct. Mater.* **2013**, *23*, 5585 (b) R. Haldar, K. V. Rao, S. J. George, T. K. Maji, *Chem. Eur. J.* **2012**, *18*, 5848 (c) C. Y. Lee, O. K. Farha, B. J. Hong, A. A. Sarjeant, S. T. Nguyen, J. T. Hupp, *J. Am. Chem. Soc.* **2011**, *133*, 15858 (d) T. Zhang, W. Lin, *Chem. Soc. Rev.* **2014**, *43*, 5982 (e) K. V. Rao, K. K. R. Datta, M. Eswaramoorthy, S. J. George, *Chem. Eur. J.* **2012**, *18*, 2184 (f) K. V. Rao, A. Jain, S. J. George, *J. Mater. Chem. C* **2014**, *2*, 3055 (g) Y. Cui, Y. Yue, G. Qian, B. Chen, *Chem. Rev.* **2012**, *112*, 1126 (h) C.Y. Sun, X. L. Wang, X. Zhang, C. Qin, P. Li, Z.M. Su, D.X. Zhu, G. G. Shan, K. Z. Shao, H. Wu, J. Li, *Nat. Commun.* **2013**, *4*, 2717.
3. (a) M. Li, D. Li, M. O'Keefe, O. M. Yaghi, *Chem. Rev.* **2014**, *114*, 1343 (b) T. Enoki W. Lin, *Chem. Soc. Rev.* **2014**, *43*, 5982.
4. (a) J. R. Li, J. Sculley, H. C. Zhou, *Chem. Rev.* **2012**, *112*, 869 (b) L. E. Kreno, K. Leong, O. K. Farha, M. Allendorf, R. P. V. Duyne, J. T. Hupp, *Chem. Rev.* **2012**, *112*, 1105 (c) J. Shi, Y. Jiang, X. Wang, H. Wu, D. Yang, F. Pan, Y. Suad, Z. Jiang, *Chem. Soc. Rev.* **2014**, *43*, 5192 (d) M. Yoon, R. Srirambalaji, K. Kim, *Chem. Rev.* **2012**, *112*, 1196 (e) M. D. Allendorf, C. A. Bauer, R. K. Bhakta, R. J. T. Houk, *Chem. Soc. Rev.* **2009**, *38*, 1330 (f) S. Roy, A. Chakraborty, T. K. Maji, *Coord. Chem. Rev.* **2014** *273*, 139 (g) R. Haldar, S. K. Reddy, V. M. Suresh, S. Mohapatra, S. Balasubramanian, T. K. Maji, *Chem. Eur. J.* **2014**, *20*, 4347 (h) A. Hazra, S. Bonakala, S. K. Reddy, S. Balasubramanian, T. K. Maji, *Inorg. Chem.* **2013**, *52*, 11385 (i) R. Haldar, N. Sikdar, T. K. Maji, *Mater. Today* **2015**, *18*, 97 (j) J. C. Tan, A. K. Cheetham, *Chem. Soc. Rev.* **2011**, *40*, 1059 (k) J. M. Taylor, R. Vaidhyanathan, S. S. Iremonger, G. K. H. Shimizu, *J. Am. Chem. Soc.* **2012**, *134*, 14338.
5. (a) N. Yanai, K. Kitayama, Y. Hijikata, H. Sato, R. Matsuda, Y. Kubota, M. Takata, M. Mizuno, T. Uemura, S. Kitagawa, *Nat. Mat.* **2011**, *10*, 787 (b) D. Tanaka, S. Horike, M. Ohba, M. Hasegawa, Y. Ozawac, K. Toriumi, S. Kitagawa, *Chem. Commun.* **2007**, 3142 (c) R. Haldar, R. Matsuda, S. Kitagawa, S. J. George and T. K.

- Maji, *Angew. Chem. Int. Ed.* **2014**, *126*, 11966 (d) H. Sato, R. Matsuda, K. Sugimoto, M. Takata, S. Kitagawa, *Nat. Mater.* **2010**, *9*, 661.
6. (a) T. Enoki, A. Miyazaki, *Chem. Rev.* **2004**, *104*, 5449 (b) Q. Ye, Y. Song, G. Wang, K. Chen, D. Fu, P. W. H. Chan, J. Zhu, S. D. Huang, R. Xiong, *J. Am. Chem. Soc.* **2006**, *128*, 6554.
7. (a) G. Andric, J. F. Boas, A. M. Bond, G. D. Fallon, K. P. Ghiggino, C. F. Hogan, J. A. Hutchison, M. A. P. Lee, S. J. Langford, J. R. Pilbrow, G. J. Troup, C. P. Woodward, *Aust. J. Chem.* **2010**, *57*, 1011 (b) Z. Song, H. Zhan, Y. Zhou, *Angew. Chem. Int. Ed.* **2010**, *49*, 8444 (c) C. R. Wade, M. Li, M. Dincă, *Angew. Chem. Int. Ed.* **2013**, *52*, 13377 (d) Y. Wu, M. Frasconi, D. M. Gardner, P. R. McGonigal, S. T. Schneebeli, M. R. Wasielewski, J. F. Stoddart, *Angew. Chem. Int. Ed.* **2014**, *126*, 9630 (e) Y. Matsunaga, K. Goto, K. Kubono, K. Sako, T. Shinmyozu, *Chem. Euro. J.* **2014**, *20*, 7309 (f) T. Takada, Y. Otsuka, M. Nakamura, K. Yamana, *RSC Adv.* **2014**, *4*, 59440 (g) A. Das, M. R. Molla, B. Maity, D. Koley, S. Ghosh, *Chem. Eur. J.* **2012**, *18*, 9849.
8. (a) Y. Takashima¹, V. M. Martínez, S. Furukawa, M. Kondo, S. Shimomura, H. Uehara, M. Nakahama, K. Sugimoto, S. Kitagawa, *Nat. Commun.* **2011**, *2*, 168 (b) B. Q. Ma, K. L. Mulfort, J. T. Hupp, *Inorg. Chem.* **2005**, *44*, 4912 (c) V. M. Martínez, S. Furukawa, Y. Takashima, I. L. Arbeloa, S. Kitagawa, *J. Phys. Chem. C*, **2012**, *116*, 26084 (d) L. Han, L. Qin, L. Xu, Y. Zhou, J. Sunb, X. Zou, *Chem. Commun.* **2013**, *49*, 406 (e) A. Mallick, B. Garai, M. Addicoat, P. S. Petkov, T. Heine, R. Banerjee, *Chem. Sci.* **2015**, *6*, 1420 (f) Y. Takashima, S. Furukawa, S. Kitagawa, *CrystEngComm*, **2011**, *13*, 3360.
9. P. H. Dinolfo, M. E. Williams, C. L. Stern, J. T. Hupp, *J. Am. Chem. Soc.* **2004**, *126*, 12989.
10. SMART (V 5.628), SAINT (V 6.45a), XPREP, SHELXTL; Bruker AXS Inc. Madison, Wisconsin, USA, **2004**.
11. G. M. Sheldrick, Siemens Area Detector Absorption Correction Program, University of Göttingen, Göttingen, Germany, **1994**.
12. A. Altomare, G. Cascarano, C. Giacovazzo, A. Gualaradi, *J. Appl. Cryst.* **1993**, *26*, 343–350.

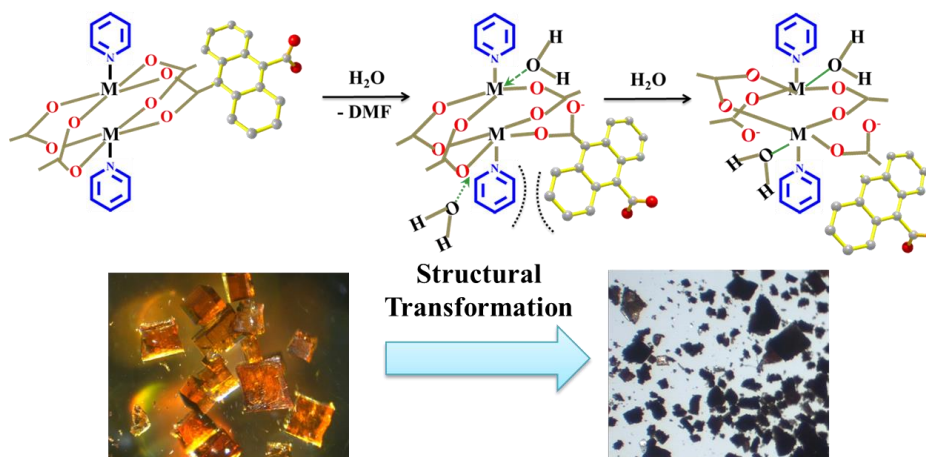
13. G. M. Sheldrick, SHELXL-97, Program for Crystal Structure Solution and Refinement; University of Göttingen, Göttingen, Germany, **1997**.
14. A. L. Spek, *J. Appl. Cryst.* **2003**, *36*, 7.
15. G. M. Sheldrick, SHELXS 97, Program for the Solution of Crystal Structure, University Göttingen, Germany, **1997**.
16. L. J. Farrugia, WinGX-A Windows Program for Crystal Structure Analysis, *J. Appl. Cryst.* **1999**, *32*, 837.
17. N. Sikdar, A. Hazra, T. K. Maji, *Inorg. Chem.* **2014**, *53*, 5993.
18. (a) S. Guha, S. Saha, *J. Am. Chem. Soc.* **2010**, *132*, 17674. (b) Y. Zeng, Z. Fu, H. Chen, C. Liu, S. Liaoa, J. Dai, *Chem. Commun.* **2012**, *48*, 8114.
19. (a) P. M. Usov, C. Fabian, D. M. D'Alessandro, *Chem. Commun.* **2012**, *48*, 3945 (b) C. F. Leong, B. Chan, T. B. Faust, P. Turner, D. M. D'Alessandro, *Inorg. Chem.* **2013**, *52*, 14246.

Chapter 3B

*Redox-Active 3D Charge Transfer
MOF: Solvent Responsive Reversible
Strut-to-Strut Electron Transfer*

Chapter 3B

Redox-Active 3D Charge Transfer MOF: Solvent Responsive Reversible Strut-to-Strut Electron Transfer



Summary: This chapter describes synthesis, structural characterization, and photophysical properties of a pillared layer framework $\{Zn_2(adc)_2(bpNDI)\cdot 4H_2O\cdot 4DMF\}_n$ (**1**) [$H_2adc = 9,10$ -anthracenedicarboxylic acid, $bpNDI = N,N'$ -di(4-pyridyl)-1,4,5,8-naphthalenediimide]. Framework **1**, built with paddle-wheel type secondary building units (SBUs), readily undergoes guest responsive structural transformation as evident by PXRD recorded at different time intervals. In depth investigations by TGA, 1H NMR, FT-IR and Raman spectroscopy revealed that this structural transformation can be attributed to the disruption of paddle-wheel $\{Zn_2(\mu-OCO)_4\}$ units in **1** due to partial hydration to the metal centers. Compound **1** shows charge transfer (CT) interaction between orthogonally oriented donor adc and acceptor $bpNDI$ linkers. However, complete long-lived charge separated state (electron transfer; ET) has been achieved upon desolvation due to spatial reorganization of adc and $bpNDI$ chromophoric linkers as supported by PXRD, EPR and spectroelectrochemical studies. This is the first account of guest responsive reversible strut-to-strut CT-to-ET interactions in a redox-active framework.

N. Sikdar, T. K. Maji, Manuscript under preparation

3B.1 Introduction

Understanding of energy and electron transfer processes in self-assembled systems is crucial for the development of light emitting devices, photovoltaics and artificial light harvesting systems.^{1a-c} The spatial organization, stoichiometry and distances between the donor-acceptor chromophores control the overall efficiency of electron transfer to afford the long-lived charge separated state.^{1a-c} Different noncovalent approaches (like π - π stacking, H-bonding, chiral auxiliaries) or covalent bonding between D-A chromophores were documented in organic self-assembled supramolecular nanostructures with prolong life time of excitons.^{1d-e} In this context coordination driven self-assembly of two different D-A chromophoric organic linkers toward fabrication of photoactive metal-organic frameworks (MOFs) would be another design strategy to afford long-lived charge separated state. Here charge recombination would be inhibited due to the periodic organization of D-A pair associated by hydrogen bonding or π -stacking in the extended structure which is paramount for photovoltaic application.^{1d-e}

Metal-organic frameworks (MOFs) are crystalline porous materials with tunable structural topology, modifiable pore surface and surface area.²⁻³ One of the most intriguing characteristics of MOFs is structural flexibility with response to different external stimuli like temperature, pressure and light.²⁻³ Thus, design of programmable framework structure with complex molecular functionality is the key to fabricate materials with tailorable properties. Reversible structural transformation with response to specific guest molecules is of paramount importance for selective encapsulation/separation, molecular recognition and sensing application.⁴⁻⁶ MOFs composed of mixed chromophoric linkers with electron donor and acceptor properties are underexplored.⁷ Such MOFs would provide a platform to study the opto-electronic properties and find applications in photo-voltaic, artificial light harvesting antennae and photo-conductivities.⁸ Furthermore, porosity of the framework would allow for non-covalent encapsulation of suitable guests for energy transfer application and also a long lived charge-separated state can be achieved based on electron transfer between host and suitable guest molecule. In MOF recently, we have documented reversible photo-induced strut-to-strut and unidirectional guest-to-strut electron transfer (ET) in a mixed chromophoric entangled framework, however specific guest responsive reversible strut-

to-strut electron transfer is yet to be realized.⁷ We envisage that manipulating the organization and distances between D-A building units is fundamentally crucial for stabilizing complete charge separated state in MOF.⁷ Guest responsive structural reorganization of linkers is common in 3rd generation MOF materials, and such rearrangement of the chromophoric linkers can induce significant change in magnetism or opto-electronic properties of the MOF materials, such studies are unexplored.

Unlike the work mentioned in chapter 2 and 3A, here, bulky anthracene dicarboxylate (adcH₂) linker has been strategically used to avoid the possibility of entanglement in the 3D net. Using adc and bpNDI as donor-acceptor linker, respectively, a new redox-active 3D framework {Zn₂(adc)₂(bpNDI)}·4H₂O·4DMF}_n (**1**) [H₂adc = 9,10-anthracenedicarboxylic acid, bpNDI = *N,N'*-di(4-pyridyl)-1,4,5,8-naphthalenediimide] has been synthesized. In the as-synthesized compound **1**, donor adc chromophore and acceptor bpNDI form a ground state charge transfer (CT) complex due to their orthogonal spatial disposition. Upon removal of the guest DMF molecules framework shows significant structural transformation driven by the deformation of paddle-wheel Zn₂(COO)₄ SBU. Such structural change resulted a long-lived stable charge separated state in **1** based on electron transfer from adc to bpNDI linker at ambient condition. Detailed PXRD, TGA, ¹HNMR, spectro-electrochemistry and different spectroscopic (IR, EPR and Raman) studies corroborated the structural change and concomitant guest responsive reversible electron transfer phenomenon in framework **1**. To the best our knowledge this is first report of this kind in MOF system.

3B.2 Experimental section

3B.2.1 Materials

All the reagents employed were commercially available and used as provided without further purification. Zn(NO₃)₂·6H₂O was obtained from Spectrochem. 9, 10-anthracenedicarboxylic acid (adc), anhydrous acetonitrile (CH₃CN), [(*n*-Bu)₄N]PF₆ (TBAP) were obtained from Sigma Aldrich chemicals. *N,N'*-di(4-pyridyl)-1,4,5,8-naphthalenediimide (bpNDI) was synthesized following the literature procedure.⁹

3B.2.2 Physical measurements

Elemental analyses were carried out using a Thermo Fischer Flash 2000 Elemental Analyzer. Thermogravimetric analyses (TGA) were carried out on METLER TOLEDO TGA850 in nitrogen atmosphere (flow rate = 50 mL min⁻¹) in the temperature range of 30–700 °C (heating rate 3 °C min⁻¹). Powder XRD patterns of compound **1** were recorded by Bruker D8 Discover (operating at 40 kV and 30 mA) using Cu-K_α radiation. FT-IR spectra were recorded on a Bruker IFS 66v/S spectrophotometer using KBr pellets in the region 4000-400 cm⁻¹. Electronic absorption and emission spectra were recorded on a Perkin Elmer Lambda 900 UV-VIS-NIR Spectrometer and Perkin Elmer Ls 55 Luminescence Spectrometer, respectively. ¹H NMR spectra were measured in a Bruker AVANCE 400 (400 MHz) Fourier transform ¹H NMR spectrometer with chemical shifts reported in parts per million (ppm). For EPR spectra measurements, Bruker EMX spectrometer has been used in the X-band operating at 9.43 GHz. Raman spectra of samples were recorded by using a 632 nm He-Ne laser on a Jobin Yvon LabRam HR spectrometer.

3B.2.3 X-ray crystallography

X-ray single-crystal diffraction data of **1** was collected on a Bruker D8 VENTURE equipped with a microfocus X-ray source with graphite monochromated Mo-K_α radiation ($\lambda = 0.71073 \text{ \AA}$) operating at 50 kV and 30 mA. A crystal of suitable size was chosen, covered with paratone oil and mounted in a glass capillary of size 0.5 mm. The data were collected at 293 K. The program SAINT¹⁰ was used for integration of diffraction profiles and absorption correction was made with SADABS program.¹¹ The crystal structure was solved by SIR 92¹² and refined by full matrix least square method using SHELXL-97.¹³ All the hydrogen atoms were fixed by HFIX and placed in ideal positions. Potential solvent accessible area or void space was calculated using the PLATON multipurpose crystallographic software. All crystallographic and structure refinement data of **1** are summarized in Table 1. All calculations were carried out using SHELXL 97,¹⁴ PLATON¹⁵ and WinGX system, Ver 1.70.01.¹⁶ The details of bond distances and bond angles are summarized in Table 2-3.

3B.2.4 Electrochemical studies

All the electrochemical measurements were recorded on an electrochemical workstation (CHI760E). Electrochemical measurements were carried out in conventional three electrode system where in compound coated glassy carbon electrode acts as a working electrode, large Pt foil and Ag wire act as auxiliary and reference electrodes, respectively. A known amount (7 mg) of bpNDI/1 was dispersed in 1 mL of ethanol and 20 μ L of Nafion solution for 30 min. A 20 μ L aliquot of the above dispersion was drop casted onto pre-cleaned glassy carbon electrode and dried under ambient conditions for fabrication of working electrode. Electrochemical measurements were performed in distilled acetonitrile under N_2 saturated conditions. 0.1 M TBAP ($[(n\text{-Bu})_4\text{N}]\text{PF}_6$) acts as a supporting electrolyte.

UV-Vis spectroelectrochemistry (SEC) data are collected using a JAZ portable extended range UV/VIS preconfigured spectrometer (JAZ-EL200-XR1). Electrochemical experiments are performed in a plastic cuvette with a Teflon SEC cell comprising three side arms for accommodating a platinum-wire auxiliary electrode and an Ag/Ag^+ wire quasi-reference electrode and indium-tin oxide (ITO) coated quartz slide working electrode. Experiments are done in 0.1 M TBAP/ CH_3CN solution. Bulk Electrolysis with Coulometry (BE) technique is applied at desired potential range for recording data.

3B.2.5 Adsorption study

The adsorption isotherms of N_2 (at 77 K) and CO_2 (at 195 K) using the desolvated samples of **1** (**1'**) was measured by using AUTOSORB IQ2 instrument. Compound **1** was activated at 160 $^\circ\text{C}$ under 1×10^{-1} Pa vacuum for about 8 h prior to measurement of the isotherms. Helium gas (99.999% purity) at a certain pressure was introduced in the gas chamber and allowed to diffuse into the sample cell by opening the valve. The amount of gas adsorbed was calculated readily from pressure difference ($P_{\text{calc}} - P_e$), where P_{calc} is the calculated pressure with no gas adsorption and P_e is the observed equilibrium pressure. All operations were computer-controlled and automatic.

3B.2.6 Syntheses of $\{\text{Zn}_2(\text{adc})_2(\text{bpNDI})\} \cdot 4\text{H}_2\text{O} \cdot 4\text{DMF}\}_n$ (**1**)

A mixture containing $\text{Zn}(\text{NO}_3)_2 \cdot 6\text{H}_2\text{O}$ (0.008 g, 0.025 mmol), H_2adc (0.007 g, 0.025 mmol) and bpNDI (0.006 g, 0.025 mmol) was suspended in DMF (4 mL) and

heated to 120 °C for a period of 2 days. Dark orange colored crystals of **1** were then collected and washed with DMF for three times. Yield: 80 % (**1**) with respect to metal. Elemental analysis for **1** calcd. (%) for $\text{Zn}_2\text{C}_{68}\text{O}_{20}\text{H}_{48}\text{N}_8$: C: 53.28; H: 4.09; N: 9.56; Found C: 53.97; H: 3.72; N: 9.91. FT-IR (4000–400 cm^{-1}): 3684 (w), 3065 (w), 2924 (w), 1741 (s), 1704 (s), 1623 (s), 1609 (w), 1575 (s), 1512 (w), 1444 (s), 1430 (s) cm^{-1} .

3B.3 Results and discussion

3B.3.1 Crystal structure description of $\{\text{Zn}_2(\text{adc})_2(\text{bpNDI})\} \cdot 4\text{H}_2\text{O} \cdot 4\text{DMF}\}_n$ (**1**)

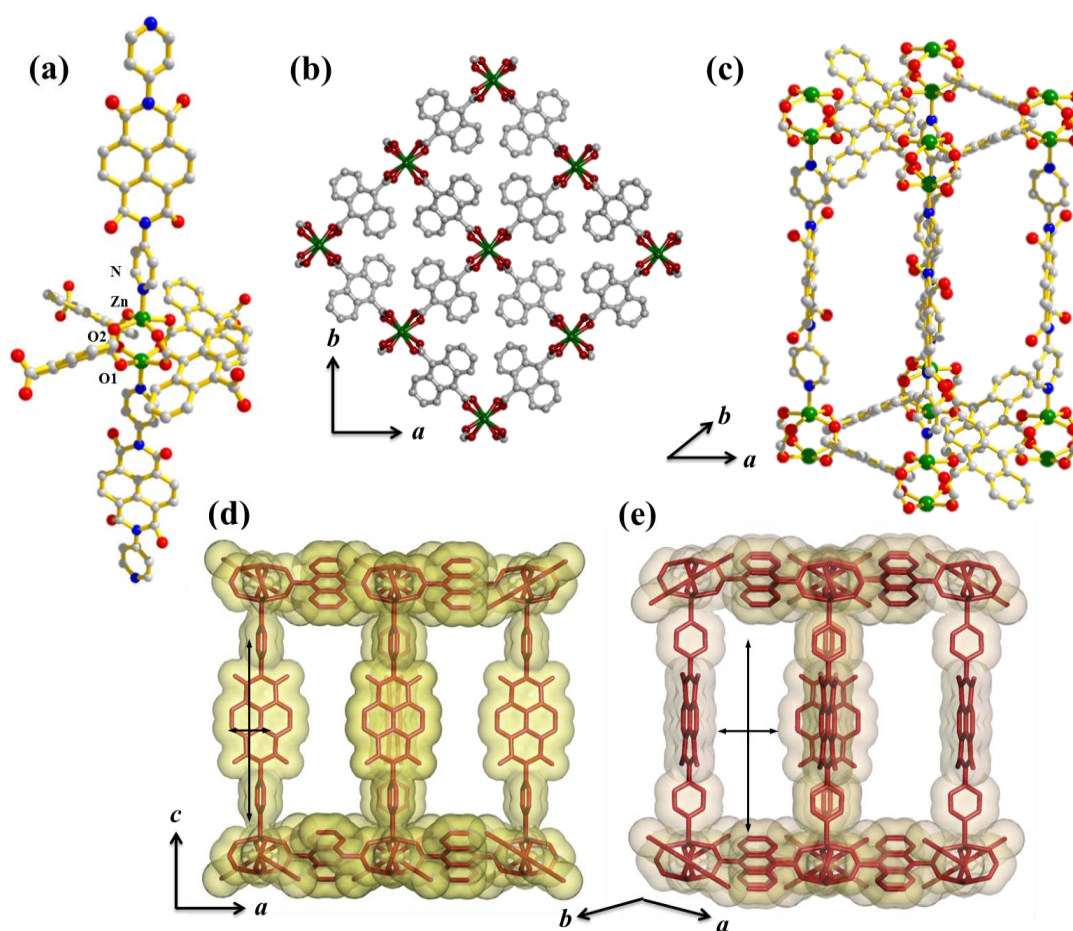


Figure 1: (a) Coordination environment of Zn^{II} in **1**, (b) 2D layer of **1**, (c) formation of 3D framework by pillaring the 2D sheets with bpNDI linkers for **1**, (d) pore view of **1** along b -direction and (e) $[101]$ direction, respectively.

Single crystal X-ray diffraction analysis suggests that **1** crystallizes in orthorhombic $Ibam$ space group. **1** has a non-catenated pillared layer 3D structure with α -

Polonium topology. Here, a paddle wheel type $\{\text{Zn}_2(\text{COO})_4\}$ secondary building unit (SBU) (Figure 1a) act as nodes and these are connected by the adc linkers to construct 2D network along ab plane (Figure 1b). These 2D layers are further pillared by the bpNDI linker through pyridyl-N along c direction to generate a 3D framework (Figure 1c). The Zn-O and Zn-N bond distances of **1** are in the range of 2.029(4) and 2.049(3) Å, respectively. Framework **1** shows bidirectional channels and the corresponding channel sizes are $3.2 \times 14.8 \text{ \AA}^2$ and $4.5 \times 13.7 \text{ \AA}^2$ along (101 plane) and b direction, respectively (Figure 1d-e). The channels are filled with guest DMF and water molecules as confirmed from TGA (Figure 3a), $^1\text{H NMR}$ (Figure 3b), and elemental analyses. Calculation using PLATON suggests the presence of void volume of $\sim 6682 \text{ \AA}^3$ (64 %) for **1** upon complete removal of guest molecules.

Table 1. Crystal data and structure refinement parameters of **1**.

Parameters	Compound 1
Empirical formula	$\text{C}_{34}\text{H}_{24}\text{ZnN}_4\text{O}_{10}$
Formula weight	711
Crystal system	Orthorhombic
Space group	<i>Ibam</i>
a , Å	15.2753(9)
b , Å	15.3070(8)
c , Å	44.471(3)
α , deg	90.00
β , deg	90.00
γ , deg	90.00
V , Å ³	10398.0(10)
Z	8
T , K	293
μ , mm ⁻¹	0.513
D_{calcd} , g/cm ³	0.910
$F(000)$	2918
Reflections [$I > 2\sigma(I)$]	3615
Total reflections	6543
Unique reflections	1268
$\lambda(\text{Mo-K}\alpha)$	0.71073
R_{int}	0.0721
GOF on F^2	1.267
$R_1 [I > 2\sigma(I)]^a$	0.0915
$R_w [\text{all data}]^b$	0.3440

$$^a R_1 = \frac{\sum ||F_o| - |F_c||}{\sum |F_o|}, \quad ^b R_w = \left[\frac{\sum \{w(F_o^2 - F_c^2)^2\}}{\sum \{w(F_o^2)\}} \right]^{1/2}$$

Table 2. Selected bond lengths (Å) for **1**.

Zn-O2	2.029(4)	Zn-O1	2.029(4)	N-Zn	1.996(8)
-------	----------	-------	----------	------	----------

Table 3. Selected bond angles (°) for **1**.

N-Zn-O2	102.17(12)	N-Zn-O1	100.31(12)	O2-Zn-O2	155.7(2)
O2-Zn-O1	88.08(14)	O2-Zn-O1	87.59(14)	O1-Zn-O1	159.4(2)

3B.3.2 PXRD, thermal stability and ¹HNMR analyses

The PXRD pattern of the as-synthesized **1** has been recorded immediately after taking out the crystals from the mother solution (Figure 2a). The sharp Bragg's diffraction peaks and well correspondence with the simulated pattern indicate highly crystalline nature and high purity of the sample. Distinct changes are observed in PXRD when the crystals were kept in open atmosphere (Figure 2b). After keeping the crystals for two hours (designated as **1_2h**) in an open atmosphere, a significant change is noticed, in particular the relative intensity of (200) peak decreases although the overall pattern remains same. However, (200) diffraction completely disappear on keeping the crystal for 24 hour (designated as **1_24h**) suggesting significant reorientation in the framework structure. Re-soaking the crystals (**1_DMF dipped**) in fresh DMF produces a PXRD pattern similar to that of as-synthesized one, suggesting reversibility in structural transformation. Further insight on the structure of compound **1** suggests that (200) plane at 2θ of 3.97° belongs to a 2D plane containing 2D $\{\text{Zn}(\text{adc})\}_n$, and disappearance of (200) plane suggest changes in Zn-adc spatial conformation. These results clearly confirm that **1** undergoes structural transformation when kept in open atmosphere at ambient condition for long time. Furthermore bright golden-orange colour of the crystals transform to brown crystals in open atmosphere as observed in optical images recorded at different time interval clearly suggest significant reorientation in the packing of the chromophoric linkers in the crystals (Figure 2b).

Thermogravimetric analysis (TGA) of **1** shows a total 28.5 % (cald. 28.9 %) weight loss in the temperature range of 150-200 °C, corresponding to four DMF and four water molecules. Presence of water molecules can be confirmed from IR spectroscopy. After keeping for two hour, **1_2h** shows a total 12.9 % weight loss for two guest DMF

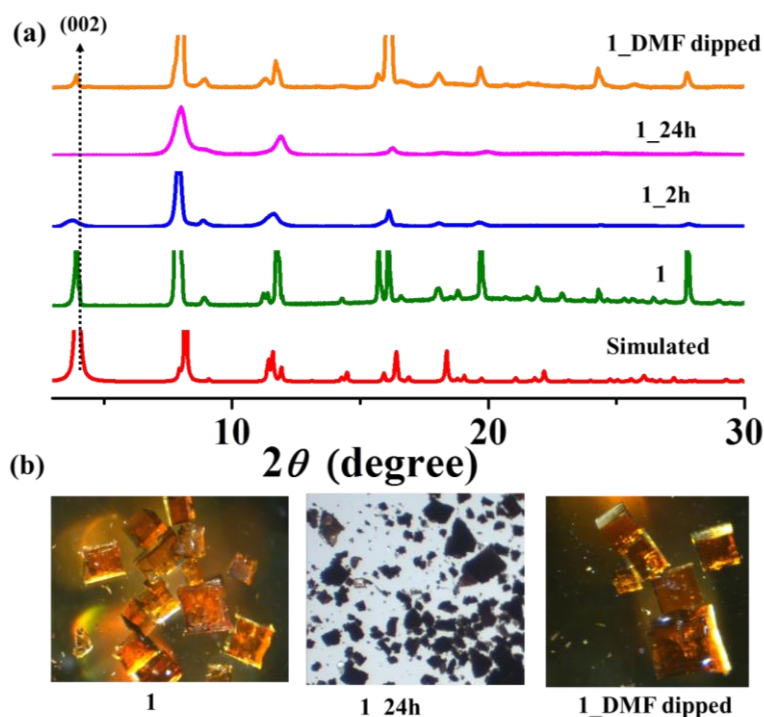


Figure 2: (a) PXRD patterns of **1** recorded under different condition, (b) optical images of single crystals of **1** recorded at different states.

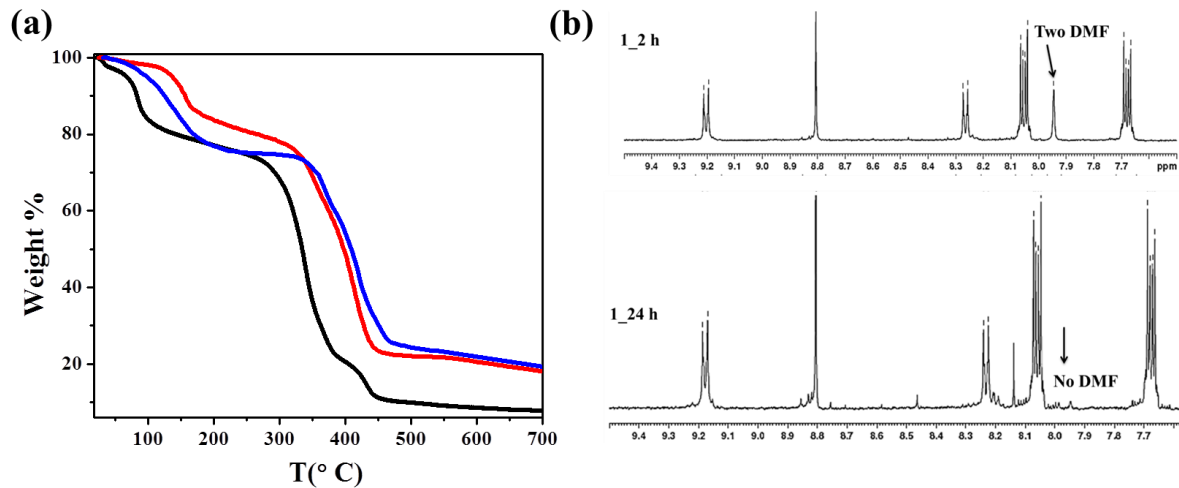


Figure 3: (a) TGA profiles for **1** (blue), **1_2h** (red), **1_24h** (black) in the temperature range 30–700 °C, (b) ^1H NMR spectra of **1_2h** and **1_24h** in DMSO-d_6 after digesting in DCl .

molecules (calcd. 12.7 %) in the temperature range of 150–180 °C (Figure 3a). The resultant desolvated framework (**1'**) is stable up to 290 °C without further weight loss. However, **1_24h** exhibits step wise weight loss of guest and desolvated framework is

stable up to $\sim 300^\circ\text{C}$. High temperature release of water molecules can be correlated to the presence of metal bound water along with non-coordinated guest water molecules. These results suggest that keeping the crystals in open atmosphere release all the guest DMF molecules (also confirmed from $^1\text{H NMR}$; Figure 3b) and slowly adsorb the moisture and change the structure of the framework.

3B.3.3 FT-IR and Raman spectroscopy

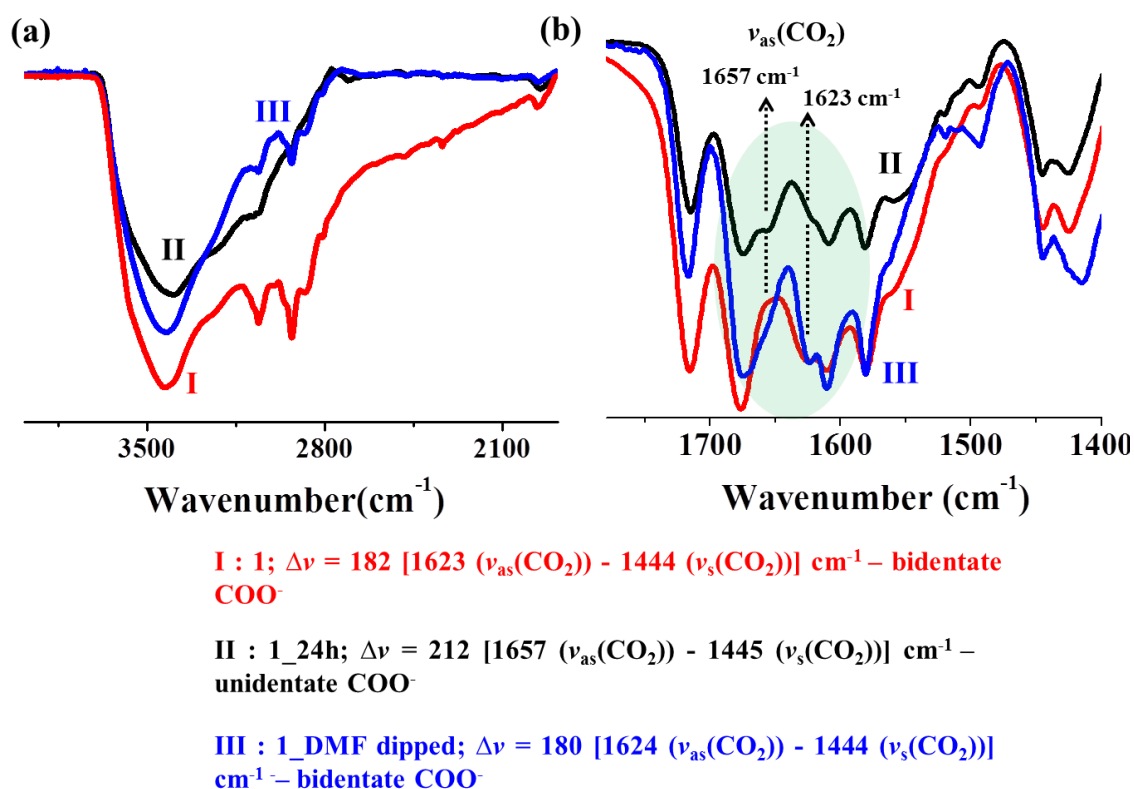


Figure 4: FT-IR spectra of **1**, **1_24h** and **1_DMF dipped**.

To understand the structural transformation we have performed IR and Raman spectroscopic studies of the compound in different stages as carboxylate vibrational modes are very sensitive to small change in their binding to metal ions. In **1**, the difference between asymmetric and symmetric stretching frequency ($\Delta\nu$) of $-\text{COO}^-$ group is 182 [$\nu_{\text{as}}(-\text{COO}^-) = 1623$ and $\nu_{\text{s}}(-\text{COO}^-) = 1444 \text{ cm}^{-1}$], confirming bidentate carboxylate coordination mode of adc linkers in the paddle wheel SBU (Figure 4b).¹⁶⁻¹⁷ Interestingly, in **1_24h**, $\nu_{\text{as}}(-\text{COO}^-)$ intensity at 1623 cm^{-1} decreases and a new band at 1657 cm^{-1}

appears with $\Delta\nu$ of 212 cm^{-1} , indicating monodentate $-\text{COO}^-$ coordination mode. This significant difference between ν_{as} and ν_{s} ($\Delta\nu$) is attributed to the change in carboxylate binding mode, i.e., from bidentate (**1**) to monodentate (**1_24h**) of adc linkers in 2D plane.¹⁶⁻²⁰ In **1_DMF dipped** phase, the $\nu_{\text{as}}(-\text{COO}^-)$ band at 1657 cm^{-1} disappears and the 1624 cm^{-1} band intensifies as similar to **1**. This suggests that bidentate mode reform on resolution (**1_DMF dipped**), which also supports the structural reversibility observed in PXRD studies.

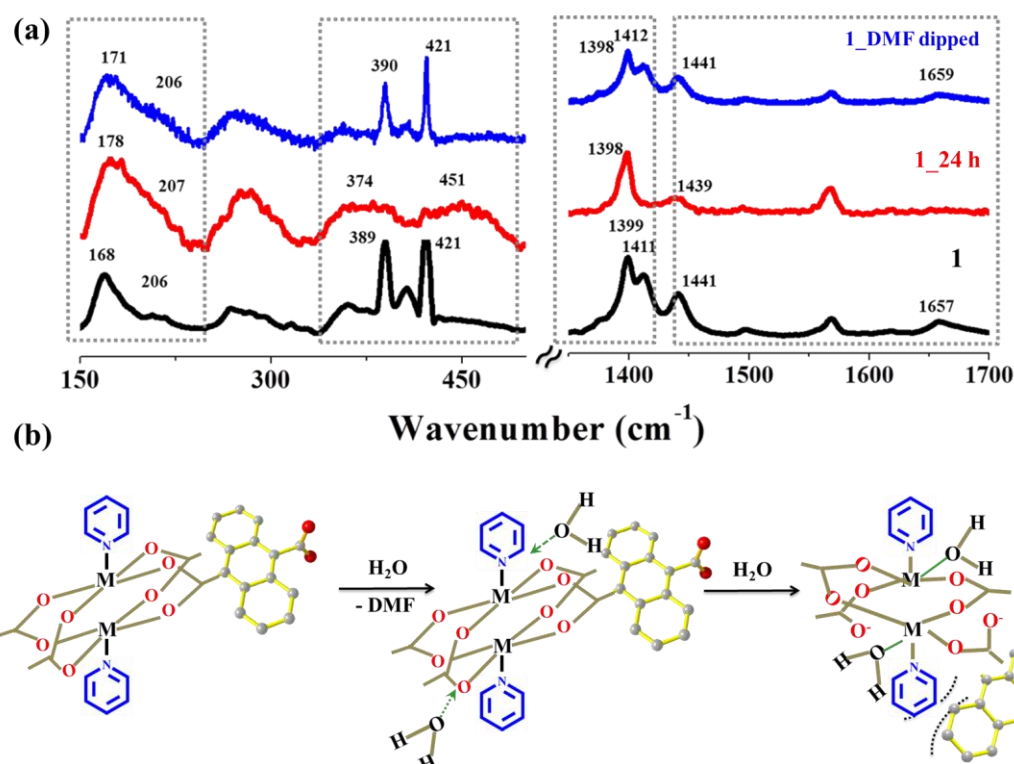


Figure 5: (a) Raman spectra of **1** (black), **1_24h** (red) and **1_DMF dipped**, (b) plausible mechanism of paddle wheel breaking on water molecule condensation to the metal centres.

Furthermore, Raman spectra obtained at different conditions provide additional information about the local environment of the paddle-wheel SBU and associated coordination modes of the carboxylate groups (Figure 5a). First, in the low frequency region, the doublet mode in the $168\text{--}206\text{ cm}^{-1}$ (in **1**) range can be attributed to Zn-Zn asymmetric vibration mode which is replaced by a single broad peak (178 cm^{-1}) with a low intensity band of 205 cm^{-1} in the sample **1_24h** (Figure 5a). Such a change in Raman bands indicating deformation of paddle-wheel SBU due to the breaking of some Zn-

carboxylate bond and probably stabilized through hydration as suggested by IR spectroscopy (Figure 4b). The broad and strong IR band in higher frequency region of 3800 to 2700 cm^{-1} for DMF removed **1_24h** phase is further supporting this fact. Such changes in Zn..Zn Raman bands are consistent with reported results related to the deformation of paddle-wheel core.²¹⁻²² The doublet mode reappears again at 171-206 cm^{-1} in **1_DMF dipped** on solvation (Figure 5a) due to reformation of paddle wheel SBU in a reversible fashion. The modes at 389 and 421 cm^{-1} are for Zn-O stretching modes which are broadened and slightly shifted to lower and higher frequency of 374 and 451 cm^{-1} , respectively, suggesting weakening and strengthening of coordination modes in **1_24h**, which reverts back to the vibrational modes as similar to **1** on resolution (**1_DMF dipped**). In the high frequency region, the bands at 1399, 1411 and 1441, 1657 cm^{-1} in **1** have been assigned as $\nu_s(-\text{COO}^-)$ and $\nu_{as}(-\text{COO}^-)$ vibration modes of the adc linkers, respectively. Interestingly, 1411 and 1657 cm^{-1} vibration modes completely disappeared in **1_24h** but reappears in resolved **1_DMF dipped**, clearly suggesting that the breakage of paddle-wheels which changes in spatial conformation of adc linker and corresponding 2D layer. Combining all these IR-Raman analyses, it can be corroborated that in this framework, $\text{Zn}_2(\text{COO})_4$ paddle-wheel SBU is prone to hydrolysis and this changes bidentate to monodentate carboxylate coordination. On resolution of DMF molecules, the bidentate coordination reform again and construct the as-synthesized structure. The PXRD, TGA, ¹HNMR data suggest that guest DMF molecules in the big void space of **1** tend to come out at ambient condition probably due to poor interaction with the framework. Such room temperature release of the DMF molecules which facilitates structural transformation can be confirmed based on the following conjecture. The careful analysis of the structure suggests that three phenyl rings of the adc chromophore are not in the same 2D plane [(002) plane] which connects the centroid of the paddle-wheel cores, and the dihedral angle between the two planes is about 31.54 ° (degree of tiltiness). This strained arrangement along the (200) plane of 2D $\{\text{Zn}(\text{adc})_n\}$ layer is relaxed by the deformation of the paddle-wheel which changes orientation of the adc linkers as shown in Figure 5b. This is also supported by the disappearance of only (200) plane in **1_24h** while the rest of the framework remains intact. The water molecules coordinated to the Zn^{II} centres provide the stability after the deformation as reported earlier.

3B.3.4 Adsorption studies

To check the permanent porosity of the desolvated framework **1'**, N₂ (kinetic diameter 3.64 Å) adsorption isotherm is carried out at 77 K (Figure 6). It exhibits type II profile which can be attributed to the structural change associated with the desolvated framework as the pore size is sufficient enough in the as-synthesized framework for the occlusion of N₂ molecules. CO₂ (kinetic diameter 3.3 Å) adsorption measurement at 195 K exhibits typical type I profile suggesting microporous nature of the framework (Figure 6). The total CO₂ uptake is about 26 cm³ g⁻¹ (5.1 wt%, 0.9 CO₂ per formula unit). The

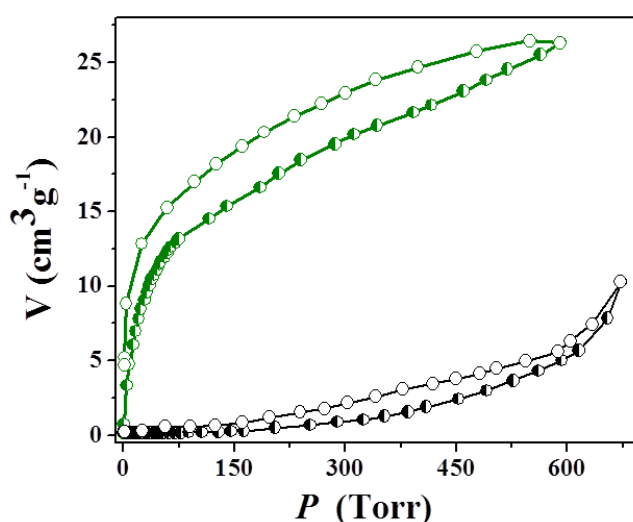


Figure 6: Adsorption isotherms of **1'**: N₂ (black) and CO₂ (green) at 77 and 195 K, respectively; (half-filled = adsorption, open = desorption).

corresponding Langmuir and BET surface areas calculated from the CO₂ isotherm are ~ 91 and 85 m² g⁻¹. The hysteretic adsorption profile is attributed to the strong interaction of the CO₂ molecules with the adsorptive sites (e.g. π -cloud of aromatic ring, C=O of bpNDI, C=N sites etc) of the framework.²³ It is also reflected in the high value of isosteric heat of adsorption value of q_{st} , ϕ , ~ 29.6 for **1'** as calculated from the Dubinin–Radushkevich (DR) equation.²³

3B.3.5 Photophysical studies

We have studied the photophysical properties of compound **1** in details (Figure 7). The UV-Vis spectrum of compound **1** measured in solid state shows characteristic π - π^* and n - π^* transitions in UV region, however, an additional broad band (400-800 nm) is

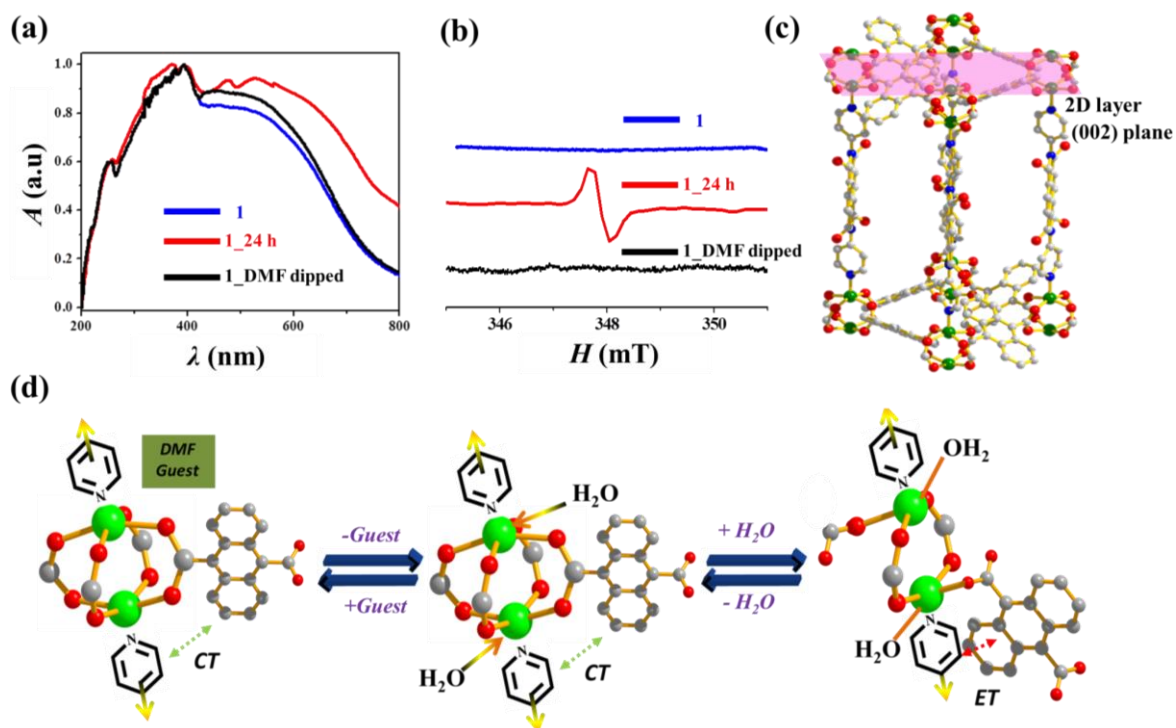


Figure 7: (a) UV-Vis absorption spectra of **1**, **1_24h** and **1_DMF dipped**, (b) EPR spectra of **1**, **1_24h** and **1_DMF dipped**, (c) single building unit showing the 2D plane, (d) plausible mechanism of CT to ET interaction.

also observed which can be attributed to ground state charge-transfer (CT) interaction between the donor adc linker and bpNDI acceptor (Figure 7a). This strong ground state interaction can be correlated with the structure where the donor and acceptor molecules are orthogonally oriented (the distance of carboxylate oxygen of the adc linker to the Zn-coordinated pyridyl ring is 2.59 Å). Surprisingly, keeping the crystal in open atmosphere for one day (**1_24h**) brought in further changes in the UV-Vis spectrum; two new distinct bands at λ_{\max} of 476 and 524 nm appeared due to formation of bpNDI radical anion,²⁴ also confirmed by EPR spectroscopy (Figure 7b). On the contrary, the as-synthesized phase did not show any EPR signal suggesting there is no charge separation in that state. Interestingly, resoluted **1_DMF dipped** reproduced a UV-Vis spectrum similar to that of as-synthesized **1**, suggesting complete reversibility of charge separated state to CT state, also confirmed from EPR spectra. The previous FT-IR, Raman analyses confirms the water molecules' coordination indeed affects the paddle-wheel coordination environment and supports the changes in bidentate to monodentate coordination of $-\text{COO}$ group of adc in **1_24h**. Such changes along the 2D plane as mentioned earlier facilitate the face-to-face

orientation of the adc linker with bpNDI and bring the donor-acceptor pairs in the closest proximity (Figure 7c-d) to form complete charge separated state based through formation of adc radical cation and bpNDI radical anion.

3B.3.6 Electrochemical studies

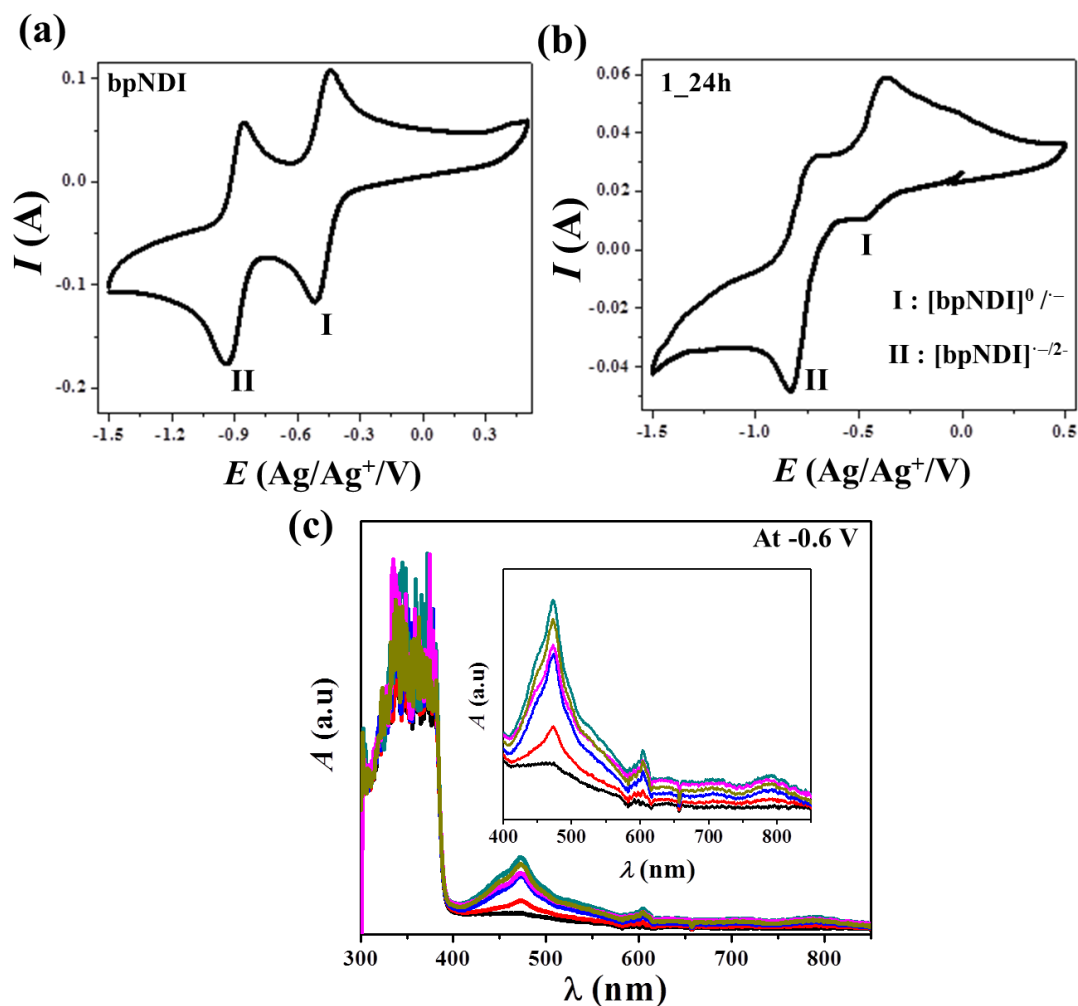


Figure 8: Cyclic voltammograms (CV) of (a) bpNDI, (b) **1** and (c) solution state spectroelectrochemistry of bpNDI linker where the potential was held at -0.6 V [coulometric technique, showing gradual appearance of bands with time].

Cyclic voltammograms (CV) are recorded by coating compounds on a GC electrode for understanding the redox states of the bpNDI ligand and compound **1** (Figure 8a-b). The solid state CV data of bpNDI clearly reveals the existence of two sets of fully reversible redox peaks of [bpNDI]⁻ at $E_{1/2} = -0.51$ V and [bpNDI]²⁻ at $E_{1/2} = -0.94$ V (Figure 8a).²⁵⁻²⁷ However, drastic changes in the voltammogram of **1_24h** have been

observed when compared with pristine bpNDI (Figure 8b). The very small current of peak I ($[\text{bpNDI}]^{0/-}$ at $E_{1/2} = -0.49$ V) compared to peak II ($[\text{bpNDI}]^{-/2-}$ at $E_{1/2} = -0.95$ V) suggests that bpNDI is in a mono radical anion state formed by the electron transfer from adc. This also suggests that minute amount of bpNDIs are yet to be in $[\text{bpNDI}]^{-}$ state. The higher peak current for peak II can be attributed to the combination of both electrochemical reduction and chemically generated mono anion radicals ($[\text{bpNDI}]^{0/-}$ and un-reduced bpNDI linkers).²⁴

Based on these further investigations are conducted using solution state UV-Vis spectroelectrochemistry (SEC) of bpNDI to understand the optical properties of the redox states at molecular level (Figure 8c).²⁸⁻²⁹ Solid state SEC studies of bpNDI in 0.1 M TBAP/ CH_3CN solution at -0.6 V shows gradual appearance of four peaks at 472, 605, 711 and 792 nm corresponding to the $[\text{bpNDI}]^{-}$ redox state. This is in accord with the literature, studied on bpNDI based systems. These bands are absent in the neutral state of the bpNDI ligand at 0 V. This is also in coherent with the newly appeared bands in the UV-Vis spectra of **1_24h**, hence, further supports the formation of $[\text{bpNDI}]^{-}$ state due to adc to bpNDI electron transfer process.

3B.4 Conclusion

In this chapter, a redox-active 3D pillared-layer framework $\{[\text{Zn}_2(\text{adc})_2(\text{bpNDI})] \cdot 4\text{H}_2\text{O} \cdot 4\text{DMF}\}_n$ (**1**) [adc = 9,10-anthracenedicarboxylic acid, bpNDI = *N,N'*-di(4-pyridyl)-1,4,5,8-naphthalenediimide] has been synthesized using adc and bpNDI as donor and acceptor linkers, respectively. The framework is permanently porous and undergoes guest responsive reversible structural transformation attributed to the breakage of the paddle-wheel $\text{Zn}_2(\text{COO})_4$ SBUs. The donor adc ligands being orthogonally oriented with the acceptor linkers in as-synthesized framework, involve in charge transfer interactions which transforms into complete charge separated state due to associated structural changes as characterized from PXRD, IR, UV-Vis, Raman and EPR spectroscopy. Such unique photophysical process is solvent dependent, reversible and has been observed for the first time in MOF system.

3B.5 References

1. (a) N. Kishi, M. Akita, M. Yoshizawa, *Angew. Chem. Int. Ed.* **2014**, *53*, 3604 (b) A. P. H. J. Schenning, E. W. Meijer, *Chem. Commun.* **2005**, 3245 (c) M. Kumar, K. V. Rao, S. J. George, *Phys. Chem. Chem. Phys.* **2014**, *16*, 1300 (d) T. Enoki, A. Miyazaki, *Chem. Rev.* **2004**, *104*, 5449 (e) Q. Ye, Y. Song, G. Wang, K. Chen, D. Fu, P. W. H. Chan, J. Zhu, S. D. Huang, R. Xiong, *J. Am. Chem. Soc.* **2006**, *128*, 6554.
2. (a) J. R. Li, J. Sculley, H. C. Zhou, *Chem. Rev.* **2012**, *112*, 869 (b) L. E. Kreno, K. Leong, O. K. Farha, M. Allendorf, R. P. V. Duyne, J. T. Hupp, *Chem. Rev.* **2012**, *112*, 1105 (c) J. Shi, Y. Jiang, X. Wang, H. Wu, D. Yang, F. Pan, Y. Suad, Z. Jiang, *Chem. Soc. Rev.* **2014**, *43*, 5192 (d) M. Yoon, R. Srirambalaji, K. Kim, *Chem. Rev.* **2012**, *112*, 1196 (e) M. D. Allendorf, C. A. Bauer, R. K. Bhakta, R. J. T. Houk, *Chem. Soc. Rev.* **2009**, *38*, 1330 (f) S. Roy, A. Chakraborty, T. K. Maji, *Coord. Chem. Rev.* **2014**, *273*, 139 (g) R. Haldar, S. K. Reddy, V. M. Suresh, S. Mohapatra, S. Balasubramanian, T. K. Maji, *Chem. Eur. J.* **2014**, *20*, 4347.
3. (a) A. Hazra, S. Bonakala, S. K. Reddy, S. Balasubramanian, T. K. Maji, *Inorg. Chem.* **2013**, *52*, 11385 (b) R. Haldar, N. Sikdar, T. K. Maji, *Mater. Today*, **2015**, *18*, 97 (c) J. C. Tan, A. K. Cheetham, *Chem. Soc. Rev.* **2011**, *40*, 1059 (d) J. M. Taylor, R. Vaidhyanathan, S. S. Iremonger, G. K. H. Shimizu, *J. Am. Chem. Soc.* **2012**, *134*, 14338.
4. L. Sarkisov, R. L. Martin, M. Haranczyk, B. Smit, *J. Am. Chem. Soc.* **2014**, *136*, 2228.
5. Z. Chang, D. H. Yang, J. Xu, T. L. Hu, X. H. Bu, *Adv. Mater.* **2015**, *27*, 5432.
6. A. Schneemann, V. Bon, I. Schwedler, I. Senkowska, S. Kaskel, R. A. Fischer, *Chem. Soc. Rev.* **2014**, *43*, 6062.
7. N. Sikdar, K. Jayaramulu, V. Kiran, K. V. Rao, S. Sampath, S. J. George, T. K. Maji, *Chem. Eur. J.* **2015**, *21*, 11701.
8. (a) T. Enoki, A. Miyazaki, *Chem. Rev.* **2004**, *104*, 5449. (b) Q. Ye, Y. Song, G. Wang, K. Chen, D. Fu, P. W. H. Chan, J. Zhu, S. D. Huang, R. Xiong, *J. Am. Chem. Soc.* **2006**, *128*, 6554.

9. P. H. Dinolfo, M. E. Williams, C. L. Stern, J. T. Hupp, *J. Am. Chem. Soc.* **2004**, *126*, 12989.
10. SMART (V 5.628), SAINT (V 6.45a), XPREP, SHELXTL; Bruker AXS Inc. Madison, Wisconsin, USA, **2004**.
11. G. M. Sheldrick, Siemens Area Detector Absorption Correction Program, University of Göttingen, Göttingen, Germany, **1994**.
12. A. Altomare, G. Cascarano, C. Giacovazzo, A. Guagliardi, *J. Appl. Cryst.* **1993**, *26*, 343.
13. G. M. Sheldrick, SHELXL-97, Program for Crystal Structure Solution and Refinement; University of Göttingen, Göttingen, Germany, **1997**.
14. A. L. Spek, *J. Appl. Cryst.* **2003**, *36*, 7.
15. G. M. Sheldrick, SHELXS 97, Program for the Solution of Crystal Structure, University Göttingen, Germany, **1997**.
16. G. B. Deacon, R. J. Phillips, *Coord. Chem. Rev.* **1980**, *33*, 227.
17. M. Pajtasova, D. Ondrusova, E. Jona, S. C. Mojumdar, S. L'alikova, T. Bazylakova, M. J. Gregor, *Therm. Anal. Calorim.* **2010**, *100*, 769.
18. D. Zacher, K. Yusenko, A. Betard, M. Meilikhov, T. Ladnorg, O. Shekhah, A. Terfort, C. Wöll, R. A. Fischer, *Chem. Eur. J.* **2011**, *17*, 1448.
19. A. C. Valderrama-Negron, W. A. Alves, A. S. Cruz, S. O. Rogero, D. D. O. Silva, *Inorg. Chim. Acta.* **2011**, *367*, 85.
20. M. Tafipolsky, S. Amirjalayer, R. J. Schmid, *J. Phys. Chem. C*, **2010**, *114*, 1440.
21. K. Tan, N. Nijem, P. Canepa, Q. Gong, J. Li, T. Thonhauser, Y. J. Chabal *Chem. Mater.* **2012**, *24*, 3153.
22. K. Tan, N. Nijem, Y. Gao, S. Zuluaga, J. Li, T. Thonhauser, Y. J. Chabal, *CrystEngComm*, **2015**, *17*, 247.
23. N. Sikdar, S. Bonakala, R. Haldar, S. Balasubramanian, T. K. Maji, *Chem. Eur. J.* **2016**, *22*, 6059.
24. N. Sikdar, Jayaramulu K, V. Kiran, K. V. Rao, S. Sampath, S. J. George, T. K. Maji, *Chem. Eur. J.* **2015**, *21*, 11701.
25. C. R. Wade, M. Li, M. Dincă, *Angew. Chem. Int. Ed.* **2013**, *52*, 13377.
26. P. M. Usov, C. Fabian, D. M. D'Alessandro, *Chem. Commun.* **2012**, *48*, 3945.

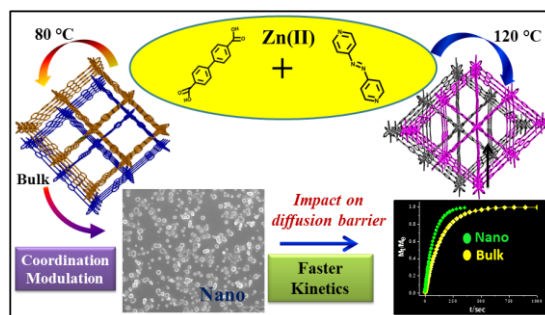
27. C. F. Leong, B. Chan, T. B. Faust, P. Turner, D. M. D'Alessandro, *Inorg. Chem.* **2013**, 52, 14246.
28. C. Hua, A. Baldansuren, F. Tuna, D. Collison, D. M. D'Alessandro, *Inorg. Chem.* **2016**, 55, 7270.
29. Pavel M. Usov, Cesimiro Fabian, D. M. D'Alessandro, *Chem. Commun.* **2012**, 48, 3945.

Chapter 4A

*Stoichiometry-Controlled Two
Flexible Interpenetrated
Frameworks: Higher CO₂ Uptake in
a Nanoscale Counterpart Supported
by Accelerated Adsorption Kinetics*

Chapter 4A

Stoichiometry-Controlled Two Flexible Interpenetrated Frameworks: Higher CO₂ Uptake in a Nanoscale Counterpart Supported by Accelerated Adsorption Kinetics



Summary: This chapter reports synthesis, structural characterizations and gas storage properties of two new two-fold interpenetrated 3D frameworks, $\{[\text{Zn}_2(\text{bpdc})_2(\text{azpy})] \cdot 2\text{H}_2\text{O} \cdot 2\text{DMF}\}_n$ (**1**) and $\{[\text{Zn}_3(\text{bpdc})_3(\text{azpy})] \cdot 4\text{H}_2\text{O} \cdot 2\text{DEF}\}_n$ (**2**) [H_2bpdc = 4,4'-biphenyldicarboxylic acid; azpy = 4,4'-azobipyridine], obtained from a same set of organic linkers. Compound **1** has been successfully miniaturized to spherical nanoscale (**MOF1N**) morphology through coordination modulation method to study size dependent adsorption properties. The two different SBUs, dinuclear paddle-wheel $\{\text{Zn}_2(\text{COO})_4\}$ of **1** and trinuclear $\{\text{Zn}_3(\mu_2\text{-OCO})_2(\text{COO})_4\}$ of **2**, direct the different network topologies of the frameworks that render different adsorption characteristics into the systems. Both frameworks show guest induced structural transformations as supported by PXRD studies. Adsorption studies of **1** and **2** show CO₂ selectivity over several other gases (such as N₂, H₂, O₂ and Ar) under identical experimental condition. Interestingly, **MOF1N** exhibits significant higher CO₂ uptake than bulk **1** and that can be attributed to the smaller diffusion barrier at nanoscale as supported by water vapour adsorption kinetics. The respective kinetic rate constant (k , sec⁻¹) of **MOF1N** ($k = 1.29 \times 10^{-2}$ sec⁻¹) is considerably higher than **1** ($k = 7.1 \times 10^{-3}$ sec⁻¹) as obtained from the linear driving force (LDF) model. This is the first account where a new interpenetrated MOF has been scaled down to nanoscale through coordination modulation method and their difference in gas uptake properties has been correlated by higher rate of mass diffusion as obtained from kinetics of adsorption.

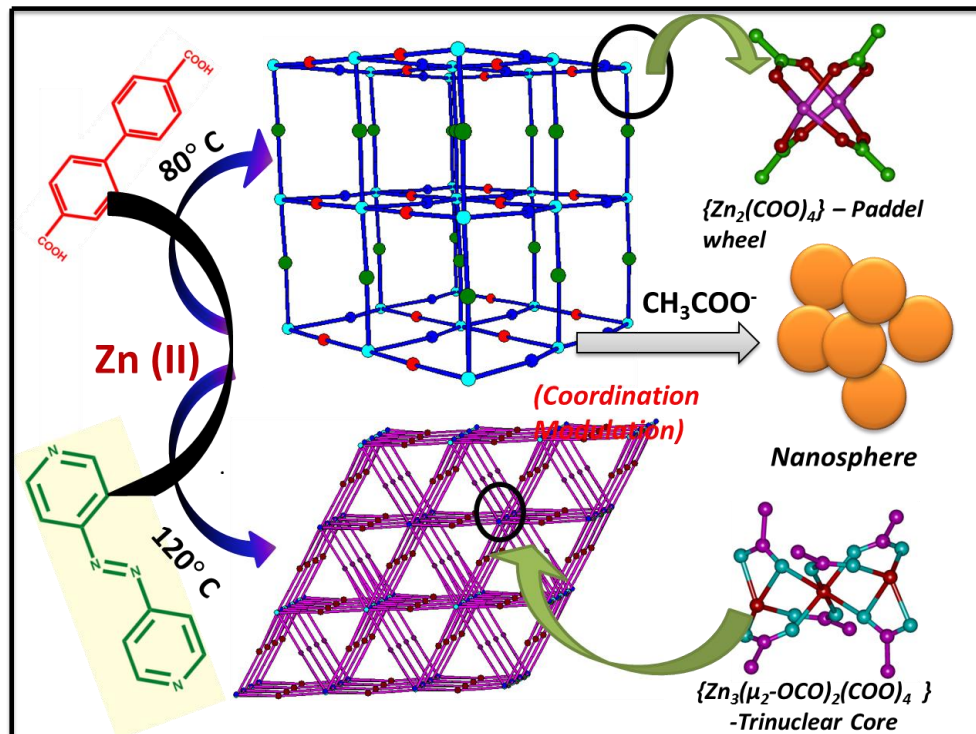
N. Sikdar, A. Hazra, T. K. Maji, *Inorg. Chem.* 2014, 53, 5993.

4A.1 Introduction

Metal–organic frameworks (MOFs) or porous coordination polymers (PCPs) represent an interesting new research field that has attracted a significant attention in recent years due to its potential applications in various fields such as gas storage and separation, luminescence, sensing, ion exchange, catalysis, magnetism, and in optoelectronics.^{1–7} MOFs are composed of metal ions or metal clusters and predefined polydentate organic linkers and thus allow tailoring of pore size and inner pore functionality. The properties of MOFs solely depend upon their framework structures and so, there has always been a drive to synthesize different MOFs by tuning the reaction parameters. It has been well established that changes in the reaction conditions such as stoichiometry, temperature, solvent and pH greatly influence the self-assembly process and thereby it is possible to construct versatile MOFs by varying those parameters.^{7e, 7f} Such modulation of framework dimensionalities, topologies for a similar-metal linker system is yet to be properly explored.^{8a} The structural diversities stem from the characteristic of metal ions, linkers and secondary building unit (SBU) and all these finally control the overall geometry, dimensionalities, interpenetration and flexibility of the framework structures.^{8b} Flexible or dynamic interpenetrated MOFs represent an unique class of materials which exhibit reversible changes in their structure and properties on response to external stimuli.^{9,10–14} One of the most interesting features of these flexible MOFs is their stepwise sorption behaviour caused by guest induced structural transformation.^{15–16} The total storage capacity, the structural transformation during adsorption and the onset pressure of step or gate opening are highly sensitive to the nature of the guest molecules and their interactions with the host along with kinetics and thermodynamics of adsorption processes. Therefore, understanding of the adsorption processes in a better way would help to unravel the structure property relationship of this kind of materials.

To date, research has been mainly centered on the synthesis, structural characterizations of bulk MOFs and especially correlation of their versatile physicochemical properties according to its crystal structure. But recently there has been a radical transition for fabrication of nanoscale MOFs (NMOFs) of different morphologies for controlling and tuning the size dependent material properties.^{17–21} The most important characteristic of nanomaterials is their higher surface area (higher S/V

ratio) compared to their respective bulk counterparts, thereby, is possible to incorporate versatile properties into nanoscale in a better way.^{8c} The lesser the particle size, the smaller is the diffusion barrier and it is expected to strongly influence the catalytic activities, separation processes, ion exchange, sensing and sorption properties over the respective bulk MOF.¹⁷ NMOFs also show enhanced solution processability which is useful for biological applications such as internalization into cells as drug delivery vehicles, for imaging, diagnostic purposes and also for device fabrication.¹⁷ These are also expected to show highly desirable size-dependent optical, electrical and magnetic properties.¹⁷ It has been found that crystal size and crystal surface environment dramatically affects the diffusion kinetics.¹⁸ But in order to understand these aspects in bulk and nanoscale, the most important criteria is to keep the structural features invariant even in nanoscopic dimension. Most attempts are prioritised to fabricate nanoscale MOFs to explore the effect of crystal morphology and size on adsorption properties.^{19, 20} There is only one report so far where the effect of particle size on solvent vapour adsorption kinetics has been discussed and it is necessary to explore further.²¹



Scheme 1: Schematic representation for the synthesis of two different interpenetrated frameworks 1, 2 and MOF1N using different reaction conditions.

In this chapter, synthesis, structural characterizations, and porous properties of two novel two-fold interpenetrated 3D frameworks $\{[\text{Zn}_2(\text{bpdc})_2(\text{azpy})]\cdot 2\text{H}_2\text{O}\cdot 2\text{DMF}\}_n$ (**1**) and $\{[\text{Zn}_3(\text{bpdc})_3(\text{azpy})]\cdot 4\text{H}_2\text{O}\cdot 2\text{DEF}\}_n$ (**2**) [H_2bpdc = 4,4'-biphenyldicarboxylic acid, azpy = 4,4'-azobipyridine] have been studied in details. Both the frameworks have been synthesized from same organic linkers under different reaction conditions (Scheme 1). Both of the frameworks show selective CO_2 uptake at 195 K. Furthermore, bulk framework **1** has been successfully miniaturized to nanosphere (**MOF1N**) through bottom up coordination modulation approach.^{8c, 22a} **MOF1N** is further studied for adsorption measurements and exhibit ~ 10 wt% higher CO_2 storage capacity compared to bulk **1**. Solvent (water) vapour adsorption measurement at 298 K shows higher water affinity in **MOF1N** than bulk **1** with completely different uptake profile. Measurement of water vapour adsorption kinetics shows higher rate of mass diffusion inside the micropores of **MOF1N** than bulk due to higher surface area and smaller diffusion path length.

4A.2 Experimental section

4A.2.1 Materials

All the reagents employed were commercially available and used as provided without further purification. $\text{Zn}(\text{NO}_3)_2\cdot 6\text{H}_2\text{O}$ was obtained from Spectrochem. H_2bpdc was obtained from Sigma Aldrich Co. Azpy was synthesized following the literature procedure.^{22k}

4A.2.2 Physical measurements

Elemental analyses were carried out using a Thermo Fischer Flash 2000 Elemental Analyzer. IR spectra were recorded on a Bruker IFS 66v/S spectrophotometer using KBr pellets in the region $4000\text{--}400\text{ cm}^{-1}$. Thermogravimetric analysis (TGA) were carried out on METTLER TOLEDO TGA850 in nitrogen atmosphere (flow rate = 50 mL min^{-1}) in the temperature range of $30\text{--}750\text{ }^\circ\text{C}$ (heating rate $5\text{ }^\circ\text{C min}^{-1}$). Powder XRD pattern of the compounds were recorded by using $\text{Cu-K}\alpha$ radiation (Bruker D8 Discover; 40 kV, 30 mA). The patterns were agreed with those calculated from single crystal structure determination. The scanning electron microscopy images were obtained using Nova Nanosem 600, FEI field emission scanning electron microscope (FESEM). The samples were prepared by dispersing the powder sample in MeOH and then dropping 5

μL of the solution onto a small piece of silicon wafer and drying into air. Transmission electron microscopy (TEM) images were taken with a JEOL JEM-3010 transmission electron microscope operating at 300 kV. The samples were prepared in the same way as described above but the drop cast was made onto carbon-coated TEM grid.

4A.2.3 X-ray crystallography

X-ray single-crystal structure data of **1** and **2** were collected on a Bruker Smart-CCD diffractometer equipped with a normal focus, 2.4 kW sealed tube X-ray source with graphite monochromated Mo-K α radiation ($\lambda = 0.71073 \text{ \AA}$) operating at 50 kV and 30 mA. The program SAINT^{22b} was used for integration of diffraction profiles and absorption correction was made with SADABS^{23a} program. All the structures were solved by SIR92^{22c} and refined by full-matrix least-squares method using SHELXL-97.^{22d} All the hydrogen atoms were fixed by HFIX and placed in ideal positions. Single crystals of both **1** and **2** are extremely susceptible to immediate loss of crystallinity upon exposure to air. To avoid this, after isolating the crystals from mother liquor, immediately these are covered with paraffin oil and X-ray single-crystal diffraction experiments are carried out at low temperature. The guest solvent molecules are extremely disordered and could not be located properly. No satisfactory disorder model could be achieved, hence the presence of solvent molecules are calculated from ¹HNMR, TGA, FTIR, and elemental analysis. Potential solvent accessible area or void space was calculated using the PLATON multipurpose crystallographic software.^{22e} All the crystallographic and structure refinement data of **1** and **2** are summarized in Table 1. Selected bond lengths and angles for **1** and **2**, are given in Table 2-5, respectively. All calculations were carried out using SHELXL 97,^{22d} PLATON,^{22e, 22f} and WinGX system, Ver 1.80.05.^{22g}

4A.2.4 Adsorption study

The adsorption isotherms of CO₂ (at 195, 273 and 293 K), H₂ (at 195 K), N₂ (at 77 and 195 K), Ar (at 195 K) and O₂ (at 195 K) using the dehydrated samples of **1** (**1'**), **2** (**2'**) and MOF1N (MOF1N') were measured by using QUANTACHROME QUADRASORB-SI analyser and AUTOSORB IQ2 instrument. The compound **1** and MOF1N have been activated at 150 °C whereas **2'** has been prepared at 170 °C under 1×10^{-1} Pa vacuum for about 12 h prior to measurement of the isotherms. All the gases

used for adsorption measurement are of scientific/research grade with 99.999% purity. Dead volume was measured with helium gas. The adsorbates were placed into the sample tubes, and then the change of the pressure was monitored and the degree of adsorption was determined by the decrease in pressure at the equilibrium state. All operations were computer-controlled and automatic.

The adsorption isotherms of different solvents (MeOH, at 293 K and H₂O, C₆H₆ at 298 K) for **1'**, **2'** and H₂O for **MOFN1'** were measured in the vapour state by using a BELSORP-aqua volumetric adsorption instrument from BEL, Japan. All the samples of about ~100–150 mg were prepared by adopting a similar procedure mentioned earlier (*vide supra*) prior to measurement of the isotherms. The solvent molecules used to generate the vapour were degassed fully by repeated evacuation. Dead volume was measured with helium gas. The adsorbate was placed into the sample tube, then the change of the pressure was monitored, and the degree of adsorption was determined by the decrease in pressure at the equilibrium state. All operations were computer controlled and automatic.

4A.2.5 Analysis of gas adsorption isotherms

Carbon dioxide adsorption isotherms of **MOFN1'** are fitted to the Langmuir-Freundlich^{22h} equation instead of the more commonly used Langmuir equation to get better fitting.²²ⁱ An accurate fit was obtained by using this equation which results a precise prediction over the quantity of gas adsorbed at saturation. A variant of the Clausius-Clapeyron equation was used to calculate enthalpy of adsorption.

$$\ln\left(\frac{P_1}{P_2}\right) = \Delta H_{\text{ads}} \times \left(\frac{T_2 - T_1}{R \times T_2 T_1}\right)$$

Where, P_n is = Pressure for isotherm n

T_n = Temperature for isotherm n

R = Universal Gas constant = 8.314 J mol⁻¹ K⁻¹

Pressure as a function of amount of adsorption was determined by using the Langmuir-Freundlich fit for each isotherm.

$$\frac{Q}{Q_m} = \frac{B \times P_t^{\frac{1}{n}}}{1 + B \times P_t^{\frac{1}{n}}}$$

Where, Q = moles adsorbed, Q_m = moles adsorbed at saturation, P = Pressure, B and t = constant. By rearranging this equation we get

$$P = \left(\frac{\frac{Q}{Q_m}}{B - B \times \frac{Q}{Q_m}} \right)^t$$

Substituting this into Clausius-Clapeyron equation we get

$$\Delta H_{\text{ads}} = \frac{B \times T_2 \times T_1}{T_2 - T_1} \ln \frac{\left(\frac{\frac{Q}{Q_{m1}}}{B_1 - B_1 \times \frac{Q}{Q_{m1}}} \right)^t}{\left(\frac{\frac{Q}{Q_{m2}}}{B_2 - B_2 \times \frac{Q}{Q_{m2}}} \right)^t}$$

Where, the subscript 1 and 2 are representing the data corresponding to 273 and 293 K respectively.

4A.2.6 Synthesis of $\{[\text{Zn}_2(\text{bpdc})_2(\text{azpy})] \cdot 2\text{H}_2\text{O} \cdot 2\text{DMF}\}_n$ (**1**)

A mixture containing $\text{Zn}(\text{NO}_3)_2 \cdot 6\text{H}_2\text{O}$ (0.1 mmol, 0.030 g), bpdc (0.1 mmol, 0.024 g) and azpy (0.05 mmol, 0.009 g) was suspended in DMF/ethanol (1:1) mixture (10 mL) in a glass vial (30 mL) and then heated to 80 °C for a period of 3 days. The dark red block shaped crystals of **1** were then collected after washing with DMF/ ethanol for several times. Yield: 87 % (with respect to metal). Anal. Calc. for $\text{C}_{44}\text{H}_{42}\text{Zn}_2\text{N}_6\text{O}_{12}$: C: 54.05; H: 4.33; N: 8.59; Found C: 53.98; H: 4.21; N: 8.56. FT-IR (KBr pellet, 4000–400 cm^{-1}): 3222 (s), 3091 (w), 2387 (w), 1940 (w), 1662 (m) 1604 (S), 1525 (m), 1396 (s).

4A.2.7 Synthesis of $\{[\text{Zn}_3(\text{bpdc})_3(\text{azpy})] \cdot 4\text{H}_2\text{O} \cdot 2\text{DEF}\}_n$ (**2**)

A mixture containing $\text{Zn}(\text{NO}_3)_2 \cdot 6\text{H}_2\text{O}$ (0.1 mmol, 0.03 g), bpdc (0.1 mmol, 0.024 g) and azpy (0.2 mmol, 0.036 g) was suspended in DEF/2-methoxy ethanol (1:1) mixture (10 mL) and heated to 120 °C for a period of 3 days. The resulting dark red crystals of **2** were filtered and washed with DMF/2-methoxy ethanol for several times. Yield: 75 % (with respect to metal). Anal. Calc. for $\text{C}_{62}\text{H}_{62}\text{Zn}_3\text{N}_6\text{O}_{18}$: C: 54.14; H: 4.54; N: 6.11;

Found C: 54.08; H: 4.49; N: 6.00. FT-IR (KBr pellet, 4000–400 cm^{-1}): 3220(S), 3064(w), 2933(w), 2283(w), 1929 (w), 1670 (m), 1543(s), 1402(s).

4A.2.8 Synthetic procedure for nanosphere (MOF1N)

A mixture containing $\text{Zn}(\text{OAc})_2 \cdot 2\text{H}_2\text{O}$ (0.1 mmol, 0.022 g), bpdc (0.1 mmol, 0.024 g) and azpy (0.05 mmol, 0.09 g) was suspended in DMF/ethanol (1:1; 10 mL) in a glass vial (30 mL) and heated to 80 °C for a period of 3 days. After that the vial has been taken out from the oil bath and cooled to room temperature. The dark red powder **MOF1N** was obtained instead of single crystals and then collected after washing with DMF/ethanol for several times and air dried. Yield: 60% (with respect to metal). Anal. Calc. for $\text{C}_{44}\text{H}_{42}\text{Zn}_2\text{N}_6\text{O}_{12}$: C: 54.05; H: 4.33; N: 8.59; Found C: 53.99; H: 4.32; N: 8.58. FT-IR (KBr pellet, 4000–400 cm^{-1}): 3250 (s), 3069 (w), 2932 (w), 2508 (w) 1947 (w), 1663 (m) 1605 (s), 1536 (s), 1388 (s).

4A.3 Results and discussion

4A.3.1 Crystal structure description of $\{\text{Zn}_2(\text{bpdc})_2(\text{azpy})\} \cdot 2\text{H}_2\text{O} \cdot \text{DMF}\}_n$ (1) and $\{[\text{Zn}_3(\text{bpdc})_3(\text{azpy})] \cdot 4\text{H}_2\text{O} \cdot 2\text{DEF}\}_n$ (2)

Single crystal X-ray diffraction analysis suggests that **1** crystallizes in triclinic $P\bar{1}$ space group and has a two-fold interpenetrated 3D pillared-layer framework with α -Po type topology. There are two Zn^{II} ions, two bpdc and one azpy ligand in the asymmetric unit. Two such Zn^{II} centres form a $\{\text{Zn}_2(\text{COO})_4\}$ paddle-wheel type secondary building unit (SBU) (Figure 1a) which are linked through bpdc linkers to construct a 2D network along ab plane (Figure 1b). The 2D networks are further pillared by the azpy along c direction to generate an extended 3D framework (Figure 1c). Each five coordinated Zn^{II} is in a square pyramidal geometry and connected with four carboxylate O atoms [Zn–O bond distances are in the range of 2.018(4)–2.048(3) Å] from four bpdc linkers and one N atom [Zn–N bond distances are 2.033(3) and 2.040(3) Å] from a azpy pillar (Figure 1a) and (Table 2-3). The presence of long linkers results large void space that induces self-catenation in the framework (Figure 1d). As a result of two-fold interpenetration, the pore volume and dimensions reduced significantly and these are of $4.2 \times 6.9 \text{ \AA}^2$, $3.5 \times 6.7 \text{ \AA}^2$ and $7.2 \times 8.2 \text{ \AA}^2$ along a , b and c direction (Figure 1e), respectively. These 3D channels are filled with guest DMF and water molecules. Estimation of these guests was confirmed

by ^1H NMR (Figure 3), TGA (Figure 5), and elemental analysis. Structural analysis with TOPOS reveals 2,6-c net with stoichiometry $(2\text{-c})_3(6\text{-c})$ and the corresponding Schläfli symbol for the net is $\{8^{12};12^3\}\{8\}3$ (Figure 1f).^{23b, 23c} Calculation using PLATON suggests the presence of void volume of $\sim 2219 \text{ \AA}^3$ i.e. $\sim 61\%$ of the total cell volume.

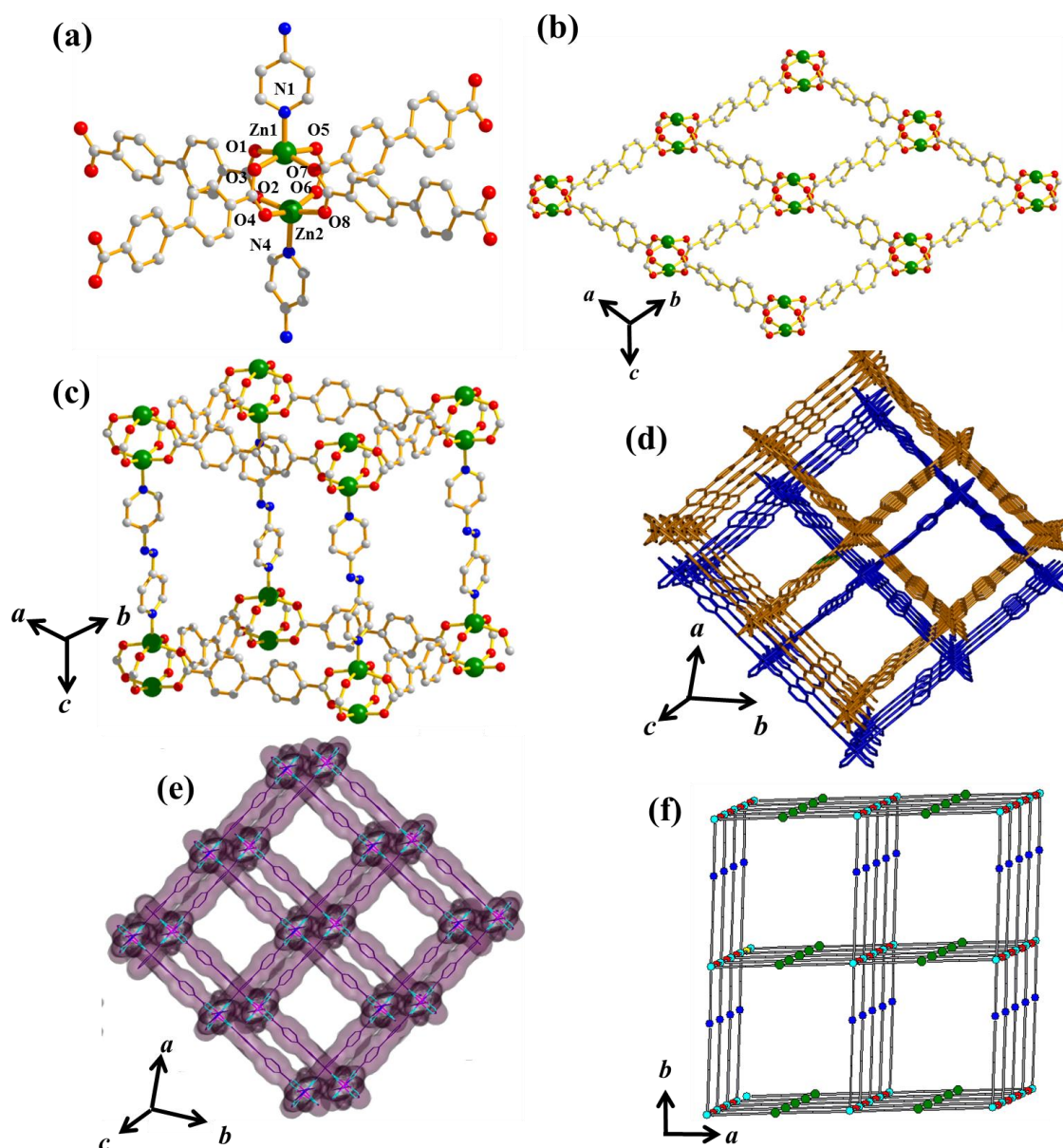


Figure 1: (a) Coordination environment of Zn^{II} in **1**, (b) view of 2D sheet along *ab* plane, (c) formation of a single net by joining the 2D sheets through azpy linkers, (d) view of two fold interpenetration along *c* direction, (e) view of the square shaped pores along *c* direction, (f) topological figure of **1**.

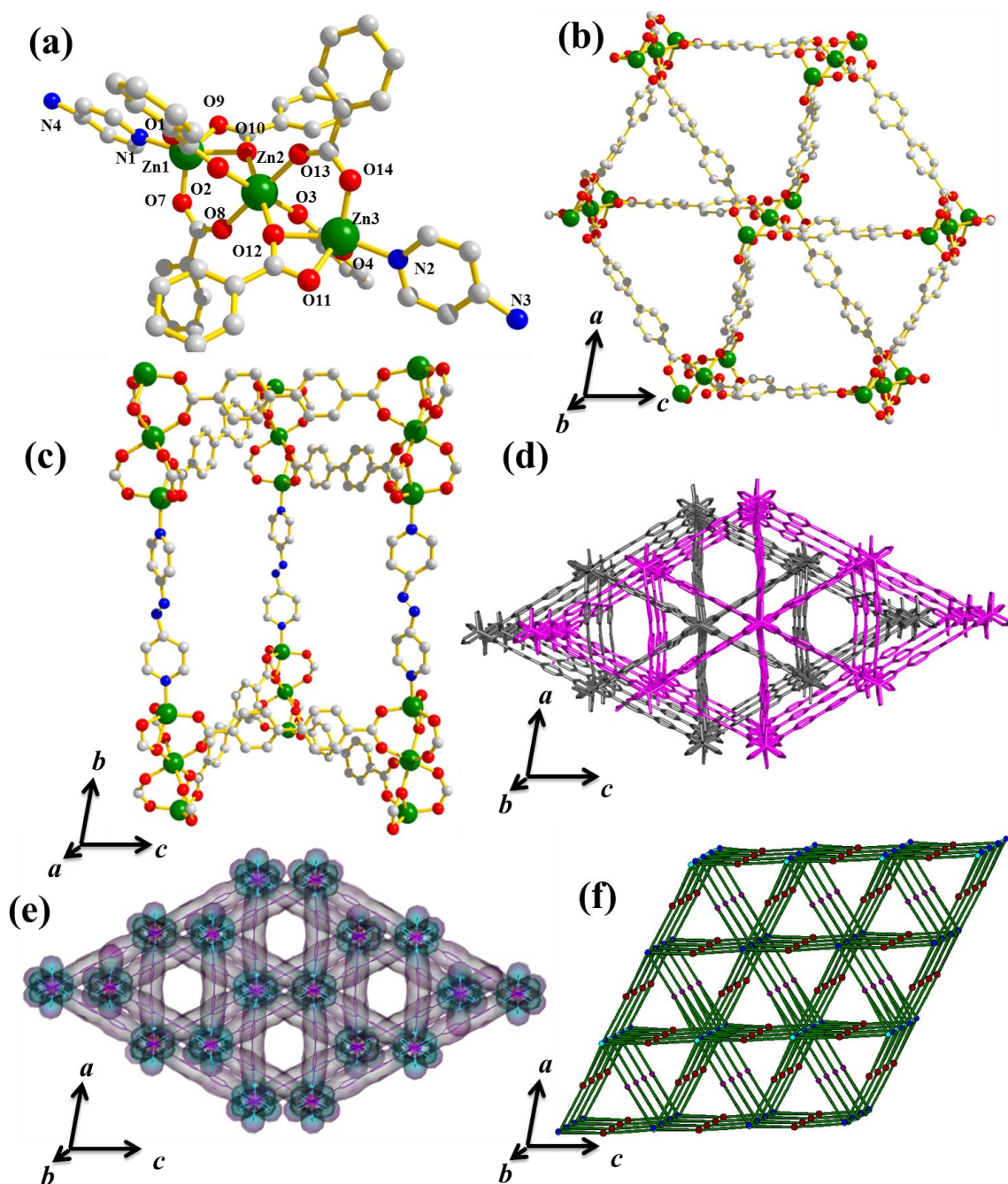


Figure 2: (a) Coordination environment of Zn^{II} in **2**, (b) view of 2D net along *ac* plane, (c) azpy linkers are connecting the 2D sheets through coordination to Zn1 and Zn3 centers to form a single net, (d) view of two fold interpenetration along *b* direction, (e) hexagonal 1D pores in **2** along *b* direction, (f) topological figure of **2**.

Compound **2** is crystallized in monoclinic $P2_1/n$ space group and has a two-fold interpenetrated pillared-layer 3D framework. The asymmetric unit of **2** is consisting of three Zn^{II} centres (Zn1, Zn2 and Zn3), three bpdc ligands and one azpy linker. The carboxylate oxygens μ_2 -O10 and μ_2 -O12 and four carboxylate groups from six different bpdc linkers bridged the three Zn^{II} centres that results into trinuclear secondary building unit (SBU), $\{Zn_3(\mu_2-OCO)_2(COO)_4\}$ (Figure 2a). Each SBU is connected to six such SBUs through bpdc linkers resulting in a 2D triangular sheet along the ac plane (Figure 2b). 2D sheet is further extended by azpy linker along b direction resulting in a 3D framework (Figure 2c) with a large cavity with a dimension of $11.9 \times 11.2 \text{ \AA}^2$. In the framework, octahedral Zn2 is centered in the middle of SBU and is linked to six different carboxylate oxygens (O2, O3, O7, μ_2 -O10, μ_2 -O12 and O13) from bpdc whereas Zn1 and Zn3 are in distorted trigonal bipyramidal geometry, each one is connected to four

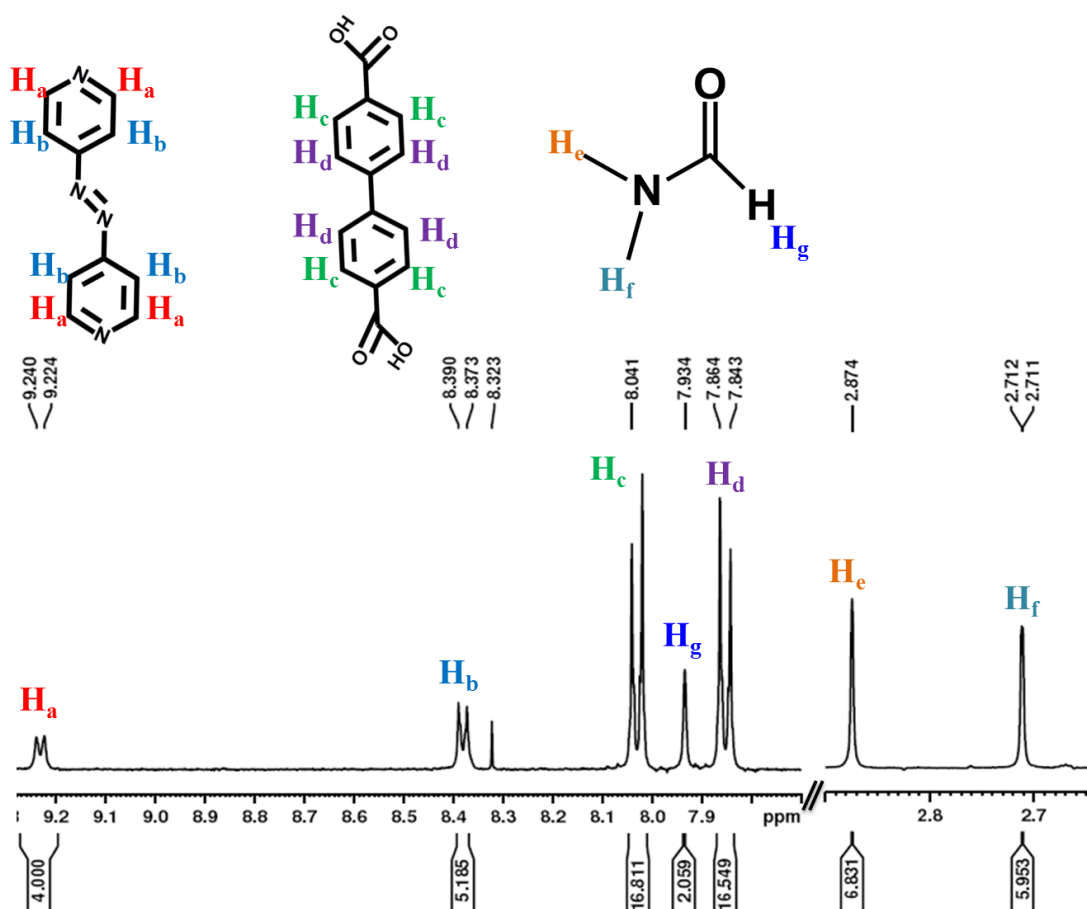


Figure 3: 1H NMR of **1** in DMSO- d_6 after digesting in DCl.

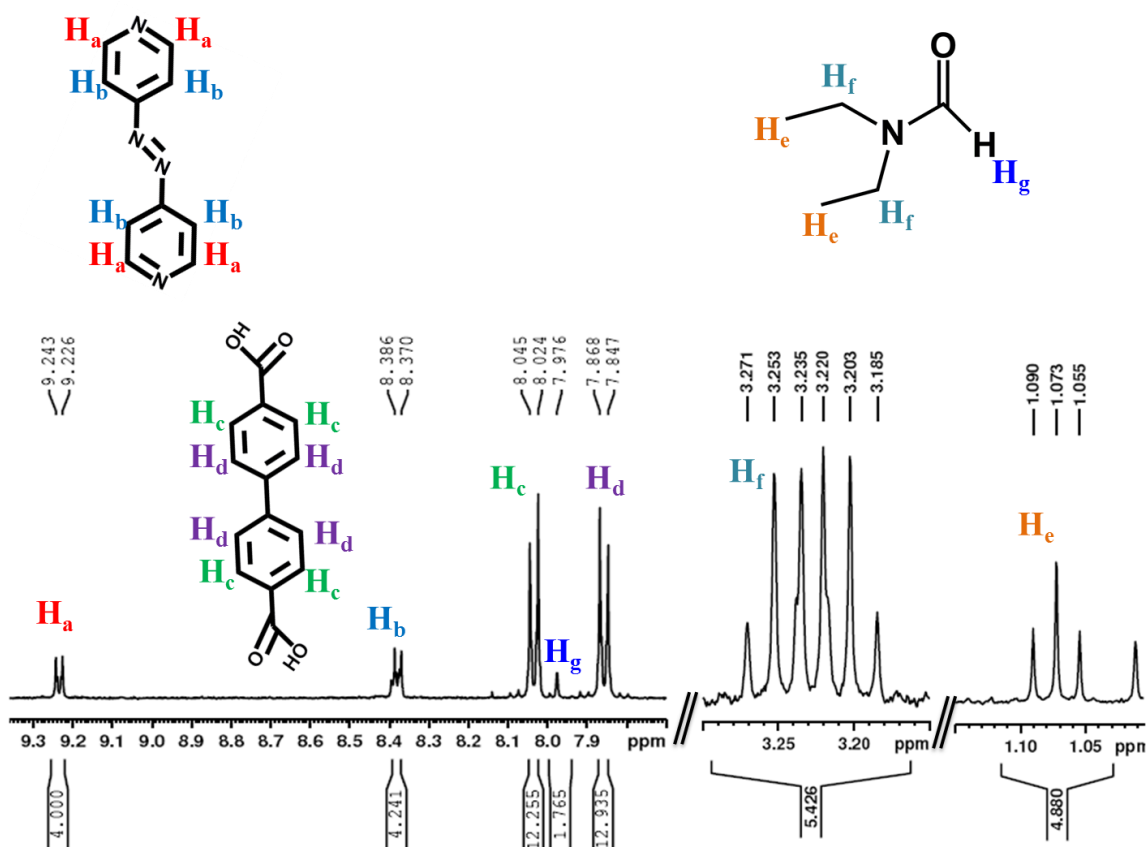


Figure 4: ¹H NMR of **2** in DMSO-d₆ after digesting in DCl.

carboxylate oxygens (Zn1 is coordinated to O4, O8, O11, μ_2 -O12 and for Zn3 these are O1, O9, μ_2 -O10, O14) from three different bpdc and one nitrogen from azpy linker (for Zn1 is N1 and Zn3 is N2) (Figure 2a). The Zn-O and Zn-N bond distances are in the range of 1.940(4)-2.226(3) Å, and 2.069(4)-2.071(4) Å, respectively (Table 4-5). Similar to **1**, **2** also undergoes two-fold interpenetration due to presence of large void space and possesses 1D channels (along *b* direction) with dimension of 7.3×7.1 Å² (Figure 2d and 2e). This 1D channel is filled with guest DEF and water molecules. Presence of these guests was confirmed by ¹H NMR (Figure 4), TGA (Figure 5), and elemental analysis. Structural analysis with TOPOS shows 3-nodal 2,8-c net with stoichiometry (2-c)4(8-c) and the corresponding Schläfli symbol for the net is {6⁶;8¹⁸;10³;12}{6}3{8} (Figure 2f).^{23b,23c} Calculation of void space using PLATON after removal of guest molecules suggests the presence of void volume of ~ 3319 Å³ i.e. 45 % of the total cell volume.

Table 1: Crystal data and structure refinement parameters of **1** and **2**.

Parameters	Compound 1	Compound 2
Empirical formula	C ₄₄ H ₄₂ Zn ₂ N ₆ O ₁₂	C ₆₂ H ₆₂ Zn ₃ N ₆ O ₁₈
Formula weight	977	1374
Crystal system	Triclinic	Monoclinic
Space group	<i>P</i> $\bar{1}$	<i>P</i> 2 ₁ / <i>n</i>
<i>a</i> , Å	15.2090(4)	14.1046(5)
<i>b</i> , Å	15.2245(4)	19.9260(7)
<i>c</i> , Å	15.8758(4)	25.9898(9)
α , deg	92.427(1)	90
β , deg	99.183(1)	90.005(1)
γ , deg	90.052(1)	90
<i>V</i> , Å ³	3625.55(16)	7304.4(4)
<i>Z</i>	2	4
<i>T</i> , K	240	240
μ , mm ⁻¹	0.690	1.028
<i>D</i> _{calcd.} , g/cm ³	0.729	1.083
<i>F</i> (000)	808	2412
Reflections[<i>I</i> > 2 σ (<i>I</i>)]	9792	8762
Total reflections	48826	70418
Unique reflections	12681	14830
λ (Mo-K α)	0.71073	0.71073
<i>R</i> _{int}	0.0534	0.0587
GOF on <i>F</i> ²	1.126	1.033
<i>R</i> ₁ [<i>I</i> > 2 σ (<i>I</i>)] ^a	0.0645	0.0672
<i>R</i> _w [all data] ^b	0.2371	0.2320

$$^a R = \sum |F_o| - |F_c| / \sum |F_o|. \quad ^b R_w = [\sum \{w(F_o^2 - F_c^2)^2\} / \sum \{w(F_o^2)^2\}]^{1/2}.$$

Table 2. Selected bond lengths (Å) for **1**.

Zn1-O2	2.026(3)	Zn1-O4	2.045(3)	Zn1-N1	2.033(3)	Zn1-O6_b	2.047(3)
Zn1-O8_f	2.038(3)	Zn2-O1	2.048(3)	Zn2-O3	2.018(3)	Zn2-O5_b	2.033(3)
Zn2-N4_d	2.038(3)	Zn2-O7_f	2.036(3)				

Table 3. Selected bond angles (°) for **1**.

O2-Zn1-O4	88.49(12)	O2-Zn1-N1	102.52(13)
O2-Zn1-O6_b	88.38(12)	O7_f-Zn2-N4_d	102.33(16)
O2-Zn1-O8_f	161.14(13)	O4-Zn1-N1	99.02(12)
O4-Zn1-O6_b	157.70(16)	O4-Zn1-O8_f	88.55(12)
O6_b-Zn1-N1	103.22(16)	O8_f-Zn1-N1	96.34(12)
O6_b-Zn1-O8_f	87.32(13)	O1-Zn2-O3	87.87(12)
O1-Zn2-O5_b	87.65(15)	O1-Zn2-N4_d	99.46(16)
O1-Zn2-O7_f	158.20(13)	O3-Zn2-O5_b	161.65(13)

O3-Zn2-N4_d	99.86(16)	O3-Zn2-O7_f	88.73(12)
O5_b-Zn2-N4_d	98.42(16)	O5_b-Zn2-O7_f	88.85(16)

Symmetry transformations used to generate equivalent atoms in **1**: b = x,-1+y,z, d = x,y,1+z, f = 1+x,y,z

Table 4. Selected bond lengths (Å) for **2**.

Zn-O1	1.947(4)	Zn1-O14	1.943(3)
Zn1-O9	2.085(4)	Zn1-O10	2.223(4)
Zn1-N2	2.070(4)	Zn2-O2	2.051(4)
Zn2-O13	2.052(3)	Zn2-O10	2.133(4)
Zn2-O12_b	2.144(4)	Zn2-O3_i	2.050(3)
Zn2-O7_j	2.047(4)	Zn3-O11	2.072(3)
Zn3-O12	2.216(3)	Zn3-N1_d	2.071(4)
Zn3-O4_k	1.947(4)	Zn3-O8_l	1.940(4)

Table 5. Selected bond angles (°) for **2**.

O1-Zn1-O9	113.74(19)	O7_j-Zn2-O12_b	92.14(16)
O1-Zn1-O10	97.03(15)	O3_i-Zn2-O7_j	92.41(15)
O1-Zn1-O14	120.50(17)	O11-Zn3-O12	59.26(15)
O1-Zn1-N2	95.04(17)	O11-Zn3-C65	29.76(17)
O1-Zn1-C42	107.10(17)	O11-Zn3-N1_d	94.93(19)
O9-Zn1-O10	59.69(15)	O4_k-Zn3-O11	123.65(19)
O9-Zn1-O14	123.32(19)	O8_l-Zn3-O11	113.40(19)
O9-Zn1-N2	93.88(16)	O12-Zn3-C65	29.51(17)
O9-Zn1-C42	29.97(17)	O12-Zn3-N1_d	154.12(19)
O10-Zn1-O14	97.43(15)	O4_k-Zn3-O12	97.33(15)
O10-Zn1-N2	153.53(16)	O8_l-Zn3-O12	97.48(15)
O10-Zn1-C42	29.73(17)	N1_d-Zn3-C65	124.7(2)
O14-Zn1-N2	96.56(17)	O4_k-Zn3-C65	113.52(17)
O14-Zn1-C42	113.42(17)	O8_l-Zn3-C65	107.09(17)
N2-Zn1-C42	123.85(18)	O4_k-Zn3-N1_d	95.87(17)
O2-Zn2-O10	91.88(15)	O8_l-Zn3-N1_d	94.83(17)
O2-Zn2-O13	92.50(15)	O4_k-Zn3-O8_l	120.47(17)
O2-Zn2-O12_b	89.67(15)	O2-Zn2-O3_i	178.93(16)
O2-Zn2-O7_j	87.80(15)	O10-Zn2-O13	89.64(15)
O10-Zn2-O12_b	177.96(15)	O7_j-Zn2-O10	89.25(16)
O3_i-Zn2-O10	89.17(15)	O3_i-Zn2-O13	87.31(15)
O12_b-Zn2-O13	88.96(15)	O3_i-Zn2-O12_b	89.27(15)
O7_j-Zn2-O13	178.86(16)		

Symmetry transformations used to generate equivalent atoms in **2**: b = 1+x,y,z, d = 1+x,1+y, z i = 1/2+x,1/2-y,-1/2+z, j = 1/2+x,1/2-y,1/2+z, k = 3/2+x,1/2-y,-1/2+z, l = 3/2+x,1/2-y,1/2+z

4A.3.2 TGA and PXRD analyses

Thermogravimetric analysis (TGA) of **1** shows rapid initial weight loss of 4.1 wt% in the temperature range of 90-100 °C corresponding to two bound guest water molecules (Figure 5). The next consecutive steps exhibit release of two guest DMF molecules from the framework (expt. 14 wt%, calcd., 14.3 wt%) in the temperature range of 190-210 °C. The desolvated **1'** is thermally stable up to 325 °C and then decomposes to unidentified product. Similarly, **2** shows first initial weight loss of 6.0 wt% corresponding to four water molecules within 100 °C followed by further 15.6 wt% loss of two DEF molecules (calcd., 15.7 wt%). The desolvated **2'** is thermally stable up to 345 °C and then decomposes. TGA of **MOF1N** shows similar trend as of **1**, first 4.0 wt% loss correspond to two water molecules and then release of two DMF within 180-200 °C and the desolvated framework exhibits thermal stability up to 325 °C similar to **1**.

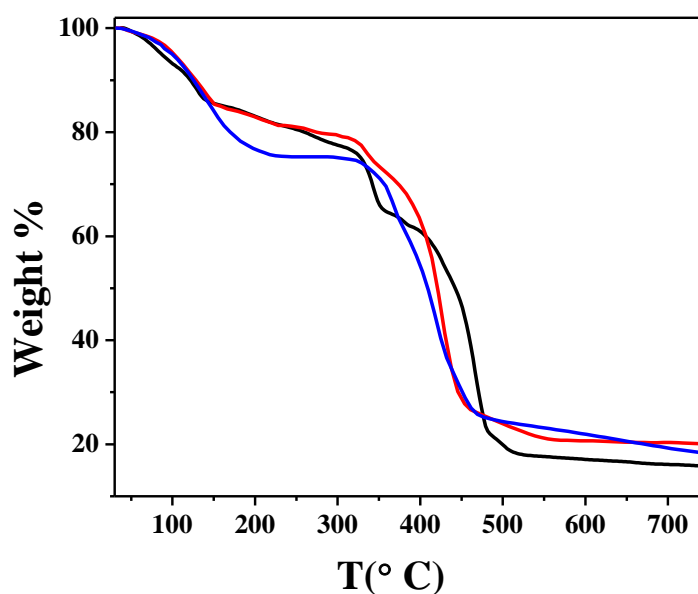


Figure 5: TGA curves for **1** (black), **2** (blue) and **MOF1N** (red) in the temperature range 30–750 °C.

The PXRD patterns of the as-synthesized crystals are recorded immediately after taking out from the mother solution. As-synthesized **1** (Figure 6) shows sharp peaks, suggesting high crystallinity and well correspondence with the simulated pattern indicates high purity of the sample. Very minute shifting of some of the Bragg's reflection is probably due to partial desolvation at room temperature. On complete removal of solvent molecules, Bragg's diffractions get shifted to higher 2θ angle (e.g the lowest angle peak) along with

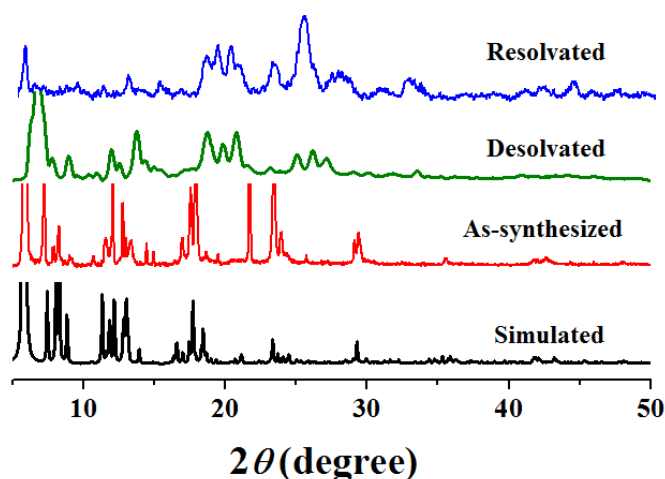


Figure 6: PXRD patterns of **1** recoded at different states.

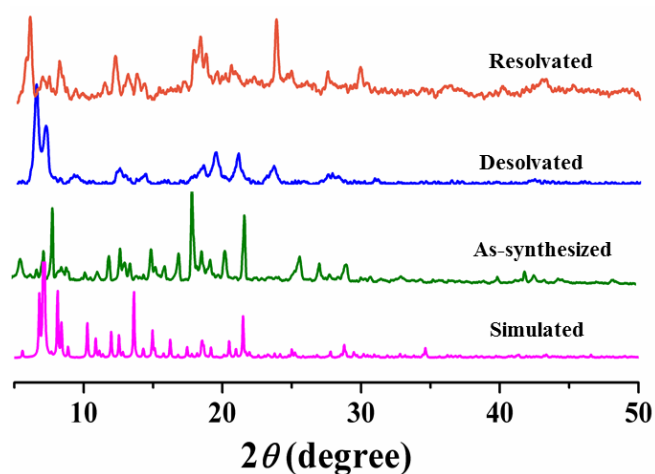


Figure 7: PXRD patterns of **2** recoded at different states.

regeneration of some new peaks indicating significant structural transformation. Broadening of the diffraction peaks suggesting poor crystallinity of the sample in the desolvated state. On exposure with DMF/EtOH, **1'** shows clear regeneration of the low angle peak but still dissimilarity with the as-synthesized phase suggests flexible nature of the framework. The as-synthesised pattern of **2** shows presence of all peaks but among them some are significantly shifted probably due to the fast release of solvent molecules at room temperature (Figure 7). This is also realized from the loss of transparency on the surfaces of the crystals on keeping outside from mother solution for some time (Figure 8). On desolvation, PXRD pattern of **2** shows significantly shifted and newly generated broaden peaks indicating structural change on guest removal with poor crystalline nature.

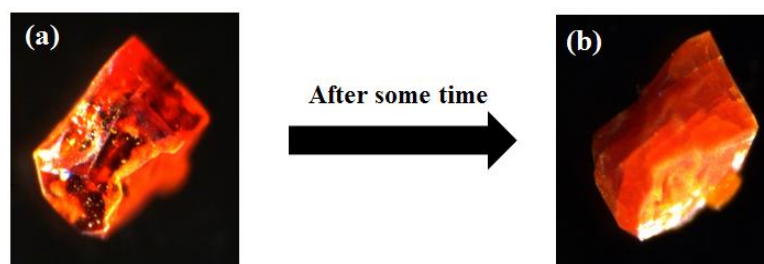


Figure 8: Optical images of one single crystal of **2** (a) in transparent state (b) after some time on exposure in open air.



Figure 9: Optical images of **2** (a) single crystals in mother solution (b) after complete drying in open atmosphere.

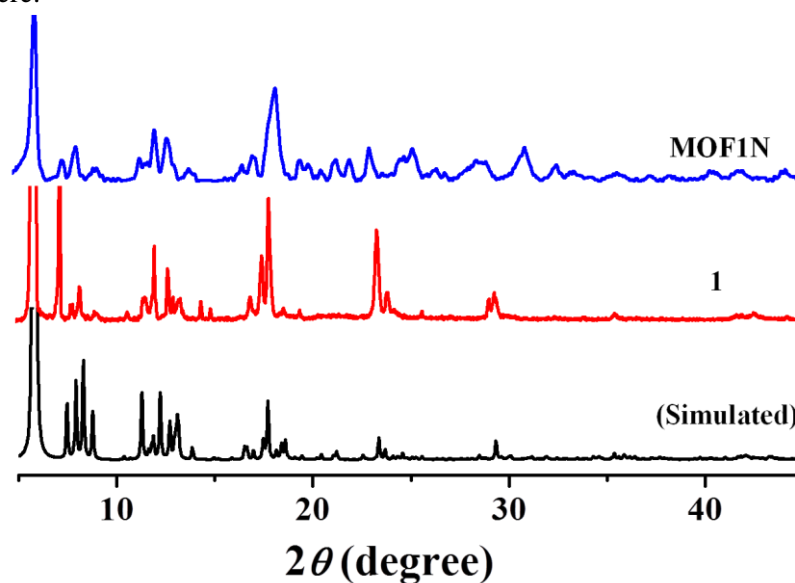


Figure 10: PXRD patterns of simulated, **1** and MOF1N.

Colour change from dark red crystals to orange one also supports above explanation (Figure 9). On resolution with DEF/2-methoxyethanol, it does not completely go back to the as-synthesized phase, which means structure is flexible in nature.

4A.3.3 Characterizations of nanoscale MOF (MOF1N)

It has been possible to fabricate the bulk MOF **1** to nanoscale (MOF1N) by adopting a well-established coordination modulation method in a solvothermal way.^{22a} Here the choice of metal precursor is $\text{Zn}(\text{OAc})_2$ ^{25c} by hypothesizing that OAc^- ions would act as modulator, and the two OAc^- can be considered as equivalent to two carboxylate groups of one bpdc linker. The red powder obtained with $\text{Zn}(\text{OAc})_2$ in a

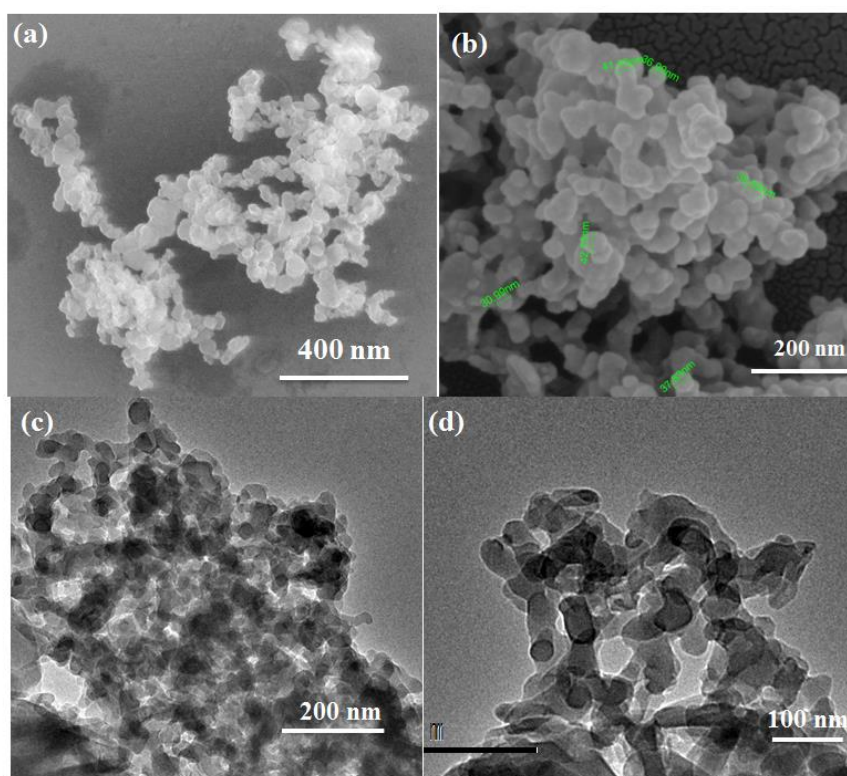


Figure 11: (a-b) FESEM images of nanospheres, (c-d) TEM images of nanospheres.

similar reaction as of **1** has been characterized through elemental analysis, IR, TGA (Figure 5), PXRD (Figure 10) and other microscopic technique such as FESEM (field emission scanning electron microscopy) and TEM (transmission electron microscopy). IR spectrum shows presence of the functional groups of the struts. Elemental analysis and TGA suggest the similar molecular formula as of **1**. Similar diffraction patterns of MOF1N and bulk **1** clearly confirms the formation of pure phase compound with similar periodic structural characteristics. Noticeably, the broadening of the Bragg's reflections is observed, suggesting formation of much smaller sized crystals compared to bulk **1**.

FESEM and TEM (Figure 11) clearly reveals formation of nanoscale particles with spherical morphology and the average diameters of the nanospheres are in the range of $\sim 40 \pm 20$ nm (Figure 12). All of the microscopic images clearly show that all the particles are highly agglomerated. And this is only possible when the surface of the nanoparticles is not properly capped with stabilizing agent *i.e.* no external capping agent.^{18, 24} ¹HNMR study of **MOF1N**, after digestion with DCl, shows the absence of acetate anions (methyl H in $-\text{CH}_3$ group) (Figure 13), suggesting that the surface of the nanoparticles is not capped with modulator OAc^- . These bare spherical nanoparticles, being very small in size possess high surface energy, thus have high tendency for agglomeration in solution phase.²⁴ Here, the OAc^- ions are helping to grow smaller particles by inhibiting the bulk crystal growth through *in situ* competitive interactions with bpdc. Further, similar carboxyl functional group of bpdc and OAc^- would have helped to preserve the structural

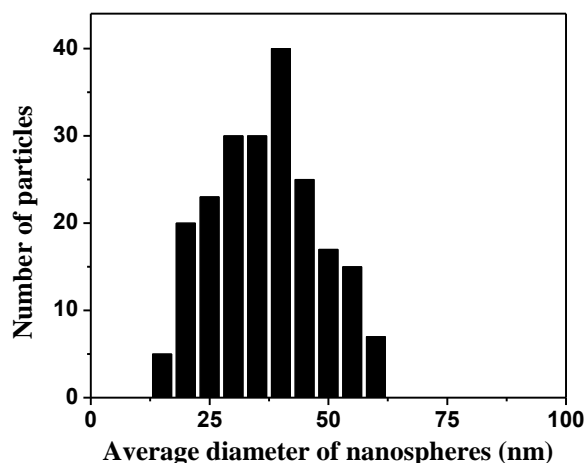


Figure 12: Particle size distribution of **MOF1N**.

integrity in the nanoscale as of bulk **1**.^{22a} Therefore without using of an external capping agent (long alkyl chain monocarboxylic acid or different organic polymers), only by choosing a suitable metal salt (e.g. here $\text{Zn}(\text{OAc})_2$ with modulator anion, it is possible to alter the metal-ligand coordination equilibrium during the nucleation and crystal growth. In a similar way we have also tried to fabricate the second framework **2** to a nanoscale, but our repeated attempt did not materialize probably due to the different trinuclear SBU in **2** compared to **1**.

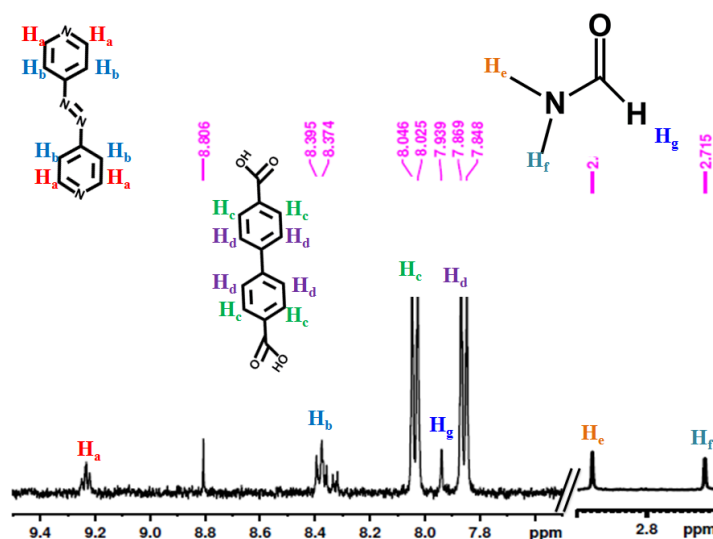


Figure 13: ^1H NMR of MOF1N in DMSO- d_6 after digesting in DCl.

4A.3.4 Adsorption studies

N_2 adsorption measurements at 77 K are carried out for **1'** and **2'** for determination of surface areas for both of the frameworks. Despite of having sufficient pore sizes in as synthesized frameworks, both, the desolvated frameworks **1'** and **2'**, show typical type II N_2 adsorption isotherms (kinetic diameter 3.64 Å) (Figure 14). Three probable reasons might be considered to this non-porous nature to N_2 ; (a) it might be associated with the low thermal energy of the adsorbate relative to the high diffusion barrier at 77 K,^{25a} (b) in other way, both of the frameworks contain nitrogen phobic pore surfaces as the presence of $-\text{N}=\text{N}-$ groups on the pore walls repel N_2 molecules, thus would not allow diffusion^{26a}

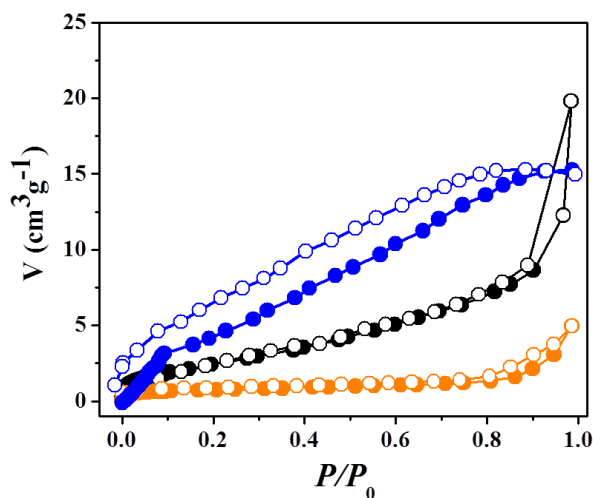


Figure 14: N_2 adsorption isotherms of **1'**- orange, **2'**- blue and **MOF1N'**- black at 77 K.

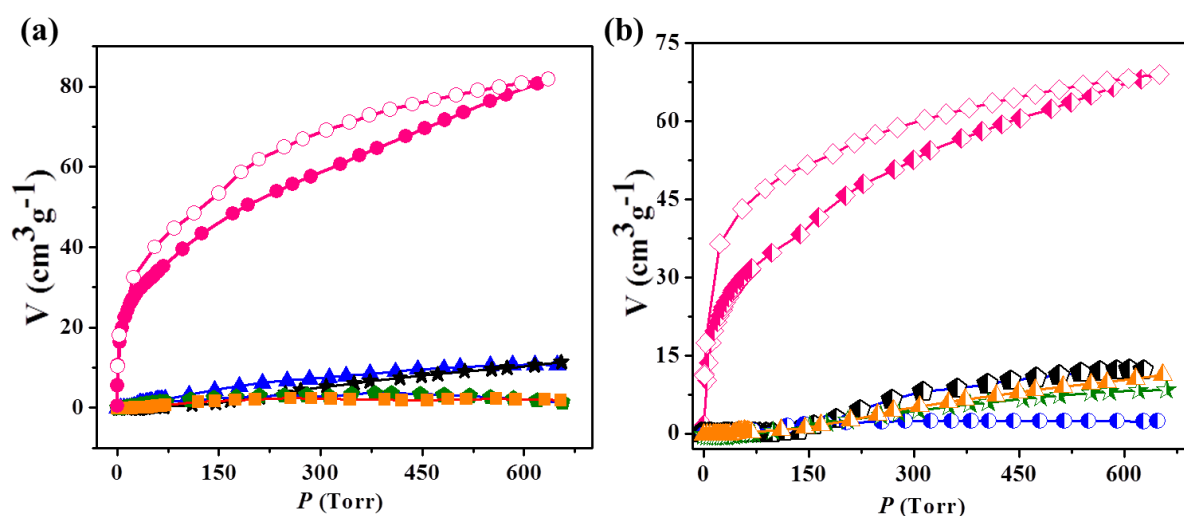


Figure 15: Gas adsorption isotherms of (a) **1'** and (b) **2'** measured at 195 K showing selective uptake of CO₂ (pink) over Ar (orange), N₂ (black), H₂ (green) and O₂ (blue).

and (c) pore size is not sufficient enough to capture bigger N₂ molecules in the activated sample. On the other hand, CO₂ (kinetic diameter 3.3 Å) adsorption measurements at 195 K for both **1'** and **2'** exhibit typical type I profile suggesting microporous nature of the frameworks (Figure 15). The Langmuir and BET surface areas calculated from the CO₂ isotherms are ~ 251 and 235 m² g⁻¹ for **1'** and ~ 214 and 200 m² g⁻¹ for **2'** respectively. The storage capacities of **1'** and **2'** are of about 16 wt% (81 cm³ g⁻¹, 2.8 CO₂ per formula unit) and 13.5 wt% (69 cm³ g⁻¹, 3.4 CO₂ per formula unit), respectively. The hysteretic sorption profiles in both cases are attributed to the diffusion barrier during desorption, resulted from the strong interaction of the CO₂ molecules with the adsorptive sites (e.g. –N=N– and –COO) of the framework. Both of the frameworks reveal to be CO₂-philic in nature *i.e.* CO₂ selective as realized from exclusion over other gases (N₂/Ar/O₂/H₂) at 195 K. Such selective CO₂ uptake characteristics of both of the frameworks can be explained from the strong interaction between CO₂ molecules (quadrupole moment of CO₂: -1.4 × 10⁻³⁹ C m²) and framework wall decorated with polar functional groups and aromatic π cloud of the linkers. It is also reflected in the high values of isosteric heat of adsorption, q_{st} , ϕ , ~ 33.6 and 31.5 kJ mol⁻¹ for **1'** and **2'**, respectively as calculated from the Dubinin–Radushkevich (DR) equation.^{25b}

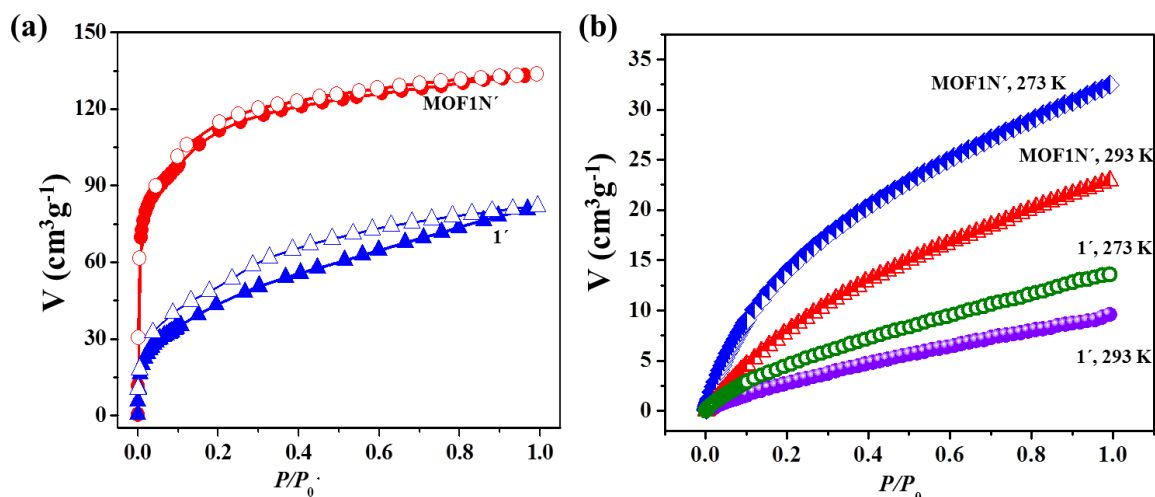


Figure 16: (a) CO₂ adsorption isotherms (at 195 K) of **1'** (blue triangle) and **MOF1N'** (red circle), (b) CO₂ adsorption isotherms of **1'** and **MOF1N'** measured at 273 and 293 K.

MOF1N' shows interesting adsorption behaviour compared to bulk **1**. N₂ Adsorption isotherm of **MOF1N'** at 77 K shows similar signature as of bulk **1'** (Figure 14). But the CO₂ adsorption isotherm shows typical type I adsorption profile with significant higher uptake i.e. 133 cm³g⁻¹ corresponding to 26.2 wt% (4.7 CO₂ per formula unit) (Figure 16a). This value is higher than bulk **1'** by ~10 wt%. The Langmuir and BET surface areas calculated from the CO₂ isotherm of **MOF1N'** are 412, 385 m² g⁻¹ respectively. Interestingly, higher CO₂ uptake is also observed at 273 K (**1'** = 2.5 wt% and **MOF1N'** = 6.2 wt%) and at 293 K (**1'** = 1.7 wt% and **MOF1N'** = 4.3 wt%) (Figure 16b) for **MOF1N'** than **1**.

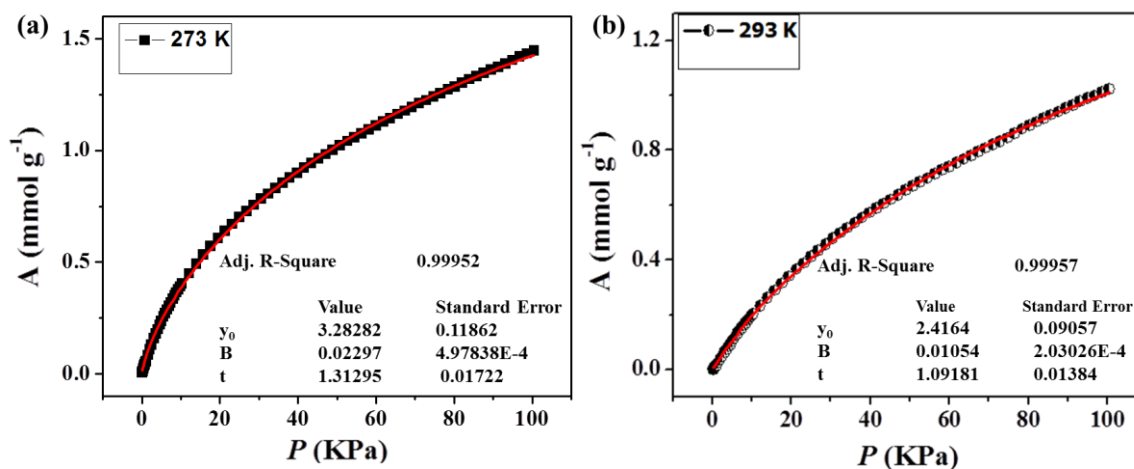


Figure 17: CO₂ adsorption isotherms for **MOF1N'** at (a) 273 and (b) 293 K. The solid line represents the best fit to the data using the Langmuir-Freundlich equation, as described above.

The enhanced CO₂ uptake of **MOF1N'** under all experimental conditions is certainly because of higher specific surface area and smaller diffusion barrier in nanoscale. Furthermore, the adsorption isotherms measured at 273 and 293 K are used for the calculation of enthalpy of adsorption (ΔH_{ads}) applying Clausius–Clapeyron equation which provides a value of 41 kJ mol⁻¹ significantly higher compared to **1'** (Figure 17-18). However, we could not get proper fitting for **1'** using Clausius–Clapeyron equation probably because of very poor uptake CO₂ at 293 and 273 K.

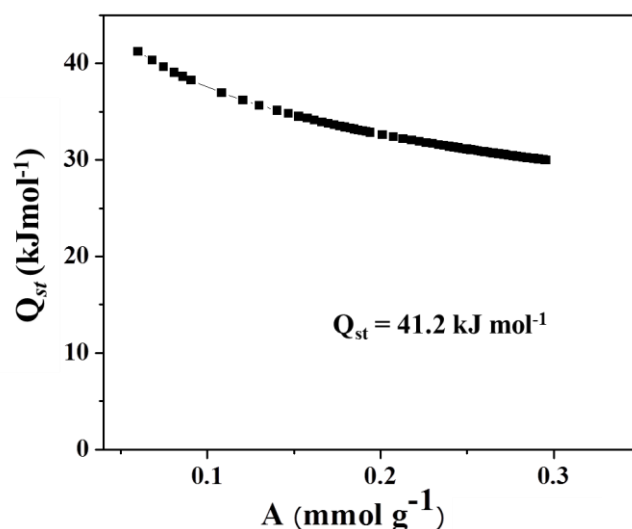


Figure 18: Enthalpy of CO₂ adsorption for **MOF1N'** as calculated using Clausius-Clapeyron equation.

4A.3.5 Solvent vapour adsorption isotherms

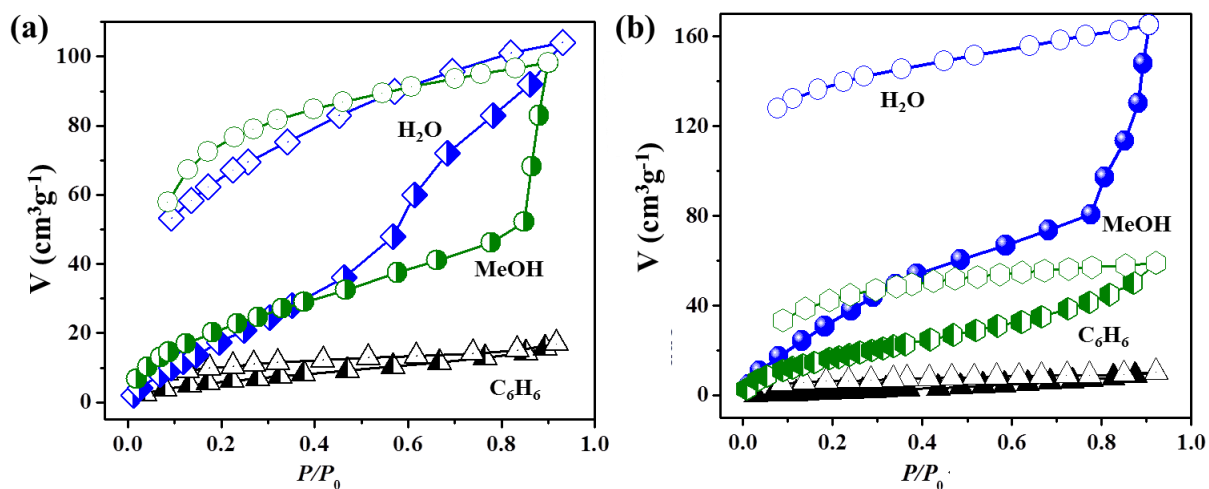


Figure 19: Solvent vapour adsorption isotherms of (a) **1'** and (b) **2'**: H₂O at 298 K, MeOH at 293 K and C₆H₆ at 298 K.

For further understanding of the nature of pore surfaces of **1'** and **2'**, we have carried out solvent vapour adsorption studies with different solvent molecules (H_2O , C_6H_6 at 298 K and MeOH at 293 K) with different polarities (Figure 19). The H_2O (kinetic diameter, 2.64 Å) vapour adsorption profile of **1'**, reveals double step adsorption with a total uptake of $103 \text{ cm}^3 \text{ g}^{-1}$ corresponding to 3.6 H_2O molecules per formula unit (Figure 19a). The existence of second step at $P/P_0 = 0.46$ indicates the presence of different adsorption sites which are not easily accessible due to diffusion barrier, has been overcome by means of structural transformation for further uptake of solvent molecules.²⁷ In case of MeOH (kinetic diameter, 3.6 Å), the first steep type I uptake ($P/P_0 = 0.84$ ($52 \text{ cm}^3 \text{ g}^{-1}$)) is followed by an almost linear increase and finally ended with a total uptake of $98 \text{ cm}^3 \text{ g}^{-1}$ (3.5 MeOH per formula unit). In case of **2'** also, water vapour adsorption isotherm shows double step broad hysteretic profile with a total uptake of $165 \text{ cm}^3 \text{ g}^{-1}$ (8 H_2O molecules per formula unit) (Figure 19b). But, the MeOH profile is type I in nature and the uptake amount is $60 \text{ cm}^3 \text{ g}^{-1}$ (3 MeOH molecules per formula unit). The broad hysteresis in all the H_2O and MeOH isotherms of **1'** and **2'** can be attributed to the vapour induced structural transformation based on different adsorption sites in the frameworks resulting in a diffusion barrier during the desorption. All the profiles are analyzed by the DR equation and the magnitude of adsorbate-adsorbent affinities (for different adsorbates), represented by βE_0 , reflect reasonable high values of 5.00 kJ mol^{-1} for H_2O , 5.78 kJ mol^{-1} for MeOH for **1'**. Similar trend is also followed by **2'**, 4.91 kJ mol^{-1} H_2O and 5.75 kJ mol^{-1} for MeOH. For both cases, non-polar solvent benzene (kinetic diameter, 5.3 Å) adsorption measurements are carried out and found to be excluded by both the frameworks. These observations are indicative of hydrophilic polar pores surfaces in both **1**, and **2** as both the frameworks composed of the similar linkers. These results also support that the azo, carboxylate groups and additional aromatic π clouds from azpy and bpdC linkers make the ideal polar pore surfaces for selective CO_2 uptake at 195 K.

4A.3.6 Solvent vapour adsorption isotherms of MOF1N' vs. **1'** and kinetic studies

We have already mentioned that MOF1N' shows 10 wt% higher CO_2 uptake compared to bulk **1'**. To support our proposed conjecture based on diffusion barrier, water vapour adsorption measurement is carried out with both bulk and nano to understand

from thermodynamic and kinetic point of view. The water vapour adsorption isotherm of **MOF1N'** (Figure 20a) shows type I nature rather than stepwise profile with a total uptake of $129 \text{ cm}^3 \text{ g}^{-1}$ ($4.6 \text{ H}_2\text{O}$ per formula unit), higher than **1'**. In order to compare the rate of diffusion of adsorbates in nanoscale **MOF1N'** and bulk **1'**, the measurements of water

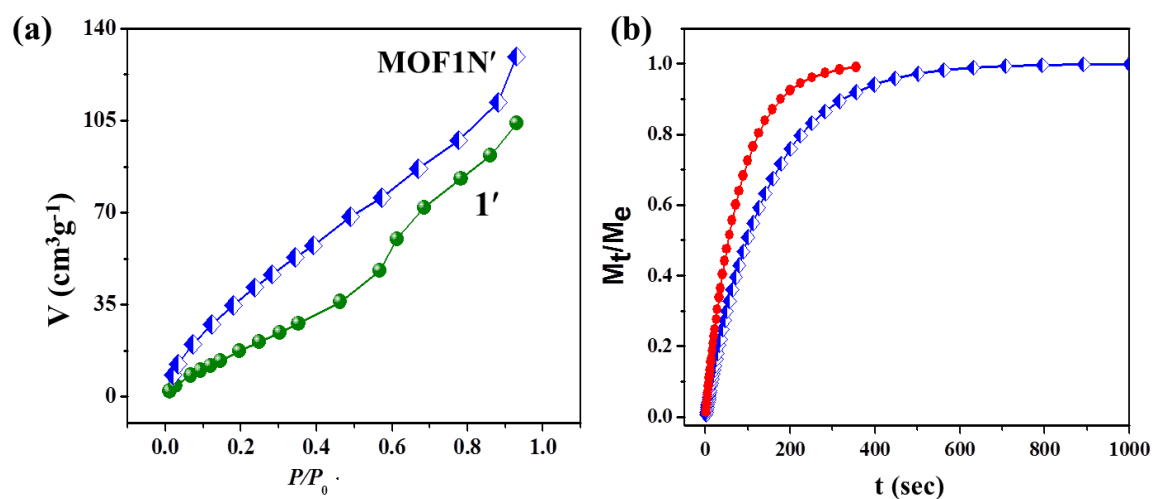


Figure 20: (a) Water vapour adsorption isotherms at 298 K, (b) kinetics of adsorption of water on **1'** (blue square) and **MOF1N'** (red circles) at 298 K (fitted into LDF mass diffusion model); shows higher mass diffusion in **MOF1N'** compared to bulk phase **1'**.

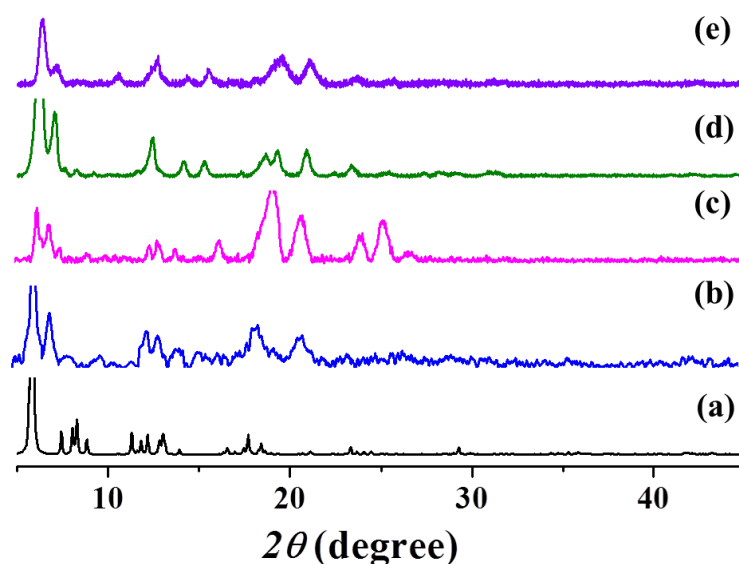


Figure 21: PXRD of (a) simulated, (b) **1'** desolvated, (c) **1'** after adsorption, (d) **MOF1N'** desolvated and (e) **MOF1N'** after adsorption.

vapour adsorption kinetics have been carried out considering the convenience and available instrumental set up. The kinetic data have been fitted next to linear driving force mass transfer (LDF) model because this LDF model is found to provide satisfactory descriptions in most cases of adsorption kinetics of various gases/vapours on carbon molecular sieves, active carbons and even MOF.^{21, 28-31} The LDF model is described by the following equation,

$$M_t/M_e = 1 - \exp(-kt)$$

Where M_t is the mass uptake at time t , M_e is the mass uptake at equilibrium, and k is the kinetic rate constant. Plot of M_t/M_e vs t shows distinct differences between rate of mass diffusion between **1'** and **MOF1N'** at a particular time (Figure 20b). It is observed that the **MOF1N'** shows much faster rate of adsorption compared to **1'** and M_t/M_e value reaches to 1 i.e. towards equilibrium. It is also evident from the kinetic rate constant values; for **1'** ($P/P_0 = 0.1078$) and **MOF1N'** ($P/P_0 = 0.1041$), the values are $7.1 \times 10^{-3} \text{ sec}^{-1}$ and $1.29 \times 10^{-2} \text{ sec}^{-1}$ respectively. This result unequivocally suggests that the diffusion barrier is significantly small in **MOF1N'** compared to bulk **1** as realized from the higher H₂O uptake in nanoscale assisted by higher mass transfer kinetics. The type I profile in **MOF1N'** rather than step wise uptake in **1'** also indicates ease of diffusion at nanoscale. In nanoscale, the path length for accessing different adsorptive sites in the consecutive pores, i.e. diffusion path length is considerably small compared to bulk scale. Therefore we did not observe any step for nanocrystal. PXRD measured after adsorption shows similar pattern for both, **1'** and **MOF1N'** (Figure 21). This is clear that by changing the crystal size and morphology, the kinetic behaviour of crystals is altered significantly. This argument is also applicable for higher CO₂ uptake in **NMOF1** than bulk. Probably due to this size related effect, the activation energy required for structural transformation is altered significantly.²¹ It is also possible that the intermediate state during the adsorption might have changed due to the different crystal size, morphology which affect the overall adsorption kinetics.^{21, 26b}

4A.4 Conclusion

In this chapter, SBU directed two different 3D frameworks have been synthesized from identical organic struts under different reaction conditions. Both the flexible frameworks show selective CO₂ uptake properties. Furthermore, for the first time we have

miniaturized one of these flexible frameworks to nanoscale with spherical morphology through coordination modulation method. Here, OAc^- anions are acting as a coordination modulator directly obtained from metal salt precursor. Furthermore, we have performed a systematic comparative study of adsorption properties in bulk and nanoscale and analysed the results from thermodynamic and kinetic point of view. In nanoscale, the CO_2 storage capacity is improved by 10 wt %. This is also reflected in the solvent vapour adsorption isotherms. These observations are further correlated to higher rate of mass diffusion into the nanophase of the MOF than bulk as supported by accelerated H_2O vapour adsorption kinetics. These systematic detailed investigations will not only help to understand adsorption phenomena deeply but also will certainly contribute to unravel the crystal size-property relationships in a better way that would be useful for development of superior gas separation and catalytic materials.

4A.5 References

1. (a) G. Férey, *Chem. Soc. Rev.* **2008**, *37*, 191 (b) S. Kitagawa, R. Kitaura, S. I. Noro, *Angew. Chem., Int. Ed.* **2004**, *43*, 2334 (c) T. K. Maji, S. Kitagawa, *Pure Appl. Chem.* **2007**, *79*, 2155 (d) T. K. Maji, R. Matsuda, S. Kitagawa, *Nat. Mater.* **2007**, *6*, 142 (e) R. Haldar, T. K. Maji, *CrystEngComm.* **2013**, *15*, 9276.
2. (a) H. K. Chae, M. Eddaoudi, J. Kim, S. I. Hauck, J. F. Hartwig, M. O'Keeffe, O. M. Yaghi, *J. Am. Chem. Soc.* **2001**, *123*, 11482 (b) M. Eddaoudi, D. B. Moler, H. L. Li, B. L. Chen, T. M. Reineke, M. O'Keeffe, O. M. Yaghi, *Acc. Chem. Res.* **2001**, *34*, 319 (c) L. Pan, B. Parker, X. Huang, D. H. Olson, J. Y. Lee, J. J. Li, *J. Am. Chem. Soc.* **2006**, *128*, 4180 (d) R. Matsuda, R. Kitaura, S. Kitagawa, Y. Kubota, R. V. Belosludov, T. C. Kobayashi, H. Sakamoto, T. Chiba, M. Takata, Y. Kawazoe, Y. Mita, *Nature* **2005**, *436*, 238 (e) J. Sahu, M. Ahmad, P. K. Bharadwaj, *Cryst. Growth Des.* **2013**, *13*, 2618.
3. (a) P. Kanoo, R. Matsuda, M. Higuchi, S. Kitagawa, T. K. Maji, *Chem. Mater.* **2009**, *21*, 5861 (b) P. Kanoo, K. L. Gurunatha, T. K. Maji, *J. Mater. Chem.* **2010**, *20*, 1322 (c) Ma, S. Q.; Sun, D. F.; Simmons, J. M.; Collier, C. D.; Yuan, D. Q.; Zhou, H. C. *J. Am. Chem. Soc.* **2008**, *130*, 1012 (d) A. Santra, I. Senkovska, S. Kaskel, P. K. Bharadwaj, *Inorg. Chem.* **2013**, *52*, 7358.
4. (a) H. K. Liu, W. Y. Sun, W. X. Tang, T. Yamamoto, N. Ueyama, *Inorg. Chem.* **1999**, *38*, 6313 (b) M. V. Suresh, S. J. George, T. K. Maji, *Adv. Funct. Mater.* **2013**, *23*, 5585

- (c) S. Mohapatra, B. Rajeswaran, A. Chakraborty, A. Sundaresan, T. K. Maji, *Chem. Mater.* **2013**, *25*, 1673 (d) K. Jayaramulu, S. K. Katla, S. J. George, M. Eswaramoorthy, T. K. Maji, *Chem. Commun.* **2013**, *49*, 3937 (e) P. Chaturbedy, S. Chatterjee, R. B. Selvi, A. Bhat, M. K. Kavitha, V. Tiwary, A. B. Patel, T. K. Kundu, T. K. Maji, M. Eswarmurthy, *J. Mater. Chem. B*, **2013**, *1*, 939.
5. (a) J. Fan, W. Y. Sun, T. A. Okamura, J. Xie, W. X. Tang, N. Okamura, *New J. Chem.* **2002**, *26*, 199 (b) A. N. Parvulescu, G. Marin, K. Suwinska, V. C. Kravtsov, M. Andruh, V. Parvulescu, V. I. J. Parvulescu, *J. Mater. Chem.* **2005**, *15*, 4234 (c) P. K. Thallapally, J. Tian, R. K. Motkuri, C. A. Fernandez, S. J. Dalgarno, B. P. McGrail, J. E. Warren, J. L. Atwood, *J. Am. Chem. Soc.* **2008**, *130*, 16842.
6. (a) P. Horcazada, C. Serre, M. Sebban, F. Taulelle, G. Férey, *Angew. Chem. Int. Ed.* **2006**, *45*, 5974 (b) P. Horcazada, C. Serre, G. Maurin, N. A. Ramsahye, F. Balas, M. Vallet-Regi, M. Sebban, F. Taulelle, G. Férey, *J. Am. Chem. Soc.* **2008**, *130*, 6774 (c) B. Liu, O. Shekhah, H. K. Arslan, J. Liu, C. Wöll, R. A. Fischer, *Angew. Chem. Int. Ed.* **2012**, *51*, 807.
7. (a) S. Henke, R. Schmidt, J. D. Grunwaldt, *Chem. Eur. J.* **2010**, *16*, 14296 (b) Z. Q. Wang, S. M. Cohen, *J. Am. Chem. Soc.* **2009**, *131*, 16675 (c) P. K. Thallapally, J. W. Grate, R. K. Motkuri, *Chem. Commun.* **2012**, *48*, 347 (d) H. Arslan, O. Shekhah, F. Wieland, M. Paulus, C. Sternemann, M. Schrör, S. M. Tolan, R. A. Fischer, C. Wöll, *J. Am. Chem. Soc.* **2011**, *133*, 8158.
8. (a) S. Ma, D. Sun, M. Ambrogio, J. A. Fillinger, S. Parkin, H. C. Zhou, *J. Am. Chem. Soc.* **2007**, *129*, 1858 (b) D. J. Tranchemontagne, J. L. Mendoza-Cortés, M. O'Keeffe, O. M. Yaghi, *Chem. Soc. Rev.* **2009**, *38*, 1257 (c) S. Diring, S. Furukawa, Y. Takashima, T. Tsuruoka, S. Kitagawa, *Chem. Mater.* **2010**, *22*, 4531.
9. G. Férey, C. Serre, *Chem. Soc. Rev.* **2009**, *38*, 1380.
10. D. Bradshaw, J. E. Warren, M. J. Rosseinsky, *Science* **2007**, *315*, 977.
11. M. P. Suh, Y. E. Cheon, *Aust. J. Chem.* **2006**, *59*, 605.
12. C. J. Kepert, *Chem. Commun.* **2006**, *7*, 695.
13. A. J. Fletcher, K. M. Thomas, M. J. Rosseinsky, *J. Solid State Chem.* **2005**, *178*, 2491.
14. K. Uemura, R. Matsuda, S. Kitagawa, *J. Solid State Chem.* **2005**, *178*, 2420.

15. A. Kondo, H. Noguchi, L. Carlucci, D. M. Proserpio, G. Ciani, H. Kajiro, T. Ohba, H. Kanoh, K. Kaneko, *J. Am. Chem. Soc.* **2007**, *129*, 12362.
16. P. L. Llewellyn, S. Bourrelly, C. Serre, Y. Filinchuk, G. Férey, *Angew. Chem. Int. Ed.* **2006**, *45*, 7751.
17. A. Carne, C. Carbonell, I. Imaz, D. MasPOCH, *Chem. Soc. Rev.* **2011**, *40*, 291.
18. T. Uemura, Y. Hoshino, S. Kitagawa, K. Yoshida, S. Isoda, *Chem. Mater.* **2006**, *18*, 992.
19. P. Horcajada, C. Serre, D. Grosso, C. Boissière, S. Perruchas, C. Sanchez, G. Férey, *Adv. Mater.* **2009**, *21*, 1931.
20. O. K. Farha, A. M. Spokoyny, K. L. Mulfort, S. Galli, S. Hupp, C. A. Mirkin, *Small*, **2009**, *5*, 1727.
21. D. Tanaka, A. Henke, K. Albrecht, M. Moeller, K. Nakagawa, S. Kitagawa, J. Groll, *Nature* **2010**, *2*, 410.
22. (a) T. Tsuruoka, S. Furukawa, Y. Takashima, K. Yoshida, S. Isoda, S. Kitagawa, *Angew. Chem. Int. Ed.* **2009**, *48*, 4739 (b) SMART (V 5.628), SAINT (V 6.45a), Xprep, SHELXTL; Bruker AXS Inc. Madison, Wisconsin, USA, 2004 (c) A. Altomare, G. Cascarano, C. Giacovazzo, A. Gualaradi, *J. Appl. Crystallogr.* **1993**, *26*, 343 (d) Sheldrick, G. M., SHELXL 97, Program for Crystal Structure Solution and Refinement, University of Göttingen, Göttingen, Germany, 1997 (e) A. L. Spek *J. Appl. Crystallogr.* **2003**, *36*, 7 (f) G. M. Sheldrick. G. M. SHELXS 97, Program for the Solution of Crystal Structure, University of Göttingen, Germany, 1997 (g) L. J. Farrugia, *J. Appl. Crystallogr.* **1999**, *32*, 838 (i) R. T. Yang, *Gas Separation by Adsorption Processes*, Butterworth, Boston, 1997 (j) F. Rouquerol, J. Rouquerol, K. Sing, *Adsorption by Powders and Solids, Principles, Methodology, and Applications*, Academic Press, London, 1999 (k) P. Kanoo, A. C. Ghosh, S. T. Cyriac, T. K. Maji, *Chem. Eur. J.* **2012**, *18*, 237.
23. (a) G. M. Sheldrick, *SADABS: Empirical Absorption Correction Program; University of Göttingen: Göttingen, Germany*, 1997 (b) V. A. Blatov, L. Carlucci, G. Ciani, D. M. Proserpio, *CrystEngComm.* **2004**, *6*, 378 (c) V. A. Blatov, A. P. Shevchenko, V. N. Serezhkin, *J. Appl. Cryst.* **2000**, *33*, 1193.
24. J. Y. Park, C. Aliaga, J. R. Renzas, H. Lee, G. A. Somorjai, *Catal. Lett.* **2009**, *129*, 1.
25. (a) C. M. Nagaraja, R. Haldar, T. K. Maji, C. N. R. Rao, *Cryst. Growth Des.* **2012**, *12*, 975 (b) M. M. Dubinin, *Chem. Rev.*, **1960**, *60*, 235 (c) P. Horcajada, C. Serre, D. Grosso,

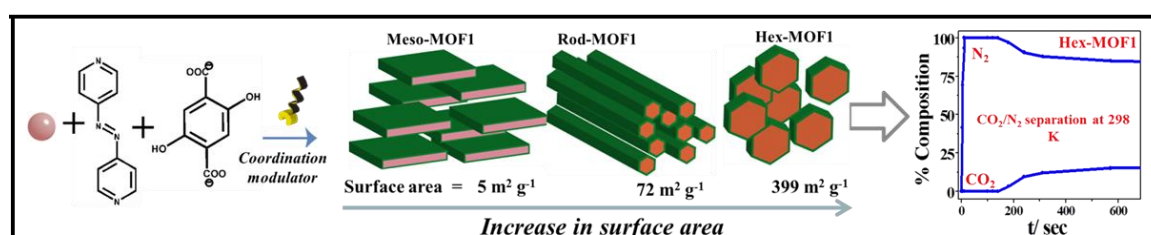
- C. Boissière, S. Perruchas, C. Sanchez, G. Férey, *Adv. Mater.* **2009**, *21*, 1931 (d) A. Umemura, A. Diring, S. Furukawa, H. Uehara, T. Tsuruoka, S. Kitagawa, *J. Am. Chem. Soc.* **2011**, *133*, 15506.
26. (a) H. A. Patel, S. H. Je¹, J. Park¹, P. Dennis, D. P. Chen, Y. Jung, C. T. Yavuz¹, A. Coskun, *Nat. Comm.* **2013**, *4*, 1357 (b) Y. Sakata, S. Furukawa, M. Kondo, K. Hirai, N. Horike, Y. Takashima, H. Uehara, N. Louvain, M. Meilikhov, T. Tsuruoka, S. Isoda, W. Kosaka, O. Sakata, S. Kitagawa, *Science*, **2013**, *339*, 193.
27. P. Kanoo, K. L. Gurunatha, T. K. Maji, *J. Mater. Chem.* **2010**, *20*, 1322.
28. A. J. Fletcher, E. J. Cussen, T. J. Prior, M. Rosseinsky, C. J. Kepert, K. M. Thomas, *J. Am. Chem. Soc.* **2001**, *123*, 10001.
29. C. R. Reid, I. P. O'koye, K. M. Thomas, *Langmuir* **1998**, *14*, 2415.
30. C. R. Reid, Thomas, K. M. *Langmuir* **1999**, *15*, 3206.
31. A. W. Harding, N. J. Foley, P. R. Norman, D. C. Francis, K. M. Thomas, *Langmuir* **1998**, *14*, 3858.

Chapter 4B

*Oriented Attachment Growth of
Anisotropic Meso/Nanoscale MOFs:
Tunable Surface Area and CO₂
separation*

Chapter 4B

Oriented Attachment Growth of Anisotropic Meso/Nanoscale MOFs: Tunable Surface Area and CO₂ separation



Summary: Scaling down bulk MOFs to meso/nanoscale is of paramount importance due to improved diffusion kinetics and surface area. To achieve this, crystal growth mechanism and evolution of different morphologies and dimensions of MOFs in nano/meso regime need to be fully understood. This chapter reports downsizing of a mixed-linker based 3D MOF, $\{[\text{Zn}_2(\text{H}_2\text{dht})(\text{dht})_{0.5}(\text{azpy})_{0.5}(\text{H}_2\text{O})] \cdot 4\text{H}_2\text{O}\}_n$ [H_4dht = 2,5-dihydroxyterephthalic acid azpy = 4,4'-azobipyridine] and to nano/mesoscale by coordination modulation method using *n*-dodecanoic acid as a modulator. We demonstrate changes in morphology and dimensionality (hexagonal nanoparticle to nanorod to mesosheet) with modulator concentration. The time-dependent FESEM studies of the products at different stages of synthesis suggest that the transformation to different morphologies is driven by the kinetically controlled oriented attachment (OA) growth mechanism. Among the various morphologies, hexagonal nanoparticles show strikingly improved BET surface area (399 m² g⁻¹, from N₂ adsorption at 77 K) compared to its bulk form due to reduced diffusion barrier at nanoscale inferred from higher mass transfer kinetics. This is also reflected in better CO₂/N₂ separation efficiency in breakthrough column experiment at ambient conditions. This unprecedented on/off porosity with respect to N₂ in nano vs. bulk MOF, respectively, is theoretically explained in terms of energetics of adsorption, atomic structural changes and electrostatic interactions between the MOF and adsorbate molecules.

N. Sikdar, M. Bhogra, U. V. Waghmare, T. K. Maji, submitted

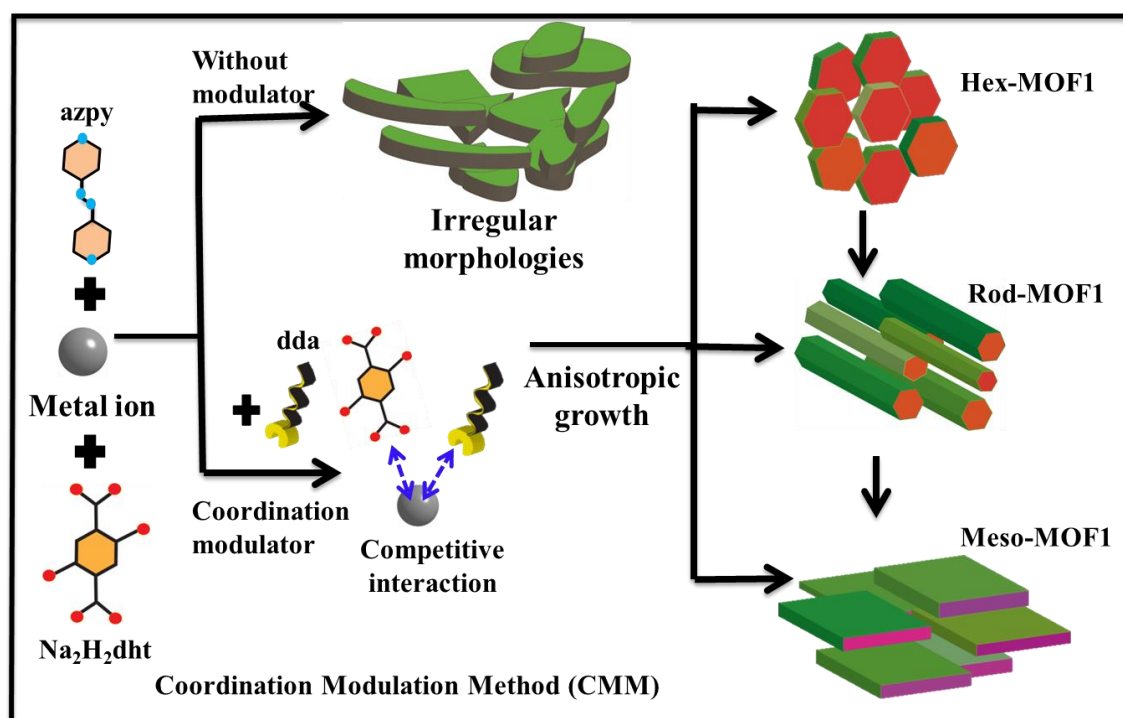
4B.1 Introduction

Nano-sized metals, metal oxides and metal chalcogenides have found widespread applications due to their versatile size, shape and morphology-dependent optical, electronic, magnetic, catalytic and electrochemical properties.¹⁻¹⁰ In recent years, nanoscale metal organic frameworks (NMOFs) have received special attention as they offer significantly enhanced and novel properties compared to their bulk analogue.¹¹⁻¹⁴ Increased textural porosity and active external surface at nanoscale augment the mass transfer kinetics and pore accessibility, thus improving gas sorption and separation, drug delivery and catalytic properties.¹⁵⁻¹⁸ NMOFs also show crystal size, shape and morphology dependent properties, thus making them potential materials with tunable functionalities with the same underlying bulk MOF structure.¹⁵⁻¹⁸ For example, Kitagawa *et al.* have reported that a meta-stable open phase can be realized by crystal downsizing of a flexible MOF and demonstrated the ‘molecular-scale shape-memory effect’.¹⁹ Recent reports have elegantly showed that 2D nanosheets of MOFs can act as superior molecular sieving membrane for gas separation with higher separation selectivity than their other morphologies.^{16, 20-22} However, synthesis of free standing defect free 2D nano/mesosheets is a challenging assignment as the top down approaches based on delamination from bulk MOFs results in irregular morphology with structural damage.¹³

Crystal downsizing of MOFs has been realized by rapid nucleation based on ultrasound, microwave and inverse microemulsion techniques.¹⁴ However, size, shape and dimensionality of MOF particles cannot be precisely controlled with these techniques. The underlying growth mechanism towards different shapes and dimensions is yet to be fully understood, though it was shown in a couple of reports that low dimensional anisotropic crystal growth is feasible by coordination modulation method.^{15, 23-26} Coordination modulation method (CMM) is known as a highly rational approach, wherein a modulator with a similar functional group as that of the linkers is employed.¹⁴ The competitive interactions between linkers and the modulator alter the coordination equilibrium at the interface during crystal growth process, and modulation on specific crystallographic planes leads to anisotropic crystal growth (i.e. 1D, 2D nanomaterials etc.). Generally, kinetically controlled oriented attachment (OA) growth of nanocrystals is a well-studied mechanism for designing and fabrication of different inorganic metal/metal oxide anisotropic nanomaterials.²⁷⁻²⁸ Similarly, by adjusting growth rates of different crystal facets should be pertinent approach for the growth of anisotropic low dimensional

MOF materials based on a particular modulator by inhibiting crystal growth in certain crystallographic directions. With this approach, scaling down of a particular MOF to different dimensions/morphologies would not only help for understanding the underlying thermodynamics and kinetics of growth mechanism, but also will allow the study of shape and morphology dependent tailorable properties.

To the best of our knowledge, dimensionality controlled tunable surface area in nanoscale for a particular MOF is yet to be explored. Furthermore, there is little theoretical understanding of the mechanism of anisotropic growth to different dimensional forms and size-dependent gas diffusion in terms of energetics and atomic structural changes in such systems. Recently, Zeng *et al.* have reported different nanomorphologies from a low symmetry MOF, Cu-HBTC-1.²⁹ However, modulation planes and growth mechanisms in such low-symmetry MOFs are yet to be understood, which is paramount to synthesis of NMOFs for tailorable morphology.



Scheme1: Schematic representation for fabrication of 3D metal–organic framework to different nano/meso morphologies by applying conventional coordination modulation method.

Here, we have strategically chosen a mixed-linkers based low symmetry 3D MOF $\{Zn_2(H_2dht)(dht)_{0.5}(azpy)_{0.5}(H_2O)\} \cdot 4H_2O$ (**1**), [$H_4dht = 2,5$ -dihydroxyterephthalic acid azpy = 4,4'-azobipyridine] reported earlier by our group, for scaling down to

nano/mesoscale as it contains crystallographically independent three different dicarboxylate linkers (H_2dht_a , dht and H_2dht_b) along three different directions.³⁰ We envisage that a suitable monocarboxylate modulator would modulate the different crystallographic plane based on its concentration which will ensure the low dimensional anisotropic growth toward nano/mesoscale. Here, dodecanoic acid (dda) has been used as a modulator and synthesized three different nano/meso scale MOFs *viz.* hexagonal nanoparticle (**hex-MOF1**), 1D nanorod (**rod-MOF1**) and 2D mesosheet (**meso-MOF1**) (Scheme 1). We observed an unprecedented change in dimensionality, 0D→1D→3D by oriented attachment growth. **Hex-MOF1** showed surface area of $399\text{ m}^2\text{ g}^{-1}$ based on N_2 adsorption at 77 K and high CO_2 uptake (at 298 K, $P \sim 1$ bar) compared to its bulk counterpart. We provide a detailed explanation for the differences in adsorption in terms of energetics of adsorption, atomic structural changes and electrostatic interactions between MOF and adsorbates. The size-dependent uptake of N_2/CO_2 is further reflected in high breakthrough time of CO_2 in NMOF compared to bulk **1**. To the best of our knowledge, such in-depth analysis of size and dimensionally controlled microporosity or gas adsorption property in bulk/NMOF has been carried out for the first time and it is important both fundamentally and technologically, to understand crystal growth mechanism toward tailorable applications.

4B.2 Experimental section

4B.2.1 Materials

All the reagents employed were commercially available and used as provided without further purification. $Zn(NO_3)_2 \cdot 6H_2O$ was obtained from Spectrochem. 2,5-dihydroxyterephthalic acid, dodecanoic acid were obtained from Sigma Aldrich Co. 4,4'-azobipyridine was synthesised following the literature procedure.³⁰

4B.2.2 Physical measurements

Elemental analysis was carried out using a Thermo Fischer Flash 2000 Elemental Analyzer. IR spectra were recorded on a Bruker IFS 66v/S spectrophotometer using KBr pellets in the region $4000\text{--}400\text{ cm}^{-1}$. Thermogravimetric analysis (TGA) was carried out on METTLER TOLEDO TGA850 in nitrogen atmosphere (flow rate = 50 mL min^{-1}) in the temperature range of $30\text{--}700\text{ }^\circ\text{C}$ (heating rate $3\text{ }^\circ\text{C min}^{-1}$). Powder XRD pattern of the compounds were recorded by using $Cu\text{-K}\alpha$ radiation (Bruker D8 Discover; 40 kV, 30

mA). The scanning electron microscopy images were obtained using Nova Nanosem 600, FEI field emission scanning electron microscope (FESEM). Transmission electron microscopy (TEM) images were taken with a JEOL JEM-3010 transmission electron microscope operating at 200 kV. A Bruker diInnova scanning probe microscope used in a tapping mode was employed for all atomic force microscopy (AFM) experiments. Measurements were made using silicon cantilevers. The drive frequency for tapping mode was set near the resonance frequency of cantilevers (250-350 KHz). Images were recorded in a $20 \times 20 \mu\text{m}$ and $7.6 \times 7.6 \mu\text{m}$ scan size window at a scan speed of 1 KHz and resolution of 512×512 . The Nanoscope software was used to obtain the three-dimensional image representations and quantitative measurements of surface topological features.

4B.2.3 Adsorption studies

The adsorption isotherms of N_2 (77 K) and CO_2 at (298 K) using the dehydrated sample of **1** (**1'**), **rod-MOF1**, **meso-MOF1** and **hex-MOF1** were measured by using QUANTACHROME QUADRASORB-SI analyser. The MOF **1** and NMOFs were activated at 150 °C for 24 hour under 1×10^{-1} Pa vacuum prior to measurement of the isotherms. All the gases used for adsorption measurement are of scientific/research grade with 99.999% purity. Dead volume was measured with He gas. The adsorbates were placed into the sample tubes, and then the change of the pressure was monitored and the degree of adsorption was determined by the decrease in pressure at the equilibrium state. All operations were computer-controlled and automatic.

The adsorption isotherms of MeOH measured in the vapour state at 293 K by using a BELSORP-aqua volumetric adsorption instrument from BEL, Japan. All the samples of about ~ 100 – 150 mg were prepared by adopting a similar procedure mentioned earlier (*vide supra*) prior to measurement of the isotherms. The solvent molecules used to generate the vapour were degassed fully by repeated evacuation. Dead volume was measured with He gas. The adsorbate was placed into the sample tube, then the change of the pressure was monitored, and the degree of adsorption was determined by the decrease in pressure at the equilibrium state. All operations were computer controlled and automatic.

Breakthrough experiments were performed using a column (packed with about ~ 250 mg of **1'** and **hex-MOF1** powder) with 3 cm long length and 0.3 cm diameter. The

sample was first activated at 150 °C for 12 h prior to loading in column. After loading the sample was again activated with He flow for 30 mins. CO₂/N₂ (15/85) stream was passed through the column with He. The flow was continuous and the flow rate was regulated by MFC. The partial pressure of the gas mixture was kept at $p = 5$ kPa. The gas stream at the outlet of the column was analyzed on-line with a GC. The space velocity was kept at 4.31 min⁻¹.

4B.2.4 Preparation of SEM and TEM samples

For SEM and TEM, samples were prepared by dispersing the powder samples in MeOH. 5 μL solution was drop cast onto a small piece of silicon wafer and dried in air for FESEM. The samples were prepared in the same way as described above but the drop cast was made onto carbon-coated TEM grid for TEM.

4B.2.5 Computational details

Our calculations are based on first-principles density functional tight binding (DFTB) method as implemented in DFTB+.^{31a} Slater-Koster files are used from parameter sets *znorg-0-1* and *mio-1-1* to parameterize the interactions between the elements of MOF framework. van der Waals (vdW) interactions are included with a Lennard-Jones dispersion,^{31b} as implemented in DFTB+, with parameters taken from Universal Force Field (UFF).^{31c} The atomic positions of the experimental structure of bulk-MOF are relaxed, keeping cell vectors fixed, to obtain a minimum energy structure. The energy convergence tests with respect to \mathbf{k} mesh show (1×1×1) mesh is sufficiently accurate (6 meV/unit cell) for the present calculations. The average heat of adsorption (ΔH) is calculated by the relation:

$$\Delta H_{\text{ads}} = (E_{\text{MOF-N}_2/\text{CO}_2} - E_{\text{MOF}} - E_{\text{nN}_2/\text{CO}_2})/n$$

Partial atomic charges (δ) are obtained from Mulliken population analysis, which allows us to understand the electronic changes on the atoms in the MOF framework with gas adsorption or introduction of a surface.

4B.2.6 Synthesis of bulk 1

Bulk **1** was prepared following the same procedure mentioned earlier.³⁰ Synthetic conditions for bulk is also tabulated in Table 1.

Table 1. Tabulated form of experimental details.

		Conc. (mmol)	ratio (r) = dda/Na ₂ H ₂ dht	Weight taken (g)	Solvent taken
Na ₂ H ₂ dht (Ligand)	Bulk 1	0.187		0.048	Water (5 mL)
Azpy (Ligand)		0.062		0.011	+
Zn(NO ₃) ₂ · 6H ₂ O		0.25		0.074	2- Methoxyethanol (45 mL)
Dodecanoic acid (dda)	Meso- MOF1	0.0625	0.33	0.0125	Methanol (50 mL)
	Rod- MOF1	0.125	0.66	0.025	
	Hex- MOF1	0.25	1.33	0.05	

4B.2.7 Synthesis of hex-MOF1, rod-MOF1 and meso-MOF1 using dodecanoic Acid (dda) as a modulator

Three different metal solutions containing Zn(NO₃)₂·6H₂O (0.25 mmol, 0.074 g) and dda [with the concentration of 0.062 (0.0125 g), 0.125 (0.025 g) and 0.25 (0.050 g) mmol] are prepared for **meso-MOF1**, **rod-MOF1** and **hex-MOF1**, respectively in 50 mL MeOH. The ligand solution is prepared by dissolving disodium salt of 2,5-dihydroxyterephthalic acid (Na₂H₂dht) (0.187 mmol, 0.048 g) and 4,4'-azobipyridine (azpy) (0.062 mmol, 0.011 g) in a 50 mL solution of 2-methoxyethanol/water (9:1). The ligand solution is stirred for 30 minutes and then metal solution is added to the ligand solution dropwise followed by continuous stirring for thirty minutes. The red coloured precipitates are collected, centrifuged for 3 to 4 times with MeOH and dried in room temperature. The details of syntheses of all these compounds are given in Table 1. These compounds are characterized through PXRD, TGA, FT-IR and elemental analysis. Anal. Calcd.(%) for **meso-MOF1** [Zn₂C₁₇O₁₄H₁₉N₂] C: 53.28; H: 4.09; N: 9.56; found C:

53.11; H: 3.87; N: 9.31. FT-IR (4000–400 cm^{-1}): 3340 (w), 3051 (w), 1604 (s), 1445-1510 (s) cm^{-1} . Anal. Calcd.(%) **rod-MOF1** [$\text{Zn}_2\text{C}_{17}\text{O}_{14}\text{H}_{19}\text{N}_2$] C: 53.28; H: 4.09; N: 9.56; found C: 53.01; H: 3.50; N: 9.12. FT-IR (4000–400 cm^{-1}): 3245 (w), 3051 (w), 1605 (s), 1445-1509 (s) cm^{-1} . Anal. Calcd.(%) **hex-MOF1** [$\text{Zn}_2\text{C}_{17}\text{O}_{14}\text{H}_{19}\text{N}_2$] C: 53.28; H: 4.09; N: 9.56; found C: 53.34; H: 3.55; N: 9.50. FT-IR (4000–400 cm^{-1}): 3280 (w), 3053 (w), 1605 (s), 1446-1510 (s) cm^{-1} .

4B.3 Results and discussion

4B.3.1 Modulation of bulk framework to nanoscale

As reported, **1** is a 3D non-interpenetrating porous framework consisting of crystallographically distinct $\text{H}_2\text{dht}/\text{dht}$ (H_2dht_a , dht and H_2dht_b) and azpy linkers.³⁰ First, H_2dht_a and azpy linkers coordinate to Zn^{II} to build a zigzag chain-like structure, and two such 1D chains form a curvy motif (viewed along c -axis) (Figure 1a). These motifs are further interconnected by the second type of dht linkers to form 2D networks along ac plane (Figure 1b), which are pillared by the third H_2dht_b along b axis to generate a 3D framework (Figure 1c). Bulk **1** has been synthesized by adding a methanolic $\text{Zn}(\text{NO}_3)_2$ solution to a mixed-ligand (azpy and $\text{Na}_2\text{H}_2\text{dht}$) solution of 2-methoxyethanol/water under stirring conditions for 30 mins.³⁰ The well correspondence of the powder diffraction pattern with the simulated one suggests the phase purity of the bulk **1** (Figure 2). FESEM image show large micron-sized particles of irregular shapes (Figure 3). Following the same procedure and stoichiometry of metal ions and linkers as for the bulk MOF, we have isolated three different products on addition of different concentrations of dodecanoic acid (dda) as a modulator, as detailed in Table 1. Interestingly, red precipitation occurs immediately at the onset of reaction when $\text{dda}/\text{Na}_2\text{H}_2\text{dht}$ (r) is 0.33, while onset of product formation gradually increases to ~5-6 and 10 minutes for $r = 0.66$ and $r = 1.33$ with increasing dda concentration. The PXRD patterns of all the three products show similar diffractions as bulk **1** indicating retention of periodic structure as of bulk **1**, and the gradual peak broadening suggesting subsequent downsizing of MOF particles with increasing r (Figure 2). The FESEM and TEM images of the compound obtained at $r = 0.33$, reveal the formation of large 2D mesosheets (**meso-MOF1**). The average length and width of **meso-MOF1** are 5 ± 2 and 3 ± 2 μm , respectively (Figure 1d-e, 4), and the average thickness of the mesosheets are 550 ± 50

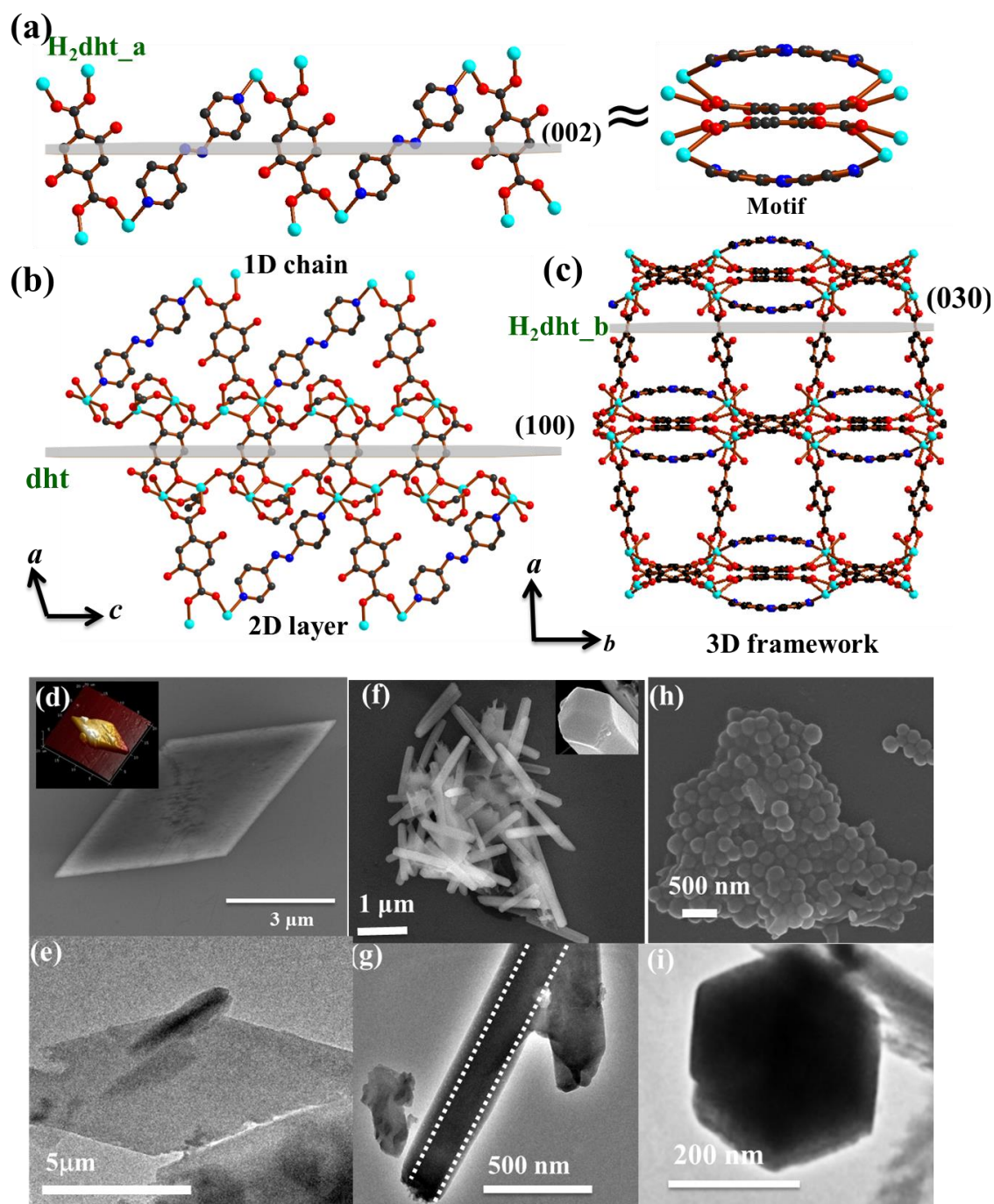


Figure 1: Structural representation of bulk **1** along different crystallographic directions: (a) 1D chain made of azo and dht linker coordinated to Zn^{II} (view of convex motif made of 1D chains), (b) view of 2D layer along ac plane, (d) 3D framework showing three different linkers, (d, f, h) FESEM images of **meso-MOF1** (inset is AFM image of meso sheet along $20 \times 20 \mu m$ scan), **rod-MOF1** and **hex-MOF1**, respectively and (e, g, i) are corresponding TEM images.

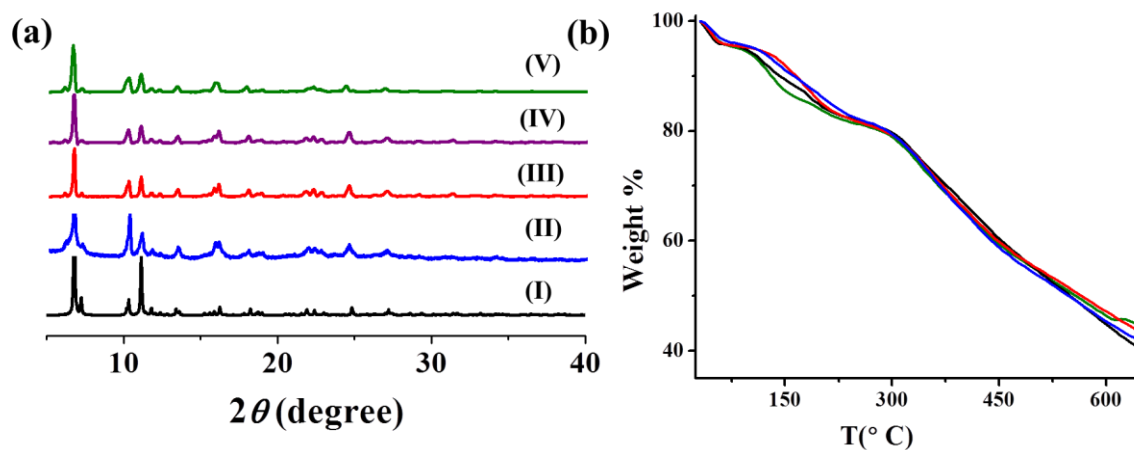


Figure 2: (a) PXRD patterns of bulk and NMOFs: (I) simulated (II) bulk **1** (III) **meso-MOF1** (IV) **rod-MOF1** (V) **hex-MOF1**, (b) TGA profiles for bulk and NMOFs: blue: **1**, red: **rod-MOF1**, black: **meso-MOF1** and green: **hex-MOF1**.

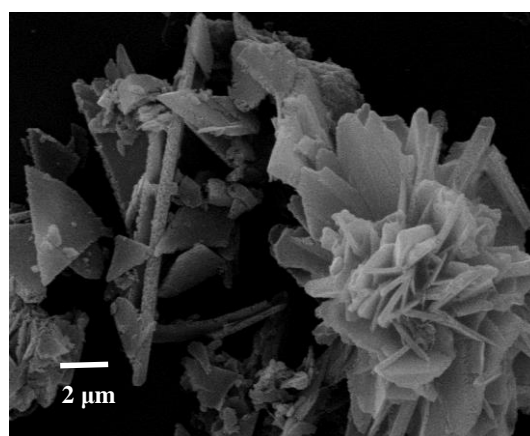


Figure 3: Morphology of bulk **1** without modulator.

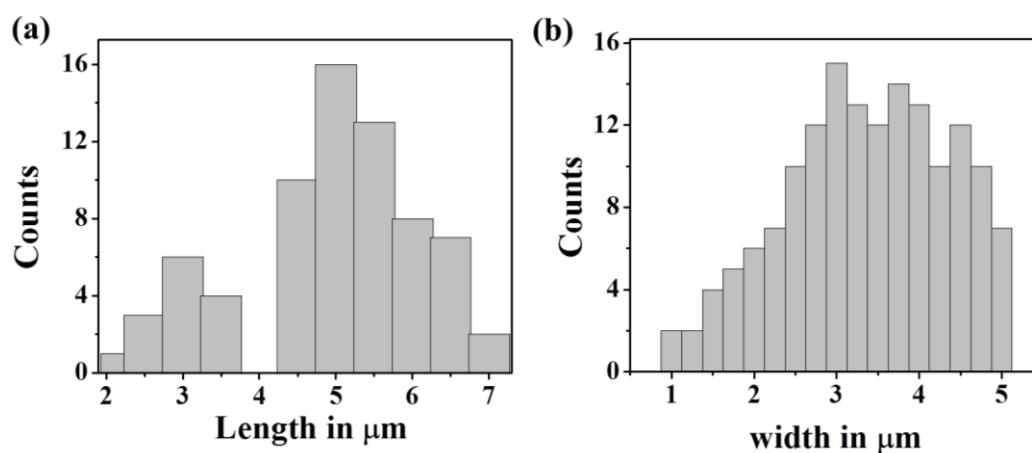


Figure 4: (a) Length distribution of **meso-MOF1**, (b) width distribution of **meso-MOF1**.

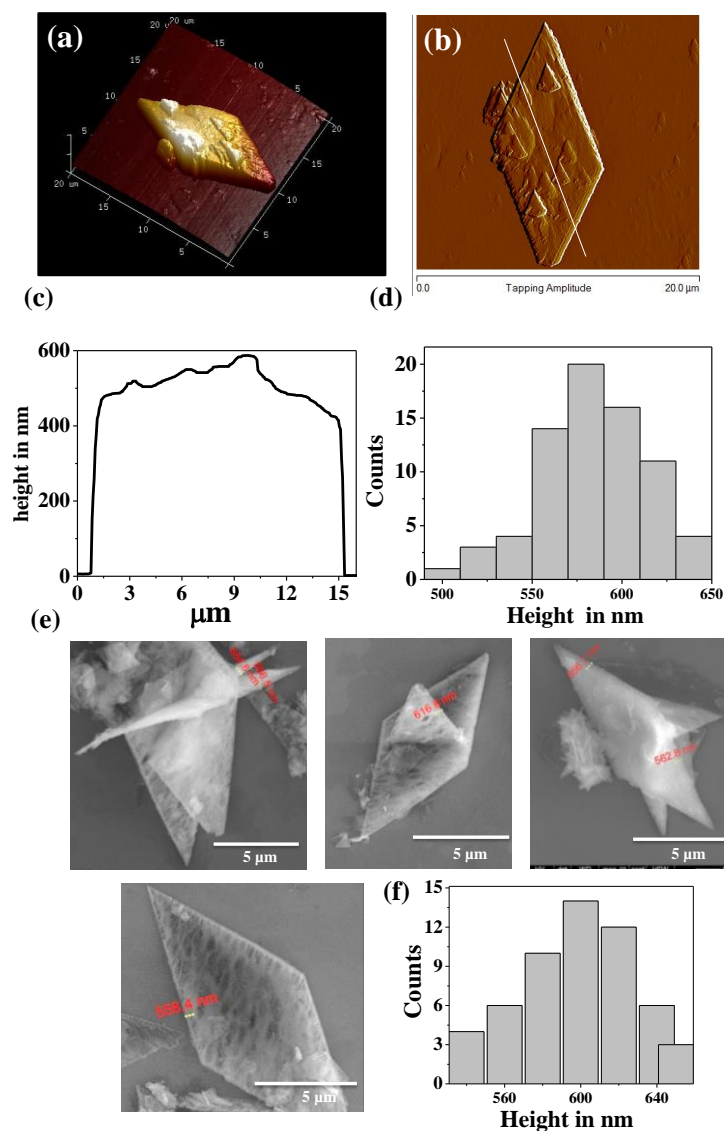


Figure 5: (a-b) AFM images of mesosheet (c) corresponding height profile, (d) distribution of average height of **meso-MOF1**, (e) FESEM images of mesosheet formation stage showing the average height of different mesosheets, (f) average height distribution.

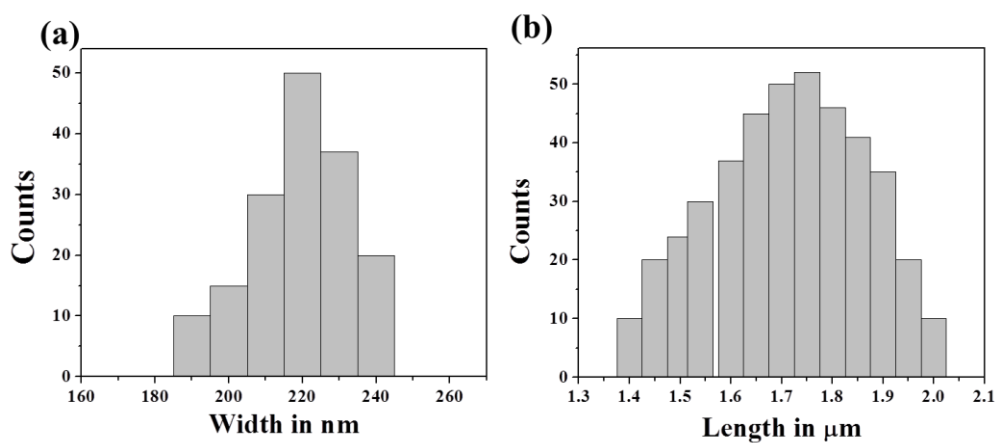


Figure 6: (a) Distribution of diameter **rod-MOF1**, (b) length distribution of **rod-MOF1**.

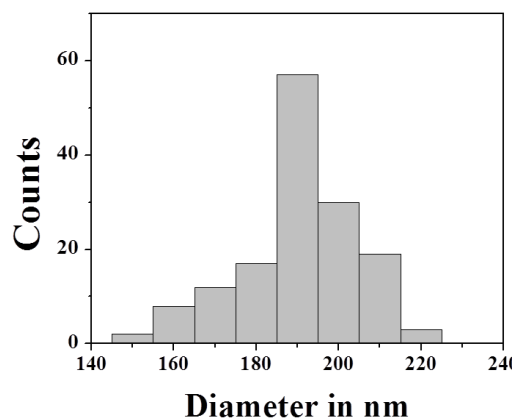


Figure 7: Distribution of diameter of **hex-MOF1**.

nm as characterized by cross-sectional AFM analysis (Figure 1d inset, 5). FESEM studies of the NMOF obtained with $r = 0.66$ show 1D nanorod like morphology (**rod-MOF1**) with an average length (major axis) and diameter (minor axis) of $1.7 \pm 0.5 \mu\text{m}$ and $220 \pm 40 \text{ nm}$, respectively (Figure 1f-g, 6). Interestingly, the product obtained with $r = 1.33$ is hexagonal nanoparticles (**hex-MOF1**) as realized from FESEM studies. In **hex-MOF1**, the length is significantly reduced and an average diameter is about $190 \pm 30 \text{ nm}$ (Figure 1h-i, 7). The time dependent crystallites formation with dda concentration can be understood in terms of the rate of de-protonation of dda (a weak organic acid with a dissociation constant K_a of 5.3 and a dielectric constant of 2.295 at $20 \text{ }^\circ\text{C}$) in the reaction medium, and its attachment with the crystallites (capping behaviour).²² On the addition of small concentrations of dda to the ligand ($\text{Na}_2\text{H}_2\text{dht/azpy}$, $\text{pH} = 9.1$) solution (e.g. $r = 0.33$), the de-protonation of dda [$\text{R}(=\text{C}_{11}\text{H}_{23})\text{CO}_2^- + \text{H}^+$] is almost instantaneous, leading to an immediate nucleation of MOF crystallites. Further, increasing dda concentration interferes $\text{H}_2\text{dht-Zn}$ coordination during nucleation process and slows down the reaction.²³

To uncover the growth mechanism to different dimensionalities, we have carried out FESEM analysis of the products obtained at different time intervals of the reaction performed at $r = 1.33$. The product obtained after five minutes suggests the formation of small nanocrystals with an average diameter of $40 \pm 10 \text{ nm}$ (Figure 8a, 9a). After 15 mins, the isolated product shows the growing phase of **hex-MOF1** with uneven surface based on assembly of these smaller particles (Figure 8b). Thus formation of hexagonal shaped nanocrystals is stemmed by the fusion of smaller primary nanocrystals.^{27-28, 31d} Hexagonal particles with smooth surface form in ~ 30 minutes with an average diameter of 200 ± 30

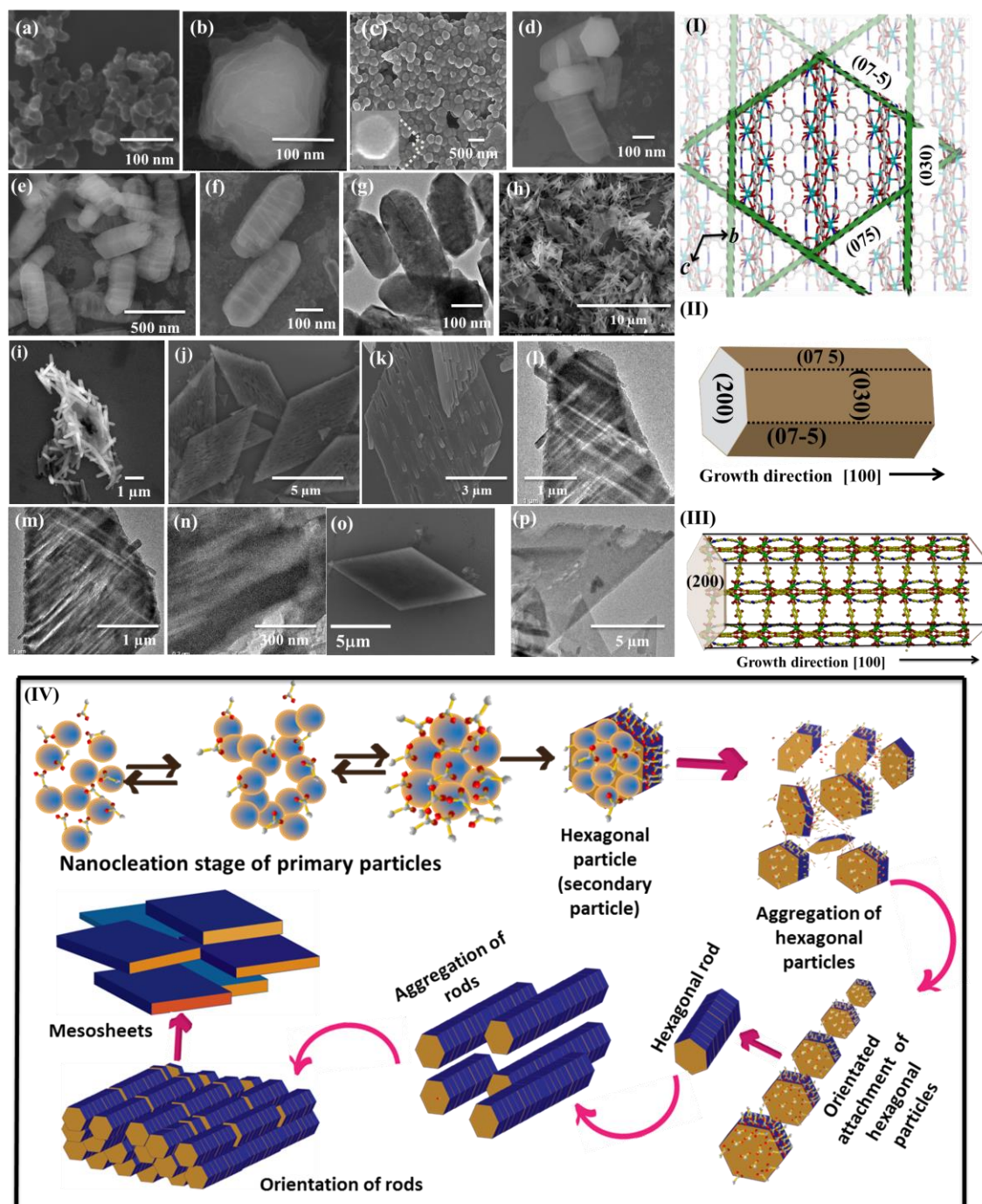


Figure 8: Time dependent study of morphological transformation: (a) FESEM images of small nanoparticles obtained at 5 min, (b) FESEM image showing growing stage of hexagonal nanoparticle obtained at 15 min, (c) FESEM image of hexagonal nanoparticle with smooth surface obtained at 30 min, (d-g) FESEM and TEM images of intermediate hexagonal nanorods (with horizontal stacking on the surface) obtained at 1 hour, (h-i) FESEM images of longer nanorods obtained at two hour, (j-m) FESEM and TEM images of mesosheet formation owing to attachment of nanorods (n) TEM image showing closure view of nanorods stacking in mesosheet (o-p) smoothing of mesosheet surface (I, II, III) modulation and growth planes of hexagonal rod (IV) proposed morphological transition from hexagonal particle *via* nanorods to mesoscale sheets by oriented attachment growth mechanism.

nm (Figure 8c, 9b). Then we continued the same reaction and with one hour of reaction time, we observed a change in morphology based on assembly of the hexagonal particles. This is an intermediate phase of rod-shaped morphology with an average length of 600 ± 40 nm. The horizontal striations on the facets of these rods and the coherence in their average diameters of 210 ± 40 nm with the **hex-MOF1** strongly suggest their formation by successive stacking of **hex-MOF1** (Figure 8d-g). Though the width of nanorod remains constant with time, its average length increases to 1.6 ± 0.3 μm (**rod-MOF1**) at two hour (Figure 8h-i, 10). Then we have continued the reaction to 5 h, and surprisingly observed that the nanorods are laterally attached with each other forming mesosheet type morphology (Figure 8j-n). This eventually attains a smooth surface at eight hour of reaction time (**meso-MOF1**) with average length, width and height of 6 ± 2 , 4 ± 2 μm and 600 ± 50 nm, respectively (Figure 8o-p, 5e-f). The average height distribution reveals the gluing of 2 to 3 layers of nanorods. This investigation clearly demonstrates that the growth kinetics of **rod-MOF1** and **meso-MOF1** is driven by non-classical oriented attachment (OA) mechanism (Figure 8IV).^{13, 27-28} At first, the Brownian collisions of nanocrystals (primary particles) in the solution result in the nucleation of hexagonal nanoparticles. For further minimization of excess surface energy, these nanoparticles align in a face-to-face fashion to grow as anisotropic nano-rod, which then attach laterally to form a final mesosheet. This is the first report of anisotropic growth of 2D nano/mesocrystal (NMOF) through oriented attachment growth as characterized by intermediate phases.

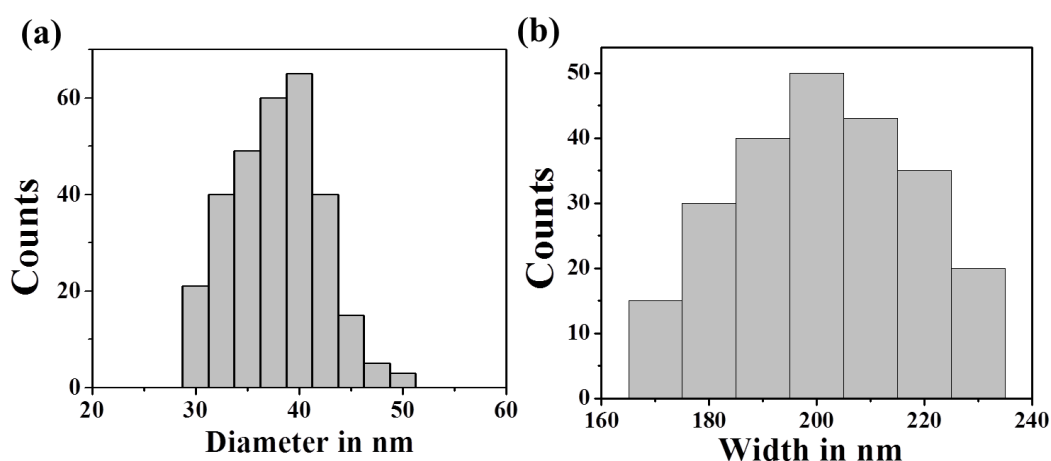


Figure 9: (a) Distribution of diameter of small nanoparticles obtained in five minutes and (b) smoothen hexagonal particles obtained in thirty minutes.

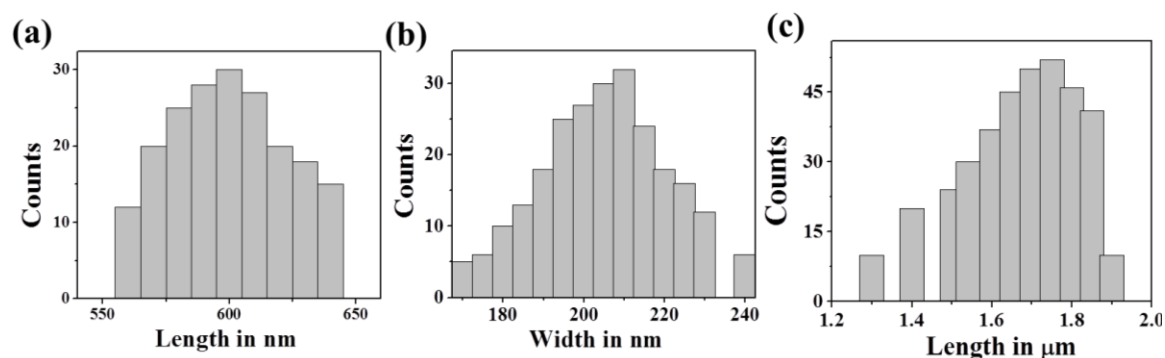


Figure 10: (a) Distribution of width and (b) length of hexagonal rods obtained in one hour, (c) distribution of length of hexagonal rods obtained in two hour.

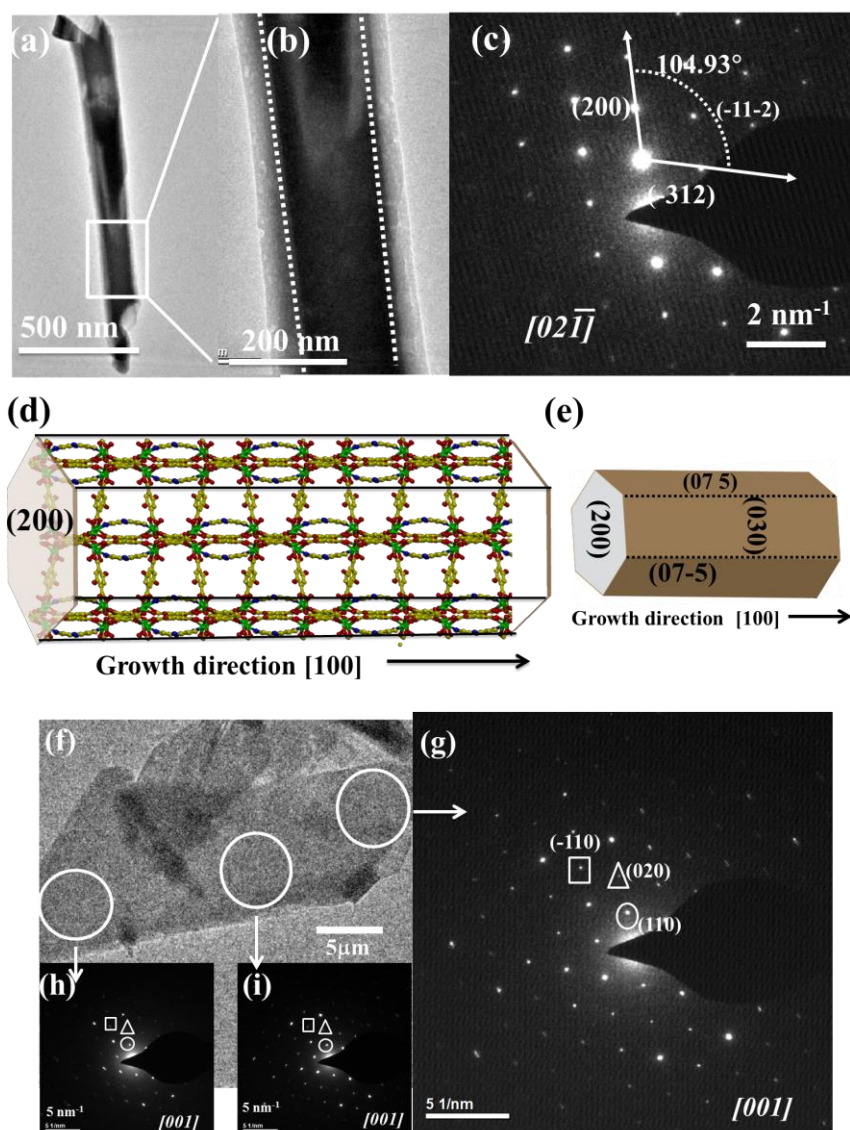


Figure 11: (a) TEM image of a **rod-MOF1**, (b) magnified section of nanorod shown in (a), (c) SAED pattern of the particle viewed along $[02\bar{1}]$ zone axis, (d-e) growth and modulation planes of nanorod with hexagonal cross section, (f) TEM image of a **meso-MOF1**, (g-i) ED patterns of selected areas (white circles) shows the same diffraction pattern viewed along $[001]$ zone axis.

The topology and crystallographic features of **hex-MOF1**, **rod-MOF1** and **meso-MOF1** are obtained from a detailed TEM analysis (Figure 8I-III, 11). The SAED pattern recorded at the marked portion of a nanorod reveals single-crystalline nature of the nanocrystals. All the diffraction spots are indexed on the basis of monoclinic unit cell and the zone axis of the nanorod is $[02\bar{1}]$. The growth direction of the nanorod is calculated to be along $[100]$ (Figure 8I-III, 11a-e). For **meso-MOF1**, the diffraction pattern shows identical spot matrix and lattice plane orientation throughout the sheet confirming regular lateral attachment of nanorods, with $[001]$ as the zone axis (Figure 11f-i).³¹ The relative intensity ratio of (020) and (200) peaks in PXRD pattern of **meso-MOF1**, **rod-MOF1**, and **hex-MOF1** are 5.16, 3.54 and 1.29, respectively, thus suggesting (200) is a growth plane as it is exposed the most in **hex-MOF1** (Figure 12).

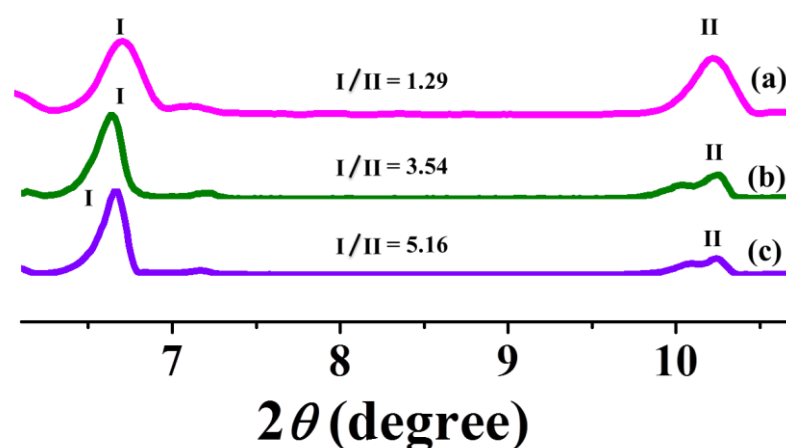


Figure 12: PXRD patterns of (a) **hex-MOF1**, (b) **rod-MOF1** and (c) **meso-MOF1** showing the relative intensity difference of (200) plane from mesosheet to nanorod to hexagonal nanoparticles.

4B.3.2 Surface energy calculation

The formation of hexagonal nano-crystals and their anisotropic attachment along $[100]$ direction to form nanorods, which subsequently attach laterally to form mesosheets, suggest that modulation and growth in NMOFs are dictated by the energetics of cleavage along various planes in bulk 1 crystal. The tendency of modulation is accessed by the cleavage energies, $\Upsilon_c(hkl)$ *i.e.* the energy spent to separate a crystal into two halves across (hkl) plane with an area A_{hkl} ,³² for instance, along the three crystallographic planes (100), (010) and (001). However, due to the complex structure of the MOF framework, not all the cleavage planes are equivalent along a direction, *e.g.*, (010) and (020) planes are structurally inequivalent. Thus, we determined Υ_c of planes across which a fewer number

of bonds are broken during cleavage, *i.e.* (100), (030) and (001) in the present work.

$$\gamma_c(hkl) = \frac{E_{Surface} - E_{BulkMOF}}{A_{hkl}}$$

$\gamma_c(hkl)$ determines the equilibrium structure of a nano-crystal; plane with the lowest γ_c dominates its morphology, and one with the highest γ_c tends to disappear during growth.³³ Our estimates of

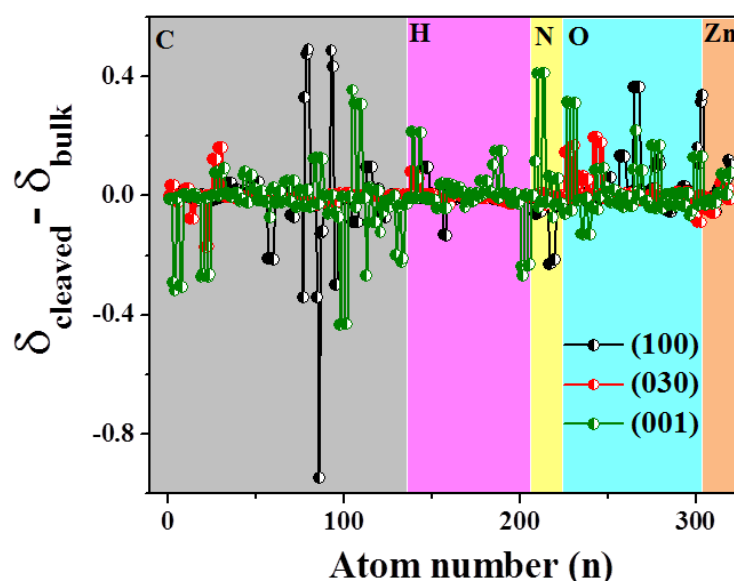


Figure 13: Difference in Mulliken charges (δ) of atoms in cleaved MOF structures on (100), (030) and (001) with respect to that in bulk **1**. The shaded regions show the atomic types viz. C, H, N, O and Zn.

$\gamma_c(001)$, $\gamma_c(030)$ and $\gamma_c(100)$ are 1.16, 0.67 and 1.57 J m⁻² respectively, which clearly suggest that (030) facets (Figure 13) control the morphology of the surface at the onset of modulation and the formation of **meso-MOF1** at low dda concentrations. The appearance of hexagonal cross-section in **rod-MOF1** and **hex-MOF1** suggests cleavage along a family of planes at an angle of 120° to (030). A set of (hkl), (075) and (07-5) planes can be realized as the facets of **hex-MOF1**, which pass through Zn-O coordination bonds, and thus, can be the preferred sites for modulation (Figure 8I-III). Furthermore, the comparison of $\gamma_c(100)$ and $\gamma_c(001)$ indicates cleavage of fewer number of bonds along [100], indicating a possibility of modulation. However, a closer look at the MOF structure shows H₂dht, azpy and dht linkers along [100], which on cleavage tends to disrupt the

MOF structure. This is evident from the changes in partial charges (δ) on atoms in the vicinity of (100) as compared to (001) surface (Figure 13), signifying a higher degree of structural dis-integration on (100) modulation, and confirming preferential growth of nanorods along [100]. This is in contrast to the surface cleavage in high-symmetry cubic MOF structures where identical linker molecules constitute the (100) crystallographic planes.²⁶ Hence, our estimates of the surface energy confirm the planes of modulation and growth direction, corroborating the TEM analyses.

4B.3.3 Adsorption studies

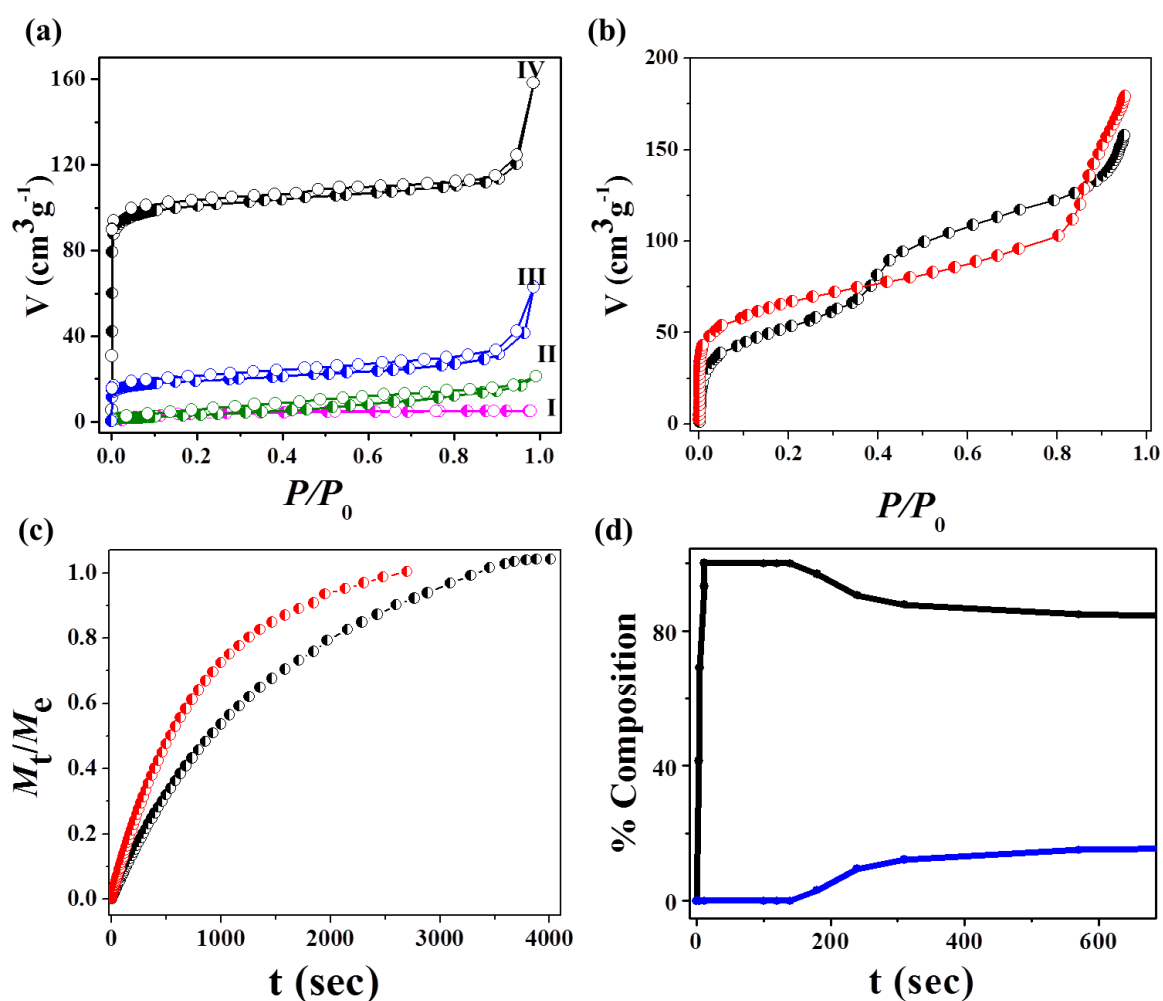


Figure 14: (a) N_2 adsorption isotherms of NMOFs at 77 K: (I) **1'** (II) **meso-MOF1** (III) **rod-MOF1** (IV) **hex-MOF1**, (b) MeOH vapour adsorption isotherms of **1'** (black) and **hex-MOF1** (red) at 293 K, (c) kinetics of MeOH vapour adsorption of **1'** (black) and **hex-MOF1** (red) at 293 K (fitted into LDF mass diffusion model); shows higher mass diffusion in **hex-MOF1** compared to bulk phase **1'**, (d) breakthrough profile of CO_2/N_2 separation of **hex-MOF1**; CO_2 = blue and N_2 = black at 298 K.

To study the porous structure and adsorption behaviours in nanostructured MOFs relative to the bulk-MOF, we recorded N₂ and CO₂ sorption isotherms (Figure 14-15, Table 2) at 77 K and 298 K, respectively. Despite of adequate pore size ((6.6 × 4.4) Å along [001] and (4 × 6.7) Å along [101])³⁰ guest removed bulk **1'** shows a low N₂ (kinetic diameter 3.64 Å) uptake of 5 cm³ g⁻¹ (BET surface area = 3 m² g⁻¹) at 77 K (Figure 14a). Downsizing of bulk MOF increases the N₂ uptake drastically with 21 cm³ g⁻¹ in **meso-MOF1**, 72 cm³ g⁻¹ in **rod-MOF1**, and 158 cm³ g⁻¹ in **hex-MOF1** and corresponding BET surface areas are 5, 72 and 399 m² g⁻¹ (~133 fold increase as of bulk **1**), respectively. Noticeably, a typical type II N₂ adsorption profile is obtained for **meso-MOF1**, suggesting surface adsorption. On contrary, the adsorption is dominated by microporosity in **rod-MOF1** and a typical type I profile is prominent in **hex-MOF1**, clearly supporting that the enhancement in the surface area is due to decrease in diffusion barrier in nanoscale. Inspired from this, the CO₂ adsorption isotherms of **hex-MOF1** is measured at 298 K and the uptake is 50 cm³ g⁻¹ (9.8 wt%), which is much higher than the uptake of bulk **1'**, 15 cm³ g⁻¹ (2.8 wt%) at 298 K (Figure 15), suggesting easy diffusion in **hex-MOF1**. Further, to understand the kinetics of gas adsorption in NMOF and bulk **1'**, we analysed the MeOH vapour adsorption kinetics at 293 K (Figure 14b-c, Table 2).³³ While in **hex-MOF1**, the MeOH vapour adsorption isotherm shows steep and higher uptake at low pressure region compared to **1'**, indicates a more obstructed diffusion in bulk than in NMOF. It is also important to note that the total uptake of 179 cm³ g⁻¹, in **hex-MOF1**, is higher than the total uptake (157 cm³ g⁻¹) observed for bulk **1'**. Further, the LDF (Linear Driving Force) model fitted adsorption kinetic plots of M_t/M_e vs. time show that the rate of mass transfer is higher for **hex-MOF1** ($k = 1.3 \times 10^{-3} \text{ sec}^{-1}$) than in bulk **1'** ($k = 7.1 \times 10^{-4} \text{ sec}^{-1}$). This unambiguously suggests a significant lowering in diffusion barrier for **hex-MOF1** compared to that in bulk **1'**.

At 298 K, the adsorption isotherms of N₂/CO₂ in **hex-MOF1** show significant difference in their uptakes (Figure 14d, 15-18); a very low uptake of 0.5 cm³ g⁻¹ for N₂ in contrast to 50 cm³ g⁻¹ for CO₂. This differential adsorption is desirable for gas separation ability of MOF and prompted us to carry out breakthrough column experiments of binary CO₂/N₂ mixture (15:85) in **hex-MOF1** at 298 K.³⁵ N₂ breakthrough occurs immediately because of poor interaction with the pore surface, followed by CO₂ breakthrough at 150 seconds (2.3 min), thus indicating high selectivity of CO₂ over N₂. Interestingly, bulk **1'** does not show such separation ability as CO₂ starts coming out instantaneously with N₂.

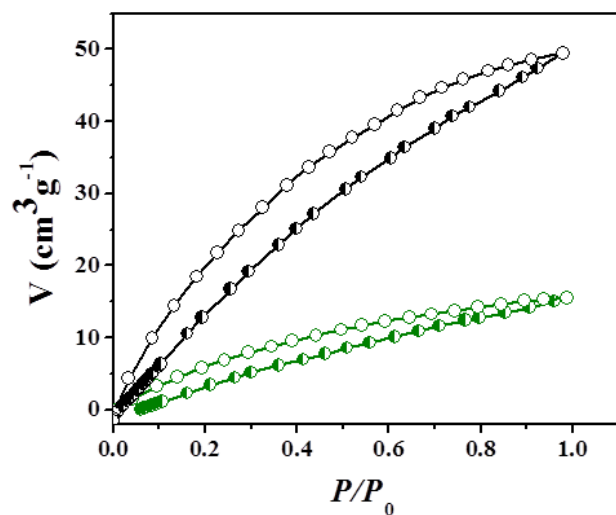


Figure 15: CO₂ adsorption isotherms at 298 K: black = **hex-MOF1** and green= **1'**.

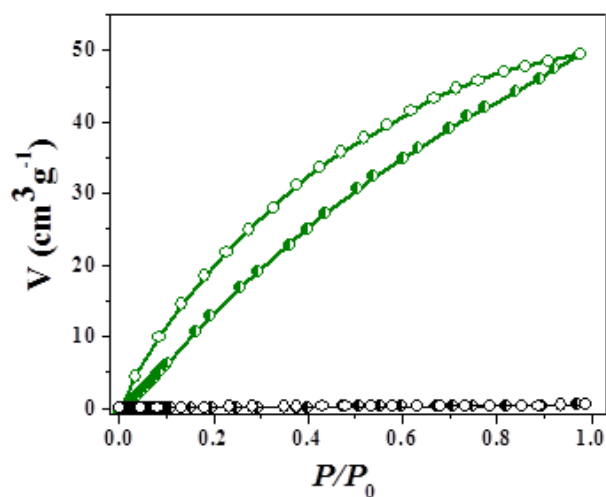


Figure 16: CO₂ and N₂ adsorption isotherms of **hex-MOF1** at 298 K.

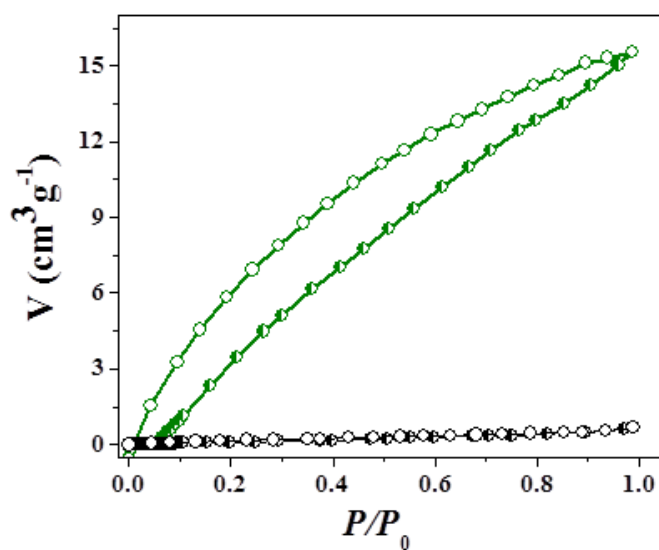


Figure 17: CO₂ and N₂ adsorption isotherms of **1'** at 298 K.

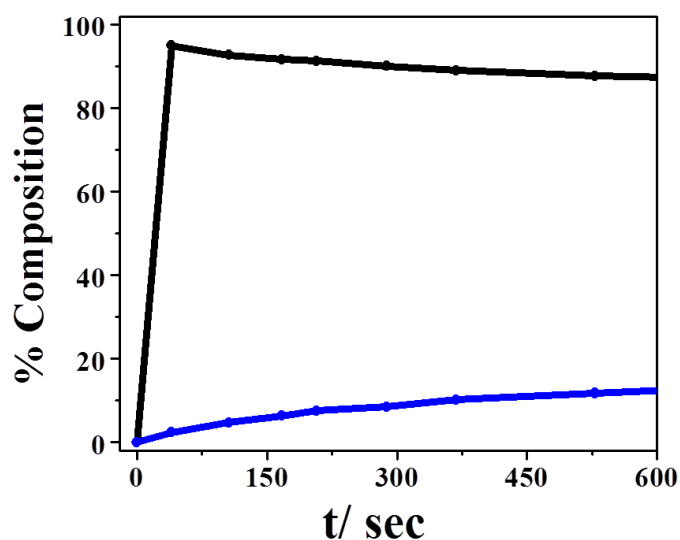


Figure 18: Breakthrough profile of CO₂/N₂ separation of 1'; CO₂ = blue and N₂ = black at 298 K.

Table 2: Adsorption details of bulk 1 and NMOFs

Compounds	N ₂ at 77 K (cm ³ g ⁻¹) ¹⁾	BET surface area (m ² g ⁻¹)	Langmuir surface area (m ² g ⁻¹)	CO ₂ at 298 K (cm ³ g ⁻¹ /wt %)	MeOH at 293 K (cm ³ g ⁻¹)	No. of MeOH molecules /formula unit
Bulk 1'	5	3	4	15/2.8	157	3.7
Meso-MOF1	21	5	6	-	-	-
Rod-MOF1	63	72	77	-	-	-
Hex-MOF1	158	399	431	50/9.8	179	4.2

4B.3.4 Theoretical perspective

This contrast in adsorption behaviours of N₂ and CO₂ in bulk 1' and different morphologies at nanoscale is further probed through theoretical analysis of energetics of gas absorption, and the associated electronic and atomic-structural distortions.³⁶⁻³⁷ As has been shown in our previous work³⁰ on the MOF structure, the size of calyx-shaped

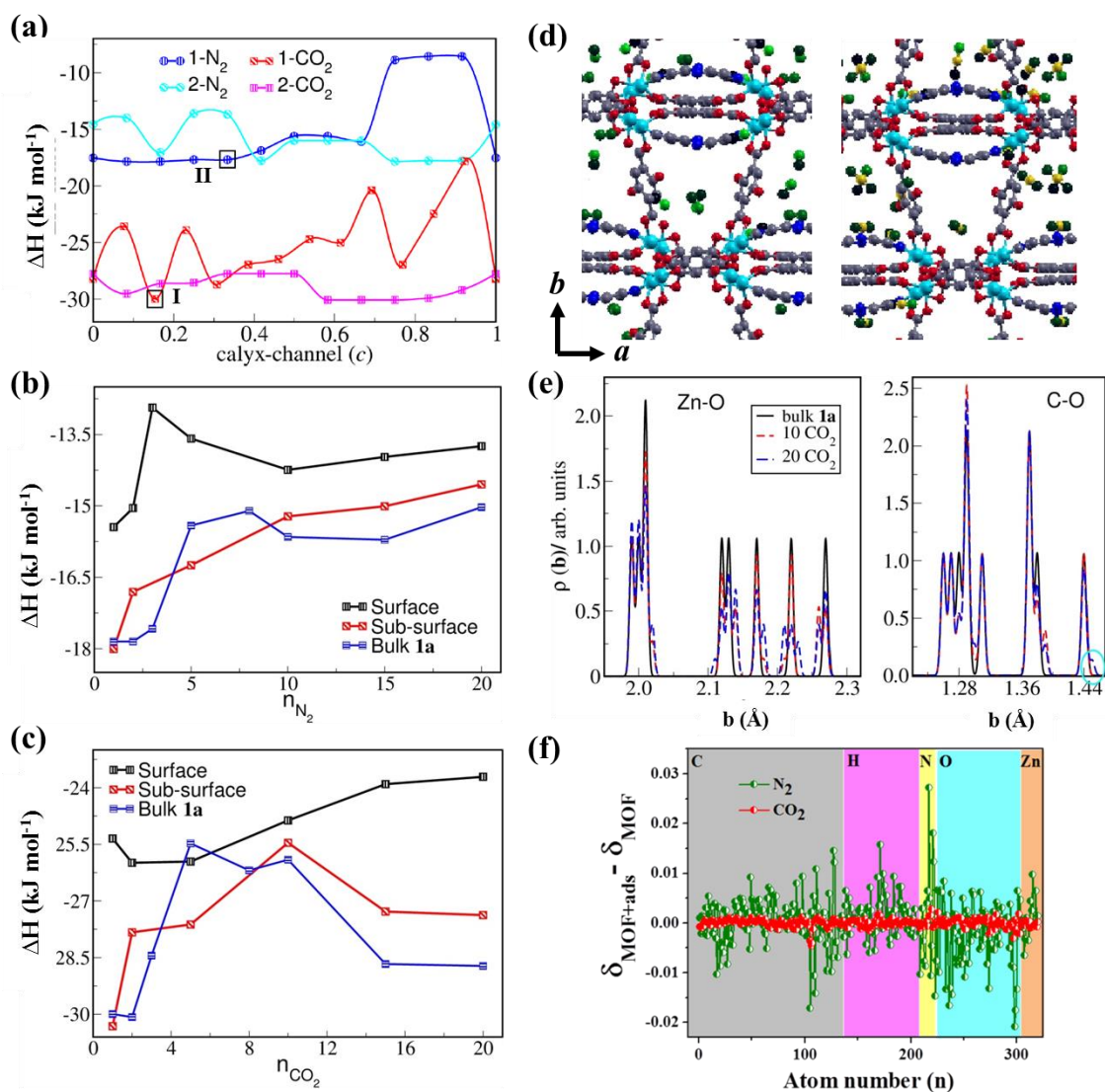


Figure 19: Adsorption in bulk and NMOF: (a) ΔH for 1 and 2 molecules of N_2 and CO_2 in bulk MOF placed along the calyx-channel, I and II indicate stable positions of CO_2 and N_2 molecules, respectively, (b-c) average ΔH of adsorption in different regions of MOF showing higher uptake of adsorbants becoming energetically feasible at higher concentrations, (d) dipoles generated on CO_2 and N_2 placed in bulk-MOF structure, in terms of atomic charges, shown with the gradient in the color green, (f) resulting electrostatic interactions of CO_2 with the MOF framework and (e) structural distortions on CO_2 adsorption in bulk **1a**.

channel along [001] is larger than rectangle-shaped along [101]. We systematically studied the adsorption of N_2 and CO_2 at various sites along the bigger (i.e. [001] or c -direction) channel in bulk **1a** (geometry optimized desolvated MOF). Site-specific energies of adsorption (ΔH) for one and two gas molecules (concentration: 0.125 and 0.25 mol/formula unit (f.u.), respectively) is carried out by adding adsorbent molecule(s) at

sites separated by different intervals along [001] and atomic relaxation constrained in the (001) plane (Figure 19a). The energy landscape (Figure 19a) shows $\Delta H_{\text{CO}_2} \sim -30.00 \text{ kJ mol}^{-1}$, which is in excellent agreement with the isosteric ΔH_{CO_2} fitted with D-R (Dubinin-Radenkevich) equation³⁰ and is about twice as compared to ΔH_{N_2} ($-17.71 \text{ kJ mol}^{-1}$), suggesting a higher diffusion barrier for N_2 adsorption. Addition of the second adsorbent molecule to the second calyx channel of MOF keeping the first molecule at lowest-energy position (marked as I and II in Figure 19a) results in a monotonous decrease in the average ΔH_{CO_2} , whereas N_2 adsorption is favoured only when the molecules are well-separated (Figure 20) and the inversion symmetry of II is preserved. The curvy motif consisting of H_2dht_a is the preferred site for gas adsorption at low concentrations.

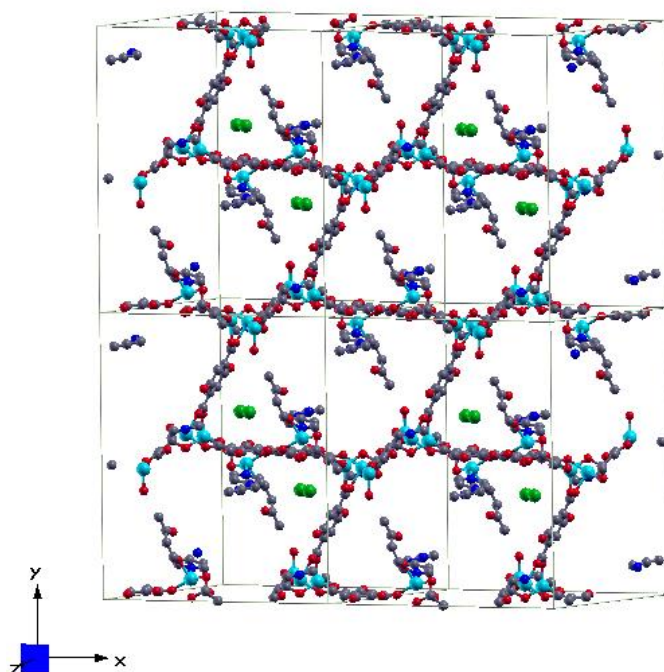


Figure 20: Figure showing, N_2 adsorption is favoured only when the molecules are well-separated.

Increase in concentration of N_2 and CO_2 adsorption in bulk **1a** leads to an initial increase in average ΔH , which remains roughly constant for N_2 at higher concentrations whereas significantly decreases in the case of CO_2 (Figure 19b-c, 21), corroborating the higher uptake of CO_2 (2.56 molecules/f.u.) than N_2 (0.25 molecules/f.u.) in **1a** at ambient pressures. Investigation of electrostatic effects on N_2 and CO_2 in bulk **1a** clearly shows induced dipole moments in the adsorbed state (displayed as gradients of green colour in (Figure 19d and 21). The dipoles on CO_2 change the effective charges on MOF atoms

indicating electrostatic interactions and hydrogen bonding (Figure 19f), in addition to dispersive interactions. This leads to slight structural distortions in bulk **1a** to allow charge delocalization; with changes in C-O and Zn-O bond lengths (Figure 19e), and consequent reduction in energy at higher concentrations of CO₂. This is in contrast to the dominantly dispersive interactions at higher concentrations of N₂ with no electrostatic effects on **1a**, and negligible structural changes.

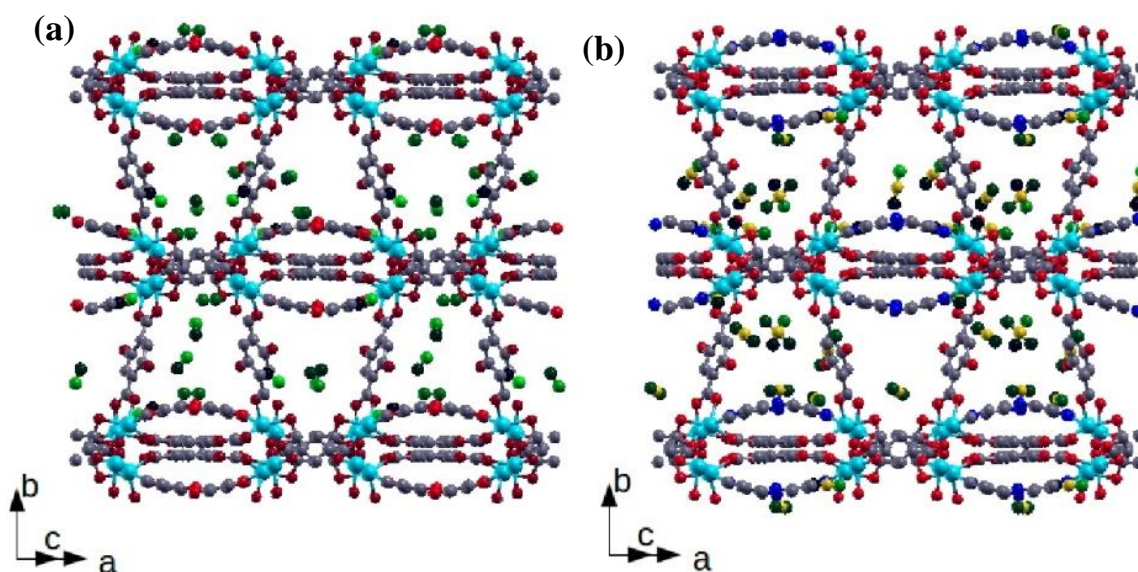


Figure 21: Dipoles generated on N₂ (a) and CO₂, (b) placed in bulk-MOF structure, in terms of atomic charges, shown with the gradient in the colour green.

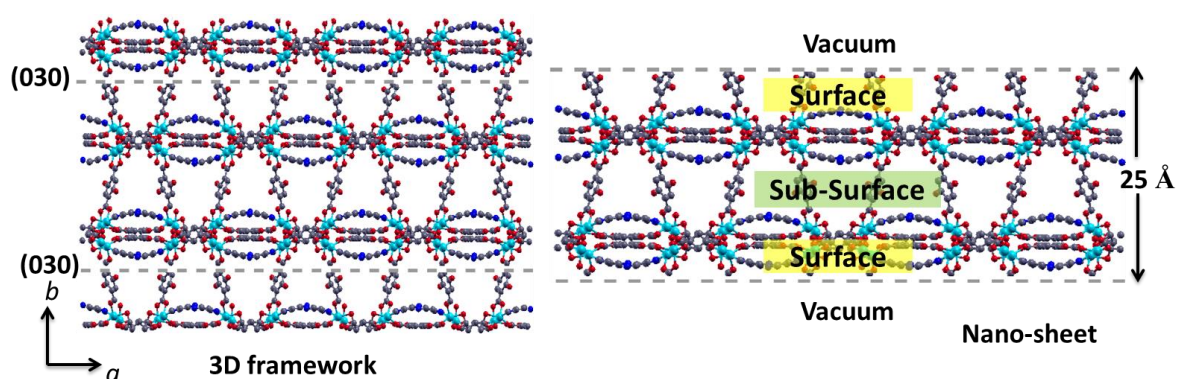


Figure 22: Nanosheet of MOF along *c*-direction.

We now present results of our simulations on NMOF and its interactions with CO₂ and N₂. Different morphologies of NMOF can be characterized by their shape, growth direction and their surface area-to-volume ratio. The cleavage along a plane is dominated

by $\Upsilon_c(hkl)$, which is least for (030) in the crystal structure (Figure 1c), thus increasing the plausibility of modulation along [010]. We created a nanosheet of MOF (Figure 22), perpendicular to the *b*-direction, and analyzed the adsorption behaviour of N₂ and CO₂ at the surface and sub-surface (MOF channel just below the surface) with reference to bulk **1a**. The sub-surface adsorption shows the tendency of molecules to enter the NMOF structure when their concentration at the surface is high. Interestingly, for higher concentrations (greater than 8 N₂ and 10 CO₂) of adsorbent molecules, the average ΔH for surface adsorption is fairly higher than that for the sub-surface, which in turn is higher than in the bulk **1a** (Figure 19b-c). This strongly suggests a downhill diffusion of adsorbents from the surface into the interior of the framework in **hex-MOF1**. The relatively higher average ΔH for N₂ and CO₂ in NMOF is attributed to a significant structural deformation of the framework with changes in C-C, C-O and Zn-O bond lengths.

4B.4 Conclusion

In summary, this chapter reports, design and fabrication of a lower symmetric mixed linker based bulk MOF $\{[Zn_2(H_2dht)(dht)_{0.5}(azpy)_{0.5}(H_2O)] \cdot 4H_2O\}_n$ have been carried out to multiscale nano/meso morphologies. Use of dodecanoic acid as coordination modulator enabled nano/mesoscale multidimensional anisotropic crystal growth of hexagonal nanoparticles, 1D nanorod and 2D mesosheet. We have unveiled the crystal growth mechanism from the time dependent study, showing a stepwise morphological transition governed *via* kinetically controlled oriented attachment (OA) growth. This understanding highlights the role of crystallographically distinct planes in modulating complex nanomorphologies in presence of modulator. The size and shape of different morphologies have deep impact on inherent porous properties of the MOFs. In comparison to the bulk MOF, the smallest sized hexagonal particle shows ~133 fold increment in BET surface area (3 to 399 m² g⁻¹), and has been observed for the first time. We exploited the consequent improvement in CO₂ uptake at ambient condition for CO₂/N₂ kinetic separation through breakthrough column experiment. Giving critical information about the morphological transformation and improvement in porous properties at nanoscale, our work opens up route to development anisotropic NMOFs from low symmetry frameworks and their application to reversible gas storage and separation.

4B.5 References

1. S. A. Maier, M. L. Brongersma, P.G. Kik, S. Meltzer, A. A. G. Requicha, H. A. Atwater, *Adv. Mater.* **2001**, *13*, 1501.
2. D. V. Talapin, J. S. Lee, M. V. Kovalenko, E. V. Shevchenko, *Chem. Rev.* **2010**, *110*, 389.
3. A. Sundaresan, R. Bhargavi, N. Rangarajan, U. Siddesh, C. N. R. Rao, *Phys Rev. B* **2006**, *74*, 161306.
4. E. M. McGarrigle, E. L. Myers, O. Illa, M. A. Shaw, S. L. Riches, V. K. Aggarwal, *Chem. Rev.* **2007**, *107*, 5841.
5. N. Mammen, S. Narasimhan, S. de Gironcoli. *J. Am. Chem. Soc.* **2011**, *133*, 2801.
6. L. N. Lewis, *Chem. Rev.* **1993**, *93*, 2693.
7. M. Shao, T. Yu, J. H. Odell, M. Jin, Y. Xia, *Chem. Commun.* **2011**, *47*, 6566.
8. S. Carencó, D. Portehault, C. Boissière, N. Mézailles, C. Sanchez, *Chem. Rev.* **2013**, *113*, 7981.
9. D. Grosso, G.J. A. A. S. Illia, E. L. Crepaldi, B. Charleux, C. Sanchez, *Adv. Func. Mater.* **2003**, *13*, 37.
10. P. Ganter, L. M. Schoop, B. V. Lotsch, *Adv. Mater.* **2017**, DOI: 10.1002/adma.201604884.
11. H. J. Lee, J. We, J. K. Kim, D. Kim, W. Cha, E. Lee, J. Sohn, M. Oh, *Angew. Chem. Int. Ed.* **2015**, *54*, 10564.
12. A. L. Robinson, V. Stavila, T. R. Zeitler, M. I. White, S. M. Thornberg, J. A. Greathouse, M. D. Allendorf, *Anal. Chem.* **2012**, *84*, 7043.
13. E. A. Flügel, A. Ranft, F. Haase, B. V. Lotsch, *J. Mater. Chem.* **2012**, *22*, 10119.
14. A. Carne´, C. Carbonell, I. Imaz, D. MasPOCH, *Chem. Soc. Rev.* **2011**, *40*, 291.
15. H. J. Lee, J. We, J. O. Kim, D. Kim, W. Cha, E. Lee, J. Sohn, M. Oh, *Angew. Chem. Int. Ed.* **2015**, *54*, 10564.
16. Y. Peng, Y. Li, Y. Ban, H. Jin, W. Jiao, X. Liu, W. Yang, *Science* **2014**, *346*, 1356.
17. R. Gref, T. Baati, P. K. Allan, G. Maurin, P. Couvreur, G. Férey, R. E. Morris, C. Serre, *Chem. Rev.* **2012**, *112*, 1232.
18. A. Herbst, A. Khutia, C. Janiak, *Inorg. Chem.* **2014**, *53*, 7319.
19. Y. Sakata, S. Furukawa, M. Kondo, K. Hirai, N. Horike, Y. Takashima, H. Uehara, N. Louvain, M. Meilikhov, T. Tsuruoka, S. Isoda, W. Kosaka, O. Sakata, S. Kitagawa, *Science* **2013**, *339*, 193.

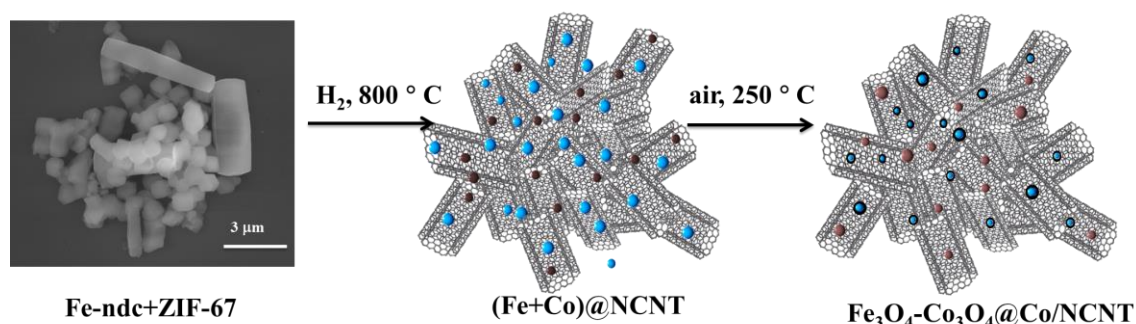
20. T. Rodenas, I. Luz, G. Prieto, B. Seoane, H. Miro, A. Corma, F. Kapteijn, F. X. Llabrés i Xamena, J. Gascon, *Nat. Mater.* **2015**, *14*, 48.
21. J. Dechnik, F. Mühlbach, D. Dietrich, T. Wehner, M. Gutmann, T. Lühmann, L. Meinel, C. Janiak, K. M. Buschbaum, *Eur. J. Inorg. Chem.* **2016**, 4408.
22. Lars Heinke, Min Tu, Suttipong Wannapaiboon, Roland A. Fischer, Christof Wöll, *Micropor. Mesopor. Mat.* **2015**, *216*, 200.
23. T. Tsuruoka, S. Furukawa, Y. Takashima, K. Yoshida, S. Isoda, S. Kitagawa, *Angew. Chem. Int. Ed.* **2009**, *48*, 4739.
24. H. Guo, Y. Zhu, S. Wang, S. Su, L. Zhou, H. Zhang, *Chem. Mater.* **2012**, *24*, 444.
25. S. Diring, S. Furukawa, Y. Takashima, T. Tsuruoka, S. Kitagawa, *Chem. Mater.* **2010**, *22*, 4531.
26. A. Umemura, S. Diring, S. Furukawa, H. Uehara, T. Tsuruoka, S. Kitagawa, *J. Am. Chem. Soc.* **2011**, *133*, 15506.
27. J. Zhang, F. Huang, Z. Lin, *Nanoscale*, **2010**, *2*, 18.
28. E. J. H. Lee, C. Ribeiro, E. Longo, E. R. Leite, *J. Phys. Chem. B* **2005**, *109*, 20842.
29. G. Zhan, H. C. Zeng, *Adv. Funct. Mater.* **2016**, *26*, 3268.
30. P. Kanoo, A. C. Ghosh, S. T. Cyriac, T. K. Maji, *Chem. Eur. J.* **2012**, *18*, 237.
31. (a) N. H. Moreira, G. Dolgonos, B. Aradi, A. L. da Rosa, T. Frauenheim, *J. Chem. Theory Comput.* **2009**, *5*, 605 (b) M. Elstner, P. Hobza, T. Frauenheim, S. Suhai, E. Kaxiras, *J. Chem. Phys.* **2001**, *114*, 5149 (c) A. K. Rappe, C. J. Casewit, K. S. Colwell, W. A. Goddard, W. M. Skiff, *J. Am. Chem. Soc.* **1992**, *114*, 10024 (d) H. M. Qian, Q. Zhao, B. S. Dai, L. J. Guo, J. X. Zhang, J. J. Liu, J. T. Zhang, H. S. Zhu, *NPG Asia Mater.* **2015**, *7*, e152.
32. E. Moreno-Calvo, T. Calvet, M. A. Cuevas-Diarte, D. Aquilano, *Crystal Growth & Design* **2010**, *10*, 4262.
33. P. Hartman, W. G. Perdok, *Acta Cryst.* **1955**, *8*, 521.
34. N. Sikdar, A. Hazra, T. K. Maji, *Inorg. Chem.* **2014**, *53*, 5993.
35. N. Sikdar, S. Bonakala, R. Haldar, S. Balasubramanian, T. K. Maji, *Chem. Eur. J.* **2016**, *22*, 6059.
36. A. Torrisi, R. G. Bell, C. Mellot-Draznieks, *Cryst. Growth Des.* **2010**, *10*, 2839.
37. A. Torrisi, R. G. Bell, C. Mellot-Draznieks, *Micropor Mesopor Mater.* **2013**, *168*, 225.

Chapter 5A

*Dual-MOFs Derived Bi-functional
Electrocatalyst Fe_3O_4 -
 Co_3O_4 @Co/NCNT for Oxygen
Reduction and Evolution Reactions*

Chapter 5A

Dual-MOFs Derived Bi-functional Electrocatalyst Fe₃O₄-Co₃O₄@Co/NCNT for Oxygen Reduction and Evolution Reactions



Summary: This chapter describes synthesis of a new bi-functional electrocatalyst (Fe₃O₄-Co₃O₄@Co/NCNT), derived from a mixture of two different MOFs (dual-MOFs); viz {[Fe(1,4-ndc)(μ-OH)](H₂O)}_n (H₂ndc = 1,4-naphthalenedicarboxylic acid; Fe-ndc) and {Co(Mim)₂·xMeOH} (Mim = 2-methylimidazole; ZIF-67) (Fe-ndc + ZIF-67). Pyrolysis of (Fe-ndc + ZIF-67) mixed-MOFs under H₂ atmosphere (at 800 °C) yielded Fe/Co nanoparticles, embedded in dense N-doped carbon nanotube matrix (NCNT). On further mild calcination, this composite transformed to Fe₃O₄ and Co₃O₄@Co core-shell nanoparticles encapsulated in NCNT. During pyrolysis, ZIF-67 nanoparticles not only act as an additional C and N source, the growth of NCNTs is also catalysed by the *in situ* formed metallic Co nanoparticles. This catalyst shows bi-functional activity towards both oxygen reduction reaction (ORR) and oxygen evolution reaction (OER) processes. Fe₃O₄-Co₃O₄@Co/NCNT shows an ORR activity close to that of commercial Pt/C and a superior performance to RuO₂ or IrO₂. It also shows OER activity as good as RuO₂ and better than IrO₂, Pt/C. Overall, the figure of merit value of bi-functional activity, is calculated to be 0.95 V (ORR at a current density of -1 mA cm⁻² and OER at 10 mA cm⁻²), which is much lower than other standard noble metal based catalysts examined in this chapter.

N. Sikdar, T. K. Maji, Manuscript under preparation

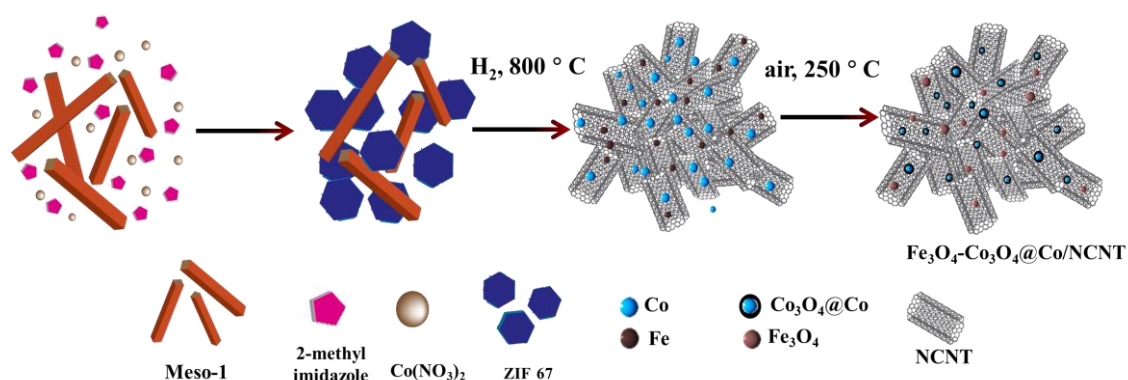
5A.1 Introduction

Understanding of oxygen electrochemistry is of paramount importance for clean and sustainable electrochemical energy storage and conversion systems.¹⁻⁷ In particular, metal air batteries, solar based energy storage systems and unitized regenerative fuel cells (URFC) would play a major role in fulfilment of our quest in green living.¹⁻⁷ URFC generates electricity in galvanic mode operation and does water electrolysis to produce H₂ and O₂ which again used in fuel cell operation.⁸⁻¹² Hence, oxygen reduction reaction (ORR) and oxygen evolution reactions (OER) are vital in realization of this grand goal. Thus developing bi-functional catalysts catering to both the reactions with high efficiency is a core challenge in URFC or in metal–air batteries.¹³⁻¹⁵ ORR and OER involves multi-electron transfer steps with different mechanisms, and sluggish reaction kinetics is limitation of these reactions. The best ORR catalysts are noble metal Pt and its alloys,¹⁶⁻²² but show poor OER activity and in contrast, IrO₂ and RuO₂ are extraordinary OER catalyst,²³ but show negligible ORR activity. The best bi-functional catalyst should have low overpotentials for both reactions and should be made of low cost and earth abundant materials. Recently, significant research effort has been directed for developing such catalysts based on carbon based nanomaterials and also doping with several heteroatoms like B, N, and S on them.³²⁻³⁸ These materials show good electrocatalytic activity for reactions carried out in fuel cells. Furthermore, introduction of transition metal or metal oxides like, Co, Fe, Ni or CoO, Co₃O₄, Fe₂O₃, Fe₃O₄, NiO, Mn₃O₄, Mn₂O₃ into the carbon based nanostructures has been found to significantly improve the overall catalytic efficacy and stability of the composite materials.^{1-7,39-40}

Recently, metal-organic frameworks (MOFs)⁴¹⁻⁴⁶ have drawn significant attention as self-sacrificial template for the preparation of carbonaceous materials with or without metal /metal oxide.⁴⁷⁻⁵⁰ Feasibility of easy hetero-atom (like N, S etc) doping by changing the linkers or by encapsulating the different guest molecules makes them attractive candidates for fabrication of high surface area carbon nanostructures with potential applications in supercapacitor, lithium ion batteries and as electrode material for fuel cells. Recently, bi-functional core-shell electrocatalysts Co@Co₃O₄@NCNT (N-doped carbon nanotube) derived from a Co-based MOF (ZIF-67) have been reported by Muhler *et al.*¹⁵ In this context, we envisage that stabilization of mixed-metal oxides like

$\text{Mn}_3\text{O}_4/\text{Co}_3\text{O}_4$ or Fe_3O_4 or $\text{Fe}_2\text{O}_3/\text{Co}_3\text{O}_4$ in nitrogen doped carbon matrices will act as better electrocatalysts.

In this chapter, a mixture of a mesoscale MOF, *i.e.*, $\{[\text{Fe}(1,4\text{-ndc})(\mu\text{-OH})](\text{H}_2\text{O})\}_n$ (H_2ndc = 1,4-naphthalenedicarboxylic acid, meso-Fe-ndc) and a nanoscale Co-based MOF, *i.e.*, $\text{Co}(\text{Mim})_2 \cdot x\text{MeOH}$ (Mim = 2-methylimidazole; ZIF-67) ($\text{Fe-ndc} + \text{ZIF-67}$) has been used as self-sacrificial template for synthesis of $(\text{Fe+Co})@\text{carbon}$ ($(\text{Fe+Co})@\text{NCNT}$) electrocatalyst under H_2 atmosphere at 800°C (Scheme 1). Here, carbonaceous matrix is nitrogen doped porous carbon nanotube (NCNT). Mild calcination of H_2 pyrolyzed $(\text{Fe+Co})@\text{NCNT}$ produces core-shell $\text{Co}_3\text{O}_4@\text{Co}$ nanoparticles and Fe_3O_4 nanoparticles and finally yielded $\text{Fe}_3\text{O}_4\text{-Co}_3\text{O}_4@\text{Co}/\text{NCNT}$ composite material. $\text{Fe}_3\text{O}_4\text{-Co}_3\text{O}_4@\text{Co}/\text{NCNT}$ showed substantially improved bi-functional catalytic activity compared to state-of-art benchmark electrocatalysts under similar conditions. The difference between the overpotentials measured at current densities of -1 mA cm^{-2} for the ORR and 10 mA cm^{-2} for the OER for $\text{Fe}_3\text{O}_4\text{-Co}_3\text{O}_4@\text{Co}/\text{NCNT}$ is 0.95 V , which is much lower than other standard noble metal catalysts examined in this chapter.



Scheme 1: Schematic of meso-Fe-ndc, along with Co^{2+} ions and 2-methylimidazole (Mim), forming dual-MOFs ($\text{Fe-ndc} + \text{ZIF-67}$) followed by carbonization to form $\text{Fe}_3\text{O}_4\text{-Co}_3\text{O}_4@\text{Co}/\text{NCNT}$ (NCNT = N-doped carbon nanotube).

5A.2 Experimental section

5A.2.1 Materials

All reagents and solvents employed were commercially available and used as supplied without further purification. $\text{Fe}(\text{NO}_3)_2 \cdot 9\text{H}_2\text{O}$, $\text{Co}(\text{NO}_3)_2 \cdot 6\text{H}_2\text{O}$, 2-

methylimidazole (Mim) and 1,4-naphthalenedicarboxylic acid (H₂ndc) are obtained from Spectrochem. RuO₂, IrO₂, Pt/C are obtained from Sigma Aldrich.

5A.2.2 Synthesis of single crystals of $\{[\text{Fe}(\text{1,4-ndc})(\mu\text{-OH})](\text{H}_2\text{O})\}_n$ (Fe-ndc-1) and mesoscale Fe-ndc (meso-Fe-ndc)

To prepare bulk single crystals of Fe-ndc-1, 0.5 mmol (0.170 g) of Fe(NO₃)₃·9H₂O, 0.5 mmol (0.108 g) of H₂ndc and 1 mmol (0.056 g) of KOH are mixed together in 10 mL distilled water and then the reaction mixture is stirred for 30 minutes. Then reaction mixture is transferred to a 23 mL Teflon-lined autoclave and autoclave was kept at 180 °C for five days. The needle shaped yellowish orange crystals are collected and washed with water/ethanol solution for several times, left overnight for drying. Yield: 80 % with respect to metal. FT-IR (KBr pellet, 4000–400 cm⁻¹): 3444 (br), 1610 (s), 1590 (w), 1412 (s). Elemental analysis (%) calcd. for C₁₂H₉O₆Fe: C, 47.21; H, 2.950. Found: C, 46.59; H, 2.84.

To prepare meso-Fe-ndc, a completely different procedure has been adopted. 2.5 mmol (0.542 g) of H₂-ndc is dissolved in 4.7 mL of 0.005 M KOH solution followed by addition of 50 mL distilled water to it. 2.5 mmol (0.851 g) of Fe(NO₃)₃·9H₂O is dissolved in 200 mL water and added to the ligand solution. Then the reaction mixture is stirred at 70 °C for three days. Orange coloured precipitate is collected and washed with water/ethanol mixture for several times and then dried for overnight. The phase purity is further confirmed by the PXRD measurement and elemental analysis. Yield: 89 % with respect to metal. FT-IR (KBr pellet, 4000–400 cm⁻¹): 3444 (br), 1610 (s), 1590 (w), 1412 (s). Elemental analysis (%) calcd. for C₁₂H₉O₆Fe: C, 47.21; H, 2.950. Found: C, 45.87; H, 2.75.

5A.2.3 Synthesis of dual-MOFs (Fe-ndc + ZIF-67)

For the synthesis of Fe-ndc + ZIF-67, 100 mg of meso-Fe-ndc crystals are taken in 25 mL MeOH and sonicated for some time (~ 15 min) to get a very good homogeneous dispersion. To this solution, 4.1 mmol (1.2 g) Co(NO₃)₂·6H₂O and 26.2 mmol (2.15 g) of 2-Mim are added, respectively. The whole mixture is stirred for three days at ambient condition. The reddish purple coloured precipitate is collected, washed with MeOH and dried overnight.

5A.2.4 Synthesis of mixed-metallic Fe₃O₄-Co₃O₄@Co/NCNT

The as-synthesised dual-MOFs i.e., (Fe-ndc + ZIF-67) (0.8 g) is placed in a ceramic boat, heated to 200 °C first at a rate of 5 °C min⁻¹ and maintained for 2 h in a tube furnace under H₂/Ar (10% H₂ in 90% Ar) atmosphere. The temperature in the furnace is further raised to 800 °C at a rate of 5 °C min⁻¹ and kept at that temperature for 1 h. After cooling to room temperature, the sample is further calcined at 250 °C in air for 2 h. Finally, the resulting sample is stirred with 1 M HCl solution under ambient condition for 12 h, washed with water/ethanol solution for several times and then dried. Finally, different characterizations and experiments suggest the resulting sample is a mixed-metallic Fe₃O₄-Co₃O₄@Co/NCNT composite material.

5A.2.5 Physical characterizations

Powder XRD patterns of the products were recorded using Cu-K α radiation (Bruker D8 Discover; 40 kV, 30 mA). Transmission electron microscopy (TEM) images were taken with a JEOL JEM-3010 transmission electron microscope operating at 200 kV. The samples were prepared by drop casting method onto carbon-coated TEM grids. To study the surface properties, X-ray photoelectron spectroscopy (XPS, VG Scientific ESCA LAB V) was used. Raman spectroscopy was performed at different locations of the sample using a Jobin Yvon LabRam HR spectrometer with a 514.5 nm Ar laser. Inductively Coupled Plasma-Optical Emission Spectroscopy (ICP-OES) measurements were recorded on a Perkin Elmer Optima 7000dv ICP-OES instrument. 2 mg of Fe₃O₄-Co₃O₄@Co/NCNT is stirred in 2 mL of conc. HNO₃ overnight at 60 °C. After 12 hours, the solution was centrifuged, and each supernatant solution was diluted with milliQ water up to 10 mL. The resulting solution was used for ICP measurements.

5A.2.6 Adsorption measurements

N₂ adsorption isotherms of Fe-ndc-1, meso-Fe-ndc and Fe₃O₄-Co₃O₄@Co/NCNT were measured at 77 K using an AUTOSORB IQ2 instrument. The samples were activated at 140 °C at 1 \times 10⁻¹ Pa for about 12 h prior to measurements of the isotherms. He gas (99.999% purity) at a certain pressure was introduced into the gas chamber and allowed to diffuse into the sample cell by opening the valve. The amount of gas adsorbed was calculated from the pressure difference ($P_{\text{calc}} - P_e$), where P_{calc} is the calculated

pressure with no gas adsorption and P_e is the observed equilibrium pressure. All operations were computer-controlled and automatic.

5A.2.7 X-ray crystallography

X-ray single-crystal diffraction data of Fe-ndc-1 was collected on a Bruker D8 VENTURE equipped with a microfocus X-ray source with graphite monochromated Mo-K α radiation ($\lambda = 0.71073 \text{ \AA}$) operating at 50 kV and 30 mA. A crystal of suitable size was chosen and mounted on a glass fiber with glue. The data was collected at 293 K. The program SAINT⁵¹ was used for integration of diffraction profiles and absorption correction was made with SADABS program.⁵² The crystal structure was solved by SIR 92⁵³ and refined by full matrix least square method using SHELXL-97.⁵⁴ All the hydrogen atoms were fixed by HFIX and placed in ideal positions. Potential solvent accessible area or void space was calculated using PLATON multipurpose crystallographic software. All crystallographic and structure refinement data of Fe-ndc-1 were summarized in Table 1. All calculations were carried out using SHELXL 97,⁵⁵ PLATON⁵⁶ and WinGX system, Ver 1.70.01.⁵⁷ The details of bond distances and bond angles are summarized in Table 2-3.

5A.2.8 Electrochemical measurements

For evaluating the electrochemical performances of the pyrolyzed samples, rotating disk electrode (RDE) voltammetry and rotating ring disk electrode (RRDE) voltammetry are used. All electrochemical measurements are performed using an electrochemical workstation (CHI760E) potentiostat/galvanostat in a conventional three-electrode cell in combination with a RRDE-3A. Fe₃O₄-Co₃O₄@Co/NCNT catalyst ink has been prepared at a concentration of 5 mg mL⁻¹ in the same above mentioned solution mixture. The mixtures are then sonicated for 2 h to obtain a well-dispersed suspension. For all measurements rotating ring disk electrode (RRDE, 4 mm, 7 mm diameter) is used. Before experiments, electrode is polished on polishing cloth using different alumina pastes (3.0 - 0.05 μm) to obtain a mirror-like surface, followed by ultrasonic cleaning in water. 5 μL of the catalyst ink is drop-casted on a glassy carbon electrode and left to dry overnight under ambient conditions. The catalyst loading for Fe₃O₄-Co₃O₄@Co/NCNT on electrode is 0.21 mg cm⁻². A 0.1 M KOH solution was used as electrolyte. The counter

and reference electrodes are a platinum coil and a Ag/AgCl/3M KCl electrode, respectively. The reference electrode is calibrated with respect to the reversible hydrogen electrode (RHE). All current densities are calculated using the geometric surface area of the electrode. All potentials are rescaled to the pH-independent reversible hydrogen electrode (RHE). The electrolyte is purged for ~30 min with N₂ prior to measurements to determine the background current and later O₂ flow is maintained over the electrolyte throughout the timeframe of the experiment. All measurements have been carried out at room temperature. Linear sweep voltammetry (LSV) are performed at rotation speeds of 100, 400, 900, 1600, 2500 and 3600 rpm at a sweep rate of 5 mV s⁻¹. The glassy carbon electrode of RRDE has been used for LSV measurements. Linear sweep voltammograms for the OER are obtained using a RDE (1600 r.p.m.), corrected by *iR*-compensation in 0.1 M KOH solution at a scan rate of 5 mV s⁻¹. The solution resistance is determined by the high-frequency intercept from the Nyquist plot obtained by the electrochemical impedance spectroscopy (EIS) technique.

The number of electrons involved in the reduction process is calculated using the Koutecký–Levich (K–L) equation:

$$\frac{1}{j} = \frac{1}{j_L} + \frac{1}{j_K} = \frac{1}{B\omega^{1/2}} + \frac{1}{j_K}$$

$$B = 0.62nFC_o(D_o)^{2/3}\nu^{-1/6}$$

$$j_K = nFkC_o$$

Here, *j* is the measured current density, *j_K* and *j_L* are the kinetic and diffusion-limited current densities, ω is the angular frequency of the RDE in radians per second, *n* is the number of electrons involved in the reaction, *F* is the Faraday constant (96485 C mol⁻¹), *D₀* is the diffusion coefficient of O₂ in the electrolyte (1.93 × 10⁻⁵ cm² s⁻¹), ν is the kinematic viscosity of the electrolyte (1.01 × 10⁻² cm² s⁻¹), *C₀* is the concentration of O₂ in the electrolyte (1.26 × 10⁻⁶ mol cm⁻³) and *k* is the electron transfer rate constant.

Rotating ring disk electrode (RRDE) voltammetry was used to calculate the number of electrons and the amount of H₂O₂ formed during ORR based on the ratio of the disk and the ring current as shown in the equations given below. For the RRDE

experiments, the ring electrode was held at a potential of 1.5 V (vs. RHE) to oxidize hydrogen peroxide.

$$n_e = \frac{4I_D}{I_D + \frac{I_R}{N}}, \quad \text{H}_2\text{O}_2(\%) = \frac{\frac{I_R}{N}}{I_D + \frac{I_R}{N}} \times 200$$

$N = 0.265$ is the collection efficiency, I_D is the Faradaic disk current, and I_R is the Faradaic ring current.

5A.3 Results and discussion

5A.3.1 Structural features of $\{[\text{Fe}(1,4\text{-ndc})(\mu\text{-OH})](\text{H}_2\text{O})\}_n$ (Fe-ndc-1)

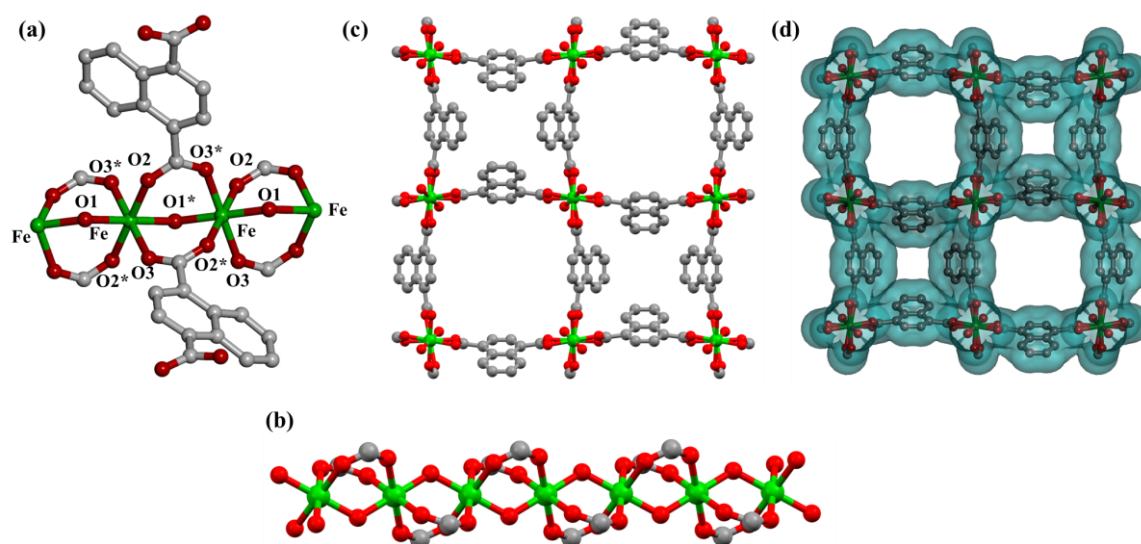


Figure 1: (a) View of the coordination environment around Fe^{III} in as-synthesized Fe-ndc-1, (b) view of zigzag $-\text{Fe}-\text{OH}-\text{Fe}-\text{OH}-$ chain, (c) view of 3D framework, (d) van der Waal surface added pore view of the 3D framework showing two different types of channels.

Single crystal X-ray diffraction analysis suggests that Fe-ndc-1 crystallizes in tetragonal, $P4_2/nmc$ space group. The Fe^{III} centre, located on an inversion centre, is in an octahedral environment connected with the four carboxyl and two μ_2 -hydroxyl oxygen atoms (Figure 1a). The FeO_6 octahedron is slightly compressed (Figure 1b), where axial $\text{Fe}-\text{O}(\mu\text{-OH}; \text{O1}, \text{O1}^*)$ bond lengths are 1.9577(9) Å, equatorial $\text{Fe}-\text{O}(\text{O2}, \text{O2}^*, \text{O3}$ and $\text{O3}^*)$ bond lengths are in the range of 2.0208(17) – 2.0265(15) Å, and the *cisoid* angles

are $87.76(7)$ - $92.24(7)^\circ$. The axial hydroxyl oxygen atoms are shared by the neighbouring octahedron, resulting in a zigzag $-\text{Fe}-\mu\text{-OH}-\text{Fe}-\mu\text{-OH}-$ chain along c axis where the $\mu\text{-Fe-OH-Fe}$ angle is $122.78(9)^\circ$. The 1D chains are cross-linked by the 1,4-ndc ligands along ab plane to form a 3D framework with 1D channels along c direction (Figure 1c-d). The 1D channels encompass two kinds of square shaped channels, $8.1 \times 8.1 \text{ \AA}^2$ and $3.35 \times 3.35 \text{ \AA}^2$, filled with guest water molecules, and the void space is estimated to be 38.7 % to the total crystal volume.^{8b} Férey *et al.*, recently reported a similar framework, $[\text{M}(1,4\text{-bdc})(\mu\text{-OH})]$, $[\text{M} = \text{V(III)} (\text{MIL-47})$ and $\text{Cr(III)} (\text{MIL-43})]$ with 1,4-benzene dicarboxylate linker having single 1D hydrophilic channel structure.⁹

Table 1: Crystal data and structure refinement parameters of Fe-ndc-1.

Parameters	Fe-ndc-1
Empirical formula	$\text{C}_{12}\text{H}_9\text{FeO}_6$
Formula weight	302.02
Crystal system	Tetragonal
Space group	$P4_2/nmc$
a , \AA	21.432(3)
b , \AA	21.432(3)
c , \AA	6.8745(10)
α , deg	90.001(2)
β , deg	90.008(4)
γ , deg	90.01(1)
V , \AA^3	3157.7(16)
Z	8
T , K	293
μ , mm^{-1}	0.690
D_{calcd} , g/cm^3	1.271
$F(000)$	1216
Reflections [$I > 2\sigma(I)$]	9792
Total reflections	48826
Unique reflections	12681
$\lambda(\text{Mo-K}\alpha)$	0.71073
R_{int}	0.0397
GOF on F^2	1.32
$R_1 [I > 2\sigma(I)]^a$	0.0628
$R_w [\text{all data}]^b$	0.0954

$$^a R_1 = \frac{\sum ||F_o| - |F_c||}{\sum |F_o|}, \quad ^b R_w = \left[\frac{\sum \{w(F_o^2 - F_c^2)^2\}}{\sum \{w(F_o^2)\}} \right]^{1/2}$$

Table 1: Bond distances (Å) for Fe-ndc-1.

Fe-O1	1.9577(9)	Fe-O1_h	1.9577(9)
Fe-O2	2.0208(17)	Fe-O2_h	2.0208(17)
Fe-O3_g	2.0265(15)	Fe-O3_p	2.0265(15)

Table 2: Bond angles (°) for Fe-ndc-1.

O1-Fe-O2	91.74(6)	O2-Fe-O3_p	87.76(7)
O1-Fe-O3_g	90.91(6)	O1_h-Fe-O3_g	89.09(6)
O1-Fe-O1_h	180.00	O2_h-Fe-O3_g	87.76(7)
O1-Fe-O2_h	88.26(6)	O3_g-Fe-O3_p	180.00
O1-Fe-O3_p	89.09(6)	O1_h-Fe-O2_h	91.74(6)
O2-Fe-O3_g	92.24(7)	O1_h-Fe-O3_p	90.91(6)
O1_h-Fe-O2	88.26(6)	O2_h-Fe-O3_p	92.24(7)
O2-Fe-O2_h	180.00		

Symmetry Code: g = 1-y,1-x,1/2-z; h = 1-x,1-y,1-z; p = y,x,1/2+z.

5A.3.2 Thermal stability and PXRD patterns of Fe-ndc-1

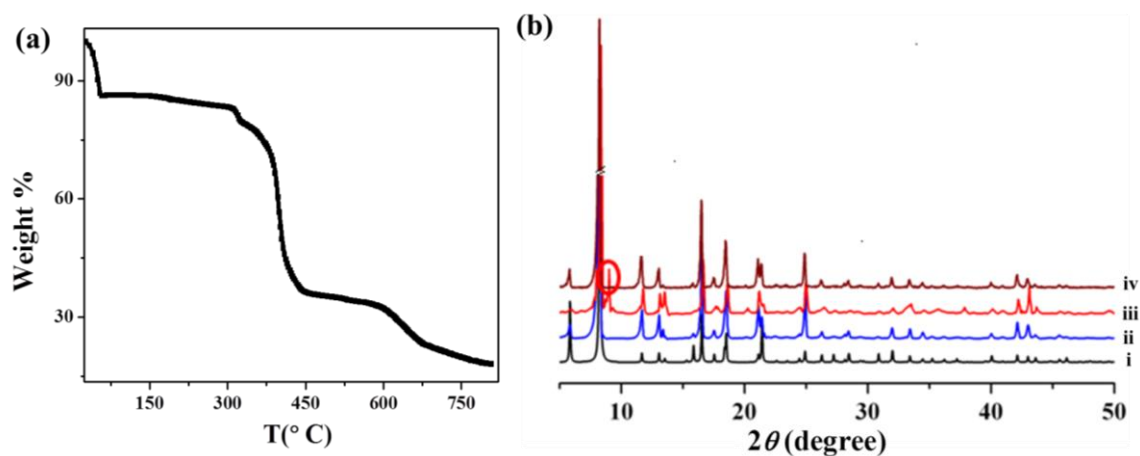


Figure 2: (a) TGA curve for Fe-ndc-1 in the temperature range 30–800 °C (3 °C min⁻¹ under N₂ atmosphere), (b) PXRD patterns of Fe-ndc-1 in different state; (i) simulated (ii) bulk-Fe-ndc-1 (iii) desolvated and (iv) rehydrated.

Thermogravimetric analysis (TGA) of Fe-ndc-1 shows a total 13.5 % weight loss corresponding to two guest water molecules (cald. 12.5 %) in the temperature range of

85-100 °C (Figure 2a). The desolvated compound of Fe-ndc-1 is thermally stable up to 300 °C and then decomposes to unidentified product.

The PXRD pattern of the as-synthesized Fe-ndc-1 has been recorded, (Figure 2b) and the sharp Bragg's diffraction peaks with well correspondence with the simulated pattern indicate highly crystalline nature and high purity of the samples. The desolvated structure of Fe-ndc-1 shows missing of first peak and appearing of one peak as marked by a circle indicating structural transformation on guest water molecules removal. Powder pattern of water vapour exposed dehydrated sample of Fe-ndc-1 (for 48 hours) shows similar PXRD pattern as as-synthesized Fe-ndc-1, suggesting reversible structural transformation.

5A.3.3 Characterizations of meso-Fe-ndc

The red yellowish orange powder obtained at 70 °C has similar diffraction patterns as bulk crystal Fe-ndc-1, clearly confirming the formation of pure phase compound with similar periodic structural characteristics (Figure 3a). Noticeably, slight broadening of the Bragg's reflections is observed, suggesting formation of smaller size crystals compared to bulk Fe-ndc-1. FESEM images show formation of meso/nanoscale square shaped rods with an average length and width in the range of $2.5 \pm 1 \mu\text{m}$ and $1 \pm 0.5 \mu\text{m}$, respectively (Figure 3b-c). Nitrogen adsorption measurements (at 77 K) are performed to check the permanent porosity and for deriving the surface area (Figure 3f). Interestingly, dehydrated form of meso-Fe-ndc show steep uptake at low pressure with a total uptake of $134 \text{ cm}^3 \text{ g}^{-1}$ (BET surface area = $350 \text{ m}^2 \text{ g}^{-1}$) compared to bulk Fe-ndc-1 form which shows non-inclusion at 77 K, suggesting decrease in diffusion barrier on downsizing the particle sizes in mesoscale.

5A.3.4 Characterizations of dual-MOFs (Fe-ndc + ZIF-67)

The PXRD pattern of dual-MOFs (Fe-ndc + ZIF-67) shows presence of diffraction peaks originating from both Fe-ndc and ZIF-67 (Figure 3a). The FESEM images reveal formation of distinct hexagonal ZIF-67 nanoparticles of $500 \pm 100 \text{ nm}$ in addition to rod shaped meso-Fe-ndc (Figure 3d-e). These images also reveal overall the presence of higher amount of ZIF-67 nanoparticles compared to meso-Fe-ndc particles.

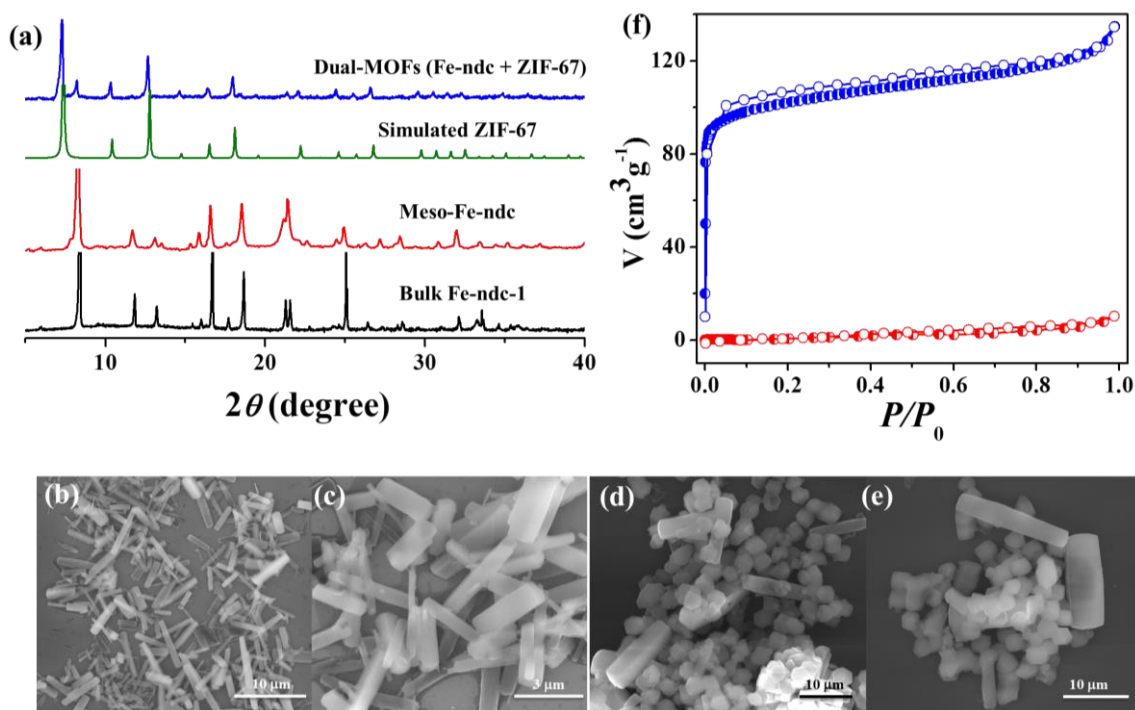


Figure 3: (a) PXRD patterns of simulated bulk Fe-ndc-1, meso-Fe-ndc, ZIF-67 and dual-MOFs (Fe-ndc + ZIF-67), (b-c) FESEM images of meso-Fe-ndc and (d-e) dual-MOFs (Fe-ndc + ZIF-67), (f) N_2 adsorption isotherms for dehydrated form of meso-Fe-ndc (blue) and bulk Fe-ndc-1 (red) at 77 K.

5A.3.5 Characterizations of dual-MOFs -derived catalyst $\text{Fe}_3\text{O}_4\text{-Co}_3\text{O}_4\text{@Co/NCNT}$

The presence of redox active $\text{Fe}^{\text{III}}/\text{Co}^{\text{II}}$ centers in Fe-ndc-1 and ZIF-67, respectively, encouraged us to pyrolyze of dual-MOFs (Fe-ndc + ZIF-67) for obtaining $\text{Fe}^{\text{II/III}}/\text{Co}^{\text{II/III}}$ metal centers rich carbonaceous matrix under different experimental conditions. (Fe-ndc + ZIF-67) is pyrolyzed in a stepwise fashion at 200 $^\circ\text{C}$ for 2 h first and then at 800 $^\circ\text{C}$ for 1 h under continuous H_2/Ar flow, followed by mild calcination in air at 250 $^\circ\text{C}$ for 2 h following a procedure as previously described to obtain $\text{Fe}_3\text{O}_4\text{-Co}_3\text{O}_4\text{@Co/NCNT}$ composite material.¹⁵ The obtained material is characterized further using PXRD, Raman spectroscopy, XPS and TEM studies (Figure 4-6). The strong XRD peaks at $2\theta = 26.1^\circ$ and 26.2° for both H_2 pyrolyzed (Fe+Co) @NCNT and $\text{Fe}_3\text{O}_4\text{-Co}_3\text{O}_4\text{@Co/NCNT}$, respectively, suggest regular graphitic stacking originated from (002) reflection (Figure 4a). The diffraction peaks at 2θ of 44.2° , 51.4° and 75.5° and 44.5° indicate formation of crystalline metallic Co and Fe phase, respectively prior to

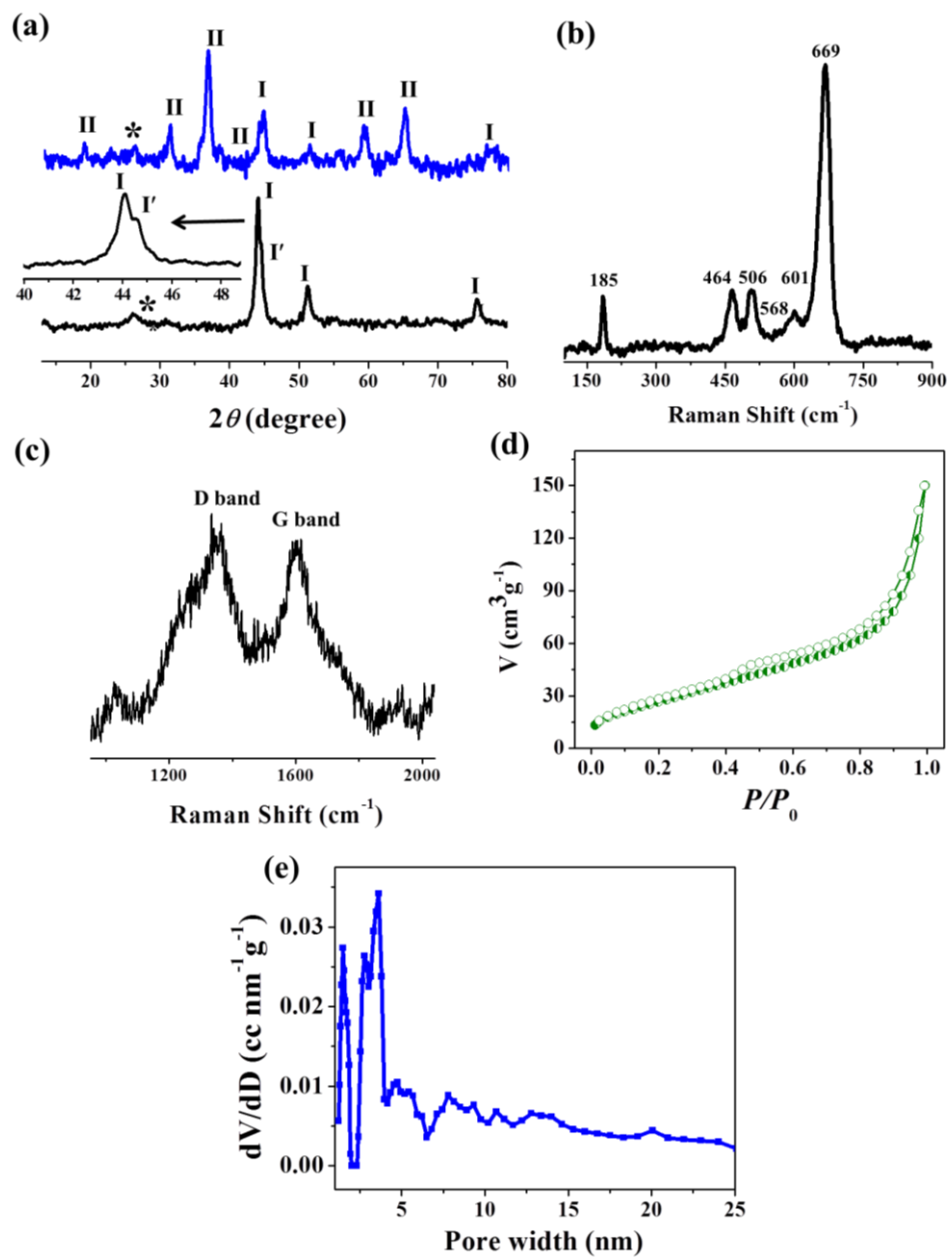


Figure 4: (a) PXRD patterns of H₂-pyrolized (Fe+Co)@NCNT (black) and Fe₃O₄-Co₃O₄@Co/NCNT (blue) showing the formation of the metallic Co/Fe phases and corresponding Co₃O₄/Fe₃O₄ phases, respectively; *, I, I', II denote the graphitic (002), Co, Fe and Co₃O₄/Fe₃O₄ peaks, respectively, (b-c) Raman spectra of Fe₃O₄-Co₃O₄@Co/NCNT showing formation of Fe₃O₄ and Co₃O₄, respectively, along with the characteristic D and G bands, (d) N₂ adsorption isotherms of Fe₃O₄-Co₃O₄@Co/NCNT at 77 K, (e) NLDFT pore size distribution of Fe₃O₄-Co₃O₄@Co/NCNT.

calcination. Mild calcination in air partially oxidizes Co to form core-shell Co₃O₄@Co nanoparticles where Fe completely oxidizes to Fe₃O₄ phase, as confirmed from the newly

appearing diffraction peaks at 2θ of 18.8° , 31.1° , 36.6° , 38.3° , 59.3° and 65.0° . Pyrolysis under H_2 atmosphere led to the formation of 45-60 nm sized metallic Co/Fe nanoparticles, homogeneously distributed in self-coiled dense carbon nanotubes (NCNT) matrix as observed in TEM analysis (Figure 5). The average diameter of the NCNTs was 10-20 nm. High resolution TEM (HRTEM) confirms the NCNTs to be multiwalled with an average wall thickness of 7-8 nm (Figure 5a, c). The lattice fringe of the Co and Fe nanoparticles are ~ 0.209 and 0.201 nm, attributed to the $\{111\}$ of cubic phase of metals as verified in the HRTEM image (Figure 5b, d).⁴⁰ Interestingly, after calcination in air, there is formation of partially oxidized core-shell $Co_3O_4@Co$ and fully oxidized Fe_3O_4 nanoparticles encapsulated in NCNT matrix. The lattice fringe of the outer shell, i.e. Co_3O_4 is 0.46 nm, attributed to the $\{111\}$ of cubic phase (Figure 5i, k),⁴⁷ on the other hand, the Fe_3O_4 has lattice fringe of 0.48 nm corresponding to $\{111\}$ of cubic structure (Figure 5j, l). Elemental mapping images of H_2 -pyrolyzed (Fe+Co)@NCNT and $Fe_3O_4-Co_3O_4@Co/NCNT$ show that presence of Fe, Co, O N elements, uniformly distributed in the matrix (Figure 5e-h, m-p). Raman spectroscopy is further carried out to confirm the formation of Fe_3O_4 , Co_3O_4 and to understand the nature of the graphitic carbon structure (Figure 4b-c). The bands at 185 cm^{-1} , 464 cm^{-1} , 506 cm^{-1} , 601 cm^{-1} , 669 cm^{-1} and 568 cm^{-1} , 669 cm^{-1} are characteristic of Co_3O_4 and Fe_3O_4 phase, respectively.^{15,58} The characteristic defect-D band and graphitic-G band at $\sim 1356\text{ cm}^{-1}$ and $\sim 1601\text{ cm}^{-1}$, with a I_G/I_D ratio of 0.9 ,⁵⁹ respectively, clearly demonstrates that a high degree of graphitization is induced during pyrolysis under H_2 atmosphere. XPS survey spectra of the samples further confirm the presence of Fe, Co, C, N and O (Figure 6). The core level Co 2p XPS spectrum of $Fe_3O_4-Co_3O_4@Co/NCNT$ is deconvoluted into four peaks, metallic Co at 778.1 eV , Co_3O_4 bands at 780.1 and 780.4 eV , the Co- N_4 environment at 781.8 eV (Figure 6a).⁶⁰ The core level Fe 2p spectrum has four peaks. The binding energies of Fe $2p_{3/2}$ and Fe $2p_{1/2}$ obtained from the present study are 711.0 and 724.8 eV , respectively. The satellite peak at 714.09 eV is for the Fe^{2+} ions and the $2p_{3/2}$ satellite at about 719 eV is characteristic of the Fe^{3+} ions (Figure 6b).⁶¹⁻⁶² The C 1s spectrum consists of C-O peak at 285.2 eV , C-O-C peak at 286.3 eV , C-N/C=N peaks at 287.2 eV and O-C=O peak at 288.3 eV (Figure 6c),⁶³ suggesting the formation of a N-doped graphitic matrix. Notably, the enhanced C-O peak intensity at 285.2 eV in $Fe_3O_4-Co_3O_4@Co/NCNT$ is probably due to an increased C-O functionalization during the mild calcination process (Figure 6c).

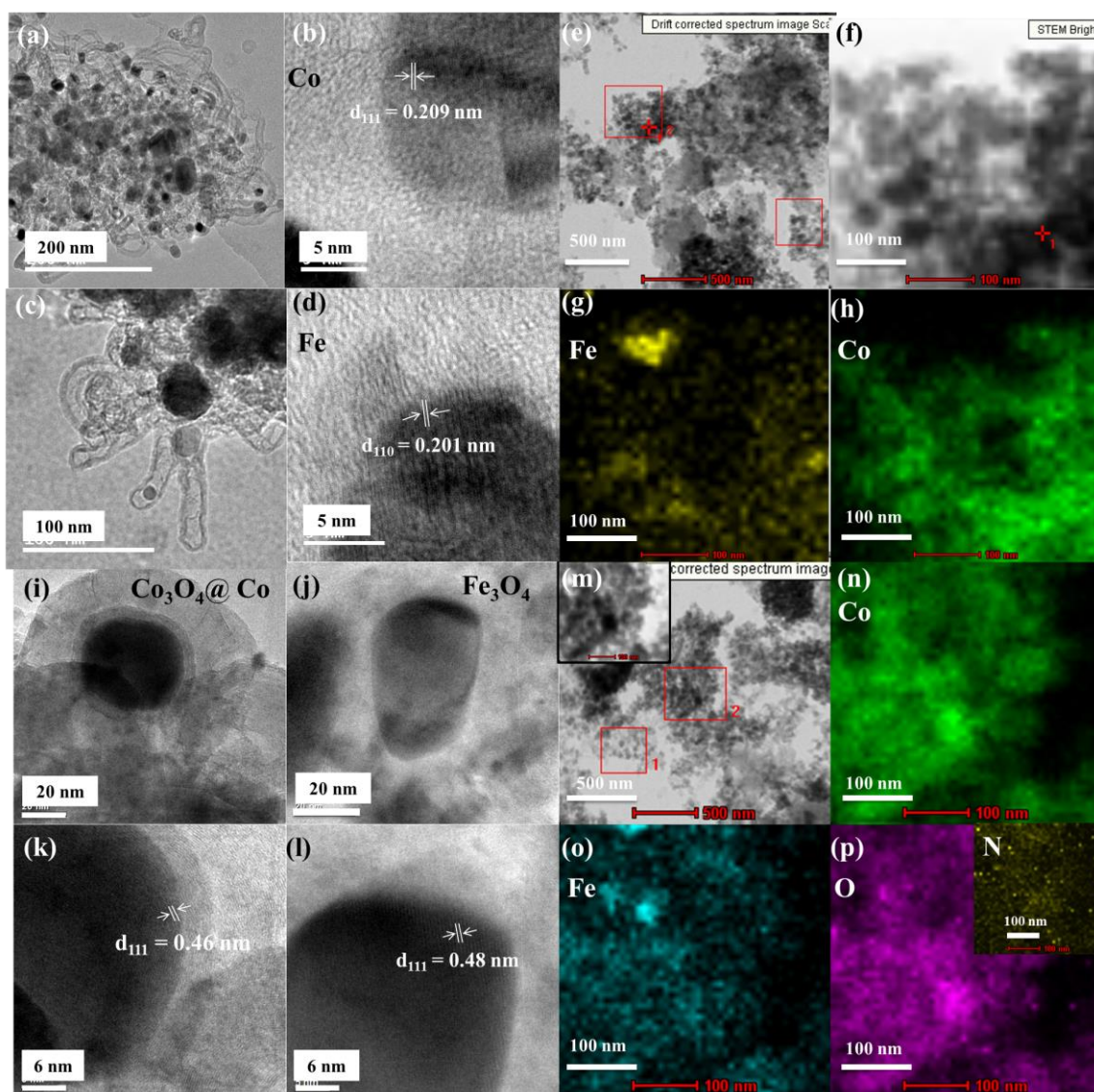


Figure 5: (a, c) TEM images of metal nanoparticles dispersed in NCNT matrix of $\text{Fe}_3\text{O}_4\text{-Co}_3\text{O}_4\text{@Co/NCNT}$, (b) HRTEM image of one Co nanoparticle and (d) Fe nanoparticle showing lattice fringes, (e-h) corresponding element mapping images showing presence of Co and Fe, (i) one core-shell $\text{Co}_3\text{O}_4\text{@Co}$ nanoparticle, (j) one Fe_3O_4 nanoparticle, (k) HRTEM images of $\text{Co}_3\text{O}_4\text{@Co}$ and (l) Fe_3O_4 nanoparticle showing corresponding lattice fringes, (m-p) corresponding element mapping images showing presence of Fe, Co, O and N.

Core level N 1s XPS spectra are deconvoluted into three bands at 398.2 eV, 401.2 eV and 403.9 eV attributed to pyridinic, pyrrolic and graphitic N, respectively (Figure 6d).⁶⁴ The surface nitrogen content calculated from the XPS measurements is 4.13 %. The lesser N-content is due to pyrolysis at higher temperature.⁶⁴ The Co and Fe content are 38 and 18

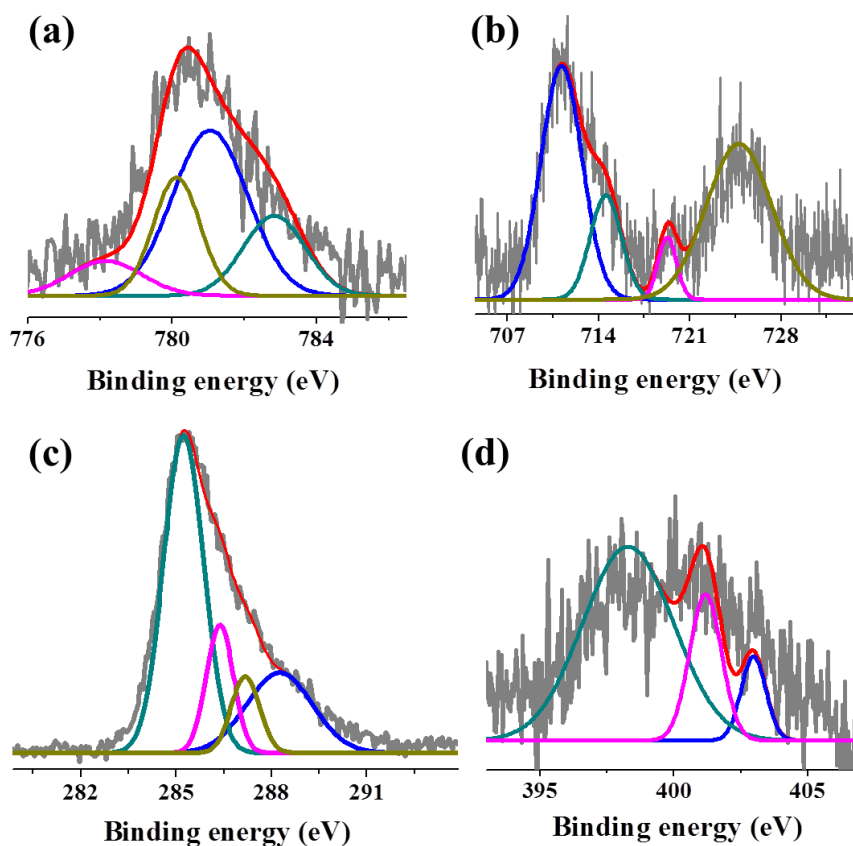


Figure 6: (a) Co 2p core level, (b) Fe 2p core level, (c) C 1s core level and, (d) N 1s core level XPS spectra of $\text{Fe}_3\text{O}_4\text{-Co}_3\text{O}_4\text{@Co/NCNT}$.

wt% as determined by ICP-OES analyses.

The activated $\text{Fe}_3\text{O}_4\text{-Co}_3\text{O}_4\text{@Co/NCNT}$ features typical type IV N_2 adsorption isotherm which corresponds to BET surface areas of $101 \text{ m}^2 \text{ g}^{-1}$ (Figure 4d). The pore size distribution shows a high contribution from *in-situ* generated mesopores with dimensions in the range of 2–15 nm as calculated using the NLDFIT method (Non-Local Density Functional Theory) (Figure 4e) with a pore volume of $0.189 \text{ cm}^3 \text{ g}^{-1}$. This data indicates that the high temperature H_2 treatment generated a porous matrix, indicating possible impact on gas diffusion during ORR/OER activity.

5A.3.6 Electrochemical activity and stability of $\text{Fe}_3\text{O}_4\text{-Co}_3\text{O}_4\text{@Co/NCNT}$

The electrocatalytic activity of as prepared $\text{Fe}_3\text{O}_4\text{-Co}_3\text{O}_4\text{@Co/NCNT}$ was examined using cyclic voltammetry (CV) in 0.1 M KOH solution with a catalyst loading 0.21 mg cm^{-2} . As shown in the CVs (Figure 7a), no appreciable redox peaks were

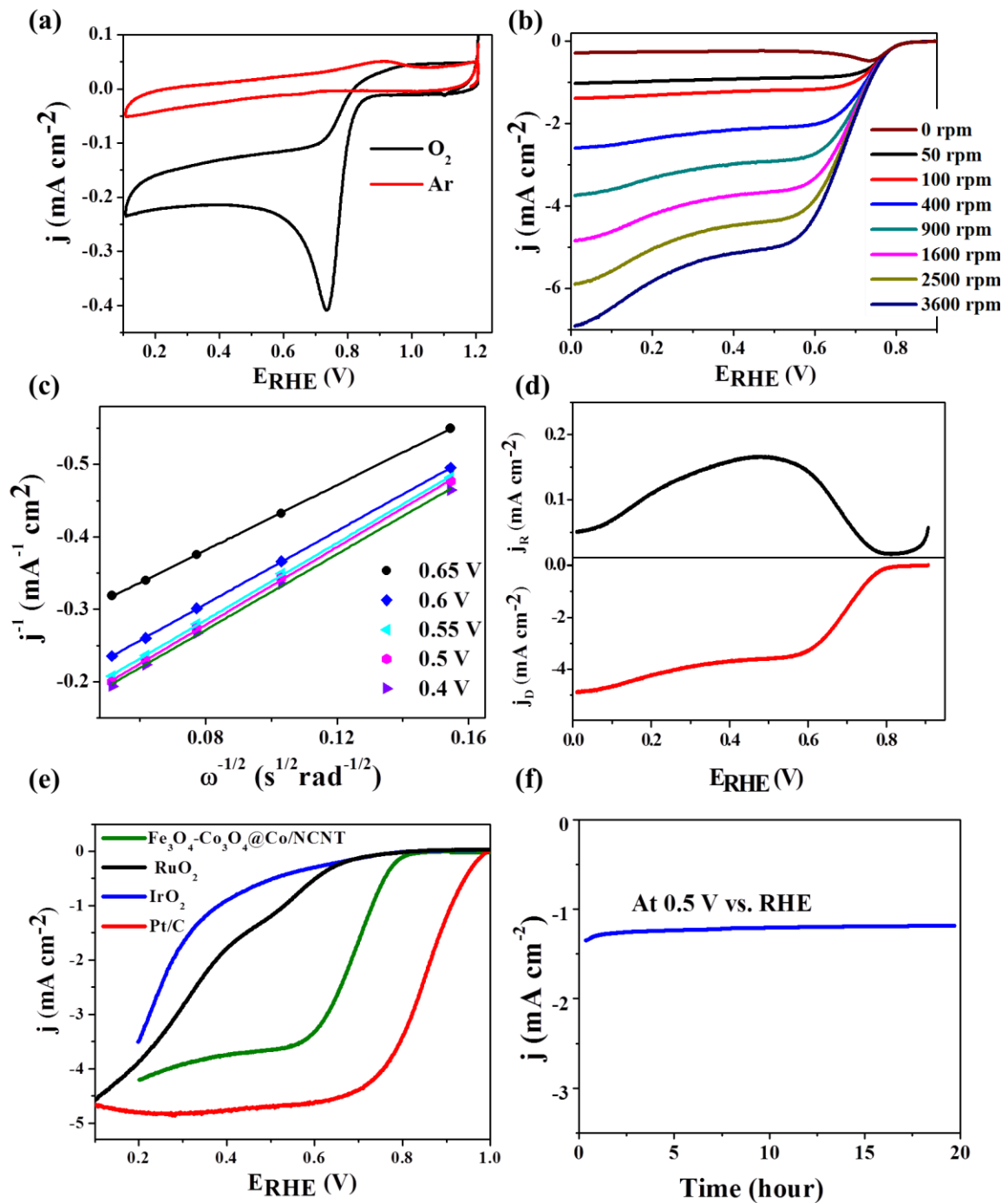


Figure 7: CVs for $\text{Fe}_3\text{O}_4\text{-Co}_3\text{O}_4\text{@Co/NCNT}$ recorded at a scan rate of 5 mV s^{-1} in O_2 and Ar-saturated 0.1 M KOH solution, (b) LSV curves recorded at various rotation speeds, (c) Koutecky-Levich (K-L) plots at different potentials, (d) RRDE polarization curves for the ORR at 1600 rpm, (e) iR -corrected linear sweep voltammograms of different electrocatalysts collected at 1600 rpm in O_2 -saturated 0.1 M KOH solution, (f) chronoamperometric stability recorded at 0.5 V vs. RHE .

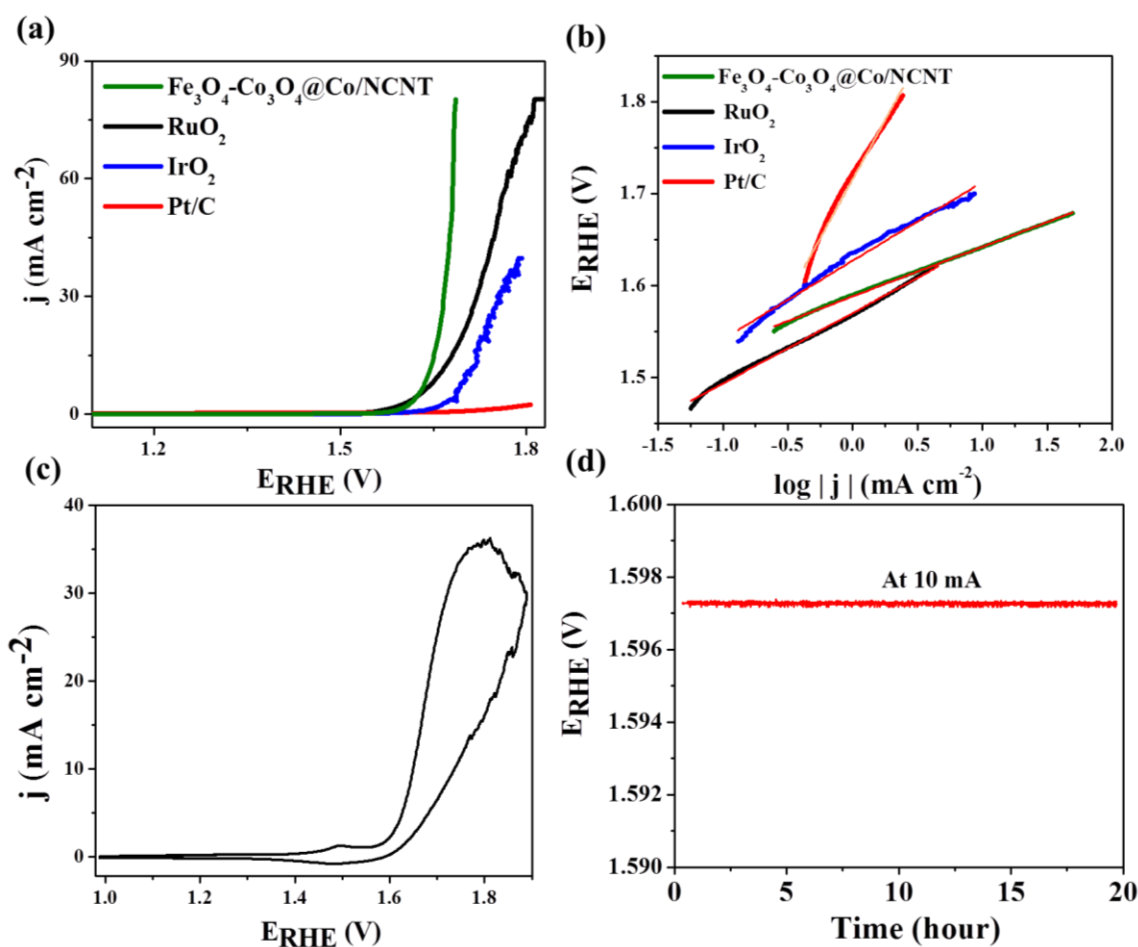


Figure 8: (a) iR -corrected linear sweep voltammograms of OER for different electrocatalysts at 1600 rpm at a scan rate of 5 mV s⁻¹, (b) OER Tafel plots, (c) CV of Fe₃O₄-Co₃O₄@Co/NCNT, (d) chronopotentiometric stability of Fe₃O₄-Co₃O₄@Co/NCNT at 10 mA cm⁻².

observed for the catalysts in Ar-saturated KOH. In contrast, when the electrolyte was saturated with O₂, Fe₃O₄-Co₃O₄@Co/NCNT reduces oxygen at an onset potential of ~0.80 V (Figure 7b). Linear sweep voltammograms (LSV) recorded in the ORR potential region using a rotating disk electrode (RDE) at different rotation speed are shown in Figure 7b. LSV at different rotation speeds shows increase in cathodic current as a function of rotation rate due to the improved mass transport (Figure 7b). The onset and half wave potential of this catalyst is 0.82 and 0.7 V vs. RHE at 1600 rpm. The kinetic parameters as calculated from Koutecky-Levich (K-L) plot shows good linearity and parallelism in the range of 0.65 and 0.4 V vs. RHE and the electron transfer numbers are calculated to be 3.6-3.8 (Figure 7c). The RRDE experiment shows that the H₂O₂ generated during the oxygen reduction process is 26.65 % and the calculated electron

transfer number is 3.46 at 0.5 V, supporting the $4e^-$ transfer pathway (Figure 7d). Compared to commercial Pt/C, RuO₂ and IrO₂ nanomaterials used as reference catalysts within this study, Fe₃O₄-Co₃O₄@Co/NCNT reveals an ORR activity close to that of commercial Pt/C with an overpotential of 0.16 V and a superior performance than RuO₂ or IrO₂ (Figure 7e).

Furthermore, this catalyst is investigated for OER activity as summarized in Figure 8. The Fe₃O₄-Co₃O₄@Co/NCNT catalyst has an onset potential of 1.59 V vs. RHE and reaches 10 mA cm⁻² at a potential of 1.65 V vs. RHE (Figure 8a). This value is close to benchmark catalyst, RuO₂ (1.66 V vs. RHE) and better than IrO₂ (1.70 V vs. RHE) at the same current density. The Tafel slopes calculated for the OER of Fe₃O₄-Co₃O₄@Co/NCNT, Pt/C, RuO₂ and IrO₂ are 53.9, 256.8, 76.6 and 85.3 mV dec⁻¹, respectively, in the potential range of 1.45 V and 1.85 V, suggesting that the OER process is kinetically much faster for Fe₃O₄-Co₃O₄@Co/NCNT, making it a highly potent electrocatalyst (Figure 8b). A pair of redox peaks at 1.49 V (anodic) and 1.48 V (cathodic) vs. RHE is observable in CV, which can be assigned to Co^{IV}/Co^{III} redox couple, identified as intermediate for water oxidation process (Figure 8c).^{31,66} The sum of overvoltage between ORR and OER is considered to be an important parameter for evaluating bi-functional electrocatalytic activity. Notably, the overpotential difference between ORR at a current density of -1 mA cm⁻² and OER at 10 mA cm⁻² is 0.95 V (Figure 9, Table 4), emphasizing the efficiency of Fe₃O₄-Co₃O₄@Co/NCNT in catalyzing

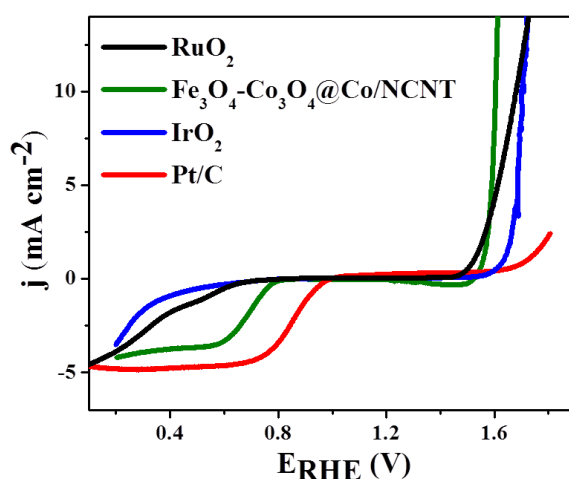


Figure 9: *i*R-corrected linear sweep voltammograms recorded at 1600 rpm in O₂ saturated solution: comparison of bi-functional electrocatalytic activities of different catalysts for ORR and OER reactions.

both ORR and OER. The figure of merit values for other state-of-art catalysts such as Pt/C, RuO₂, IrO₂ are summarized in Table 4. Finally, the stability of bi-functional catalyst is tested for its practical operation in any real energy application. The catalyst is thus subjected to chronoamperometric and chronopotentiometric stability tests by continuous polarization at 0.5 V vs. RHE and maintaining at 10 mA cm⁻², respectively (Figure 7f, 8d). It shows excellent stability with no significant decline of the current on continuous polarization. This also confirms that the metal oxide nanoparticles are well embedded in the graphitic backbone, making it highly durable when performing under harsh condition.

These results suggest that the carbonization under H₂ atmosphere has significant impact on the catalytic property.¹⁵ The N-doped graphitic CNT matrix improves the overall conductivity of the material. The presence of abundant catalytically active M-N-C sites in the porous carbon structure is considered to be ORR/OER active sites.⁶⁷ The addition of metal/semiconductor core-shell nanoparticles (Co₃O₄@Co) are known to improve the overall charge transfer kinetics.¹⁵ In fact, the presence of Fe centres is also known to enhance the activity of the CNTs towards catalysis. In fact, this graphitic backbone also improves the overall robustness of the catalyst.

Table 4. The bi-functional activities of different electrocatalysts for ORR and OER.

Catalyst	E _{ORR} (V) (E ₁) at -1 mA cm ⁻²	Current at half-wave potential (E _{1/2})	E _{OER} (V) (E ₂) at 10 mA cm ⁻²	Tafel slope mV dec ⁻¹	ΔE (V) (E ₁ -E ₂)	ΔE (V) (E _{1/2} -E ₂)
Fe ₃ O ₄ -Co ₃ O ₄ @Co/NCNT	0.74	0.7	1.65	53.9	0.91	0.95
Pt/C	0.99	0.84	-	256.8	-	-
RuO ₂	0.53	0.35	1.66	76.6	1.13	1.31
IrO ₂	0.38	0.29	1.70	85.3	1.32	1.32

5A.4 Conclusion

In this chapter, a dual-MOFs (Fe-ndc + ZIF-67) pyrolysis strategy has been adopted for preparation of mixed-metallic Fe₃O₄-Co₃O₄@Co/NCNT electrocatalyst. Interestingly, the physical mixture of these dual-MOFs converts into a single N-doped carbon nanotube (CNT) matrix on heat treatment under H₂/Ar atmosphere. ZIF-67 nanoparticles not only provide the additional C and N source, the growth of NCNTs is also catalysed by the metallic Co nanoparticles formed *in situ*. This catalyst exhibits remarkable electrocatalytic activity and stability, and even outperforms commercial Pt/C, state-of-art RuO₂ and IrO₂ electrocatalysts as a bi-functional electrocatalyst. The electrocatalytic activity might be mainly attributed to the chemical composition and structure of metal oxide/core-shell nanoparticles doped NCNTs formed, as well as their robust overall framework structure. The facile strategy demonstrated here can be applied for the preparation of many other MOF-derived functional nanomaterials and opens up a new avenue for developing highly active MOF-derived electrocatalysts for different electrochemical energy technologies.

5A.5 References

1. G. Chen, S. R. Bare, T. E. Mallouk, *J. Electrochem. Soc.* **2002**, *149*, A1092.
2. J. S. Lee, S. T. Kim, R. Cao, N. S. Choi, M. Liu, K. T. Lee, J. Cho, *Adv. Energy Mater.* **2011**, *1*, 34.
3. M. Shao, Q. Chang, J. P. Dodelet, R. Chenitz, *Chem. Rev.* **2016**, *116*, 3594.
4. D. Wang, H. L. Xin, R. Hovden, H. Wang, Y. Yu, D. A. Muller, F. J. DiSalvo, H. D. AbruÇa, *Nat. Mater.* **2013**, *12*, 81.
5. G. Wu, K. L. More, C. M. Johnston, P. Zelenay, *Science*, **2011**, *332*, 443.
6. A. Morozan, F. Jaouen, *Energy Environ. Sci.* **2012**, *5*, 9269.
7. M. D. Allendorf, C. A. Bauer, R. K. Bhakta, R. J. T. Houk, *Chem. Soc. Rev.* **2009**, *38*, 1330.
8. A. A. Gewirth, M. S. Thorum, *Inorg. Chem.* **2010**, *49*, 3557.
9. H. A. Gasteiger, N. M. Marković, *Science*, **2009**, *324*, 48.
10. H. A. Gasteiger, S. S. Kocha, B. Sompalli, F. T. Wagner, *Appl. Catal. B*, **2005**, *56*, 9.

11. M. G. Walter, E. L. Warren, J. R. McKone, S. W. Boettcher, Q. X. Mi, E. A. Santori, N. S. Lewis, *Chem. Rev.* **2010**, *110*, 6446.
12. K. Maeda, K. Teramura, D. L. Lu, T. Takata, N. Saito, Y. Inoue, K. Domen, *Nature*, **2006**, *440*, 295.
13. Y. C. Lu, Z. Xu, H. A. Gasteiger, S. Chen, K. Hamad-Schifferli, Y. Shao-Horn, *J. Am. Chem. Soc.* **2010**, *132*, 12170.
14. M. Busch, N. B. Halck, U. Kramm, S. Siahrostami, P. Krtil, J. Rossmeisl, *Nano Energy*, **2016**, *29*, 334.
15. A. Aijaz, J. Masa, C. Rçsler, W. Xia, P. Weide, A. J. R. Botz, R. A. Fischer, W. Schuhmann, M. Muhler, *Angew. Chem. Int. Ed.* **2016**, *55*, 4087.
16. L. Arroyo-Ramírez, D. Rodríguez, W. Otaño, C. R. Cabrera, *ACS Appl. Mater. Interfaces* **2012**, *4*, 2018.
17. S. I. Choi, S. U. Lee, W. Y. Kim, R. Choi, K. Hong, K. Nam, S. W. Han, J. T. Park, *ACS Appl. Mater. Interfaces* **2012**, *4*, 6228.
18. R. Choi, S. Choi, C. H. Choi, K. M. Nam, S. I. Woo, J. T. Park, S. W. Han, *Chem. Eur. J.* **2013**, *19*, 8190.
19. Y. Gorlin, T. F. Jaramillo, *J. Am. Chem. Soc.* **2010**, *132*, 13612.
20. H. Y. Jung, S. Park, B. N. Popov, *J. Power Sources* **2009**, *191*, 357.
21. F. D. Kong, S. Zhang, G. P. Yin, Z. B. Wang, C. Y. Du, G. Y. Chen, N. Zhang, *Int. J. Hydrogen Energy* **2012**, *37*, 59.
22. F. D. Kong, S. Zhang, G. P. Yin, N. Zhang, Z. B. Wang, C. Y. Du, *J. Power Sources* **2012**, *210*, 321.
23. a) D. Wang, H. L. Xin, R. Hovden, H. Wang, Y. Yu, D. A. Muller, F. J. DiSalvo, H. D. Abruça, *Nat. Mater.* **2013**, *12*, 81 b) I. Katsounaros, S. Cherevko, A. R. Zeradjanin, K. J. J. Mayrhofer, *Angew. Chem. Int. Ed.* **2014**, *53*, 102 c) Y. Gorlin, T. F. Jaramillo, *J. Am. Chem. Soc.* **2010**, *132*, 13612.
24. C. C. L. McCrory, S. Jung, J. C. Peters, T. F. Jaramillo, *J. Am. Chem. Soc.* **2013**, *135*, 16977.
25. J. Masa, W. Xia, I. Sinev, A. Zhao, Z. Sun, S. Grützke, P. Weide, M. Muhler, W. Schuhmann, *Angew. Chem. Int. Ed.* **2014**, *53*, 8508.
26. D. Kong, J. J. Cha, H. Wang, H. R. Lee, Y. Cui, *Energy Environ. Sci.* **2013**, *6*, 3553.

27. Z. Peng, D. Jia, A. M. Al-Enizi, A. A. Elzatahry, G. Zheng, *Adv. Energy Mater.* **2015**, 5, 1402031.
28. L. A. Stern, L. Feng, F. Song, X. Hu, *Energy Environ. Sci.* **2015**, 8, 2347.
29. J. Li, J. Li, X. Zhou, Z. Xia, W. Gao, Y. Ma, Y. Qu, *ACS Appl. Mater. Interfaces*, **2016**, 8, 10826.
30. Y. Zhang, B. Ouyang, J. Xu, G. Jia, S. Chen, R. S. Rawat, H. J. Fan, *Angew. Chem. Int. Ed.* **2016**, 55, 8670.
31. J. Masa, P. Weide, D. Peeters, I. Sinev, W. Xia, Z. Sun, C. Somsen, M. Muhler, W. Schuhmann, *Adv. Energy Mater.* **2016**, 6, 1502313.
32. Q. Li, R. Cao, J. Cho, G. Wu, *Adv. Energy Mater.* **2014**, 4, 1301415.
33. R. Bashyam, P. Zelenay, *Nature* **2006**, 443, 63.
34. Y. Liang, Y. Li, H. Wang, H. Dai, *J. Am. Chem. Soc.* **2013**, 35, 2013.
35. Y. Ji, L. Huang, J. Hu, C. Streb, Y. F. Song, *Energy Environ. Sci.* **2015**, 8, 776.
36. H. Wang, T. Maiyalagan, X. Wang, *ACS Catal.* **2012**, 2, 781.
37. J. Liang, Y. Jiao, M. Jaroniec, S. Z. Qiao, *Angew. Chem. Int. Ed.* **2012**, 51, 1496.
38. Y. Zhao, R. Nakamura, K. Kamiya, S. Nakanishi, K. Hashimoto, *Nat. Commun.* **2013**, 4, 2390.
39. K. Parvez, S. Yang, Y. Hernandez, A. Winter, A. Turchanin, X. Feng, K. Mullen, *ACS Nano*, 2012, **6**, 9541.
40. S. Han, D. Wu, S. Li, F. Zhang, X. Feng, *Adv. Mater.* **2014**, 26, 849.
41. Y. Liang, Y. Li, H. Wang, H. Dai, *J. Am. Chem. Soc.*, 2013, **35**, 2013.
42. Y. Ji, L. Huang, J. Hu, C. Streb, Y. F. Song, *Energy Environ. Sci.* **2015**, 8, 776.
43. H. Wang, T. Maiyalagan, X. Wang, *ACS Catal.* **2012**, 2, 781.
44. J. Liang, Y. Jiao, M. Jaroniec, S. Z. Qiao, *Angew. Chem. Int. Ed.* **2012**, 51, 1496.
45. Y. Zhao, R. Nakamura, K. Kamiya, S. Nakanishi, K. Hashimoto, *Nat. Commun.* **2013**, 4, 2390.
46. G. Wu, K. L. More, C. M. Johnston, P. Zelenay, *Science* **2011**, 332, 443.
47. Z. J. Jiang, Z. Jiang, *Sci Rep.* 2016, **6**, 27081.

48. K. Parvez, S. Yang, Y. Hernandez, A. Winter, A. Turchanin, X. Feng, K. Mullen, *ACS Nano* **2012**, *6*, 9541.
49. S. Han, D. Wu, S. Li, F. Zhang, X. Feng, *Adv. Mater.* **2014**, *26*, 849.
50. K. Shen, X. Chen, J. Chen, Y. Li, *ACS Catal.* **2016**, *6*, 5887.
51. SMART (V 5.628), SAINT (V 6.45a), XPREP, SHELXTL; Bruker AXS Inc. Madison, Wisconsin, USA, **2004**.
52. G. M. Sheldrick, Siemens Area Detector Absorption Correction Program, University of Göttingen, Göttingen, Germany, **1994**.
53. A. Altomare, G. Cascarano, C. Giacovazzo, A. Guagliardi, *J. Appl. Cryst.* **1993**, *26*, 343–350.
54. G. M. Sheldrick, SHELXL-97, Program for Crystal Structure Solution and Refinement; University of Göttingen, Göttingen, Germany, **1997**.
55. A. L. Spek, *J. Appl. Cryst.* **2003**, *36*, 7.
56. G. M. Sheldrick, SHELXS 97, Program for the Solution of Crystal Structure, University Göttingen, Germany, **1997**.
57. L. J. Farrugia, WinGX-A Windows Program for Crystal Structure Analysis, *J. Appl. Cryst.* **1999**, *32*, 837.
58. J. F. Lu, C. Jen Tsai, *Nanoscale Res. Lett.* **2014**, *9*, 216.
59. V. Chabot, D. Higgins, A. Yu, X. Xiao, Z. Chena, J. Zhang, *Energy Environ. Sci.* **2014**, *7*, 1564.
60. K. Artyushkova, S. Levendosky, P. Atanassov, J. Fulghum, *Top Catal.* **2007**, *46*, 263.
61. Z. Ban, Y. A. Barnakov, F. Li, V. O. Golub, C. J. O'Connor *J. Mater. Chem.* **2005**, *15*, 4660.
62. C. Hui, C. Shen, T. Yang, L. Bao, J. Tian, H. Ding, C. Li, H. J. Gao *J. Phys. Chem. C* **2008**, *112*, 11337.
63. H. W. Tien, Y. L. Huang, S. Y. Yang, J. Y. Wang, C. C. M. Ma, *Carbon* **2011**, 1550.
64. W. Xia, J. Zhu, W. Guo, L. An, D. Xia, R. Zou, *J. Mater. Chem. A* **2014**, *2*, 11606.
65. H. Jin, J. Wang, D. Su, Z. Wei, Z. Pang, Y. Wang, *J. Am. Chem. Soc.* **2015**, *137*, 2688.

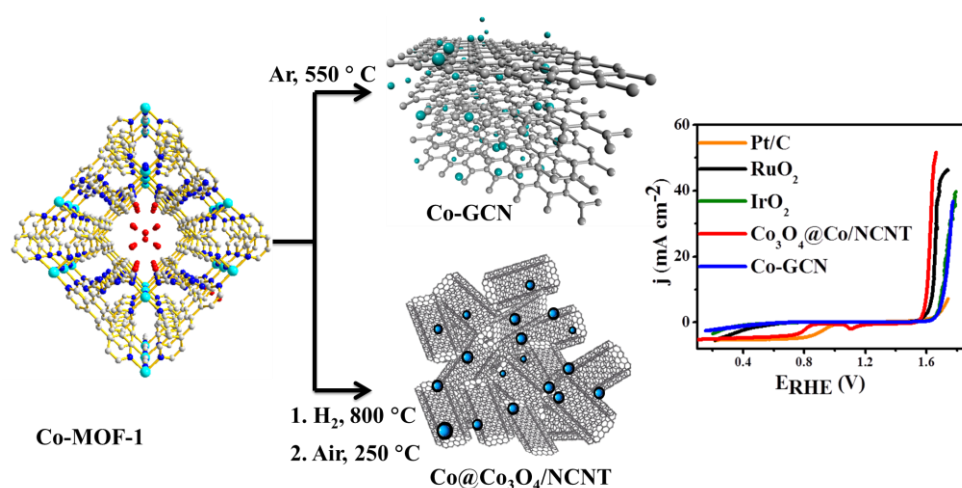
66. H.Yi Wang, S. F. Hung, H.Y Chen, T. S. Chan, H. M. Chen, B. Liu, *J. Am. Chem. Soc.* **2016**, *138*, 36.
67. C.W.B. Bezerra, L. Zhang, K. Lee, H. Liu, A.L.B. Marques, E. P. Marques, H. Wang, J. Zhang, *Electrochim. Acta.* **2008**, *53*, 4937.
68. K. Strickland, E. Miner, Q. Jia, U. Tylus, N. Ramaswamy, W. Liang, M. T. Sougrati, F. Jaouen, S. Mukerjee, *Nat. Commun.* **2015**, *6*, 7343.

Chapter 5B

*Co₃O₄@Co/NCNT Nanostructure
Derived from a Dicyanamide Based
Metal-Organic Framework as
Efficient Bi-functional
Electrocatalyst for Oxygen Reduction
and Evolution Reactions*

Chapter 5B

Co₃O₄@Co/NCNT Nanostructure Derived from a Dicyanamide Based Metal-Organic Framework as Efficient Bi-functional Electrocatalyst for Oxygen Reduction and Evolution Reactions



Summary: This chapter describes synthesis and characterizations of bi-functional electrocatalysts, derived from a dicyanamide based nitrogen rich framework $\{[\text{Co}(\text{bpe})_2(\text{N}(\text{CN})_2)] \cdot (\text{N}(\text{CN})_2) \cdot (5\text{H}_2\text{O})\}_n$ [Co-MOF-1, bpe = 1,2-bis(4-pyridyl)ethane, $\text{N}(\text{CN})_2^-$ = dicyanamide] under different pyrolysis conditions. Pyrolysis of the Co-MOF-1 under Ar atmosphere (at 550 °C) yielded Co/CoO nanoparticles embedded in a N-doped porous carbonaceous matrix (Co-GCN) while pyrolysis under a reductive H_2 atmosphere at high temperatures (at 800 °C) and further mild calcination yielded Co_3O_4 @Co core-shell nanoparticles encapsulated in N-doped carbon nanotubes (Co_3O_4 @Co/NCNT). Both catalysts show bi-functional activity towards ORR and OER, however, the Co_3O_4 @Co/NCNT nanostructure exhibited superior electrocatalytic activity for both the ORR with a potential of 0.88 V at a current density of -1 mA cm^{-2} and the OER with a potential of 1.61 V at 10 mA cm^{-2} , which is competitive with the most active bi-functional catalysts reported previously.

N. Sikdar, B. Konkena, J. Masa, W. Schuhmann, T. K. Maji, submitted

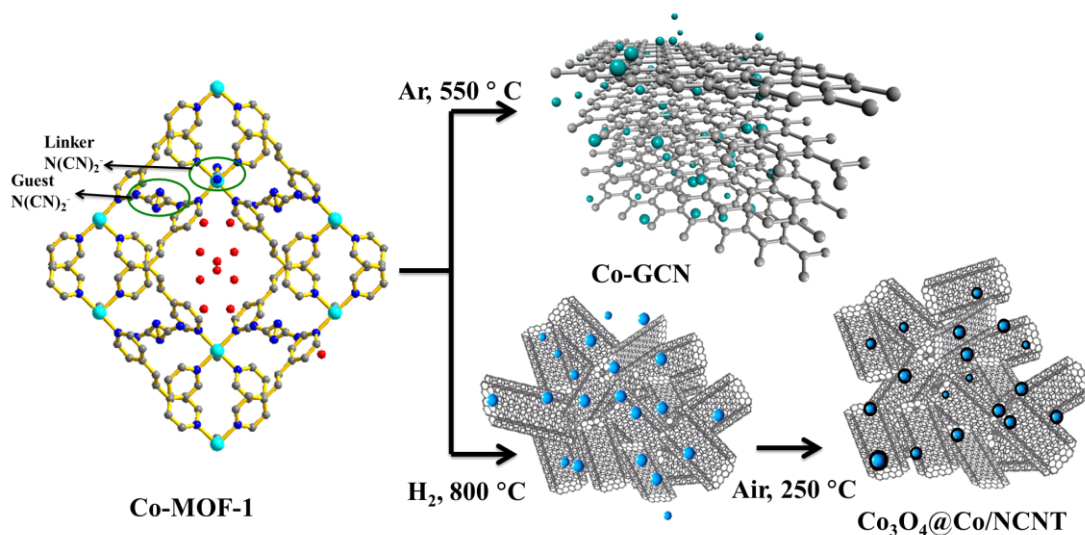
5B.1 Introduction

Increased understanding of oxygen electrochemistry will lead to wider use of the most promising clean and sustainable electrochemical energy storage and conversion systems, including, regenerative fuel cells and metal-air batteries among others.¹⁻³ Oxygen electrochemistry entails water oxidation to release molecular oxygen (oxygen evolution reaction (OER)), and the inverse reaction, oxygen reduction to produce water (oxygen reduction reaction (ORR)). The OER is of practical importance in many electrochemical systems like electrowinning,⁴ electroplating⁵ and photo-electrochemical water splitting,⁶ whereas the ORR is fundamentally essential in fuel cells.⁷ These reactions involve multi-electron transfer steps with different mechanisms associated with a variety of reaction intermediates, which require improved understanding in order to resolve the kinetic limitations of the reactions. Typically, OER and ORR have been studied and reported separately.

Bi-functional catalysts, capable of driving both reactions, for example in unitized regenerative fuel cells (URFC), demand the development of reliable catalyst materials that are abundant and cheap.⁸ Presently, well known catalysts for ORR and OER are precious metals or their alloys, and precious metal oxides.⁹⁻¹¹ Considering the high cost and scarcity of precious metals, a number of alternative earth abundant materials such as transition metal (e.g., Fe, Ni, Co and Mn) oxides,¹²⁻¹³ sulphides,¹⁴⁻¹⁵ phosphides¹⁶⁻¹⁷ and nitrides/borides¹⁸⁻¹⁹ have been introduced into the field. More recently, nanocarbon materials and their composites have been recognized as very active and stable materials.²⁰⁻²³ Furthermore, the catalytic properties are improved by introducing heteroatoms like N, B and S which modify the electronic and structural properties of carbon.²⁴⁻²⁶ The enhanced performance arises from the electronic structure, conductivity and carbon defects induced by the hetero atoms.^{27,28} However, none of these materials is efficient as bi-functional OER and ORR electrocatalysts. Thus, new synthetic methodologies need to be developed to fabricate metal free or non-precious and abundant metal based bi-functional catalysts for reversible oxygen electrodes in unitized regenerative fuel cells or metal-air batteries.^{29,30}

Recently, metal-organic frameworks (MOFs) have attracted enormous interest as self-sacrificial templates for the tunable synthesis of metal/metal-oxide encapsulated

hierarchical graphitic nanostructures under different pyrolysis conditions.³¹ MOFs are a class of coordination polymers composed of metal ions and organic ligands, and are potential materials for gas storage and separation, luminescence, sensing and catalysis among others.³²⁻³⁴ The derived materials have shown to be promising in hydrogen storage, sensing, electrochemical capacitors and in lithium-ion batteries.³¹ Notably, N-doped nanocarbon frameworks have been demonstrated to be efficient ORR and OER electrocatalysts.³⁵⁻³⁶ However, only a handful of examples of bi-functional electrocatalysts have been reported. A catalyst with low overpotential difference between ORR and OER is of prime importance for application as electrocatalyst for reversible oxygen electrodes. Notably, a subclass of MOFs, zeolitic imidazolate frameworks (ZIFs) such as Ni-ZIF, Co-ZIF, Zn-ZIF, among others, have been utilized as excellent templates for producing metal rich porous N-doped nanocarbon electrocatalysts.³⁷⁻³⁹ In a recent report, a Co based core-shell ($\text{Co}_3\text{O}_4@\text{Co}$) bi-functional electrocatalyst from Co-ZIF was synthesized, where the synergetic effect of the core-shell $\text{Co}_3\text{O}_4@\text{Co}$ structure on the electrocatalytic properties was explained.⁴⁰ We envisage that



Scheme 1: Schematic of Co-MOF-1 (grey = C, blue = N, red = O, cyan = Co) pyrolysis to prepare MOF derived Co-GCN and $\text{Co}_3\text{O}_4@\text{Co}/\text{NCNT}$ electrocatalysts under different conditions.

increasing the N-content and graphitic nature of the matrix may decrease the overpotential difference, hence, better catalytic properties. With this assumption, we considered a novel dicyanamide containing porous framework

$\{[\text{Co}(\text{bpe})_2(\text{N}(\text{CN})_2)] \cdot (\text{N}(\text{CN})_2) \cdot (5\text{H}_2\text{O})\}_n$ [Co-MOF-1, bpe = 1,2-bis(4-pyridyl)ethane), $\text{N}(\text{CN})_2^-$ = dicyanamide], reported earlier,⁴¹ as a carbonization template. Dicyanamide, being a chemical precursor for *g*-C₃N₄ can be an ideal source of N-doped graphitic matrix, rich in Co-N₄ centres. Coupling of these Co-N₄ moieties with metallic Co cores surrounded with a semiconductive Co₃O₄ shell, is expected to provide superior bi-functional electrocatalytic performance.⁴⁰

Herein, in this chapter, the syntheses of Co@N-doped graphitic (Co-GCN) and Co₃O₄@Co@N-doped carbon nanotube (CNT) matrix (Co₃O₄@Co/NCNT) have been demonstrated from a cheap and easily scalable Co-MOF-1, under tunable pyrolysis conditions (Scheme 1).⁴¹ Co₃O₄@Co/NCNT showed substantially improved bi-functional catalytic activity and durability compared to state-of-art benchmark electrocatalysts under similar conditions. Most importantly, the difference between the overpotentials measured at current densities of -1 mA cm⁻² for the ORR and 10 mA cm⁻² for the OER did not exceed 0.73 V for the Co₃O₄@Co/NCNT catalyst, suggesting that the Co₃O₄@Co/NCNT catalyst is one of the best bi-functional OER and ORR catalyst reported so far.

5B.2 Experimental section

5B. 2.1 Materials

All reagents and solvents employed were commercially available and used as supplied without further purification. Co(NO₃)₂·6H₂O was obtained from Spectrochem. 1,2-bis(4-pyridyl)ethane (bpe), sodium dicyanamide, RuO₂, IrO₂, Pt/C were obtained from Sigma Aldrich.

5B. 2.2 Synthesis of $\{[\text{Co}(\text{bpe})_2(\text{N}(\text{CN})_2)] \cdot (\text{N}(\text{CN})_2) \cdot (5\text{H}_2\text{O})\}_n$ (Co-MOF-1)

Co-MOF-1 was synthesized following a previously reported procedure.⁴¹ To prepare Co-MOF-1, 10 mL of aqueous solution of Na(N(CN)₂) (3 mmol, 0.267 g) was mixed with an ethanolic solution (10 mL) of bpe (3 mmol, 0.552 g) and stirred for 20 min to mix well. Co(NO₃)₂·6H₂O (1.5 mmol, 0.436 g) was dissolved in 20 mL of water to prepare the metal precursor solution. The ligand solution was then slowly added to the metal precursor solution and stirred for 24 h. The precipitate was washed with ethanol 4-5 times and left overnight for drying. Yield 80 %. FT-IR (KBr pellet, 4000–400 cm⁻¹):

3492(br), 3234(w), 3070(w), 2330(s), 2232(m), 2126(m), 1610(s), 1568(s), 1502(s), 1424(s), 1311(w), 1223(s), 1065(s), 1021(s), 910(w), 872(w), 829(s). Elemental analysis calculated for Co-MOF-1; $C_{28}H_{34}N_{10}CoO_5$ C, 51.79; H, 5.24; N, 21.58; found C, 52.24; H, 4.72; N, 21.37.

5B.2.3 Syntheses of Co-MOF-1 derived electrocatalysts

5B.2.3.1 Synthesis of Co-GCN

For the synthesis of Co-GCN, 800 mg of Co-MOF-1 was pyrolyzed in an alumina boat under continuous Ar flow at 550 °C (heating rate of 5 °C min⁻¹) for 5 h for complete carbonization.

5B.2.3.2 Synthesis of Co₃O₄@Co/NCNT

The as-synthesised Co-MOF-1 (800 mg) was transferred into an alumina boat and pyrolyzed under H₂/Ar (5 % H₂ in 95% Ar) flow. The sample was heated to 800 °C at a heating rate of 10 °C min⁻¹ and maintained at this temperature for 4 h. After cooling to room temperature the sample was further calcined at 250 °C in air for 2 h, forming the core-shell Co₃O₄@Co/NCNT nanocomposite.

5B.2.4 Physical characterizations

Powder XRD patterns of the products were recorded using Cu-K α radiation (Bruker D8 Discover; 40 kV, 30 mA). Transmission electron microscopy (TEM) images were taken with a JEOL JEM-3010 operating at 300 kV. The samples were prepared in the same way as described above but drop casting was made onto carbon-coated TEM grids. To study the surface properties, X-ray photoelectron spectroscopy (XPS, VG Scientific ESCA LAB V) was used. Raman spectroscopy was performed at different locations of the sample using a Jobin Yvon LabRam HR spectrometer with a 514.5 nm Ar laser. Inductively Coupled Plasma-Optical Emission Spectroscopy (ICP-OES) measurements were recorded on a Perkin Elmer Optima 7000dv ICP-OES instrument. 2 mg of Co-GCN and Co₃O₄@Co /NCNT were stirred in 2 mL of conc. HNO₃ overnight at 60 °C. After 12 hours, the solutions were centrifuged, and each supernatant solution was diluted with milliQ water up to 10 mL. The resulting solutions were used for ICP measurements.

5B.2.5 Adsorption measurements

N₂ adsorption isotherms of Co-GCN and Co₃O₄@Co/NCNT at 77 K were measured using an AUTOSORB IQ2 instrument. The samples were activated at 140 °C at 1×10⁻¹ Pa for about 12 h prior to measurements of the isotherms. Helium gas (99.999% purity) at a certain pressure was introduced into the gas chamber and allowed to diffuse into the sample chamber by opening the valve. The amount of gas adsorbed was calculated from the pressure difference ($P_{\text{calc}} - P_e$), where P_{calc} is the calculated pressure with no gas adsorption and P_e is the observed equilibrium pressure. All operations were computer-controlled and automatic.

5B.2.6 Electrochemical measurements

For evaluating the electrochemical performances of the pyrolyzed samples, rotating disk electrode (RDE) voltammetry and rotating ring disk electrode (RRDE) voltammetry were used. All electrochemical measurements were performed using an Autolab PGSTAT12 potentiostat/galvanostat in a conventional three-electrode cell in combination with a Metrohm RDE-2 rotator. The catalyst inks were prepared at a concentration of 5 mg mL⁻¹ in a mixture of milliQ water, ethanol, and Nafion (5 wt %, Sigma Aldrich) in the volume ratio of 49:49:2 as dispersion solvent. The mixture was then sonicated for 30 min to obtain a well-dispersed suspension. Glassy carbon electrodes (4 mm diameter) were used as rotating disk electrodes (RDEs). Before experiments, the glassy carbon electrodes were polished on polishing cloth using different alumina pastes (3.0 - 0.05 μm) to obtain a mirror-like surface, followed by ultrasonic cleaning in water. 5 μL of the catalyst ink was drop-cast on a glassy carbon electrode and left to dry overnight under ambient conditions. The catalyst loading for each electrode was 0.21 mg cm⁻². A 0.1 M KOH solution was used as electrolyte. The counter and reference electrodes were a platinum foil and a Ag/AgCl/3M KCl electrode, respectively. The reference electrode was calibrated with respect to the reversible hydrogen electrode (RHE). Electrochemical impedance spectroscopy was recorded at the corresponding open circuit potential using an ac perturbation of 10 mV in the frequency range from 50 kHz to 1 Hz. The solution resistance was determined from the resulting Nyquist plot, and later used for ohmic drop correction according to the relation, $E_c = E_m - iR_s$, where E_c is the corrected potential and E_m is the measured potential. All current densities were calculated using the geometric

surface area of the electrode. All potentials were rescaled to the pH-independent reversible hydrogen electrode (RHE). The long-term stability was evaluated chronopotentiometrically at a current density of -1 mA cm^{-2} on a graphite rotating disk electrode (5 mm diameter) modified with the catalyst in 0.1 M KOH solution. During the measurements, the electrode was maintained at a rotation of 1600 rpm to avoid accumulation of gas bubbles on the electrode surface. The electrolyte was purged for ~20 min with Ar prior to measurements to determine the background current and later O_2 flow was maintained over the electrolyte throughout the timeframe of the experiment. All measurements were carried out at room temperature. Linear sweep voltammetry (LSV) was performed at rotation speeds of 100, 400, 900, 1600, 2500 and 3600 rpm at a sweep rate of 5 mV s^{-1} .

The number of electrons involved in the reduction process was calculated using the Koutecký–Levich (K–L) equation:

$$\frac{1}{j} = \frac{1}{j_L} + \frac{1}{j_K} = \frac{1}{B\omega^{1/2}} + \frac{1}{j_K}$$

$$B = 0.62nFC_o(D_o)^{2/3}\nu^{-1/6}$$

$$j_K = nFkC_o$$

Here, j is the measured current density, j_K and j_L are the kinetic and diffusion-limited current densities, ω is the angular frequency of the RDE in radians per second, n is the number of electrons involved in the reaction, F is the Faraday constant (96485 C mol^{-1}), D_o is the diffusion coefficient of O_2 in the electrolyte ($1.93 \times 10^{-5} \text{ cm}^2 \text{ s}^{-1}$), ν is the kinematic viscosity of the electrolyte ($1.01 \times 10^{-2} \text{ cm}^2 \text{ s}^{-1}$), C_o is the concentration of O_2 in the electrolyte ($1.26 \times 10^{-6} \text{ mol cm}^{-3}$) and k is the electron transfer rate constant.

Rotating ring disk electrode (RRDE) voltammetry was used to calculate the number of electrons and the amount of H_2O_2 formed during ORR based on the ratio of the disk and the ring current as shown in the equations given below. For the RRDE experiments, the ring electrode was held at a potential of 1.5 V (vs. RHE) to oxidize hydrogen peroxide.

$$n_e = \frac{4I_D}{I_D + \frac{I_R}{N}}, \quad \text{H}_2\text{O}_2(\%) = \frac{\frac{I_R}{N}}{I_D + \frac{I_R}{N}} \times 200$$

$N = 0.2678$ is the collection efficiency, I_D is the Faradaic disk current, and I_R is the Faradaic ring current.

5B.3 Results and discussion

5B.3.1 Characterizations of MOF derived composites

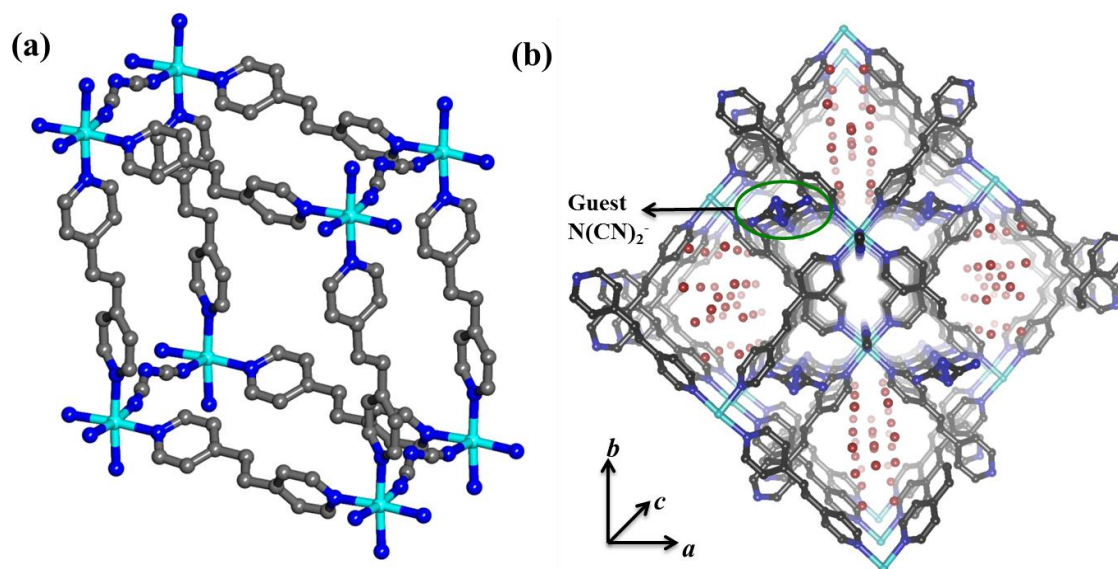


Figure 1: (a) View of building units of Co-MOF-1 [cyan = Co, blue: N, grey: C, red: oxygen], (b) N-rich 3D interpenetrated framework; the small circle represents the guest $\text{N}(\text{CN})_2^-$ and the red sticks represent free guest $\text{N}(\text{CN})_2^-$ anions.

In this study, we have deliberately chosen dicyanamide ($\text{N}(\text{CN})_2^-$) containing Co^{II} -based two-fold interpenetrated 3D framework $\{[\text{Co}(\text{bpe})_2(\text{N}(\text{CN})_2)] \cdot (\text{N}(\text{CN})_2) \cdot (5\text{H}_2\text{O})\}_n$ (Co-MOF-1) (Figure 1-2), reported previously,⁴¹ as a precursor for the synthesis of bifunctional catalysts for reversible oxygen electrodes. This flexible framework showed permanent porosity and high thermal stability. In Co-MOF-1, each metal centre is octahedrally coordinated to four bpe ligands and two $\text{N}(\text{CN})_2^-$ anions, resulting in overall $\text{Co}^{\text{II}}\text{-N}_6$ moieties (Figure 1a). The four bpe linkers are connected through Co^{II} centres to

form two dimensional sheets along ab plane which is pillared by $\text{N}(\text{CN})_2^-$ anions constructing a 3D framework (Figure 1b). Two such 3D frameworks entangle with each other resulting in a bi-porous framework occupied by the $\text{N}(\text{CN})_2^-$ ions and water molecules. By this, 24 carbon and 8 nitrogen atoms are present per formula unit of Co-MOF-1. Thus, the high carbon and nitrogen content and the abundant $\text{Co}^{\text{II}}\text{-N}_6$ centres in Co-MOF-1 encouraged us to pyrolyze it under different conditions in order to obtain Co centres embedded in a porous carbon nitride type matrix in which electrochemically active M-N-C sites are supposed to act as non-precious catalytic sites.

Co-MOF-1 was pyrolyzed at 550 °C under Ar for 6 h to prepare Co-GCN, and separately at 800 °C under continuous H_2/Ar flow for 4 h followed by mild calcination in air at 250 °C for 2 h to prepare $\text{Co}_3\text{O}_4@\text{Co}/\text{NCNT}$, following a procedure as previously described.⁴¹ The obtained materials were characterized using PXRD, Raman spectroscopy, XPS and TEM (Figure 3-5). The weak XRD peak at $2\theta = 26.5^\circ$ for Co-GCN is due to (002) reflections suggesting irregular graphitic stacking (Figure 3a). All the other peaks are assigned to the cubic metallic Co phase.⁴⁰ The PXRD pattern of $\text{Co}_3\text{O}_4@\text{Co}/\text{NCNT}$ shows a comparatively stronger (002) peak at 25.9° corroborating

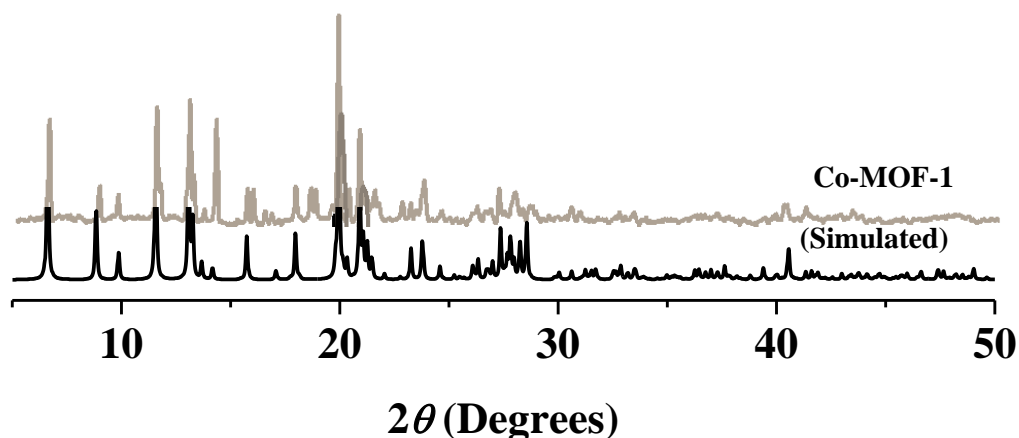


Figure 2: PXRD patterns of simulated and as-synthesized Co-MOF-1.

more regular graphitic stacking. The diffraction peaks at 2θ of 44.1° , 55.5° and 75.9° indicate formation of a crystalline Co phase prior to calcination. Mild calcination in air partially oxidizes Co to a spinel Co_3O_4 phase ($\text{Co}_3\text{O}_4@\text{Co}/\text{NCNT}$) as confirmed from the newly appearing diffraction peaks at 2θ of 19.0° , 31.4° , 35.8° , 59.3° and 65.2° , consistent

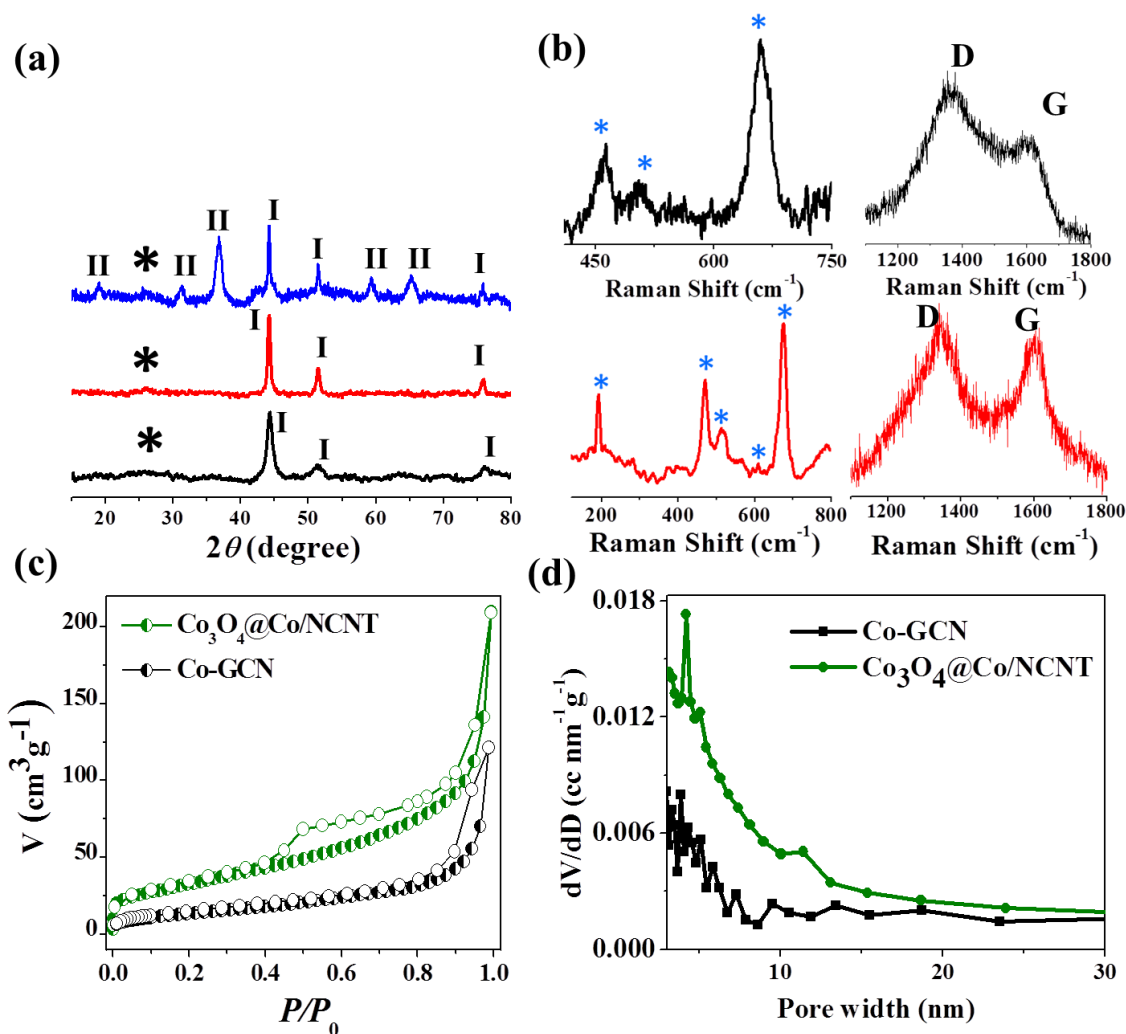


Figure 3: (a) PXRD pattern of Co-GCN (black) and H₂-pyrolized Co-MOF-1 (red) showing the formation of only the metallic Co phase and Co₃O₄@Co/NCNT (blue); *, I, II denote the graphitic (002) peak, Co peaks and Co₃O₄ peaks, respectively, (b) Raman spectra of Co-GCN (black) and Co₃O₄@Co/NCNT (red) showing CoO and Co₃O₄, respectively, along with the characteristic D and G bands, (c) N₂ adsorption isotherm of Co-GCN and Co₃O₄@Co/NCNT at 77 K, (d) BJH pore size distribution of Co-GCN and Co₃O₄@Co/NCNT.

with values given in literature.⁴⁰ Co-GCN and Co₃O₄@Co/NCNT were further characterized by Raman spectroscopy to evaluate the nature of the graphitic carbon structure (Figure 3b). Both catalysts showed the characteristic defect-D band and graphitic-G band at ~ 1356 cm⁻¹ and ~ 1609 cm⁻¹ with a I_G/I_D ratio of 0.60 and 0.87 for Co-GCN and Co₃O₄@Co/NCNT, respectively.⁴² This is clearly demonstrating that a higher degree of graphitization is induced during pyrolysis under H₂ atmosphere. Notably, Co-GCN shows bands at 464 cm⁻¹, 509 cm⁻¹ and 660 cm⁻¹, characteristic of CoO phase,

despite the CoO structure was not observed in PXRD.⁴³ On the other hand, Co₃O₄@Co/NCNT shows bands at 192 cm⁻¹, 470 cm⁻¹, 510 cm⁻¹, 609 cm⁻¹ and 675 cm⁻¹, characteristic of the Co₃O₄ spinel phase.⁴⁴ XPS survey spectra of the samples further confirm the presence of Co, C, N and O (Figure 4). The Co 2p XPS spectrum of Co-GCN shows two bands, namely one at 778.5 eV due to metallic Co 2p_{3/2}, and a second at 780.8 eV due to surface cobalt oxides (CoO) within an undersaturated Co-N₄ environment with some Co–C bonds, for example, CoC_xN_y (x + y = 4) (Figure 4a).⁴⁵ In contrast, the Co 2p spectrum of Co₃O₄@Co/NCNT is deconvoluted into four peaks, metallic cobalt at 778.0 eV, Co₃O₄ bands at 789.3 and 780.4 eV, the Co-N₄ environment at 781.4 eV and Co(CO)₄ species at 783.3 eV peaks at 2θ of 19.0°, 31.4°, 35.8°, 59.3° and 65.2°, consistent with values given in literature.⁴⁰ Co-GCN and Co₃O₄@Co/NCNT were further characterized by Raman spectroscopy to evaluate the nature of the graphitic carbon structure (Figure 3b). Both catalysts showed the characteristic defect-D band and graphitic-G band at ~1356 cm⁻¹ and ~1609 cm⁻¹ with a I_G/I_D ratio of 0.60 and 0.87 for Co-GCN and Co₃O₄@Co/NCNT, respectively.⁴² This is clearly demonstrating that a higher degree of graphitization is induced during pyrolysis under H₂ atmosphere. Notably, Co-GCN shows bands at 464 cm⁻¹, 509 cm⁻¹ and 660 cm⁻¹, characteristic of CoO phase, despite the CoO structure was not observed in PXRD.⁴³ On the other hand, Co₃O₄@Co/NCNT shows bands at 192 cm⁻¹, 470 cm⁻¹, 510 cm⁻¹, 609 cm⁻¹ and 675 cm⁻¹, characteristic of the Co₃O₄ spinel phase.⁴⁴ XPS survey spectra of the samples further confirm the presence of Co, C, N and O (Figure 4). The Co 2p XPS spectrum of Co-GCN shows two bands, namely one at 778.5 eV due to metallic Co 2p_{3/2}, and a second at 780.8 eV due to surface cobalt oxides (CoO) within an undersaturated Co-N₄ environment with some Co–C bonds, for example, CoC_xN_y (x + y = 4) (Figure 4a).⁴⁵ In contrast, the Co 2p spectrum of Co₃O₄@Co/NCNT is deconvoluted into four peaks, metallic cobalt at 778.0 eV, Co₃O₄ bands at 789.3 and 780.4 eV, the Co-N₄ environment at 781.4 eV and Co(CO)₄ species at 783.3 eV due to the mild calcination treatment (Figure 4b).⁴⁵ The C 1s spectrum of Co-GCN consists of C-C/C=C peaks at 284.7 eV, C-O peak at 285.8 eV, C-N/C=N peaks at 287.01 eV, O-C=O peak at 288.7 eV, and N-C_{sp3} peak at 289.7 eV (Figure 4c).⁴⁶ Similarly, the C 1s spectrum of Co₃O₄@Co/NCNT also exhibits peaks centred at 284.02 eV, 285.5 eV, 286.7 eV, 287.4 eV, 288.3 eV and 289.6 eV, suggesting the formation of a N-doped graphitic matrix in both cases. Notably, the enhanced C-O

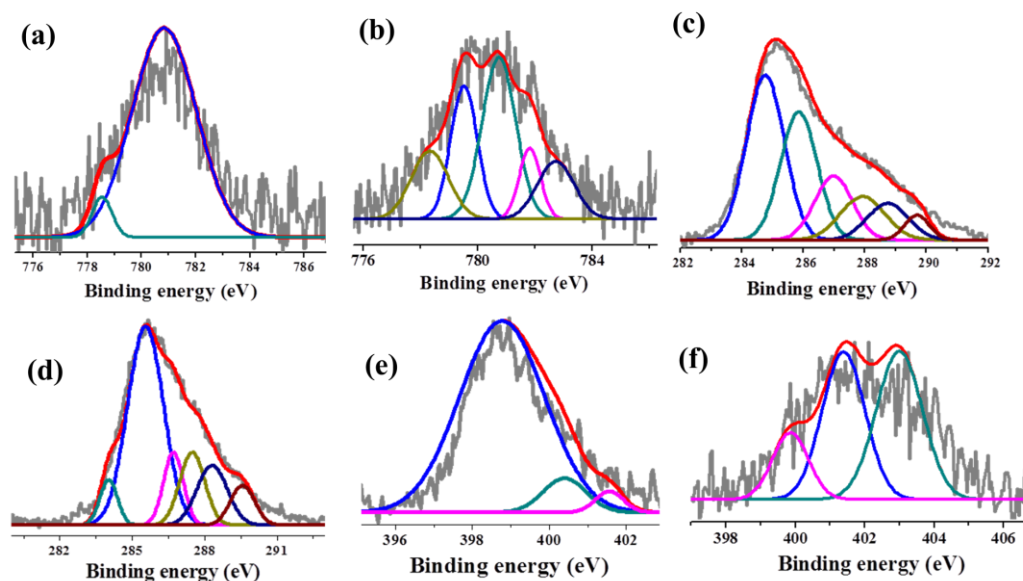


Figure 4: (a) Co 2p core level spectrum of Co-GCN and (b) of $\text{Co}_3\text{O}_4@\text{Co}/\text{NCNT}$, (c) C 1s core level XPS spectra of Co-GCN and (d) for $\text{Co}_3\text{O}_4@\text{Co}/\text{NCNT}$, (e) N 1s core level XPS spectrum of Co-GCN and (f) of $\text{Co}_3\text{O}_4@\text{Co}/\text{NCNT}$.

peak intensity at 285.8 eV in $\text{Co}_3\text{O}_4@\text{Co}/\text{NCNT}$ is probably due to an increased C-O functionalization during the mild calcination process (Figure 4d). N 1s XPS spectra of Co-GCN and $\text{Co}_3\text{O}_4@\text{Co}/\text{NCNT}$ were deconvoluted into three bands at 398.7 eV, 400.6 eV and 401.6 eV, and 399.8 eV, 401.3 eV and 402.9 eV attributed to pyridinic, pyrrolic and graphitic N, respectively (Figure 4e-f).³⁸ The surface nitrogen content calculated from the XPS measurements was 21.26 % for Co-GCN and 10.5 % for $\text{Co}_3\text{O}_4@\text{Co}/\text{NCNT}$. The lesser N-content for the later is due to pyrolysis at higher temperature.³⁸ The Co content determined by ICP-OES was 53.5 and 45 wt% for Co-GCN and $\text{Co}_3\text{O}_4@\text{Co}/\text{NCNT}$, respectively.

TEM images of Co-GCN reveal that Co nanoparticles are homogeneously distributed in a continuous carbon matrix and the size of the nanoparticles is in the range of 10-20 nm (Figure 5a-c). Pyrolysis under H_2 atmosphere also led to the formation of 40-50 nm sized metallic Co nanoparticles, however, unlike Co-GCN, the particles were homogeneously embedded in self-coiled dense carbon nanotubes (CNT) matrix (Figure 5d, g-i). Mostly, Co particles are wrapped with highly graphitic layers of CNTs and in

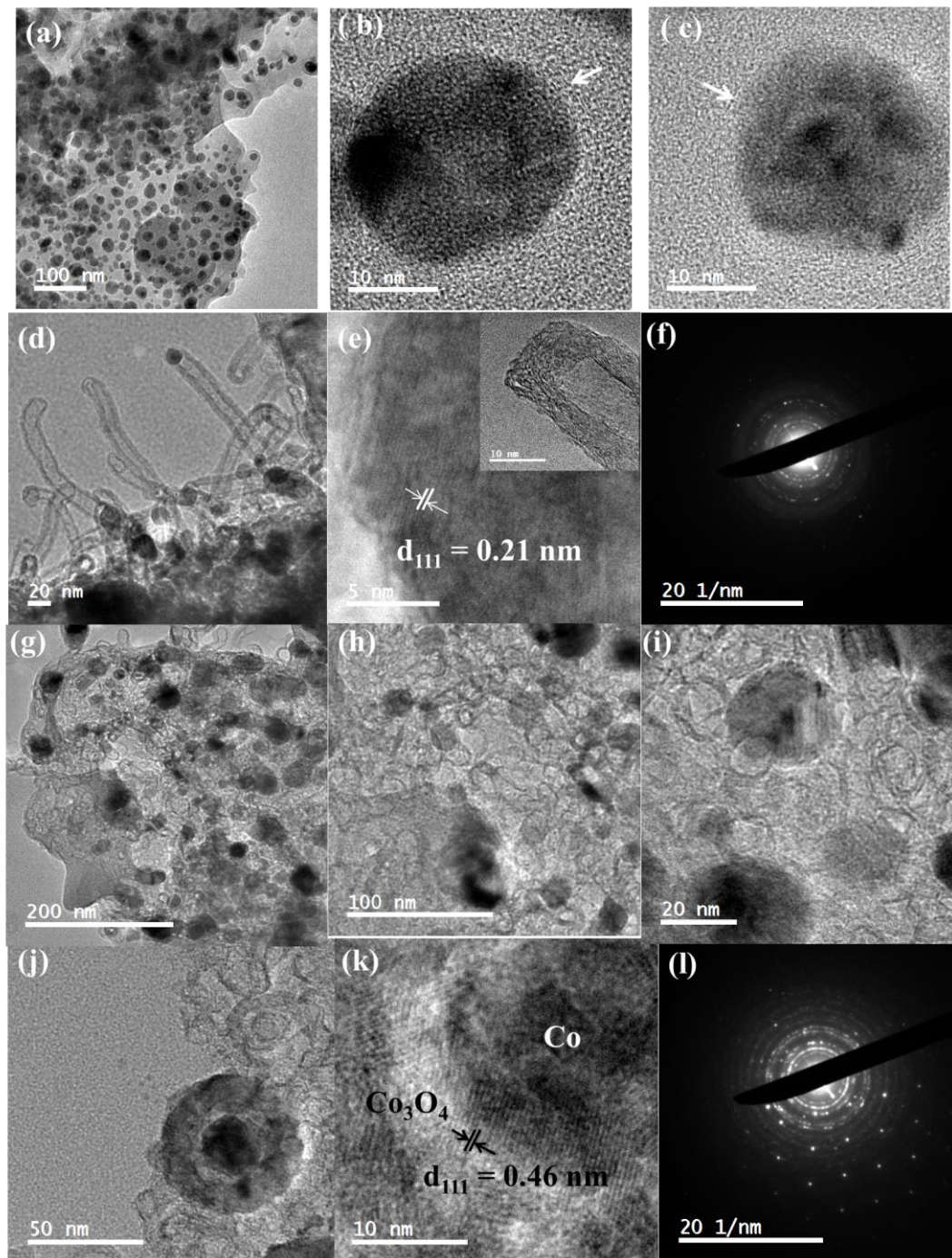


Figure 5: (a) TEM image of Co-GCN, (b-c) are HRTEM images of individual Co-nanoparticles wrapped with few layers of graphitic carbon in Co-GCN, (d) H₂-pyrolized Co-MOF-1 showing metallic Co nanoparticles dispersed in a CNT matrix, (e) HRTEM image of one Co nanoparticle with the inset showing multi-layers of a single CNT, (f) spot-ring SAED patterns of a Co nanoparticle, (g-i) self-coiled CNT matrix (j) Co₃O₄@Co core-shell nanoparticle embedded in a CNT matrix in Co₃O₄@Co/NCNT, (k) HRTEM image of a single Co₃O₄@Co nanoparticle showing lattice fringes, (l) SAED pattern of Co₃O₄@Co.

some cases; these are positioned at the tip of the CNTs. The lattice fringe of the Co nanoparticle is ~ 0.21 nm, was attributed to the $\{111\}$ of cubic metal structure as shown in the high resolution TEM (HRTEM) image (Figure 5e-f).⁴⁰ The average diameter of the CNTs was 10-20 nm with the length ranging between 100 and 200 nm. HRTEM confirms the CNTs to be multiwalled with an average wall thickness of 7-8 nm. Interestingly, after calcination in air, the $\text{Co}_3\text{O}_4@\text{Co}/\text{NCNT}$ formed crystalline core-shell type (50-60 nm sized) $\text{Co}_3\text{O}_4@\text{Co}$ nanoparticles encapsulated in a CNT matrix (Figure 5j-l). The lattice fringe of the outer core, i.e. Co_3O_4 is 0.46 nm, attributed to the cubic $\{111\}$ structure (Figure 5k).⁴⁷ SAED of the Co nanoparticle shows characteristic spot-ring type patterns, whereas, after the formation of core-shell $\text{Co}_3\text{O}_4@\text{Co}/\text{NCNT}$ nanoparticles an additional pattern of Co_3O_4 can be observed (Figure 5l).

Nitrogen adsorption measurements (at 77 K) were performed for deriving the surface area and elucidating the pore structure of the catalysts (Figure 3c-d). Co-GCN and $\text{Co}_3\text{O}_4@\text{Co}/\text{NCNT}$ show typical type-II and type-IV isotherms with BET surface areas of 48 and $118 \text{ m}^2 \text{ g}^{-1}$, respectively. The pore size distributions of both samples show a high contribution from *in-situ* generated mesopores with dimensions in the range of 2–30 nm as calculated using the Barrett-Joyner-Halenda (BJH) method (Figure 3d). The pore volumes of Co-GCN and $\text{Co}_3\text{O}_4@\text{Co}/\text{NCNT}$ were 0.179 and $0.29 \text{ cm}^3 \text{ g}^{-1}$, respectively. These data indicate that the high temperature H_2 treatment generated a more porous matrix than pyrolysis in Ar atmosphere.

5B.3.2 Electrocatalytic activity and stability

The electrocatalytic activity of as prepared Co-GCN and $\text{Co}_3\text{O}_4@\text{Co}/\text{NCNT}$ was examined using cyclic voltammetry (CV) in 0.1 M KOH solution with a catalyst loading of 0.21 mg cm^{-2} . As shown in the CVs (Figure 6a-b), no appreciable redox peaks were observed for the catalysts in Ar-saturated KOH. In contrast, when the electrolyte was saturated with O_2 , Co-GCN displays a small activity for the oxygen reduction reaction (ORR) at ~ 0.42 V with low currents, whereas $\text{Co}_3\text{O}_4@\text{Co}/\text{NCNT}$ exhibits a substantially smaller overpotential for the ORR (at ~ 0.84 V) together with a significantly increased ORR reduction current, indicating the excellent ORR catalytic activity of the latter material. Linear sweep voltammograms recorded in the ORR potential region using a rotating disc electrode (RDE) at different rotation speeds are shown in Figure 6c-d.

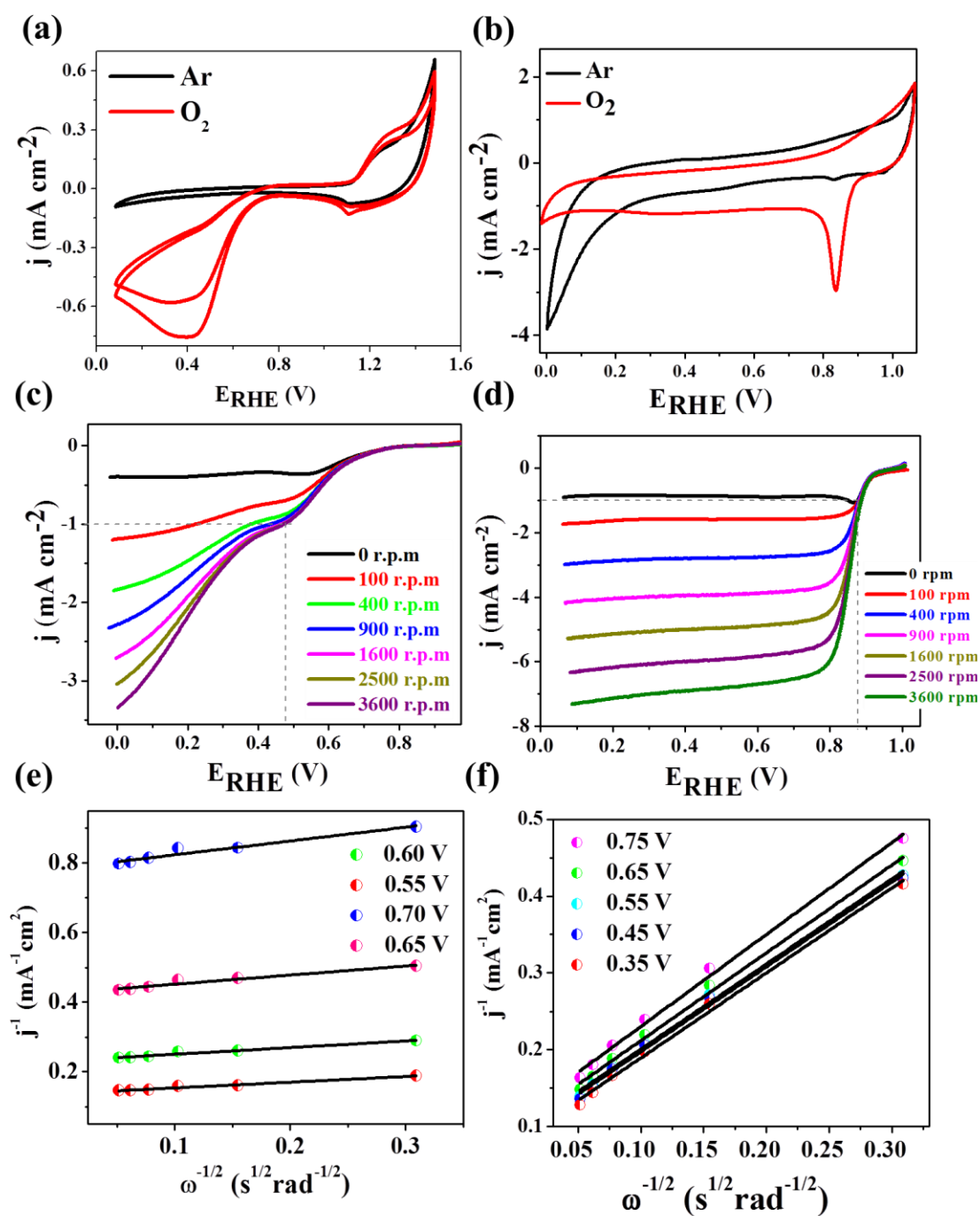


Figure 6: CVs for (a) Co-GCN, (b) Co₃O₄@Co/NCNT recorded at a scan rate of 5 mV s⁻¹ in O₂-saturated and Ar-saturated 0.1 M KOH solution, (c) LSV curves recorded at various rotation speeds for Co-GCN and (d) for Co₃O₄@Co/NCNT, (e) Koutecky-Levich (K-L) plots at different potentials for Co-GCN and (f) Co₃O₄@Co/NCNT.

Co₃O₄@Co/NCNT exhibits remarkable catalytic performance (onset potential is 0.92 V vs. RHE) for ORR affording a current density of -1 mA cm⁻² at comparatively low

overpotentials of 0.88 V as compared to Co-GCN (0.5 V) at 1600 rpm (Figure 7a). In fact, compared with commercial Pt/C, RuO₂ and IrO₂ nanomaterials applied as reference catalysts within this study, Co₃O₄@Co/NCNT reveals a very close ORR activity to that of commercial Pt/C and a superior performance than RuO₂ or IrO₂. LSV at different rotation speeds were performed showing increasing cathodic current as a function of rotation rate due to the improved mass transport (Figure 6c-d). The kinetic parameters were analysed using the Koutecky-Levich (K-L) equation. As shown in the Figure 6e-f, the linearity of the K-L plots indicate first-order reaction kinetics with respect to the dissolved oxygen concentration and the average number of electrons transferred (n) per O₂ molecule during the ORR for Co₃O₄@Co/NCNT at different potentials. For Co₃O₄@Co/NCNT, the value of n was calculated to be in the range of 3.92 to 3.96 within the potential range of 0.35 to 0.75 V, indicating the reduction of oxygen predominantly *via* the 4-electron transfer pathway. For Co-GCN, within the same potential range, n was in the range of 2.87-3.12. RRDE measurements were further carried out to monitor the hydrogen peroxide yield (% H₂O₂). As shown in Figure 7b, the amount of H₂O₂ generated decreased from 22.1% for

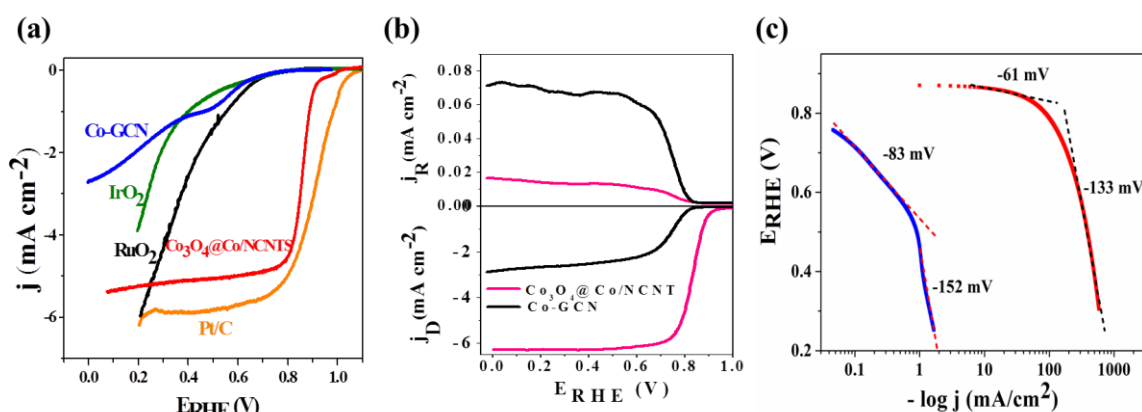


Figure 7: (a) iR corrected linear sweep voltammograms of different electrocatalysts collected at 1600 rpm in O₂-saturated 0.1 M KOH solution, (b) RRDE polarization curves for the ORR at 1600 rpm for Co-GCN and Co₃O₄@Co/NCNT, (c) ORR Tafel slopes of Co-GCN (blue) and Co₃O₄@Co/NCNT (red).

Co-GCN to 1.7% for Co₃O₄@Co/NCNT, and the calculated electron transfer number for Co₃O₄@Co/NCNT was 3.96, while it was 2.98 for Co-GCN, which is consistent with the results obtained from K-L plots based on RDE measurements. Notable differences were observed between Co-GCN and Co₃O₄@Co/NCNT clearly demonstrating that the H₂

atmosphere during pyrolysis plays an important role to produce NCNTs by favouring the formation of metallic Co nanoparticles, which in turn catalyze the growth of a $\text{Co}_3\text{O}_4@\text{Co}/\text{NCNT}$ framework. Notably, the surface area of $\text{Co}_3\text{O}_4@\text{Co}/\text{NCNT}$ is higher than that of Co-GCN. Hence, the well-structured $\text{Co}_3\text{O}_4@\text{Co}$ in $\text{Co}_3\text{O}_4@\text{Co}/\text{NCNT}$ can provide improved electron transport as compared with the disordered Co/CoO in the Co-

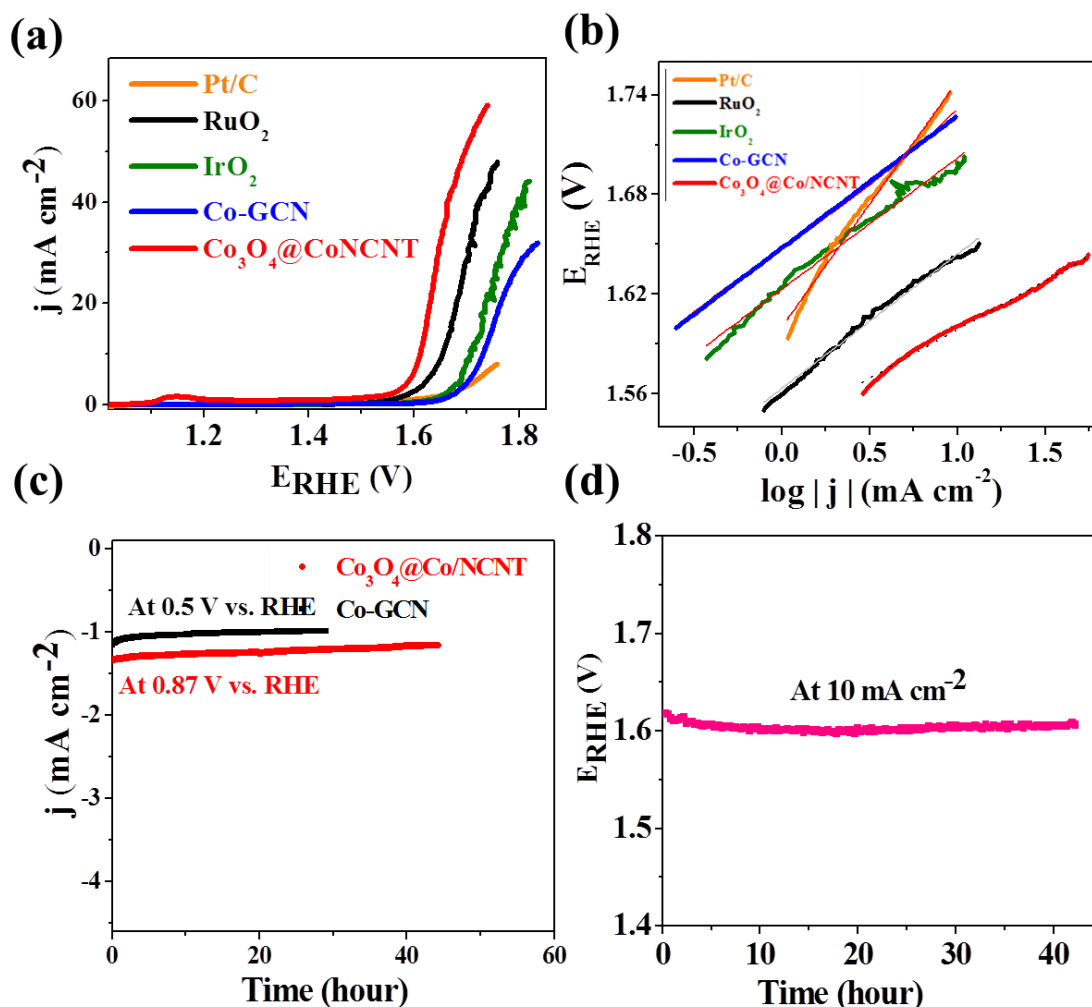


Figure 8: (a) *iR*-corrected linear sweep voltammograms of different electrocatalysts at 1600 rpm, (b) OER Tafel plots, (c) chronoamperometric stability of Co-GCN and $\text{Co}_3\text{O}_4@\text{Co}/\text{NCNT}$, (d) inset shows chronopotentiometric stability of $\text{Co}_3\text{O}_4@\text{Co}/\text{NCNT}$ at 10 mA cm^{-2} .

GCN nanostructure, which can facilitate faster mass transport of O_2 and of the electrolyte into the inner layers of the catalyst. The improved ORR activity of the $\text{Co}_3\text{O}_4@\text{Co}/\text{NCNT}$

catalyst is further suggested from the lower Tafel slope, 61 mV dec^{-1} , as compared to 83 mV dec^{-1} for Co-GCN, indicating faster reaction kinetics (Figure 7c).

Furthermore, the catalyst materials were investigated with respect to their OER activity as summarized in Figure 8. The Co-GCN nanostructure showed a comparatively lower activity reaching a current density of 10 mA cm^{-2} at 1.71 V vs. RHE at 1600 rpm . In contrast, $\text{Co}_3\text{O}_4@\text{Co/NCNT}$ attained 10 mA cm^{-2} at a potential of 1.61 V vs. RHE (Figure 8a). This value even surpasses the benchmark catalysts, RuO_2 and IrO_2 , exhibiting 1.64 and 1.69 V vs. RHE , respectively, at the same current density. The Tafel slopes for the OER of Co-GCN and $\text{Co}_3\text{O}_4@\text{Co/NCNT}$ in the potential range between 1.55 V and 1.75 V are 79.7 mV dec^{-1} and 58.7 mV dec^{-1} , respectively, while RuO_2 , IrO_2 , and Pt/C show Tafel slopes of 78.6 mV dec^{-1} , 80.7 mV dec^{-1} , and $147.8 \text{ mV dec}^{-1}$ in the same potential window, indicating 78.6 mV dec^{-1} , 80.7 mV dec^{-1} , and $147.8 \text{ mV dec}^{-1}$ in the same potential window, indicating that for $\text{Co}_3\text{O}_4@\text{Co/NCNT}$, the reaction is kinetically substantially faster, making it a highly potent electrocatalyst (Figure 8b). Another well distinguishable feature is the existence of the redox couple at $1.14/1.10$ ($\Delta E = 0.04 \text{ vs. RHE}$), which is due to the formation of $\text{Co}^{\text{III}}/\text{Co}^{\text{II}}$ (Figure 9). Thus, Co^{III} species (CoOOH) are identified as key intermediates during OER and the intensity of these bands are very low in Co-GCN.^{19,48} Notably, for $\text{Co}_3\text{O}_4@\text{Co/NCNT}$, the overpotential difference between ORR at a current density of -1 mA cm^{-2} and OER at 10 mA cm^{-2} did not exceed 0.73 V (Figure 10, and Table 1), highlighting the efficiency of $\text{Co}_3\text{O}_4@\text{Co/NCNT}$ in catalyzing both ORR and OER. The sum of the overvoltage between ORR and OER is an important parameter for evaluating bi-functional electrocatalytic activity of reversible oxygen electrodes. Values for this figure of merit, that is, the difference between the ORR potential at -1 mA cm^{-2} and OER potential at 10 mA cm^{-2} , as proposed by Jaramillo,^{9,12} are summarized in Table 1 for different catalysts. Notably, the difference of 0.73 V vs. RHE of the proposed $\text{Co}_3\text{O}_4@\text{Co/NCNT}$ is the lowest among all state-of-art catalysts, and its activity is comparable to recently reported benchmark catalysts.^{36,50} MOF pyrolyzed under reductive conditions, i.e. under H_2 atmosphere and at high temperatures ($800 \text{ }^\circ\text{C}$) and further mildly calcined yielded $\text{Co}_3\text{O}_4@\text{Co/NCNT}$, which showed a substantially enhanced bi-functional activity as compared to Co-GCN, the catalyst obtained by pyrolysis of the MOF under Ar atmosphere. We believe that the surface of $\text{Co}_3\text{O}_4@\text{Co}$ in the $\text{Co}_3\text{O}_4@\text{Co/NCNT}$ catalyst

at working potentials is different and more active than that of Co/CoO in Co-GCN surface. Another possibility is that annealing of the sample may cause discontinuities that reveal the underlying defective carbon, which increases the surface area and hence positively impacts on the ORR/OER activity. Therefore, synergistic interaction between conductive metallic Co cores and the semiconductive Co_3O_4 shell is expected to facilitate faster charge transfer reaction kinetics,^{40, 50} which is not accessible in the case of Co/CoO in Co-GCN.

Finally, the stability of a given bi-functional catalyst is a critical parameter for its robust operation in any real energy application. The catalysts were thus subjected to chronoamperometric stability tests by continuous polarization at 0.5 V for Co-GCN and

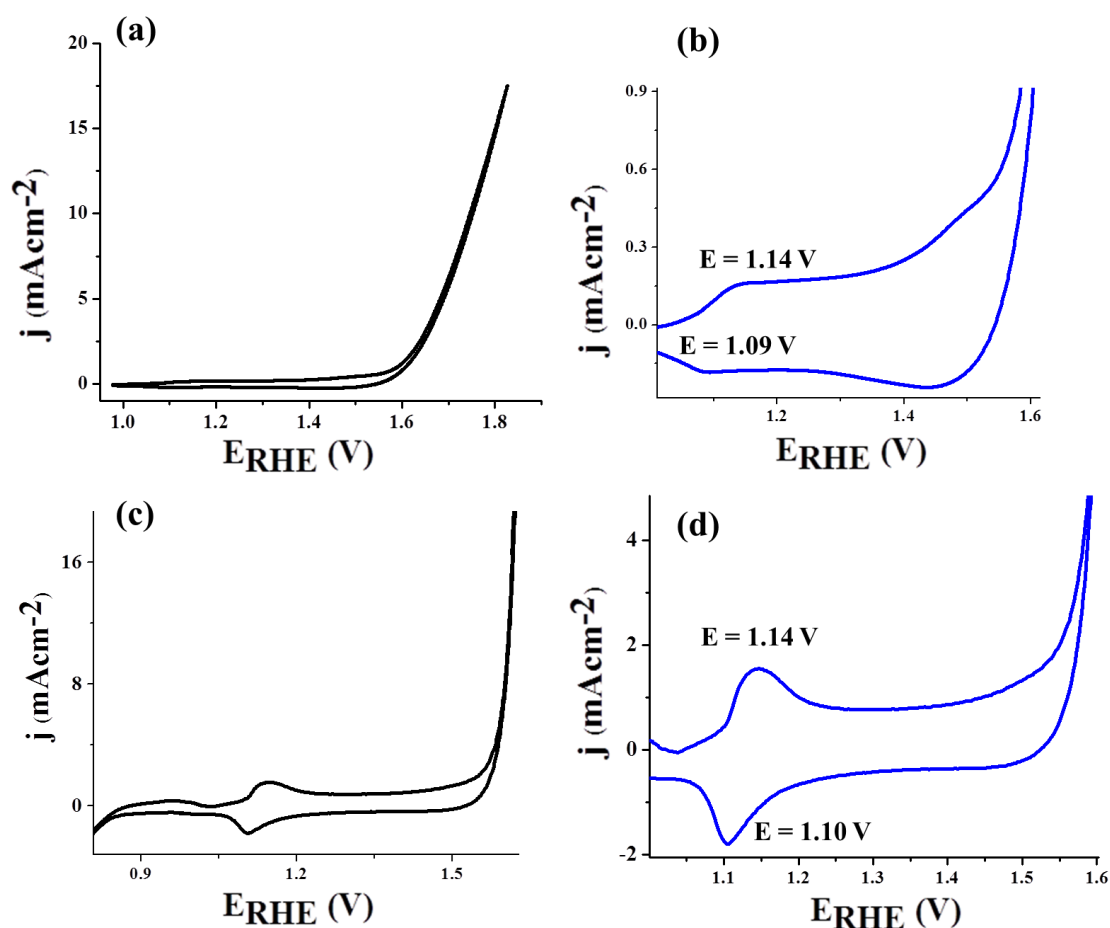


Figure 9: CV of (a) Co-GCN, (c) $\text{Co}_3\text{O}_4@Co/NCNT$ and their corresponding magnified CVs for (b) Co-GCN and (d) $\text{Co}_3\text{O}_4@Co/NCNT$, showing $\text{Co}^{\text{II}}/\text{Co}^{\text{III}}$ redox couple.

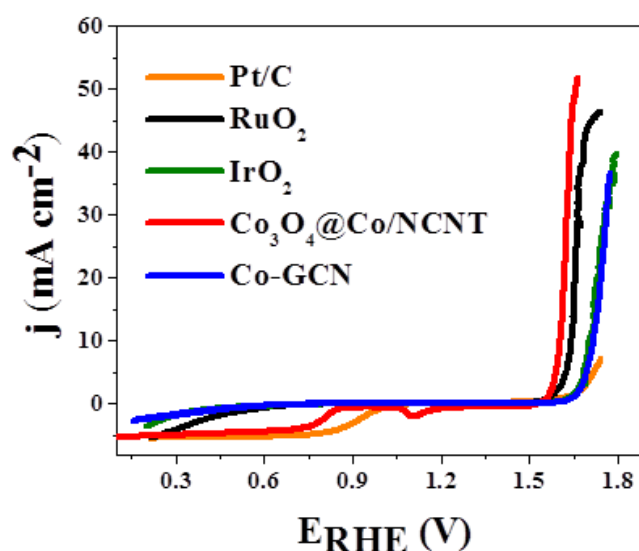


Figure 10: *iR*-corrected linear sweep voltammograms recorded at 1600 rpm in O₂ saturated solution: comparison of bi-functional electrocatalytic activities of different catalysts for ORR and OER reactions.

Table 1. The bi-functional activity of different catalysts for ORR and OER.

Catalyst	E _{ORR} (V) (E ₁) at -1 mA/cm ²	Current at half-wave potential (E _{1/2}) E _{ORR} (V)	E _{OER} (V) (E ₂) at 10 mA/cm ²	Tafel slope mV dec ⁻¹	ΔE (V) (E ₁ -E ₂)	ΔE (V) (E _{1/2} -E ₂)
Co-GCN	0.5	0.32	1.71	79.7	1.21	1.39
Co ₃ O ₄ @Co/NCNT	0.88	0.86	1.61	58.7	0.73	0.75
Pt/C	0.99	0.93	-	147.8	-	-
RuO ₂	0.56	0.38	1.64	78.6	1.08	1.26
IrO ₂	0.42	0.35	1.69	80.7	1.27	1.34

at 0.87 V for Co₃O₄@Co/NCNT (Figure 8c). Both catalysts showed excellent stability with no significant decline of the current in the course of 30-40 h of continuous polarization. Obviously, the strong intimate interaction between Co₃O₄@Co and NCNTs is leading to a highly stable material, particularly, in view of the fact that the oxide particles are embedded in a highly graphitic matrix. Co₃O₄@Co/NCNT also showed

excellent stability during OER electrolysis (Figure 8d), suggesting $\text{Co}_3\text{O}_4@\text{Co}/\text{NCNT}$ is able to tolerate harsh conditions as a bi-functional catalyst over a long period of time.

5B.4 Conclusion

In this chapter, a new $\text{N}(\text{CN})_2^-$ rich Co-MOF-1 has been chosen as sacrificial precursor for preparing metal nanoparticles embedded in a porous N-doped carbonaceous matrix at different pyrolysis conditions. Pyrolysis of the MOF under Ar atmosphere (550 °C) yielded a composite mixture of Co/CoO nanoparticles distributed in a carbon matrix. Co-MOF-1 pyrolyzed under a reductive H_2 atmosphere at high temperatures (800 °C) and further mildly calcined resulted in $\text{Co}_3\text{O}_4@\text{Co}/\text{NCNT}$, which showed greatly enhanced bi-functional activity in catalysing both ORR and OER as compared to Co-GCN. Owing to synergetic interaction between the N-doped CNT matrix and the surface of $\text{Co}_3\text{O}_4@\text{Co}$ embedded in NCNTs, $\text{Co}_3\text{O}_4@\text{Co}/\text{NCNT}$ showed excellent bi-functional catalytic activity as well as excellent stability during both the ORR and the OER. Moreover, the OER activity was even higher than that of commercial RuO_2 and IrO_2 . This clearly suggests the potential of nitrogen-rich Co-MOF-1 as novel precursor for the synthesis of $\text{Co}_3\text{O}_4@\text{Co}/\text{NCNT}$ as efficient bi-functional catalysts for the ORR and the OER.

5B.5 References

1. G. Chen, S. R. Bare, T. E. Mallouk, *J. Electrochem. Soc.* **2002**, *149*, A1092.
2. J. S. Lee, S. T. Kim, R. Cao, N. S. Choi, M. Liu, K. T. Lee, J. Cho, *Adv. Energy Mater.* **2011**, *1*, 34.
3. M. Shao, Q. Chang, J. P. Dodelet, R. Chenitz, *Chem. Rev.* **2016**, *116*, 3594.
4. D. Wang, H. L. Xin, R. Hovden, H. Wang, Y. Yu, D. A. Muller, F. J. DiSalvo, H. D. Abruça, *Nat. Mater.* **2013**, *12*, 81.
5. G. Wu, K. L. More, C. M. Johnston, P. Zelenay, *Science* **2011**, *332*, 443.
6. A. Morozan, F. Jaouen, *Energy Environ. Sci.* **2012**, *5*, 9269.
7. M. D. Allendorf, C. A. Bauer, R. K. Bhakta, R. J. T. Houk, *Chem. Soc. Rev.* **2009**, *38*, 1330.
8. M. Busch, N. B. Halck, U. Kramm, S. Siahrostami, P. Krtil, J. Rossmeisl, *Nano Energy*, **2016**, *29*, 334.

9. J. Greeley, I. E. L. Stephens, A. S. Bondarenko, T. P. Johansson, H. A. Hansen, T. F. Jaramillo, J. Rossmeisl, I. Chorkendorff, J. K. Nørskov, *Nat. Chem.* **2009**, *1*, 552.
10. M. Yagi, E. Tomita, T. Kuwabara, *J. Electroanal. Chem.* **2005**, *579*, 83.
11. K. A. Kuttiyiel, Y. M. Choi, S.-M. Hwang, G.-G. Park, T.-H. Yang, D. Su, K. Sasaki, P. Liu, R. R. Adzic, *Nano Energy*, **2015**, *13*, 442.
12. C. C. L. McCrory, S. Jung, J. C. Peters, T. F. Jaramillo, *J. Am. Chem. Soc.* **2013**, *135*, 16977.
13. J. Masa, W. Xia, I. Sinev, A. Zhao, Z. Sun, S. Grützke, P. Weide, M. Muhler, W. Schuhmann, *Angew. Chem. Int. Ed.* **2014**, *53*, 8508.
14. D. Kong, J. J. Cha, H. Wang, H. R. Lee, Y. Cui, *Energy Environ. Sci.* **2013**, *6*, 3553.
15. Z. Peng, D. Jia, A. M. Al-Enizi, A. A. Elzatahry, G. Zheng, *Adv. Energy Mater.* **2015**, *5*, 1402031.
16. L. A. Stern, L. Feng, F. Song, X. Hu, *Energy Environ. Sci.* **2015**, *8*, 2347.
17. J. Li, J. Li, X. Zhou, Z. Xia, W. Gao, Y. Ma, Y. Qu, *ACS Appl. Mater. Interfaces* **2016**, *8*, 10826.
18. Y. Zhang, B. Ouyang, J. Xu, G. Jia, S. Chen, R. S. Rawat, H. J. Fan, *Angew. Chem. Int. Ed.* **2016**, *55*, 8670.
19. J. Masa, P. Weide, D. Peeters, I. Sinev, W. Xia, Z. Sun, C. Somsen, M. Muhler, W. Schuhmann, *Adv. Energy Mater.* **2016**, *6*, 1502313.
20. Q. Li, R. Cao, J. Cho, G. Wu, *Adv. Energy Mater.* **2014**, *4*, 1301415.
21. R. Bashyam, P. Zelenay, *Nature* **2006**, *443*, 63.
22. Y. Liang, Y. Li, H. Wang, H. Dai, *J. Am. Chem. Soc.* **2013**, *35*, 2013.
23. Y. Ji, L. Huang, J. Hu, C. Streb, Y. F. Song, *Energy Environ. Sci.* **2015**, *8*, 776.
24. H. Wang, T. Maiyalagan, X. Wang, *ACS Catal.* **2012**, *2*, 781.
25. J. Liang, Y. Jiao, M. Jaroniec, S. Z. Qiao, *Angew. Chem. Int. Ed.* **2012**, *51*, 1496.
26. Y. Zhao, R. Nakamura, K. Kamiya, S. Nakanishi, K. Hashimoto, *Nat. Commun.* **2013**, *4*, 2390.
27. G. Wu, K. L. More, C. M. Johnston, P. Zelenay, *Science* **2011**, *332*, 443.
28. Z. J. Jiang, Z. Jiang, *Sci Rep.* **2016**, *6*, 27081.
29. K. Parvez, S. Yang, Y. Hernandez, A. Winter, A. Turchanin, X. Feng, K. Mullen, *ACS Nano* **2012**, *6*, 9541.
30. S. Han, D. Wu, S. Li, F. Zhang, X. Feng, *Adv. Mater.* **2014**, *26*, 849.

31. K. Shen, X. Chen, J. Chen, Y. Li, *ACS Catal.* **2016**, *6*, 5887.
32. J. R. Li, J. Sculley, H. C. Zhou, *Chem. Rev.* **2012**, *112*, 869.
33. L. E. Kreno, K. Leong, O. K. Farha, M. Allendorf, R. P. V. Duyne, J. T. Hupp, *Chem. Rev.* **2012**, *112*, 1105.
34. Y. Cui, Y. Yue, G. Qian, B. Chen, *Chem. Rev.* **2012**, *112*, 1126.
35. T. Asefa, *Acc. Chem. Res.*, **2016**, *49*, 1873.
36. J. C. Li, P. X. Hou, S. Y. Zhao, C. Liu, D. M. Tang, M. Cheng, F. Zhang, H. M. Cheng, *Energy Environ. Sci.* **2016**, *9*, 3079.
37. L. Zhang, Z. Su, F. Jiang, L. Yang, J. Qian, Y. Zhou, W. Lia, M. Hong, *Nanoscale*, **2014**, *6*, 6590.
38. W. Xia, J. Zhu, W. Guo, L. An, D. Xia, R. Zou, *J. Mater. Chem. A*, **2014**, *2*, 11606.
39. L. Shang, H. Yu, X. Huang, T. Bian, R. Shi, Y. Zhao, G. I. N. Waterhouse, L. Z. Wu, C. H. Tung, T. Zhang, *Adv. Mater.* **2016**, *28*, 1668.
40. A. Aijaz, J. Masa, C. Rçsler, W. Xia, P. Weide, A. J. R. Botz, R. A. Fischer, W. Schuhmann, M. Muhler, *Angew. Chem. Int. Ed.* **2016**, *55*, 4087.
41. T. K. Maji, R. Matsuda, S. Kitagawa, *Nature Mater.* **2007**, *6*, 142.
42. V. Chabot, D. Higgins, A. Yu, X. Xiao, Z. Chena, J. Zhang, *Energy Environ. Sci.* **2014**, *7*, 1564.
43. S. H. Johnson, C. L. Johnson, S. J. May, S. Hirsch, M. W. Cole, J. E. Spanier, *J. Mater. Chem.* **2010**, *20*, 439.
44. M. Rashad, M. R¼ising, G. Berth, K. Lischka, A. Pawlis, *J. Nanomater.* **2013**, *714853*, 1.
45. K. Artyushkova, S. Levendosky, P. Atanassov, J. Fulghum, *Top Catal.* **2007**, *46*, 263.
46. H. W. Tien, Y. L. Huang, S. Y. Yang, J. Y. Wang, C. C. M. Ma, *Carbon* **2011**, 1550.
47. H. Jin, J. Wang, D. Su, Z. Wei, Z. Pang, Y. Wang, *J. Am. Chem. Soc.* **2015**, *137*, 2688.
48. H. Yi Wang, S. F. Hung, H. Y. Chen, T. S. Chan, H. M. Chen, B. Liu, *J. Am. Chem. Soc.* **2016**, *138*, 36.
49. X. Liu, M. Park, M. G. Kim, S. Gupta, G. Wu, J. Cho, *Angew. Chem. Int. Ed.* **2015**, *54*, 9654.
50. W. Xia, R. Zou, L. An, D. Xia, S. Guo, *Energy Environ. Sci.* **2015**, *8*, 568.

Summary of Thesis and Future Outlook

The primary goal of the research contained within this thesis is design, synthesis and potential applications (gas storage/separation, photophysical and electrocatalysis) of novel metal-organic frameworks (MOFs) and MOF-derived materials in bulk and nanoscale. Our main synthetic strategy is to employ unique rational construction approach like selecting suitable molecular building block (MBB), which encompasses introducing the desired properties at the design step before actual assembly process or use of additive (capping agent) for downsizing bulk MOF to nanoscale. Depending on the applications, we have furnished pore channels, surface area and elemental composition for improvising property as discussed below.

Separation of CO₂ from flue gas and natural gas gets affected in presence of moisture, and hence, functionalized frameworks would be more helpful for better selective separation than mostly studied unsaturated metal sites (UMSs) containing frameworks. We envisage that, if these features combine with structural flexibility or dynamicity, we might get better separation materials and this concept has been detailed in chapter 2. Here, we have focused on introducing functional sites (such as NH₂, -OH or RNC=O) in pore channel for enhancing gas molecule interactions with the pore surface. Aiming this, we have chosen bpNDI (bpNDI = N,N'-bis-(4-pyridyl)-1,4,5,8-naphthalenediimide) based a two-fold interpenetrated dynamic framework $\{[\text{Zn}_2(\text{bdc})_2(\text{bpNDI})]\cdot 4\text{DMF}\}_n$ (bdc = 1,4-benzenedicarboxylate) for selective capturing of CO₂ and storing small chain hydrocarbons (e.g. C₂H₂, C₂H₄, C₂H₆ and C₃H₈) at ambient conditions. Breakthrough column experiments for binary gas mixtures, CO₂/CH₄, C₂H₆/CH₄ and CO₂/N₂ at 298 K further establishes the separation capability of this framework.

Understanding the guest responsive dynamic behaviour of flexible MOF in chapter 2, we focused on exploring novel bpNDI based frameworks in chapter 3. bpNDI is a redox-active molecule and well-known for its inherent electron accepting feature (n-type organic semiconductor). Integration of bpNDI in MOF could unfold novel photophysical properties and aiming that we have synthesized two interpenetrated and non-interpenetrated frameworks in chapter 3A and 3B, respectively. The Cd-based interpenetrated MOF $\{[\text{Cd}(\text{bpdc})(\text{bpNDI})]\cdot 4.5\text{H}_2\text{O}\cdot \text{DMF}\}_n$ (bpdc = 4,4'-biphenyldicarboxylic acid) in chapter 3A exhibits a unique photochromic behaviour resulting from inter-net strut-to-strut [bpdc to bpNDI] electron transfer. Furthermore,

impregnation of electron rich guest molecules (e.g. 1,5-/2,6-dinaphthol (1,5/2,6-DAN) and 4,*N,N*-trimethylaniline (DMPT)) into the electron deficient channels of this framework leads to very stable charge-separated states in ground state. Use of a bulkier ligand adc [$\text{H}_2\text{adc} = 9,10\text{-anthracenedicarboxylic acid}$] than bpdc, has enabled a new non-interpenetrated pillared layer framework $\{\text{Zn}(\text{adc})(\text{bpNDI})_{0.5}\cdot 2\text{H}_2\text{O}\cdot 2\text{DMF}\}_n$ in chapter 3B. The donor adc ligands being orthogonally oriented with the acceptor linkers in as-synthesized framework, involve in charge transfer interactions which transforms into complete charge separated state due to associated structural changes after removal of guest DMF molecules.

It is needless to mention that, development of nanoscale MOF has gathered special attention as there is plenty of room for tuning and improvising bulk MOF properties. Unfortunately, there is insufficient information about crystal growth and mechanistic pathways of nano MOFs, which is paramount for exploring MOFs based technology. In chapter 4, detailed in-depth studies have been carried out for understanding such concepts. In chapter 4A, synthesis, structural characterizations and gas storage properties of two new two-fold interpenetrated 3D frameworks, $\{[\text{Zn}_2(\text{bpdc})_2(\text{azpy})]\cdot 2\text{H}_2\text{O}\cdot 2\text{DMF}\}_n$ (**1**) and $\{[\text{Zn}_3(\text{bpdc})_3(\text{azpy})]\cdot 4\text{H}_2\text{O}\cdot 2\text{DEF}\}_n$ (**2**) [azpy = 4,4'-azobipyridine], have been studied from a same set of organic linkers by changing the solvent system at different temperatures. Furthermore, **1** has been downsized to nanoscale, which shows a drastic enhancement in CO_2 uptake (at 198, 273 and 293 K) than bulk analogue due to low diffusion barrier, also supported by accelerated adsorption kinetics. In chapter 4B, nano/mesoscale synthesis, characterization and growth mechanism of a mixed-linkers based 3D MOF $\{[\text{Zn}_2(\text{H}_2\text{dht})(\text{dht})_{0.5}(\text{azpy})_{0.5}(\text{H}_2\text{O})]\cdot 4\text{H}_2\text{O}\}_n$ [$\text{H}_2\text{dht} = 2,5\text{-dihydroxyterephthalic acid}$] has been studied. Addition of a suitable coordination modulator (*n*-dodecanoic acid) during MOF synthesis allowed a morphological transformation of hexagonal nanoparticle-nanorod-mesosheet driven by kinetically controlled oriented attachment (OA) growth mechanism. Hexagonal nanoparticle showed a BET surface area of $\sim 399 \text{ m}^2 \text{ g}^{-1}$, much higher than bulk analogue ($\sim 3 \text{ m}^2 \text{ g}^{-1}$) because of significant decrease in diffusion barrier in nanoscale. This has been further reflected in CO_2 uptake at 298 K, which has been implemented later for CO_2/N_2 binary gas separation. A detailed explanation for the differences in adsorption has been provided in terms of energetics of adsorption, atomic structural changes and electrostatic interactions between MOF and adsorbates.

MOF-derived carbon materials for electrochemical applications have been a pioneering research for last few years. Syntheses of MOF-derived materials provide an opportunity for tuning intrinsic material properties due to large surface area, controllable composition and pore structure. In the chapter 5, MOF derived materials have been synthesized and experimented for energy applications. A dual-MOF pyrolysis strategy has been employed in chapter 5A for the preparation of $\text{Fe}_3\text{O}_4/\text{Co}_3\text{O}_4@\text{Co}$ embedded N-doped carbon nanotube (N-CNTs) as efficient bi-functional electrocatalysts. Whereas, only $\text{Co}_3\text{O}_4@\text{Co}/\text{NCNT}$ has been studied as bi-functional electrocatalyst in chapter 5B, derived from a novel dicyanamide based nitrogen rich framework. Noticeably, both the catalysts perform better than commercially available benchmark catalysts Pt/C, RuO_2 and IrO_2 .

In summary, the topics in this thesis broadly covered the different aspects and applications of metal-organic framework (MOF) materials. The implementation of flexible interpenetrated framework in gas storage/separation would lead to work on more of such frameworks for further studies. Research on redox-active MOFs is underexplored. Our investigations have first shown that photochromism in a naphthalenediimide (bpNDI) based redox-active framework and formation of complete charge separated state on encapsulation of suitable donor guest molecules. We envision that such frameworks can be useful for photochemical CO_2 reduction, photomagnetism, and opto-electronic application. On the other hand, recently downsizing effect in nanoscale MOFs are being investigated by several groups. For the first time, we have successfully prepared a defect free 2D mesosheet MOF composed of mixed linkers via oriented attachment growth mechanism. There are reports of 2D MOF nanosheets, however, the formation mechanism is yet to be fully understood. Our successful fabrication and characterization of nano/meso scale 0D, 1D and 2D MOFs would help in future toward synthesis of multidimensional nanoscale MOFs with tunable morphologies for desirable applications. In this thesis, we have already shown how nanoscale affect the overall gas uptake, kinetics and gas separation behaviour. To our belief, this strategy can be employed to other benchmark MOF materials which would show better gas separation efficiency. Lastly, we have used dicyanamide containing Co(II) based 3D MOF as a self-sacrificial template to synthesis of porous nanocarbon electrocatalysts ($\text{Co}_3\text{O}_4@\text{Co}/\text{NCNT}$) which showed efficient bi-functional catalysis for oxygen evolution reaction (OER) and oxygen reduction reaction (ORR) with low overpotential. The concept of fabrication bi-functional (ORR and OER) electrocatalyst adopted in my thesis can be generalized to other MOF

systems as well and, therefore, impacts significantly in this field of energy and environmental sciences.

List of Publications

Included in Thesis

1. N. Sikdar, A. Hazra, T. K. Maji, *Inorg. Chem.* 2014, 53, 5993-6002.
2. N. Sikdar, K. Jayaramulu, V. Kiran, K. V. Rao, S. Sampath, S. J. George, T. K. Maji, *Chem. Eur. J.* 2015, 21, 11701-11706.
3. N. Sikdar, S. Bonakala, R. Haldar, S. Balasubramanian, T. K. Maji, *Chem. Eur. J.* 2016, 22, 6059-6070.
4. N. Sikdar, B. Konkena, J. Masa, W. Schuhmann, T. K. Maji, Submitted.
5. N. Sikdar, M. Bhogra, U. V. Waghmare, T. K. Maji, Submitted.

Not- Included in Thesis

6. N. Sikdar, D. Dutta, R. Haldar, A. J. Bhattacharya, T. K. Maji, *J. Phys. Chem. C.* 2016, 120, 13622-13629.
7. R. Haldar, N. Sikdar, T. K. Maji, *Materials Today*, 2015, 18, 97-116.
8. R. Haldar, K. L. Gurunatha, N. Sikdar, T. K. Maji, *Inorg. Chem. Front*, 2015, 2, 278-289.
9. S Roy, S Choubey, K Bhar, N Sikdar, JS Costa, P Mitra, BK Ghosh, *Dalton Transactions*, 2015, 44, 7774-7776.

Responses of the Minor Comments of Reviewer 1

1. A short commentary has been added in the synopsis part of the thesis highlighting the theme of the work.
2. A “summary of thesis and future outlook” has been added at the end of thesis.
3. Following are the responses of the minor comments made by the reviewer.

Chapter 2

1. **Page 64 (Figure 6):** A qualitative comparison of PXRD data is presented in the figure and discussed but the MeOH loaded from quite differ in my opinion. “The PXRD pattern of the MeOH exposed sample shows significant change compared to **1a** and is close to the PXRD pattern of as-synthesized **1**”. Perhaps it is the plot (and its compressed vertical scale) but these comparisons are not particularly convincing.

Response: The desolvated framework (**1a**) on MeOH exposure reverts back to close structure as as-synthesized **1** in chapter 2. We have never mentioned that the MeOH loaded structure is exactly same as the structure **1**. Framework **1** is dynamic and small changes cause structural changes. The lowest angle peak is already weak in **1** and on MeOH loading same intensity could not been achieved. On merging four PXRD patterns together, this peak is not visible much and hence, we have compressed the vertical Y-axis.

2. **Page 65-66:** The variable temperature isotherms 273-293 K suggest at room temperature (and presumably the temperature for the breakthrough experiments) that the MOF is not dynamic? Is this what is shown in Figure 7 and 8? Perhaps some discussions could be added.

Response: The MOF is dynamic as evident from stepwise CO₂ and C₂H₂ adsorption pure component isotherms at 195 K. The interactions of gas molecules with the framework are strong enough for undergoing structural changes and opening of site A at 195 K. At 273 and 298 K, the interactions are not strong enough for opening site A, therefore, second step is not observed.

3. **Page 66, Figure 8:** The figure is very complex and the PXRD data lack easily readable/relatable labels. In comparison , the PXRD data in Figure 14 is much better presented.

Response: We have enlarged the aspect ratio of the PXRD figures and replaced in the corrected thesis.

4. **Page 75:** The candidate states that the vdW-DF2 method has been satisfactorily used estimate the binding energy of C₂H₄ but no data or citations are provided to support this assertion.

Response: The binding energy of the C₂H₄ molecule as calculated by vdW-DF2 method has been given in Table 3, page 60 in chapter 2.

Chapter 3A and 3B

1. **Page 92:** Naphthalimides have been used in photosynthesis but presumably to mimic natural photosynthetic process. Perhaps this need to be reworded.

Response: Line 2 from bottom: “photosynthesis” should be “artificial photosynthesis” in chapter 3A.

2. **Page 97:** It would be easier if the NMR spectra were labelled with assignment from the various compounds in the sample (presumably ligands plus guest).

Response: The ¹HNMR spectra have been labelled accordingly in chapter 3A and replaced in the revised thesis.

3. **Page 97: 1@DMPT** appears to show some structural changes/loss of crystallinity. This should be commented upon.

Response: The PXRD pattern of **1@DMPT** in chapter 3A appears to show structural change. We have already mentioned this observation in page 109, line 6 from up. **1** is an interpenetrated framework and on guest loading it undergoes structural transformation.

4. Page 111: Please clarify for the cyclic voltammetry, what are the criteria used for reversibility? If it is peak to peak separation then this should be noted and these values provided.

Response: The criterion for reversible cyclic voltammetry is all of the initial analyte can be recovered after a forward and reverse scan cycle. For pure bpNDI in Figure 19a of chapter 3A, from the anodic (*i*_{pa}) and cathodic (*i*_{pc}) current intensity, it is evident that reduction and oxidation processes are reversible (i.e. *i*_{pa}/*i*_{pc}~1). Whereas, bpNDI molecules in framework **1**, probably do not get oxidized and reduced in a similar extent (*i*_{pa}/*i*_{pc} ≠ 1) and hence, quasi-reversible CV is obtained.

5. Page 117: The last part of summary would benefit from some rewriting to make it more concise and direct.

Response: The last part of summary in chapter 3B has been rewritten in the corrected thesis to make it more concise and direct.

6. Page 127: Raman data is often easily calculated from structural models and could support for proposed structural changes upon desolvation and water adsorption.

Response: We have already provided Raman spectra in Figure 5 of chapter 3B for understanding structural changes upon desolvation and water adsorption.

7. Page 132 (last sentence of the conclusion): The behaviour for this MOF is noted as being solvent dependent....do other coordinating solvents induce such changes?

Response: The behaviour of the MOF in chapter 3B is only DMF dependent. The other coordinating solvents do not induce such changes.

Chapter 4A and 4B

1. **Page 149/150:** The relative size of the chemdraw figures suggests a lack of care in putting these figures. Also, without integrals on the NMR signals I am not sure what this data tells us.

Response: We have changed the chemdraw figures in chapter 4A and included the integral values in the ^1H NMR plots.

2. **Page 154, Figure 6 and 7:** The caption should say “recorded” not “recoded. Also I am not convinced that the MOFs resolvate-to some extent there may be re-adsorption of solvates but the resulting materials are not very crystalline.

Response: In the respective Figure captions of chapter 4A, “recoded” should be read as “recorded”.

It is true that resolution of MOFs by solvent molecules actually is re-adsorption of solvent molecules and the desolvation-resolution process makes the crystal poor crystalline.

3. **Page 177:** The experimental section of the modulated synthesis could be rewritten to be a bit clearer (separate experimentals?)

Response: The experimental section has been already separated in chapter 4B in the thesis.

Chapter 5A and 5B

1. Page 237: References 40 and 41 seem to be mixed up.

Response: Reference 41 in line 9 from bottom in chapter 5B should be read as reference 40.

2. Page 243: Figure 6, Panel C is on a different scale compared to A.

Response: Figure 6, panel C in chapter 5B has been replaced in revised thesis.